THE DEVELOPMENT OF A HEAT TRANSFER MEASUREMENT TECHNIQUE FOR APPLICATION TO ROTATING TURBINE BLADES.

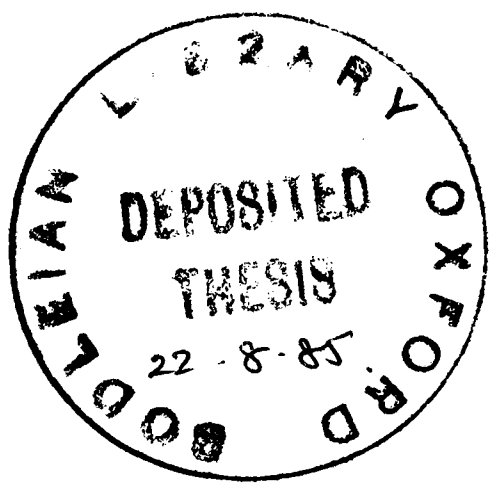

JANE E. DOORLY

SOMERVILLE COLLEGE.

March, 1985.

A thesis submitted for the degree of D.Phil, Oxford University.

Department of Engineering Science

Parks Road,

Oxford.

To Denis

CONTENTS

THE DEVELOPMENT OF A HEAT TRANSFER MEASUREMENT TECHNIQUE FOR APPLICATION TO ROTATING TURBINE BLADES.

J. E. Doorly, Somerville College.

A thesis submitted for the degree of Doctor of Philosophy of the University of Oxford, March 1985.

ABSTRACT.

The successful design of a long-lived and efficient gas turbine engine requires a good knowledge of the thermal and aerodynamic performances of the components of the turbine. Of particular importance, is the heat transfer rate from the hot gases to the cooled turbine blades, since this limits the maximum turbine entry temperatures which can be obtained.

Much gas turbine research is concentrated on experimental modelling and measurements to assist in the development of improved theoretical prediction techniques. The difficulties of instrumenting fully rotational rigs, which are necessary for a full understanding of the complex three dimensional flow in the turbine, have, however, to a large extent, limited most experimental research to stationary facilities.

A technique is described which will allow heat transfer rate measurements to be made on fully rotating test facilities using mutli-layered model turbine blades comprising an electrical insulator on a metal base. An accurate and computationally efficient method for determining the surface heat flux to a multi-layered model turbine blade is developed theoretically, together with a method for calibrating the thermal properties of the multi-layered system. This method allows the existing successful heat flux measurement technique, which utilises electronic analogue circuitry in conjunction with thin film surface thermometers on a model made from a thermal insulator, to be extended for application to multi-layered models.

The production of test models by the application of a vitreous enamel (as an electrical insulator), to a mild steel, is identified as the most suitable coating technique for experimental application.

Radiant and wind tunnel testing of multi-layered cylindrical models are described, which confirm that the method is both practical and accurate.

ACKNOWLEDGEMENTS.

There are numerous people to whom I am grateful for their advice and expertise whilst this research was performed.

I should very much like to thank my supervisor, Dr. M. L. G. Oldfield, for his guidance and help, particularly with the electronic instrumentation. Professor D. L. Schultz and Dr. T. V. Jones provided many useful suggestions on practical aspects and Professor Schultz also kindly read the thesis.

I should also like to thank members of the Turbomachinery group who contributed in many ways, especially Trevor Godfrey and John Allen for their help with model construction and thin film painting, and Kevin Grindrod, for his tunnel running expertise. I am grateful to the technical staff of the Engineering Department, at the Osney and Main Laboratory Workshops, who have always provided expert assistance. Thanks too, to Dr. Jolyon Cox and his staff, who have patiently provided excellent computer services and advice.

Assistance from other sources is also gratefully acknowledged;

Mr. Edwin Simpkins and Mr. Trevor Issitt from Ferro Enamels for their help and time;

Graham Whitehead from British Telecom Research Labs.;

Mr. Dixon-Brown and Mr. Simon Peck for performing the scanning electron and acoustic microscopy;

John Mooney, for the photographs.

The work was funded by the S.E.R.C. and N.G.T.E., whose financial assistance is acknowledged.

I am grateful to my family for all their support.

Thanks, most of all to *Denis*, without whom this thesis could not have been accomplished.

NOMENCLATURE

A	$\frac{1 - \sigma}{1 + \sigma}$
A/D	Analogue to digital
c	specific heat capacity
C	distributed capacitance/unit length
D	cylinder diameter
erf	error function
erfc	complimentary error function
h	film half width
h	heat transfer coefficient
H(t)	Heaviside function
h(t)	gauge step calibration function
H(s)	Laplace transformed step calibration function
i	current
k	thermal conductivity
k_a	analogue calibration constant
m.g.c.	machineable glass ceramic
Nu	Nusselt number
$\dot{q}_s$	surface heat transfer rate
Q	constant heat transfer rate
R,r	resistance
Re	Reynolds number

s	Laplace transform variable
T	Temperature
t	time
Tu	Overall turbulence intensity (%)
$u(t)$	unit step function
v	voltage
V_a	analogue output voltage
V_o	film set voltage
x	vertical coordinate
y	lateral coordinate
$\bar{}$	Laplace transform

Greek Symbols.

α	thermal diffusivity
α_R	temperature coefficient of resistance
λ	thermal conductivity
ρ	density
σ	$\left[\frac{\rho_2 c_2 k_2}{\rho_1 c_1 k_1}\right]^{1/2}$

Suffices

1	insulating layer
2	second layer
s	surface

Units

All values given in S.I. units

CHAPTER 1

INTRODUCTION

In times of escalating fuel costs, the desire of gas turbine engine designers to improve performance and efficiency provides a major technical challenge. It has led to extensive research programmes in material and structural design, and in combustion, heat transfer and aerodynamics. Consequently, there is a growing demand for improved test facilities, to meet the requirements of more advanced research.

The theoretical efficiency of the idealised gas turbine cycle may be shown to be a function of the pressure ratio only (i.e. the maximum/minimum cycle pressure). In practice, however, the work ratio i.e. $\frac{\text{nett work output}}{\text{turbine work}}$, depends on the turbine inlet temperature in addition to the pressure ratio; this determines the cycle susceptibility to irreversibilities, which decreases the efficiency from the theoretical value. Detailed discussions of the advantages of improved efficiency in terms of reduced specific fuel consumption are contained in AINLEY (1956) and HODGE (1955).

In addition, for a given pressure ratio, the maximum turbine entry temperature, to a large extent, determines the total power output of the plant, which is of central importance in aircraft performance. The use of higher turbine entry temperatures is constrained by the effects of the elevated temperatures on the nozzle guide vanes and turbine blades.

The arduous conditions in which turbine blades operate are such that the blades must withstand the large centrifugal loads caused by high speed rotation in the very hot operating environment, with typical conditions (as quoted by METZGER and MAYLE (1983)) of up to 9000 r.p.m. rotational speed at a radius of 0.46m, with clearances of 50μm between components, in the presence of high pressure gas (up to 30 bar) and at gas temperatures up to 1500 K.

Resistance to thermal shock and fatigue, oxidisation and corrosion are also of vital importance in determining the acceptable safe life of a turbine blade.

The successful design of a long-lived and efficient gas turbine engine depends on a good knowledge of the thermal and aerodynamic performances of the components of the turbine . The heat transfer rate from the hot gases to the cooled turbine blades is of particular importance since it limits the turbine entry temperatures that can be attained.

The turbine entry temperatures of typical modern gas turbine engines, which now reach up to 1500 K, are far higher than those at which any metal alloy or ceramic will perform with acceptable safe lives. Operation at such high temperatures has only been achieved by the use of component cooling, including film cooling, and cooling by convection in internal blade passages, which maintain the component temperatures at several hundred degrees below the inlet gas temperature. A cross section of a modern turbine blade (from an aircraft gas turbine engine) which

illustrates the typical construction and arrangement of the cooling passages is shown in figure 1.1. Cooling however, causes a loss of turbine efficiency, and the trade off between the higher permissible entry temperature and the efficiency penalty of cooling must be optimised to achieve the maximum gains.

1.2 Heat Transfer Research.

The flows in a gas turbine engine are highly complex and three dimensional, and the present state of the numerical computation of these flows is still not sufficiently reliable for heat transfer design purposes. Consequently, much gas turbine research is concentrated on experimental modelling and measurements. The measurements of the various parameters necessary for the development of high temperature gas turbines depends on a realistic laboratory simulation of real engine flow. The fully rotational experiment is obviously the most desirable test situation, but the operational costs and associated instrumentation difficulties have severely limited research in this area. Development trials inevitably employ fully rotating systems, but the limitations on instrumentation restrict the quantity parameters which may be observed.

Transient cascade facilities such as the Isentropic Light Piston Tunnel at Oxford provide a useful means of investigating the behaviour of two dimensional cascades of turbine blades, in particular the heat transfer and aerodynamic performance. The use of thin film resistance thermometers (SCHULTZ and JONES (1973)) for the measurement of heat transfer rate is well proven. This technique utilises model turbine blades made from a material such as machineable glass ceramic, which can be readily machined and instrumented with such transducers.

The question remains, however, of how far these essentially steady simulations of engine flow give sufficiently reliable indications of the performance under the actually highly unsteady engine conditions.

The flow which passes through the first high pressure turbine stage and through subsequent stator and rotor stages is unsteady in nature. The vigorous mixing processes which occur in the combustion chamber of a gas turbine produce high levels of turbulence in the resulting flow at the exit (SCHAFER et al 1971). Periodic unsteadiness in the flow is generated by the relative rotation of the rotor and stator stages in the turbine, since any distortions in the stator exit flow result in a periodically varying rotor inlet flow. The major flow distortion results from the boundary layer, which develops on the blade surfaces forming a wake at the trailing edge, which is then swept into the passages in the succeeding stages.

In addition to the wakes, distortions are produced by the secondary flow which develops along the hub casing and at the blade tip, and is also swept into the blade passages in the following stages, adding to the unsteadiness. The relative motion of the blades in the alternately rotating and stationary blade rows of a turbomachine also produces unsteadiness through the interaction of the potential flow fields around each blade.

Recent work (DOORLY (1983), HODSON (1983), DRING (1982) and PFEIL (1982)), has shown that the flow unsteadiness profoundly affects the transition of the boundary layer on the blade surface. The unsteady boundary layer effects have a major effect on the heat transfer rate as shown particularly by the work of DOORLY (1983,1985) and DUNN (1984).

Theoretical methods for predicting the heat transfer rates to turbine blades are necessarily simplistic in terms of the flow they aim

to model. As discussed by RUDEY and GRAHAM (1984), evidence strongly suggests that the ability to estimate critical metal temperatures and heat transfer rates is deficient in the accuracy and certainty required for design practice. METZGER and MAYLE (1983) discuss the state of the art in terms of the limitations of the present experimental facilities available, and argue that there is an urgent need for definitive instrumentation and testing of actual engines to provide more information on details of hot gas flow.

Consequently, investigations into the effects of the unsteady flow are imperative for a fuller understanding of the heat transfer situation in an engine. Such investigations necessitate the development of measurement techniques, which can then be adapted to high speed rotating rig facilities. The essential requirements of such heat flux instrumentation and measurement techniques would include frequency response, robustness, accuracy and suitability for warm and hot rigs.

Contents of this thesis.

In the course of the present work, a technique has been developed which will allow heat transfer rate measurements to be made on fully rotating test facilities. The method of obtaining heat transfer rate distributions in the Isentropic Light Piston Tunnel, (which has been in use at Oxford for the past decade), of instrumenting machineable glass ceramic blades with thin film resistance thermometers, is not suitable for use where the blade profiles are of a highly three dimensional nature, or for use in a fully rotating rig, because of the high tensile stress present in the blades. The technique developed here to overcome these difficulties proposes the use of metal blades coated with an

electrically insulating layer which can then be instrumented with thin film resistance thermometers.

Chapter 2 discusses the present techniques and methods for measuring heat transfer rate in stationary rigs and rotating facilities, and indicates the limitations of these techniques and the consequent desirability for more suitable methods.

Chapter 3 contains the theory behind the use of the conventional heat transfer gauge, on a single layer semi-infinite substrate. The temperature response of a thin film resistance thermometer on the surface of two-layered substrates, for the cases where the second layer is semi-infinite or finite, is considered.

A general theory for obtaining the heat transfer rate from thin film resistance thermometers on multi-layer substrates is developed and this is related to the existing method for thin film gauges on one-layer semi-infinite substrates.

The existing calibration methods of determining the constants required for obtaining the heat transfer rate from the surface temperature signal of the film gauge on single-layered semi-infinite substrates are briefly outlined in Chapter 4. The theoretical analysis which has now led to a new method to calibrate the gauges on multi-layered substrates is detailed. The deviations from the one-dimensional theory are discussed and analytic and numerical methods of predicting the effects are considered. The associated electronic instrumentation which is required for calibrating the new gauges is also described.

Chapter 5 describes the technological development of the gauges and the attempts to provide instrumented two-layer media for the validation of the calibration technique. The production of the most suitable electrically insulating layer, which was developed for simple and economic use on turbine blades is also discussed.

Calibrations from samples of two-layer media including two-layer flat plates and cylinders are presented in Chapter 6, illustrating the successful application of the methods derived theoretically in Chapters 3 and 4.

Chapter 7 describes the results of stagnation point heat transfer measurements obtained on two-layer circular cylindrical models which were tested in the Isentropic Light Piston Tunnel at Oxford. The processing method of chapters 3 and 4 are applied to the results and the heat transfer results compared with an accepted empirical correlation based on a large number of results, to illustrate the accuracy with which the new gauge can be used to measure heat transfer rate.

Chapter 8 contains the conclusions and suggestions for future work.

CHAPTER 2

HEAT TRANSFER RESEARCH

2.1 Current methods of measuring heat transfer rate

As has been discussed in Chapter 1, accurate knowledge of the heat transfer rate distribution to the various components of the gas turbine engine is essential for improved component design.

There are several types of test facilities and associated techniques of instrumentation for obtaining heat transfer measurements on gas turbine components. These facilities include the long run time steady-state cascade facility, the short duration cascade facility, the shock tube and the fully rotating engine test facility.

Detailed descriptions of the techniques of heat transfer measurement in transient facilities are contained in SCHULTZ and JONES (1973). BAYLEY and TURNER (1968) deal with general methods of heat transfer measurement as does JONES (1977). The following discussion is therefore restricted to

specific applications of heat transfer measurement techniques in particular test facilities, which are of relevance to the present study.

TURNER (1971) showed how the heat transfer coefficients around a turbine blade could be obtained from the steady state measurements of the surface temperature, together with a knowledge of the internal heat transfer conditions. In this case the blade was cooled internally using cooling air passages. The two dimensional Laplacian equation

$$\nabla^2 T = 0$$

was solved numerically and using the measured external blade surface temperature and the heat transfer rate to the internal passages, (derived from a knowledge of the coolant mass flow and temperature increase,) as boundary conditions, TURNER obtained the external heat transfer coefficients.

BAYLEY and MILLIGAN (1977) and BAYLEY and PRIDDY (1980) have subsequently used TURNER's method to determine the effect on the mean heat transfer rate distribution to a rotor blade, of high levels of freestream turbulence produced by a rotating "squirrel cage" turbulence generator. BAYLEY and MILLIGAN used two methods for measuring the surface temperature, a thick and a thin walled model. As discussed by DANIELS (1978), however, both of these methods suffer from the problem that errors caused by measuring the surface temperature at only a finite number of thermocouple locations results in greatly magnified errors in computed heat transfer rate.

Studies by HUFF (1969 and 1970) into the heat transfer to a rocket nozzle involved imposing a simple harmonic perturbation on the gas mainstream temperature. A similar method was adopted by BARRY et al (1982) and BEACOCK et al (1982), for determining local convective heat transfer coefficients around a thin walled (hollow) gas turbine rotor

blade, which was cooled internally (figure 2.1). The rotor blade was mounted in a cascade and was subjected to a steady mainstream flow. An independent cooling air flow whose temperature was varied sinusoidally over a range of frequencies, was fed to its interior. Thermocouples were used to measure the external gas temperature T_g , the coolant temperature T_c and the local wall temperatures at various positions on the model perimeter. It was shown theoretically that the knowledge of these temperatures, and examination of the frequency response of the wall temperature to a variation of the coolant temperature, would enable the external and internal heat transfer coefficients to be calculated. Application of the method to determine heat transfer coefficients on a cooled circular cylinder model in crossflow produced results which agreed well with published data, but the authors found that circumferential heat conduction produced a flattening of the heat transfer coefficient distribution. The technique was subsequently successfully applied to measure the heat transfer coefficients to a nozzle guide vane. In particular, however, for regions of very localised high heat transfer rate, such as at the blade leading edge, the effect of lateral conduction could not be satisfactorily corrected with the density of thermocouples considered to be practical.

MICHARD (1970) using a thin wall calorimeter technique, measured the heat transfer to a cascade of turbine aerofoils, by perturbing the external conditions with a step change in the mainstream gas temperature.

LOUIS (1977) used a transient hot blow down facility at M.I.T. to measure heat transfer rate and film cooling effectiveness to a highly loaded rotating rotor blade. Heat transfer rates were measured with calorimetric gauges. These comprised a thin aluminium or copper disc of thickness 0.5mm embedded in a teflon cap with a thermocouple fixed on the back. A detailed treatment of the calorimetric gauge and its use is given

in SCHULTZ and JONES (1973) and JONES (1977). The major problem with this technique lies in the fact that the calorimeter is usually of a different material from the blade model and hence there is a temperature discontinuity between the calorimeter and the blade. SCHULTZ and JONES (1973) give an analysis based on KAYS (1966) which shows that this effect may be large, and methods of correcting for the errors are given for the cases of laminar or fully developed turbulent flat plate boundary layers. In view of the rapid changes caused by a developing boundary layer on a blade, however, discontinuities in surface temperature cannot be satisfactorily corrected .

MARTIN, BROWN and GARRETT (1977) used a transient method with surface thermocouples attached to copper inserts in blades made from syndanio-asbestos, an insulator. The blades were suddenly introduced into the hot flow and the temperature-time response of the thermocouples was used to determine the local heat transfer coefficients. Again, this method suffered from the problems of the discontinuities mentioned above, which could not be satisfactorily resolved.

The desirability of transient methods for the measurement of heat transfer rates is such that major research programs using it have been undertaken during the last decade. The costs of providing the power levels of the order of 1MW or greater, necessary to achieve the conditions of high temperatures and pressures in continuous and fully rotating facilities, and for full scale engine Reynolds and Mach number simulation, have made transient facilities particularly attractive.

The energy requirements of a short duration wind tunnel are much lower than for continuous facilities. The model to be tested may be started at room temperature and the flow duration is so short that temperature rises in the working section and the model are small. Hence it is unnecessary to use expensive high temperature materials. SCHULTZ

and JONES et al (1977) describe the development of a transient cascade facility for testing two dimensional cascades of nozzle guide vanes at full scale engine Reynolds and Mach numbers. The basis of the transient cascade facility is the use of a free light piston compressor which produces uniform flow conditions for up to 1 second. The principle of the method is described in JONES, SCHULTZ et al (1973). Amongst the advantages of this type of facility are the ease with which detailed heat transfer rate and pressure measurements can be obtained. Machinable glass models (Corning Macor) instrumented with thin film surface resistance thermometers which are deposited or painted onto the surface, are used for heat transfer rate measurements. The techniques and high speed data acquisition systems are described in OLDFIELD, JONES and SCHULTZ (1978).

The same transient technique in a similar facility has subsequently been applied at the Von Karman Institute by CONSIGNY and RICHARDS (1981).

The effects of unsteadiness with frequencies ranging from as low as 100Hz to high as 100 kHz, on the heat transfer and aerodynamic performances of gas turbine components have until recently received little attention, largely as a result of the difficulties of measuring the appropriate parameters.

DUNN and HAUSE (1982) and DUNN (1984), attempt to fill this gap by making measurements of the mean heat transfer rate on a fully rotating turbine stage, in a shock tube which provides a short duration flow, using well proven transient techniques. Miniature thin film gauges were used to obtain the heat transfer rate measurements. The gauges, platinum thin film resistance thermometers on a pyrex plug of thickness 0.7mm and diameter 0.97mm were held in the turbine components by an epoxy adhesive. Again this method suffers from surface discontinuities in temperature and

surface height , the latter resulting from the difficulties of flush mounting the gauges so that the extremely thin boundary layer is not disturbed. Mean results showed a significant increase in the stator heat transfer level, owing to the presence of the downstream rotor, but lack of suitable instrumentation so far prevented detailed measurements on the rotor.

DRING et al (1982) used heated custom made DISA films which were mounted in chemically etched surface depressions, to measure the fluctuating skin friction on the rotor of a low speed rotating rig. The measurements were unscaled and intended to provide qualitative information about the unsteady boundary layer. Mean heat transfer measurements were obtained using two stator models fabricated from foam wrapped in stainless steel foil of thickness 0.0001 ins, which was glued to the surface. An electrical current was passed through the foil producing a nearly uniform surface heat flux. Thermocouples on the back of the foil were used to measure the surface temperature and thus the heat transfer coefficients were obtained. The effect of the passing rotor on the upstream stator boundary layer was found to have a significant effect.

More recently DOORLY (1983,1985)) using the I.L.P.T. at Oxford, examined the effects of "wake-passing" on the heat transfer rate to a turbine blade, by using a wake-generator comprising a turbine driven disc on which bars of appropriate diameter were mounted, to generate wakes upstream of a stationary cascade of rotor blades. Very high frequency heat transfer measurements (using the standard Oxford technique described above) were made. These measurements , in conjunction with high speed pressure and flow visualisation, successfully resolved, in clear detail, the unsteady transition behaviour responsible for the heat transfer fluctuations.

EPSTEIN et al (1984) describe a short duration blowdown facility which is capable of testing aircraft turbine stages at simulated engine conditions, with the aim of investigation of the effects of the unsteady three dimensional flow found in gas turbine stages. The test time is typically between 0.1 and 1 second, which is equivalent to between 1,000 and 10,000 blade passings. Surface heat flux is measured using temperature difference measurements across an insulator which is stuck onto the profile surface. Two temperature sensors, thin film resistance thermometers, are vacuum deposited on either side of an insulating material (a polyimide, KAPTON, of thickness 25μm. Below a certain frequency there is a direct relation between surface heat transfer rate and the temperature drop across the insulator. For frequencies above a certain level, the substrate appears semi-infinite to the upper thin film resistance thermometer. So the d.c. or low frequency heat transfer signal is measured and the a.c. component can be calculated. The study showed that for frequencies above 1.5kHz, the semi-infinite approximation was valid.

The major disadvantage of this technique lies in the construction and application of the gauges to the blade profile. The use of a polyimide such as Kapton, restricts the operating temperatures to below about 200^{o}C and limits the locations on a highly 3-D blade, where thin film resistance thermometers can be placed. Vacuum deposited gauges on such an insulating substrate have limited tolerance to bending. During the application of such transducers to, for example, the leading and trailing edges of a turbine blade, the tension produced in the metallic film element will result in cracking of the film.

GODEFROY (1981) describes the construction of similar thin film transducers for temperature and steady state heat transfer rate measurements. These comprised two thermocouples in two layers, deposited

on either side of a thin piece of Kapton, typically between 13 and 50 μm thick, figure 2.2, from which the steady state heat flux can be obtained from

$$\Phi = \frac{\lambda}{d} (T_s - T_d)$$

where λ is the thermal conductivity of the insulator, d is the thickness of the Kapton and T_s and T_d are the temperatures at the surface and backface respectively. A second leaf of Kapton was glued to the back of the first, using Epoxy glue and the whole was glued to the blade profile. Glue layers of only 2μm were obtained, after extensive research.

The previous discussion has shown that the current techniques of measuring the heat flux to turbine blades suffer from limitations of one form or another. These limitations render them unsuitable (to varying degrees) for application to studies of mean and unsteady heat transfer rate under more realistic simulations of the engine flow. Clearly there is thus a need for a method of instrumenting a turbine blade surface with heat transfer gauges such that the materials used in both blade and gauge manufacture will tolerate the high stresses caused by rotation, and will not disturb the temperature or boundary layer on the blade surface by temperature discontinuities.

CHAPTER 3

THEORY OF MULTI-LAYER HEAT TRANSFER GAUGES.

3.1 Gauges on single layer substrate.

The simplest heat transfer gauge considered here consists of a thin metal film deposited on the surface of an electrically insulating medium, which is used as a resistance thermometer (figure 3.1). The change in the resistance of the film (and hence the change in voltage across it), is proportional to the surface temperature, and it possible to extract the heat transfer rate from the measured surface temperature signal.

The theory and use of the thin film resistance thermometer to measure heat transfer rate to a one-layer semi-infinite medium was first extensively considered by VIDAL (1956). A complete treatment of thin and thick gauges is given by SCHULTZ and JONES (1973). It was shown that for most practical applications that it is valid to assume that the presence of the thin film thermometer could be considered to have negligible effect on the heat

transfer history. Typically for a film of thickness 0.1μm, the measured heat transfer rate was shown to be in error by 5% after 0.4μs, and 1% after 120μs.

For comparison with the analysis of gauges on multi-layer substrates, developed in the course of this work, a brief summary of the analysis for the simplest case of a gauge on a single layer semi-infinite substrate will now be given.

The one-dimensional heat conduction equation governs the flow in the substrate (figure 3.2) so

$$\frac{\partial^2 T}{\partial x^2} = \frac{1}{\alpha}\frac{\partial T}{\partial t} \qquad (3.1)$$

here α is the thermal diffusivity of the material, $\alpha = \frac{k}{\rho c}$, k is the material thermal conductivity, ρ is the material density and c is the material specific heat capacity.

The corresponding boundary conditions are

$$-k\frac{\partial T}{\partial x} = \dot{q}_s \qquad \text{on } x = 0 \qquad (3.2a)$$

$$T = 0 \qquad \text{at } x = \infty \qquad (3.2b)$$

with the initial condition

$$T = 0 \qquad \text{at } t = 0 \qquad (3.3)$$

where $\dot{q}_s$ is the heat transfer rate at the surface. Taking the Laplace transform of equation (3.1) gives

$$\bar{T} = \frac{\bar{\dot{q}}_s}{(\rho c k s)^{1/2}} \exp\left(-x\left[\frac{s}{\alpha}\right]^{\frac{1}{2}}\right) \qquad (3.4)$$

where the overbar denotes the Laplace transformed function and s is the transformed time variable.

At the surface x = 0, so the surface temperature $\bar{T}_s$ is given by

$$\bar{T}_s = \frac{\bar{\dot{q}}_s}{(\rho c k s)^{1/2}} \qquad (3.5)$$

If $\dot{q}_s$ is a step at t = 0, i.e. constant heat transfer rate then

$$\bar{\dot{q}} = \frac{Q}{s} \qquad \text{where Q is a constant}$$

hence
$$\bar{T}_s(s) = \frac{Q}{s^{3/2}(\rho c k)^{1/2}} \qquad (3.6)$$

and
$$T_s(t) = 2\,\frac{Q}{(\rho c k)^{1/2}}\left[\frac{t}{\pi}\right]^{1/2} \qquad (3.7)$$

so the resulting surface temperature is parabolic. For the general case where $\dot{q}_s$ is not constant equation (3.5) can be inverted using the convolution theorem to give

$$T_s(t) = \frac{1}{(\rho_1 c_1 k_1 \pi)^{1/2}} \int_0^t \frac{\dot{q}_s(\tau)}{(t-\tau)^{1/2}}\, d\tau \qquad (3.8)$$

In this case, the heat transfer rate is then given by

$$\bar{\dot{q}}_s(s) = (s\rho ck)^{1/2}\,\bar{T}_s = s\,\bar{T}_s\,\frac{1}{s^{1/2}}\,(\rho ck)^{1/2} \qquad (3.9)$$

Inverting this, again using the convolution theorem, gives

$$\dot{q}_s(t) = \left[\frac{\rho ck}{\pi}\right]^{1/2}\frac{1}{\sqrt{\pi}}\int_o^t \frac{\frac{\partial(T(\tau)}{\partial\tau}\,d\tau}{(t-\tau)^{1/2}} \qquad (3.10)$$

This can be simplified by putting $T(t) - T(\tau) = z$ as in SCHULTZ and JONES (1973) and integrating by parts to give

$$\dot{q}_s(t) = \left[\frac{\rho ck}{\pi}\right]^{1/2}\left[\frac{T(t)}{\sqrt{t}} + \frac{1}{2}\int_o^t \frac{(T(t) - T(\tau))\,d\tau}{(t-\tau)^{3/2}}\right] \qquad (3.11)$$

Although it is possible to compute $\dot{q}_s$ from a digitally recorded temperature signal, using numerical methods which reduce the errors caused by the singularity in the integral at $t = \tau$, the numerical error when digitising the film voltage waveform produces noise on the calculated $\dot{q}_s$ signal, (OLDFIELD et al (1978)). Such errors can be appreciable, since the resolution of the majority of analog to digital converters (A/D's) in use are limited to 10 bits. Even where digitisation errors are minimised by using higher resolution A/D converters, it is more convenient to use an

electrical analogue to perform the T to $\dot{q}$ transformation, (MEYER, (1960 and 1963)).

A continuous resistance capacitance transmission line is governed by the equations (figure 3.3)

$$\frac{\partial i}{\partial x} = -C\frac{\partial v}{\partial t} \qquad (3.12)$$

$$i = -\frac{1}{r}\frac{\partial v}{\partial x} \qquad (3.13)$$

$$\frac{\partial^2 v}{\partial x^2} = rC\frac{\partial v}{\partial t} \qquad (3.14)$$

where C is the distributed capacitance per unit length and r is the distributed resistance per unit length.

The equations for the flow of heat in a semi-infinite medium are

$$\frac{\partial \dot{q}}{\partial x} = -\rho c\frac{\partial T}{\partial t} \qquad (3.15)$$

$$-\dot{q}_s = k\frac{\partial T}{\partial x} \qquad (3.16)$$

$$\frac{\partial^2 T}{\partial x^2} = \frac{\rho c}{k}\frac{\partial T}{\partial t} \qquad (3.17)$$

Taking the Laplace transform of equation (3.14) gives

$$\frac{d^2\bar{v}}{dx^2} = src\bar{v} \qquad (3.18)$$

and hence

$$\bar{i} = s^{1/2}\left[\frac{C}{r}\right]^{1/2}\bar{v} \qquad (3.19)$$

Comparing equation (3.19) with equation (3.5) it can be seen that $\dot{q}$ is analogous to i and T to v.

A typical analogue is shown in figure 3.4. The current source is adjusted so that for temperature = 0, the film voltage is v_o. Hence, the voltage when the film is at any temperature T is given by

$$v = \alpha_R v_o T \qquad (3.20)$$

where α_R is the temperature coefficient of resistance of the film.

and

$$R = R_0 (1 + \alpha T) \qquad (3.21)$$

The current $$\bar{i} = s^{1/2} \left[\frac{C}{r} \right]^{1/2} \alpha_R v_0 \bar{T} \qquad (3.22)$$

so $$\bar{\dot{q}}_s = (s\rho ck)^{1/2} \bar{T}_s = \frac{(\rho ck)^{1/2}}{\alpha_R v_o} \left[\frac{r}{C} \right]^{1/2} \bar{i} \qquad (3.23)$$

Hence the surface heat transfer rate is directly proportional to the analogue current i. Full details of the analogue design are given in SCHULTZ and JONES (1973), together with the techniques used to calibrate the analogue electronically to determine the parameter $\frac{r}{C}$. Details of an analogue with a bandwidth of 0.1Hz to 100kHz, suitable for measuring fluctuations in heat transfer rate over a very wide frequency range, are given in OLDFIELD et al (1982).

The important criterion for the use of a thin film gauge on a single layer medium is the determination of the thickness of the insulator required in order that the material may be considered to be semi-infinite. Such a criterion was established by SCHULTZ and JONES (1973), by considering the

heat transfer rate at a distance x into the substrate ($\dot{q}_x$) , when a step in heat transfer was applied to the surface ($\dot{q}_s$). They showed that

$$\frac{\dot{q}_x}{\dot{q}_s} = \text{erfc} \frac{x}{\sqrt{(4\alpha t)}}$$

so that for an acceptable criterion, such as a 1% heat loss at the backwall, the appropriate minimum thickness of the insulator was determined in order that it should appear semi-infinite.

3.2. Gauges on a two-layered substrate.

The analysis which led to the method for using a thin film resistance thermometer on the surface of a two-layered composite, was developed in the course of this work by considering the temperature response of the film, where the surface is subject to a step in heat transfer rate. Such a composite, might, for example, comprise an electrically insulating layer on a metal base), to measure heat transfer rate, Two types of composite substrate will be considered; the first case is that of an insulating layer on a "semi-infinite" metal base, and the second is that of the insulating layer on a finite metal base.

3.2.1 Insulating layer on semi-infinite metal base.

This system is shown in figure 3.5. The thin film resistance thermometer is again assumed to be sufficiently thin to have negligible effect on the heat transfer processes.

The governing equations are

$$\frac{\partial^2 T_1}{\partial x^2} = \frac{1}{\alpha_1}\frac{\partial T_1}{\partial t} \qquad 0 < x < a \quad \text{region 1} \qquad (3.24)$$

$$\frac{\partial^2 T_2}{\partial x^2} = \frac{1}{\alpha_2}\frac{\partial T_2}{\partial t} \qquad a < x < \infty \quad \text{region 2} \qquad (3.25)$$

with the boundary conditions

$$-\dot{q}_s = k\frac{\partial T_1}{\partial x} \qquad \text{on } x = 0 \qquad (3.26)$$

$$T_1 = T_2 \qquad \text{on } x = a \qquad (3.27)$$

$$k_1\frac{\partial T_1}{\partial x} = k_2\frac{\partial T_2}{\partial x} \qquad \text{on } x = a \qquad (3.28)$$

and $$T_2 = 0 \qquad \text{on } x = \infty \qquad (3.29)$$

Taking the Laplace transforms of (3.24) and (3.25) and solving for $\bar{T}_1$ and $\bar{T}_2$ gives

$$\bar{T}_1 = \frac{\bar{\dot{q}}_s}{(\rho c k s)^{1/2}} \frac{[(1+\sigma)\exp\{-(x-a)(s/\alpha_1)^{1/2}\} + (1-\sigma)\exp\{x-a)(s/\alpha_1)^{1/2}\}]}{(1+\sigma)\exp(a(s/\alpha_1)^{1/2}) - (1-\sigma)\exp(-a(s/\alpha_1)^{1/2})}$$

.....(3.30)

$$\bar{T}_2 = \frac{2}{\bar{k}_1}\bar{\dot{q}}_s\left[\frac{\alpha_1}{s}\right]^{1/2}\frac{\exp\{(a-x)(s/\alpha_2)^{1/2}\}}{[(1+\sigma)\exp\{a(s/\alpha_1)^{1/2}\} - (1-\sigma)\exp\{-a(s/\alpha_1)^{1/2}\}]} \qquad (3.31)$$

where $\sigma = \left[\frac{\rho_2 c_2 k_2}{\rho_1 c_1 k_1}\right]^{1/2}$

If the heat transfer rate is constant for $t > 0$, then $\bar{\dot{q}}_s = \frac{Q}{s}$

and so, if the initial condition $T_1 = T_2 = 0$ is prescribed for $t < 0$, then

$$\bar{T}_1 = \frac{Q \; e^{-xa\sqrt{(s/\alpha_1)}}}{(\rho_1 c_1 k_1)^{1/2} s^{3/2}} \left[\frac{1 + A \exp\{2(x-a)(s/\alpha_1)^{1/2}\}}{1 - A \exp\{-2a(s/\alpha_1)^{1/2}\}}\right] \qquad (3.32)$$

where $A = \frac{1-\sigma}{1+\sigma}$

$$\text{and } \bar{T}_2 = \frac{2 \; Q \; e^{-xa\sqrt{(s/\alpha_1)}}}{(1+\sigma)(\rho_1 c_1 k_1)^{1/2} s^{3/2}} \left[\frac{\exp\{(a-x)(s/\alpha_2)^{1/2}\}}{1 - A \exp\{2a(s/\alpha_1)^{1/2}\}}\right] \qquad (3.33)$$

By expanding the denominator, $\bar{T}_1$ can be written as

$$\bar{T}_1 = \frac{Q}{(\rho_1 c_1 k_1)^{1/2} s^{3/2}} \left[\exp\{-x(s/\alpha_1)^{1/2}\} + \sum_{n=1}^{n=\infty} A^n \left[\exp -(x+2na)\frac{\sqrt{s}}{\sqrt{\alpha_1}} + \exp(x-2na)\frac{\sqrt{s}}{\sqrt{\alpha_1}}\right]\right]$$

.....(3.34)

and expanding the denominator of (3.33) gives

$$\bar{T}_2 = \frac{2Q}{(1+\sigma)(\rho_1 c_1 k_1)^{1/2} s^{3/2}} \sum_{n=0}^{n=\infty} A^n \exp\left[s^{1/2}\left[\frac{-2(n+1)a}{\sqrt{\alpha_1}} + \frac{(a-x)}{\sqrt{\alpha_2}}\right]\right] \qquad (3.35)$$

Inverting equation (3.34) gives

$$T_1(x,t) = \frac{Q}{(\rho_1 c_1 k_1)^{1/2}} \left[2(t/\pi)^{1/2} \exp\left[-\frac{x^2}{4\alpha_1 t}\right] - \frac{x}{\alpha_1} \operatorname{erfc}\left[\frac{x}{2(\alpha_1 t)^{1/2}}\right] + \right.$$

$$+ \sum_{n=1}^{\infty} \frac{2\sqrt{t}}{\sqrt{\pi}} A^n \left[\exp-\frac{(x+2na)^2}{4\alpha_1 t} + \exp-\frac{(x-2na)^2}{4\alpha_1 t}\right] -$$

$$\left. \sum_{n=1}^{\infty} \frac{2\sqrt{t}}{\sqrt{\pi}} A^n \left[\frac{(x+2na)}{\sqrt{\alpha_1}} \operatorname{erfc}\frac{(x+2na)}{2(\alpha_1 t)^{1/2}} + \frac{(2na-x)}{\sqrt{\alpha_1}} \operatorname{erfc}\frac{(2na-x)}{2(\alpha_1 t)^{1/2}}\right] \right] \quad (3.36)$$

and similarly the inverted form of equation (3.35) becomes

$$T_2(x,t) = \frac{2Q}{(1+\sigma)(\rho_1 c_1 k_1)^{1/2}} \sum_{o}^{\infty} \frac{2\sqrt{t}}{\sqrt{\pi}} A^n \left\{ \exp\left[\frac{-1}{4t}\left[\frac{(x-a)}{\sqrt{\alpha_2}} + \frac{(2n+1)a}{\sqrt{\alpha_1}}\right]^2\right] \right.$$

$$\left. + \left[\frac{(2n+1)a}{\sqrt{\alpha_1}} + \frac{(x-a)}{\sqrt{\alpha_2}}\right] \operatorname{erfc}\left\{\frac{(2n+1)a}{2\sqrt{(\alpha_1 t)}} + \frac{(x-a)}{2\sqrt{(\alpha_2 t)}}\right\} \right\} \quad (3.37)$$

The surface temperature as measured by the thin film resistance thermometer mounted on the surface, can be obtained by putting x = 0 in equation (3.36) and hence

$$T_s(t)$$

$$= \frac{2Q}{\sqrt{(\rho_1 c_1 k_1)}} \left[(t/\pi)^{1/2} + 2\sum_{n=1}^{n=\infty} A^n \{(t/\pi)^{1/2} \exp\left[\frac{-n^2 a^2}{\alpha_1 t}\right] - \frac{na}{\sqrt{\alpha_1}} \operatorname{erfc}(na/(\alpha_1 t)^{1/2})\} \right]$$

.....(3.38)

3.2.2 Insulating layer on finite metal base.

The co-ordinate system for this model is shown in figure 3.6. The effect of the thin film resistance thermometer on the heat transfer rate is again considered to be negligible and it is assumed that there is a step in heat transfer rate at the surface x = -a, so that

$$\dot{q}_s = \frac{Q}{s}$$

The equations governing the heat flow in the composite are

$$\frac{\partial^2 T_1}{\partial x^2} = \frac{1}{\alpha_1}\frac{\partial T_1}{\partial t} \qquad -a < x < 0 \qquad ....(3.39)$$

$$\frac{\partial^2 T_2}{\partial x^2} = \frac{1}{\alpha_2}\frac{\partial T_2}{\partial t} \qquad 0 < x < b \qquad .....(3.40)$$

where $\alpha_i = \frac{k_i}{\rho_i c_i}$

with the corresponding boundary conditions

$$-Q = k_1 \frac{\partial T_1}{\partial x} \qquad \text{on } x = -a \qquad (3.41)$$

$$T_1 = T_2 \qquad \text{on } x = 0 \qquad (3.42)$$

$$k_1 \frac{\partial T_1}{\partial x} = k_2 \frac{\partial T_2}{\partial x} \qquad \text{on } x = 0 \qquad (3.43)$$

$$k_2 \frac{\partial T_2}{\partial x} = 0 \qquad \text{on } x = b \qquad (3.44)$$

Taking the Laplace transforms of equations 3.39 and 3.40, gives

$$\frac{d^2\bar{T}_1}{dx^2} + \beta^2\bar{T}_1 = 0 \qquad \text{where } \beta^2 = \frac{-s}{\alpha_1} \qquad (3.45)$$

$$\frac{d^2\bar{T}_2}{dx^2} + \lambda^2\beta^2\bar{T}_2 = 0 \qquad \text{where } \lambda^2 = \frac{\alpha_1^2}{\alpha_2^2} \qquad (3.46)$$

Hence $\bar{T}_1 = A\sin\beta x + B\cos\beta x \qquad (3.47)$

and $\bar{T}_2 = D\sin\lambda\beta x + E\cos\lambda\beta x \qquad (3.48)$

The constants A,B,D,E, can now be determined using the Laplace transformed boundary conditions.

From equations 3.41 to 3.44

$$-k_1\beta A\cos\beta a - k_1\beta B\sin\beta a = Q$$

$$k_1\beta A = k_2\lambda\beta D$$

$$B = E$$

$$\lambda D\beta\cos\lambda\beta b - \lambda\beta E\sin\lambda\beta b = 0$$

Thus

$$A = \frac{-\lambda k_2 Q\sin\lambda b\beta}{k_1 s\beta(k_2\sin a\beta\cos\lambda b\beta + \lambda k_2\cos a\beta\sin\lambda\beta b)}$$

$$B = E = \frac{-Q\cos\lambda b\beta}{s\beta(k_1\beta\sin a\beta\cos\lambda b\beta + \lambda k_2\beta\cos a\beta\sin\lambda\beta b)}$$

$$D = \frac{-Q\sin\lambda b\beta}{s\beta(k_1\beta\sin a\beta\cos\lambda b\beta + \lambda k_2\beta\cos a\beta\sin\lambda\beta b)}$$

Then $$\bar{T}_1(x,s) = \frac{-Q\ (\mu\sin\lambda b\beta\sin\beta x + \cos\lambda b\beta\cos\lambda\beta x)}{s(k_1\beta\sin a\beta\cos\lambda\beta b + \lambda k_2\beta\cos a\beta\sin\lambda\beta b)} \qquad (3.49)$$

where $\mu = \frac{\lambda k_2}{k_1}$

Inverting equation 3.49 and integrating around the contour shown in figure 3.7 gives

$$T_1 = \frac{1}{2\pi i}\int_{\gamma-i\infty}^{\gamma+i\infty} \frac{-Qe^{st}ds(\mu\sin\lambda b\beta\sin\beta x + \cos\lambda\beta b\cos\beta x)}{s\beta(k_1\sin a\beta\cos\lambda b\beta + \lambda k_2\cos a\beta\sin\lambda\beta b)} \qquad (3.50)$$

The singularities of the integrand occur at $s = 0$ (effectively $\beta = 0$, since $\beta^2 = \frac{-s}{\alpha}$) which is a double pole, and at β_n (such that $\beta_n \neq 0$), where β_n are the solutions of the transcendental equation

$$(k_1\sin a\beta\cos\lambda b\beta + \lambda k_2\cos a\beta\sin\lambda\beta b) = 0 \qquad (3.51)$$

The solutions of 3.51 are all real, and simple poles ($\beta \neq 0$), as shown by CARSLAW and JAEGER (1973). The residue at each simple pole can be evaluated by writing

$p(s) = -e^{-st}Q(\mu\sin\lambda b\beta\sin\beta x + \cos\lambda b\beta\cos\beta x)$, the numerator of the integrand and

$$q(s) = s\beta(k_1\sin a\beta\cos\lambda b\beta + \lambda k_2\cos a\beta\sin\lambda\beta b)$$

as the denominator of the integrand. Then the residue at each simple pole is given by

$$\frac{p(s_n)}{q'(s_n)}$$

and the sum of the residues at β_n is found to be

$$\sum_{n=1}^{n=\infty} \frac{p(s_n)}{q'(s_n)} =$$

$$-2Q \sum_{n=1}^{\infty} e^{-\alpha_1 \beta_n^2 t} \left[\frac{(\mu \sin\lambda b\beta_n \sin x\beta_n + \cos\lambda b\beta_n \cos x\beta_n)}{\beta_n^2 [(ak_1+\lambda^2 bk_2)\cos a\beta_n \cos\lambda b\beta_n - \lambda(ak_2+bk_1)\sin a\beta_n \sin\lambda b\beta_n]} \right]$$

The residue at $\beta = 0$ can be found from CHURCHILL et al (1974) and GIERE (1965) as follows. For a function $f(z) = \frac{p(z)}{q(z)}$, where p and q are both analytic at $z = z_0$, $(z_0 \neq 0)$ and

$q(z_0) = q'(z_0) = \ldots\ldots\ldots\ldots q^{m-1}(z_0) = 0$ and $q^m(z_0) \neq 0$ then the function f has a pole of order m at $z = z_0$. For the above case, $m = 2$ at $s = 0$ and the residue of f at $s = 0$ is given by GIERE (1965) to be

$$\text{Res } (0) = \frac{2p'(0)}{q''(0)} - \frac{2p(0)q'''(0)}{3(q''(0))^2}$$

Then $p(0) = -Q$

$$p'(0) = -Qt + \frac{Q}{2k_1}[\lambda b(2\mu x - \lambda b) - x^2]$$

$$q''(0) = \frac{-2}{\alpha_1}\ (ak_1 + \lambda^2 bk_2)$$

and $q'''(0) = \frac{-1}{\alpha_1}\ [\ ak_1(a^2 + 3\lambda^2 b^2) + \lambda^2 bk_2(3a^2 + \lambda^2 b^2)]$.

$$Res(0) = \frac{Q}{(ak_1 + \lambda^2 bk_2)}\left\{\alpha_1 t - \frac{\lambda b(2\mu x - \lambda b)}{2} + \frac{x^2}{2} - \frac{(ak_1(a^2+3\lambda^2 b^2)+\lambda^2 bk_2(3a^2+\lambda^2 b^2))}{6(ak_1 + \lambda^2 bk_2)}\right\}$$

Hence

$$T_1(x,t) = Res(0) -$$

$$-2Q\sum_{n=1}^{\infty} e^{-\alpha_1 \beta_n^2 t}\left[\frac{(\mu \sin\lambda b\beta_n \sin x\beta_n + \cos\lambda b\beta_n \cos x\beta_n)}{\beta_n^2[(ak_1+\lambda^2 bk_2)\cos a\beta_n \cos\lambda b\beta_n - \lambda(ak_2+bk_1)\sin a\beta_n \sin\lambda b\beta_n]}\right]$$

.....(3.52)

Similarly,

$$T_2(x,s) = \frac{-Q\ \cos\lambda b\beta(x-b)}{s(k_1 \beta \sin a\beta \cos\lambda\beta b + \lambda k_2 \beta \cos a\beta \sin\lambda\beta b)} \qquad (3.53)$$

and $$T_2(x,t) = \frac{1}{2\pi i}\int_{\gamma-i\infty}^{\gamma+i\infty} \frac{-Qe^{st} ds\ \cos\lambda b\beta(x-b)}{s\beta(k_1 \sin a\beta \cos\lambda b\beta + \lambda k_2 \cos a\beta \sin\lambda\beta b)} \qquad (3.54)$$

which can be inverted to obtain

$$T_2(x,t) =$$

$$= \frac{Q}{(ak_1 + \lambda^2 bk_2)}\left\{\alpha_1 t + \frac{\lambda^2}{2}(x-b)^2 - \frac{(ak_1(a^2+3\lambda^2 b^2)+\lambda^2 bk_2(3a^2+\lambda^2 b^2))}{6(ak_1 + \lambda^2 bk_2)}\right\}$$

$$-2Q \sum_{n=0}^{\infty} e^{-\alpha_1 \beta_n^2 t} \left[\frac{(\cos\lambda\beta_n(x-b))}{\beta_n^2[(ak_1+\lambda^2 bk_2)\cos a\beta_n \cos\lambda b\beta_n - \lambda(ak_2+bk_1)\sin a\beta_n \sin\lambda b\beta_n]} \right]$$

.....(3.55)

Note that the sign in the expression for T_2 (3.55), before $\frac{\lambda^2(x-b)^2}{2}$ is incorrectly given as a minus sign, by GIERE.

3.2.3 Solution of the transcendental equation.

It was necessary to evaluate sufficient β_n to ensure convergence of the sum (3.52). Few roots were required for large times, but for shorter times, of the order of 1μs, up to 400 roots were required, depending on the material properties and thickness of the insulating layer.

Automatic root finding programs were written on the Oxford University Engineering Departments VAX 11/780 computer to calculate a set of 400 roots in a matter of seconds, incorporating the NAG Library routine (C05AGF). The routine calculates the root of the function $f(x) = 0$ which is closest to the starting value.

The roots were calculated to a user defined accuracy of 1.0×10^{-11} such that for $f(\beta) = k \sin a\beta \cos\lambda b\beta + \lambda k_2 \cos a\beta \sin\lambda b\beta = 0$, the approximation β_n to the zero α was determined so that one or both of the following criteria were satisfied.

(1) $|\beta_n - \alpha| < 1 \times 10^{-11}$

(2) $|f(\beta_n)| < 1 \times 10^{-11}$

The problems encountered in finding the roots were identified when two cases of likely practical importance were considered.

The first case of practical interest was for a layer of 20μm Al_2O_3 on 3mm nickel. For this case, the function $f(\beta)$ has a simple form, from figure 3.8a, and the spacing between the roots, β_n is nearly constant. Thus the successive roots could be calculated by a simple procedure as follows:

A value, $\Delta\beta$, close to the approximately constant spacing between the roots, was found by plotting the graph of $f(\beta)$ on a large scale, figure 3.8b. The approximate value of the first root (i.e. $\tilde{\beta}_1$) was set equal to $\Delta\beta$, from which the NAG routine found the exact value, β_1. Adding $\Delta\beta$ to the exact value β_1 yielded an approximation to the second root, i.e. $\tilde{\beta}_2 = \beta_1 + \Delta\beta$, and again the NAG routine was used to find the exact value β_2. Since for this simple case,

$$\frac{1}{2}|\beta_n - \beta_{n-1}| < \Delta\beta < \frac{3}{2}|\beta_n - \beta_{n-1}|,$$

the approximated $\tilde{\beta}_n = \beta_{n-1} + \Delta\beta$ is always closer to β_n than it is to either β_{n-1} or β_{n+1}, the routine successfully finds the root β_n, rather than again choosing β_{n-1} or skipping to β_{n+1}.

For the other substrate, also of practical interest, 200μm quartz on 3mm nickel, the behaviour of $f(\beta)$ is more complex as shown in figure 3.9a. For this case, a slightly modified routine was employed. Again the function $f(\beta)$ was plotted on an expanded scale, figure 3.9b. An appropriate root spacing was chosen such that for $\beta_n - \beta_{n-1} = \Delta\beta$ then min $|\Delta\beta| >>> \delta$. To find the nth root, successive approximations $\tilde{\beta}_n = \beta_{n-1} + k\delta$ were input as starting values to the NAG routine, until the routine successfully calculated the next root.

3.3 Comparison of solutions for 2-layer finite backwall and 2-layer semi-infinite backwall.

The length of time for which a thin film gauge on a composite substrate consisting of an insulating layer on top of a "finite" metal layer can be considered as behaving as if the metal layer were semi-infinite is of particular significance, just as for the simple one-layered substrate considered in 3.1. Variation in the thickness and properties of the insulating layer has a great effect on the transient behaviour of the multi-layered substrate.

This is best illustrated by the choice of three particular examples, which represent the three different types of insulating layer considered for practical application as discussed later;

(1) 20μm alumina on 3mm nickel and semi-infinite nickel

(2) 200μm quartz on 3mm nickel and semi-infinite nickel

(3) 75μm kapton (a polyimide) on 3mm nickel and semi-infinite nickel.

These substrates are shown in figures 3.10,3.11 and 3.12 respectively. The properties ρ, c and k, and $\sqrt{(\rho ck)}$ for the materials are given in table 1.

The predicted surface temperatures comparing semi-infinite and infinite for cases 1, 2 and 3 are plotted against $(\text{time})^{1/2}$ in figures 3.13,3.14 and 3.15 respectively. It can be seen from figure 3.13, that 20μm alumina on 3mm nickel can be considered semi-infinite until a time of 0.18 seconds, when the solutions for the semi-infinite and finite backwall begin to diverge. The effect of the finite backwall first becomes appreciable at 0.3 seconds for case 2 but not until 0.36 seconds for case 3. The significance of these times, lies in determining the bounds of validity of any method for obtaining the heat transfer rate from a film on a two-layer composite, which

is based on the semi-infinite back wall assumption. To illustrate the effect of the finite backwall, a computer program incorporating the NAG routine (JO6WBF), was written, to plot the temperature-time-distance responses as a three dimensional surface. The semi-infinite backwall solution for composites of types 1, 2 and 3 are shown in figures 3.16, 3.17 and 3.18 respectively, and the corresponding "finite backwall" solutions in figures 3.19,3.20 and 3.21 respectively. These figures show the process of transient conduction through the two layers.

As can be seen from examination of corresponding pairs of figures, the considerably large temperature rise of the back face of the second layer, which is exhibited by the finite backwall solution, would, because of the increased heat loss, render the semi-infinite solution invalid after a certain time. The sequence of example composites 1, 2 and 3 correspond to progressively more insulating coatings, and it is clear that as the insulating properties of the coating are improved, the effects of the finite backwall apparently diminish. This is because the temperature drop across the coating becomes proportionately greater as the insulating properties are improved, and the rate of surface temperature increase appears progressively "flatter" after the switch point. For case (3), the difference in thermal properties between Kapton and nickel is so great, that the nickel behaves almost as if it were a perfect thermal conductor in relation to Kapton, and the response after the switch point appears almost horizontal when plotted on a scale which shows the complete response.

In physical terms, the case of an insulator on a perfect conductor is similar to that where the interface temperature is held constant and equal to the initial temperature. Case 3 approximates this situation, as the temperature at the nickel interface is still very low within the timescale

of interest, and although the effect of the backwall is to raise the nickel temperature at the interface, most of the drop still occurs within the Kapton layer.

3.4 Gauges on a single layer substrate and method of obtaining heat transfer rate.

A brief description of the present methods of obtaining heat transfer rate from a gauge on a single layer substrate , which are currently used at O.U.E.L. will now be given. Further details are contained in OLDFIELD et al (1978).

In very short duration tunnels such as shock and gun tunnels, the surface temperature rise of the model during the run is very small, so the fall in heat transfer rate to the model during the run is slight. The flow duration of up to 0.5 seconds in the I.L.P.T., however, produces surface temperature rises of up to 70K, corresponding to a 50% drop in the typical driving temperature difference of 150K. For an instrumented turbine blade, the heat transfer rate at different model positions falls by differing amounts during the run, according to the local rise in surface temperature. As described by OLDFIELD at al, the heat transfer rate distributions for an isothermal blade are obtained by plotting the heat transfer rate against the surface temperature, and extrapolating the linear part of the plot back to extract the heat transfer rate for zero surface temperature rise. This method readily gives the steady-state heat transfer rate distribution and is done automatically by the computer processing routines, using a least squares linefit.

The surface temperature and the heat transfer rate signal need to be obtained for each heat transfer gauge on the turbine blade, in order to obtain the isothermal heat transfer rate distribution. As shown by OLDFIELD et al, it was possible to record either the heat transfer rate or the surface temperature only, and to calculate the surface temperature from the recorded heat transfer signal or vice versa. This maximised the amount of data recorded per run for a given number of computer channels. The method adopted was to record the $\dot{q}$ signal from the analogue and to re-compute the temperature signal, using a simple numerical procedure.The converse procedure was numerically noisier, because of digitisation errors as discussed already in section 3.1 .

It was assumed that the heat transfer rate could be approximated by a series of delayed ramp functions such that

$$\dot{q} = \sum_n H(t-t_n)\, a_n(t-t_n)$$

where a_n is the slope of the nth ramp function and H is the Heaviside step function.

From equation (3.5)

$$\bar{T} = \frac{\bar{\dot{q}}}{\sqrt{(\rho c k s)}}$$

Hence
$$\bar{T} = \frac{1}{\sqrt{(\rho c k)}} \sum a_n e^{-t_n s} \frac{1}{s^{5/2}} \qquad (3.56)$$

Inverting (3.56) gives

$$T(t) = \frac{1}{\sqrt{(\rho c k \pi)}} \sum a_n \frac{4}{3} (t - t_n)^{3/2} H(t - t_n) \qquad (3.57)$$

where $a_n = (\dot{q}_{n+1} - \dot{q}_n)/\tau - (\dot{q}_n - \dot{q}_{n-1})/\tau = (\dot{q}_{n-1} + \dot{q}_{n+1} - 2\dot{q}_n)/\tau$

Then

$$T(t) = \frac{4}{3\sqrt{(\rho c k \pi)}} \sum \frac{(\dot{q}_{n-1} + \dot{q}_{n+1} - 2\dot{q}_n)}{\tau} (t - t_n)^{3/2} H(t - t_n) \qquad (3.58)$$

If $t = m\tau$, and $t_n = n\tau$ where τ is the sample interval then

$$T(m\tau) = \frac{4\sqrt{\tau}}{3\sqrt{(\rho c k \pi)}} \sum_{n=0}^{m} (\dot{q}_{n-1} + \dot{q}_{n+1} - 2\dot{q}_n) (m - n)^{3/2} \qquad (3.59)$$

A table stored in the computer is used for $(m - n)^{3/2}$ and the digitized q data is stored by the computer as integers. The resulting computation takes only a few seconds to transform a 200 point $\dot{q}$ trace into the T trace. This method, as shown by OLDFIELD et al, gives excellent agreement between a recorded T signal and the computed T signal.

3.5 Method of obtaining heat transfer rate from multi-layered gauges.

The relationship between the surface heat transfer rate $\dot{q}_s$ and the surface temperature T_s for any thin film heat transfer gauge on a multi-layer substrate is given by

$$\bar{\dot{q}}_s = F(s)\, \bar{T}_s \qquad (3.60)$$

For a gauge on a two-layered medium with semi-infinite metal layer, for example, putting $x = 0$ in equation (3.30)

$$\bar{T}_s = \frac{\bar{\dot{q}}_s}{\sqrt{(\rho_i c_i k_i s)}} \left[\frac{(\ 1 + A \exp\{-2a\sqrt{(s/\alpha_i)}\}}{(\ 1 - A \exp\{-2a\sqrt{(s/\alpha_i)}\}}\right] \qquad (3.61)$$

$$\text{Hence } F(s) = (\rho c k s)^{1/2} \frac{(\ 1 - A \exp\{-2a\sqrt{(s/\alpha_i)}^{1/2}\})}{(\ 1 + A \exp\{-2a\sqrt{(s/\alpha_i)}^{1/2}\})} \qquad (3.62)$$

To measure surface heat transfer rate, a constant current step is passed through the thin film gauge and the change of voltage v caused by a change in surface temperature is processed by using an electrical analogue, figure (3.4).

The film voltage is given by

$$v = v_0 \alpha T \qquad (3.63)$$

where α is the temperature coefficient of resistance of the film. The analogue voltage output is given by

$$\bar{v}_a = \frac{s^{1/2}}{k_a} \bar{v} = \frac{v_0}{k_a} s^{1/2} \alpha \bar{T}_s \qquad (3.64)$$

where k_a is the analogue calibration constant, assuming the analogue is ideal.

Combining (3.60), (3.63), and (3.64) gives

$$\bar{\dot{q}}_s = \frac{k_a F(s)}{v_0 \alpha \sqrt{s}} \bar{v}_a \qquad (3.65)$$

For short times $F(s) = (\rho_1 c_1 k_1 s)^{1/2}$ (3.66)

so

$$\bar{\dot{q}}_s = \frac{k_a \bar{v}_a (\rho_1 c_1 k_1)^{1/2}}{v_0 \alpha} \quad (3.67)$$

If the analogue output is a step, then

$$\bar{v}_a = \frac{1}{s} \quad (3.68)$$

and the $\bar{\dot{q}}_s$ to give this step would be

$$\bar{\dot{q}}_s = \frac{k_a F(s) s^{-3/2}}{\alpha v_o} \quad (3.69)$$

For short times from (3.67),

$$\bar{\dot{q}}_s = \frac{k_a (\rho_1 c_1 k_1)^{1/2}}{v_0 \alpha s} \quad (3.70)$$

so $\dot{q}_s(t)$ is a step of height $\frac{k_a(\rho_1 c_1 k_1)^{1/2}}{v_0 \alpha}$ for small time.

Define the step calibration function h(t) with Laplace transform

$$H(s) = \frac{F(s)}{(\rho_1 c_1 k_1)^{1/2} s^{3/2}} \quad (3.71)$$

then from (3.65) and (3.69) for a unit step of v_a

$$\bar{\dot{q}}_s(s) = \frac{k_a H(s) (\rho_1 c_1 k_1)^{1/2}}{\alpha v_0} \qquad (3.72)$$

so

$$\dot{q}_s(t) = \frac{k_a h(t) (\rho_1 c_1 k_1)^{1/2}}{\alpha v_0} \qquad (3.73)$$

The sampled analogue output signal with Laplace transform

$$\bar{v}_a = \frac{v_0}{k_a} s^{1/2} \alpha \bar{T}_s \qquad (3.74)$$

can be considered to be a series of step functions such that

$$v_a(n\tau) = \sum_{n=1}^{n=N} a_n u(N\tau - n\tau) \qquad (3.75)$$

where $u(t-\tau)$ is the unit step function. The Laplace transform of (3.75) is

$$\bar{v}_a = \sum_{n=1}^{n=N} a_n \frac{e^{-st_n}}{s} \qquad (3.76)$$

where $t_n = n\tau$, and $a_n = v_\alpha(n\tau) - v_\alpha(n-1)\tau$

then

$$\bar{\dot{q}}_s(s) = \frac{1 k_a H(s) (\rho_1 c_1 k_1)^{1/2}}{\alpha v_0} \bar{v}_a(s) \qquad (3.77)$$

so for v_a a sum of series of step functions,

$$q_s(t) = \frac{1 k_a}{\alpha v_0} (\rho_1 c_1 k_1)^{1/2} \sum h(N-n)\tau(v(n\tau) - v(n-1)\tau) \qquad (3.78)$$

Thus if $h(n\tau)$ is known at N discrete points, then $\dot{q}_s(N\tau)$ the sampled heat transfer signal can be computed. In practice, only about 200 points per

channel of $v_a(n\tau)$ are sampled, so it is only necessary to know $h(n\tau)$ at 200 points.

For single-layer semi-infinite gauges, $h(t) = u(t)$, the unit step.

For two-layered semi-infinite gauges, from (3.62),

$$F(s) = (\rho ck s)^{1/2} \frac{1 - A \exp\{-2a\sqrt{(s/\alpha_1)^{1/2}}\}}{1 + A \exp\{-2a\sqrt{(s/\alpha_1)^{1/2}}\}}$$

$$\text{Hence } H(s) = \frac{1}{s} \frac{(1 - A\exp\{-2a\sqrt{(s/\alpha_1)^{1/2}}\})}{(1 + A\exp(-2a\sqrt{(s/\alpha_1)^{1/2}}))} \qquad (3.79)$$

Expanding the denominator gives

$$H(s) = \frac{1}{s}\left(1 + 2\sum_{m=1}^{\infty}(-1)^m A^m \exp(-2ma\sqrt{(s/\alpha_1)^{1/2}})\right) \qquad (3.80)$$

and inverting this gives

$$h(t) = 1 + 2\sum_{m=1}^{\infty}(-1)^m A^m \operatorname{erfc}(ma/\sqrt{(\alpha_1 t)}) \qquad (3.81)$$

The heat transfer rate for a gauge on a 2-layered composite with semi-infinite metal layer can thus be determined if

$$A = \frac{1-\sigma}{1+\sigma} = \frac{\sqrt{(\rho_1 c_1 k_1)} - \sqrt{(\rho_2 c_2 k_2)}}{\sqrt{(\rho_1 c_1 k_1)} + \sqrt{(\rho_2 c_2 k_2)}}$$

and $\frac{a}{\alpha_1} = \frac{a}{k_1}\sqrt{(\rho_1 c_1 k_1)}$

are known.

For multi-layer gauges h(t) cannot be determined explicitly and a method for obtaining it is given in Chapter 4.

CHAPTER 4

METHODS OF CALIBRATION

4.1 Use of heat transfer gauges on single-layered medium.

A thin film resistance thermometer on a single layered medium can be used to obtain the heat transfer rate and as shown in Chapter 3, this can be extended to obtain the heat transfer rate to a multi-layered substrate.

This chapter briefly outlines the calibrations which are necessary for the single layer case, and the methods which were developed for calibrating the two and multi-layered systems are fully described.

From equation (3.23), the heat transfer rate to a semi-infinite layer is obtained directly from the electrical analogue as

$$\dot{q} = \frac{(\rho c k)^{\frac{1}{2}}}{\alpha_R V_0} \frac{\sqrt{r}}{\sqrt{c}} i_{in}$$

The accurate determination of the temperature coefficient of resistance of the film, α_R, the analogue calibration constant $\frac{\sqrt{r}}{\sqrt{c}}$, and $(\rho ck)^{\frac{1}{2}}$ the thermal constant of the substrate is therefore necessary.

The temperature coefficient of resistance α_R, of the thin film is measured in a temperature controlled bath, over the working range of temperatures for the film. A least squares line fit through the measured data enables α to be found, and the linearity is excellent for a 'good' film, with typical correlation coefficients of 0.9999.

The analogue calibration constant $\frac{\sqrt{r}}{\sqrt{c}}$ is determined electrically by measuring the ratio of the input voltage to the output voltage at a given frequency within the working range (MEYER (1960, 1963)).

4.1.2 Measurement of $\sqrt{\rho ck}$ of substrate.

A suitable and commonly used technique for measuring the value of $\sqrt{\rho ck}$ of the substrate material is by electrical discharge methods. The change in resistance produced by passing a constant current step through the film for a short time, which is equivalent to a step in heat transfer rate at the surface, is recorded. SCHULTZ and JONES (1973) give a suitable simple circuit for the measurement of $\sqrt{(\rho_1 c_1 k_1)}$, which is shown in figure 4.1.

If the test is conducted in a vacuum, then all the heat generated in the film effectively passes to the substrate, (radiation losses can be assumed negligible as the temperature rise is small), hence

$\dot{q} = \frac{I_o^2 R_F}{A}$ W/m^2, where A is the film area. Referring to figure 4.1, for a balanced bridge

$$R_1 R_F = R_2 R_3$$

The change in voltage ΔV, caused by the small increase ΔR_F in the film resistance is given by

$$\frac{\Delta V}{I} = \frac{\Delta R_F R_1}{\Delta R_F + R_F + R_2 + R_1 + R_3}$$

Since the change in resistance ΔR_F is given by

$$\Delta R_F = \alpha_R R_F \Delta T$$

then it can be shown that

$$\sqrt{(\rho ck)} = \frac{2\alpha_I R_F^2 R_1 I_o^2}{A \Sigma R \sqrt{\pi}} \frac{\sqrt{t}}{\Delta V}$$

where $\Sigma R = R_F + R_1 + R_2 + R_3 + R_4$

By recording ΔV and plotting against $(\text{time})^{1/2}$ a straight line is obtained. Accurate determination of $\sqrt{(\rho ck)}$ thus depends on a knowledge of the film area, which for curved surfaces may be difficult to obtain accurately. The use of a double calibration technique suggested by MAULARD (1968), avoids having to determine the film area. Firstly, the film is pulse calibrated in air and $\frac{\Delta V_1}{\sqrt{t}}$ is recorded. It is then immersed in a liquid with known thermal properties, pulsed again and $\frac{\Delta V_2}{\sqrt{t}}$ is recorded. It can be shown that

$$\sqrt{(\rho ck)}_{\text{substrate}} = \frac{\sqrt{(\rho ck)}_{\text{liquid}}}{\frac{\Delta V_1/\sqrt{t}}{\Delta V_2/\sqrt{t}} - 1} \qquad (4.1)$$

The use of glycerine as a test liquid is common practice. The values of ρ, c and k for glycerine are given in table 1, and $\sqrt{(\rho ck)}$ is known to approximately ± 2%.

4.2 Calibration of gauge on two-layered substrate.

4.2.1 Semi-infinite metal layer.

It was shown in equation (3.81) that the multi-layer gauge step calibration function, h(t) could be explicitly calculated if the values of $\sqrt{(\rho_1 c_1 k_1)}$, $\sqrt{(\rho_2 c_2 k_2)}$ and $\frac{a}{\sqrt{\alpha_1}} = \frac{a}{k_1}\sqrt{(\rho_1 c_1 k_1)}$ where a is the thickness of the insulating layer, were known. The thermal product $\sqrt{(\rho_1 c_1 k_1)}$ of the insulating layer can be obtained using a standard air-glycerine test, but the major difficulty encountered was in developing a method of calibration so that the factor $\frac{a}{k_1}$ could be determined. For the insulator to be used in coating a turbine blade surface it was extremely unlikely that its thickness and thermal conductivity would be known at different locations on the highly curved surface. Although the thickness could possibly be measured accurately, determination of the conductivity of the insulating layer poses considerable difficulty. This difficulty is greatly exacerbated where the properties of the insulating layer may vary considerably according to the physical structure of the layer, which is particularly likely for vacuum deposited or glazed coatings. The large variation in the physical structure of the insulating layer may be clearly seen with microscopic examination techniques. These have proved very useful in the course of this work, and micrographs of some of the coatings considered are presented in Chapter 5.

The method of analysis of section 3.5 showed that (apart from $(\rho_1 c_1 k_1)^{1/2}$, and $(\rho_2 c_2 k_2)^{1/2}$), only the ratio $\frac{a}{\bar{k}_1}$ was necessary to determine h(t). Thus rather than seek a means of determining a and k_1 separately, it was discovered that the response of the gauge on a multi-layered substrate. to the pulsing technique, could be interpreted so as to determine the ratio $\frac{a}{\bar{k}_1}$. The method to be described allows the factor $\frac{a}{\bar{k}_1}$ to be determined at each gauge location on a model.

For a step in heat transfer rate at the surface of a two-layer substrate, with semi-infinite metal layer, from equation (3.38)

$$T_s = \frac{2Q}{\sqrt{(\rho_1 c_1 k_1)}} \left[\sqrt{(t/\pi)} + 2\sum_{n=1}^{\infty} A^n \{ \sqrt{(t/\pi)} \exp -\left[\frac{n^2 a^2}{\alpha_1 t}\right] - \frac{na}{\sqrt{\alpha_1}} \operatorname{erfc}(na/\sqrt{(\alpha_1 t)}) \} \right]$$

T_s can also be written as

$$T_s = 2Q \left[\frac{t}{\pi \rho_1 c_1 k_1}\right]^{1/2} + \frac{2Q}{\sqrt{(\rho_1 c_1 k_1)}} \sum_{n=1}^{\infty} A^n \left(2\sqrt{t}\ \operatorname{ierfc} \frac{na}{\sqrt{(\alpha t_1)}}\right) \qquad (4.2)$$

where $\operatorname{ierfcz} = \frac{2}{\pi} \int_z^{\infty} (t - z) e^{-t^2} dt$

For large t, from ABRAMOWITZ and STEGUN, the function ierfc may be represented accurately by,

$$\operatorname{ierfc} \frac{na}{\sqrt{(\alpha_1 t)}} \approx \frac{1}{\sqrt{\pi}} \left[1 + \frac{n^2 a^2}{(\alpha_1 t)}\right] - \frac{na}{\sqrt{(\alpha_1 t)}} \qquad (4.3)$$

so

$$T_s = 2Q\left[\frac{t}{\pi\rho_1 c_1 k_1}\right]^{1/2} + \frac{4Q}{\sqrt{(\rho_1 c_1 k_1)}} \sum_{n=1}^{n=\infty} A^n \left(\frac{n^2a^2}{\alpha_1\sqrt{(\pi t)}} - \frac{(na)}{\sqrt{\alpha_1}} + 2\,(t/\pi)^{1/2}\right)$$

....(4.4)

$$\text{and } \sum_{n=1}^{n=\infty} nA^n = \frac{A}{(1-A)^2} \qquad (4.5)$$

Since $\lim_{t\to\infty} \sum_{n=1}^{\infty} A^n(2n^2a^2/(\alpha_1\sqrt{(\pi t)})) \longrightarrow 0$,then for $t \to \infty$

$$T_s \to 2Q\left[\frac{t}{\pi\rho_2 c_2 k_2}\right]^{1/2} + \frac{aQ}{k_1}\left[1 - \frac{\rho_1 c_1 k_1}{\rho_2 c_2 k_2}\right] \qquad (4.6)$$

This is effectively the temperature which would be seen by a gauge on a metal alone, with an offset to account for the presence of the insulator. For short times as $t \to 0$ and

$$\sqrt{t}\,\exp-(n^2a^2/(\alpha_1 t)) \to 0 \quad \text{and erfc}\left[\frac{na}{\sqrt{\alpha_1 t}}\right] \longrightarrow 0, \text{ so}$$

$$T_g(t) = 2Q\left[\frac{t}{\pi\rho_1 c_1 k_1}\right]^{1/2} \qquad (4.7)$$

which is the temperature of a single layer insulator alone.

If the two-layered substrate is subject to a step in heat transfer rate, then for a short time, the effect of the insulator alone is seen. Figure 4.2 shows the predicted surface temperature for metal alone, insulator alone, and insulator coated metal. The time corresponding to the intersection of equations (4.6) and (4.7), (which both describe

straight lines in $\sqrt{t}$), henceforth referred to as the 'switch point', is given by

$$\sqrt{t} = \left[\frac{\pi}{2}\right]^{1/2} \frac{a}{k_1} \left[\frac{\rho_2 c_2 k_2}{\rho_1 c_1 k_1}\right]^{1/2} \{ (\rho_1 c_1 k_1)^{1/2} + (\rho_2 c_2 k_2)^{1/2} \} \qquad (4.8)$$

$(\rho_1 c_1 k_1)^{1/2}$ for the insulator is known from the standard air-glycerine test. The ratio of the slope of the line obtained in plotting $T_s(t)$ against $\sqrt{t}$ in equation (4.6) to the slope of the line obtained in plotting $T_s(t)$ against $\sqrt{t}$ in equation 4.7 is

$$\left[\frac{\rho_2 c_2 k_2}{\rho_1 c_1 k_1}\right]^{1/2}$$

hence $(\rho_2 c_2 k_2)^{1/2}$ is known. From equation 4.8, $\frac{a}{k_1}$ can then be calculated, and as has been shown, this is the required constant in the equations for obtaining the calibration function h(t).

The procedure is thus as follows;

The thin film gauge is pulsed with a constant current and its temperature response is recorded (a predicted response is shown in figure 4.3), and is plotted against $\sqrt{t}$. A line of best fit is drawn to the first part of the curve (before the switch point) and a second line of best fit is drawn to the part of the curve after the switch point. The time of intersection of these two lines can thus be determined and used in equation 4.8 to calculate $\frac{a}{k_1}$.

4.2.2 Calibration of a multi-layered gauge.

For a multi-layered gauge with more than two layers, h(t) is not determined explicitly and a different method could, in principle, be used.

An air-glycerine test is used for $t < t_1$, to obtain $(\rho_1 c_1 k_1)^{1/2}$ for the top insulating layer. If a step in heat transfer rate is applied to the gauge, then the first part of the curve, for $t < t_1$ can be scaled, since

$$\bar{T}_s = \frac{\bar{\dot{q}}_s}{\overline{F(s)}} = \frac{1}{s\overline{F(s)}} \qquad (4.9)$$

and for short times, $t < t_1$, $F(s) = (\rho_1 c_1 k_1 s)^{1/2}$ so

$$\bar{T}_s \approx \frac{s^{-3/2}}{(\rho_1 c_1 k_1)^{1/2}} \qquad (4.10)$$

or
$$T_s(t) = 2\left[\frac{t}{(\rho_1 c_1 k_1)}\right]^{1/2} \qquad (4.11)$$

Hence for $0 < t < t_1$, a parabola can, in principle, be fitted through the measured curve and the result scaled.

From 3.71,

$$H(s) = \frac{F(s)\, s^{-3/2}}{(\rho_1 c_1 k_1)^{1/2}}$$

and from equation 4.9, for a step in $\dot{q}_s$

$$F(s) = \frac{1}{s\bar{T}_s} \qquad (4.12)$$

so
$$H(s) = \frac{s^{-5/2}}{(\rho_1 c_1 k_1)^{1/2}\bar{T}_s} \qquad (4.13)$$

Thus $$H(s)[(\rho_1 c_1 k_1 s)^{1/2}\ \bar{T}_s] = \frac{1}{s^2} \qquad (4.14)$$

and putting

$$y(s) = (\rho_1 c_1 k_1 s)^{1/2}\ \bar{T}_s \qquad (4.15)$$

gives $$H(s)y(s) = \frac{1}{s^2} \qquad (4.16)$$

From the convolution theorem

$$\int_0^t h(u)y(u-t)\,du = t \qquad (4.17)$$

For $t < t_1$, $h(t) = 1$, hence

$$y(s) = (\rho_1 c_1 k_1 s)^{1/2} . (\rho_1 c_1 k_1)^{-1/2} s^{-3/2} \qquad (4.18)$$

so $y(t) = 1$ for $t << t_1$ (4.19).

Since y(t) is known for small time, numerical techniques can be used to compute y(t) from $y(s) = s^{1/2}\bar{T}_s$ without the usual difficulties. Alternatively, an analogue can be used to compute y(t) from the measured surface temperature.

The discrete form of 4.17 is

$$\sum_{n=1}^{n=N} h(n\tau)(y(N-n)\tau) = N\tau \qquad (4.20)$$

$$\text{or } h(N\tau) = N - \sum_{n=1}^{N-1} h(n\tau)(y(N-n)\tau) \qquad (4.21)$$

so $h(N\tau)$ can be computed step by step from the measured points $y(n\tau)$, derived from the measured surface temperature.

4.3 Design of a fast response $\sqrt{(\rho ck)}$ tester.

At the start of this work, an attempt was made to use a device built by SHADDOCK (1978), which was designed for measuring $\sqrt{(\rho ck)}$ on a semi-infinite single layer substrate. For the two-layer systems considered, however, with thin insulating layers (in some cases as thin as 20μm), it was discovered that an initial transient (figure 4.4), which lasted for up to 45μs,, totally obscured the response of the insulating layer. For the single layer case, this had not been important, since only the slope of the line was required. For a two-layered substrate, however, where dependence on the response of the first and second layers was essential, a circuit with faster initial response and a shorter transient was used. This circuit is shown in figure 4.5. The use of a floating battery supply eliminates the need for a differential bridge amplifier. With careful layout and the use of non-inductive components, the initial transient decayed in 5μs.

4.4 Errors introduced by electrical discharge calibration.

During pulse calibration, heat is generated only within the thin film itself, which is mounted on the surface of the substrate, and it then diffuses in two dimensions. The thin film gauge, in practical applications, is mounted on the surface of a substrate which is heated over the whole surface. The effects of lateral heat conduction are considered to be negligible, as the surface heat transfer rate is a slowly varying function compared to the scale of the film, so the one-dimensional heat conduction analysis is applicable.

The problem of surface heating which is confined to a strip , (i.e. a thin film gauge) mounted on the surface of a single layered semi-infinite substrate has been considered by LOWAN (1939) and SPENCE (1960). For a strip $-h < y < h$, Spence found that the mean surface temperature , where the surface is subject to constant heat transfer rate, and there is conduction in two dimensions, was given by

$$T_{mean} = \frac{1}{(\pi\rho ck)^{1/2}} \int_0^t \frac{Q(\tau)}{(t-\tau)^{1/2}}\, d\tau \int_{-h}^{h} \frac{\operatorname{erf}(h+y)}{2(\alpha(t-\tau))^{1/2}} + \frac{\operatorname{erf}(h-y)}{2(\alpha(t-\tau))^{1/2}}\, \frac{dy}{4h} \qquad (4.22)$$

Letting $\frac{h}{(\alpha(t-\tau))^{1/2}} = \beta$, SPENCE wrote the inner integral as

$$\frac{1}{\beta}\int_0^{\beta} \operatorname{erf} u\, du = \operatorname{erf}\beta - \frac{(1-e^{-\beta^2})}{\sqrt{\pi}\,\beta} = 1 - \frac{1}{\sqrt{\pi}\beta} + \frac{e^{-\beta^2}}{2\sqrt{\pi}\,\beta^3} + \ldots\ldots$$

Using the asymptotic expansion for erf β, as $\beta \to \infty$,

$$\operatorname{erf} z = \frac{1}{\sqrt{\pi}\,z}\, e^{-z^2} \left(1 + \Sigma \frac{(-1)^m\, 1.3\ldots\ldots(2m-1)}{(2z^2)^m} \right)$$

Spence found that for $\beta = \frac{h}{\sqrt{(\alpha t)}} >> 1$, it was sufficient to take only the first two terms, and hence for constant q,

$$T_{mean} = 2Q \left[\frac{t}{\pi\rho ck}\right]^{1/2} \left[1 - \frac{1}{2h} \left[\frac{\alpha t}{\pi}\right]^{1/2} \right] \qquad (4.23)$$

This compares with the one-dimensional surface temperature solution of

$$T = 2Q \left[\frac{t}{\pi\rho ck}\right]^{1/2} \qquad (4.24)$$

so the temperature is reduced below that which would be seen with only one-dimensional heating by a factor of

$$\left[1 - \frac{1}{2h}\left[\frac{\alpha t}{\pi}\right]^{1/2}\right] \qquad (4.25)$$

for a film of width 2h.

As $\beta \to 0$, or effectively $\beta < 1.5$, i.e. for $t \to \infty$, the asymptotic series expansion cannot be used. Instead, erf β can be expanded as a convergent series which is given by (ABROMOVITZ and STEGUN 1972) to be

$$\text{erf}\beta = \frac{2}{\sqrt{\pi}} \sum \frac{(-1)^n \beta^{2n+1}}{n!\,(2n+1)}$$

Then

$$I = \frac{1}{\beta}\int_0^{\beta} \text{erf } u \, du = \text{erf } \beta - \frac{(1-e^{-\beta^2})}{\sqrt{\pi}\,\beta} \qquad (4.26)$$

can be written by expanding $e^{-\beta^2}$, as

$$I = \frac{1}{\sqrt{\pi}} \sum_{n=0}^{\infty} \beta^{2n+1}(-1)^n \frac{1}{n(n+1)!\,(2n+1)} \qquad (4.27)$$

If $C_n = (-1)^n \frac{1}{n(n+1)!\,(2n+1)}$ then T_{mean} for constant Q becomes

$$T_{mean} = \frac{Q}{\pi\sqrt{(\rho ck)}} \int_0^t \frac{1}{(t-\tau)^{1/2}} \sum_{n=0}^{\infty} C_n \left[\frac{h}{\sqrt{(\alpha(t-\tau)}}\right]^{2n+1} d\tau \qquad (4.28)$$

Letting $w = t - \tau$, then

$$T_{mean} = \frac{Q}{\pi\sqrt{(\rho ck)}} \int_0^t \sum_{n=0}^{\infty} \frac{1}{w^{n+1}} C_n \left[\frac{h}{\sqrt{\alpha}}\right]^{2n+1} dw \qquad (4.29)$$

and hence

$$T_{mean} = \frac{Q}{\pi\sqrt{(\rho ck)}} \sum_{n=1}^{\infty} C_n \left[\frac{h}{\sqrt{\alpha}}\right]^{2n+1} \left[\frac{1}{w^n}\right]_0^t \frac{1}{n}$$

$$+ \frac{Q}{\pi\sqrt{(\rho ck)}} \frac{h}{\sqrt{\alpha}} [\log w]_0^t \qquad (4.30)$$

The second expression cannot be evaluated as t -> 0, since the convergent series expansion does not apply for $\beta \to \infty$, so a combination of the asymptotic expansion and convergent series expansion is used as follows:

$$T_{mean} = \frac{1}{(\pi\rho ck)^{1/2}} \int_0^t \frac{Q(\tau)}{(t-\tau)^{1/2}} d\tau \left[\text{erf } \beta - \frac{(1-e^{-\beta^2})}{\sqrt{\pi}\,\beta} \right] \qquad (4.31)$$

Putting $w = t - \tau$, then for constant Q,

$$T_{mean} = \frac{1}{(\pi\rho ck)^{1/2}} \int_0^t \frac{Q}{w^{1/2}} \left[\text{erf } \beta - \frac{(1-e^{-\beta^2})}{\sqrt{\pi}\,\beta} \right] dw \qquad (4.32)$$

So $w \to 0$ corresponds to $\beta \to \infty$, and $w \to \infty$ corresponds to $\beta \to 0$, and the integration can be split such that

$$T_{mean} = \frac{1}{(\pi\rho ck)^{1/2}} \int_0^{t_1} \frac{Q}{w^{1/2}} d\tau \left[\text{erf } \beta - \frac{(1-e^{-\beta^2})}{\sqrt{\pi}\,\beta} \right] dw +$$

$$\frac{1}{(\pi\rho ck)^{1/2}} \int_{t_1}^{t_2} \frac{Q}{w^{1/2}} d\tau \left[\text{erf } \beta - \frac{(1-e^{-\beta^2})}{\sqrt{\pi}\,\beta} \right] dw \qquad (4.33)$$

and referring to the first integral as I_A and the second as I_B, then $T_{mean} = I_A + I_B$, where the asymptotic expansion for erf is used for I_A and the convergent series expansion is used for I_B. Examination of the terms shows that with two terms in the asymptotic series, the error is

less than 1% provided that $\beta > 1.5$. With 6 terms in the convergent series expansion, the error is less than 1% for $\beta < 1.5$, hence the whole range of time can be covered.

A computer program was written to calculate the two-dimensional surface temperature using the above theory for gauges on one layer. This enabled a prediction of the magnitude of the two-dimensional effects to be made. 20 terms were used in the convergent series expansion and the integration was split at $\beta = 1.7$, so the error was reduced to order 0.1%.

The effects of two-dimensional (or lateral) conduction on pulse calibration of films on machineable glass is shown in figure 4.6, where the full surface temperature responses for films of widths 1 and 2mm are compared with those for one-dimensional heating. Thus the effects of 2-D conduction can be seen to be appreciable even for a good insulator such as machineable glass.

In the case of multi-layered substrates, with a metal base, the long-time response is dominated by the properties of the base metal. Consequently, 2-D effects were anticipated to be severe. In fact the dependence on the parameter β, from the single layer case, indicates that for the hypothetical case of a vanishingly thin insulating layer on say nickel, 2-D conduction would lead to error of -4.75% in a time of only 30μs seconds, for a film of width 1 mm. Therefore, it was considered essential to be able to predict satisfactorily, the effects of 2-D conduction in multi-layered media.

The calibration technique is based upon the 1-D response of the multi-layered medium to a step in heat transfer. Hence, the object of 2-D studies was firstly to determine the parameters required for the film response to behave sufficiently close to the theoretical 1-D solution for satisfactory calibration. Secondly, if these conditions proved too

restrictive,as the above analysis suggested, the object was to determine whether it would be possible to enable a 1-D analysis, with due allowance for 2-D effects to be applied to the calibration process.

In view of the complexity in the mathematical analysis, it was decided to use numerical methods for the primary investigation of 2-D effects in multi-layered regions, with the analysis for the single layered region providing a useful check on the numerical procedures. The L.O.D. (locally one-dimensional) splitting technique coupled with a simple explicit scheme was the procedure used. A brief description of the application of this method to the type of problems under consideration is given in Appendix 1, together with references to more detailed works on numerical techniques.

A comparison between the mean film temperature for a 2mm film on nickel calculated by the theoretical method of above and that calculated numerically, is shown in figure 4.7. The small error in the numerical solution is largely due to the fact that only 9 points were used to cover the film, (the error was shown to be much greater if only 5 points were used.)

A numerical experiment was performed to determine the likely scale of the 2-D effects. A 2mm wide film on 350μm machineable glass bonded to 5.85mm nickel was considered. 12 "x" increments were taken in the normal direction, in the machineable glass layer ($\Delta\eta_1 = 3.4\text{x}10^{-2}$) and 38 in the nickel ($\Delta\eta_1 = \Delta\eta_2$). The y- (i.e. lateral) step was taken as 0.157mm, thus 7 points (6.5 increments) covered the film. From the temperature distribution plot, figure 4.8, at t = 0.285 seconds, the effect of the highly conducting nickel base is clearly shown by the contours which spread far more rapidly in the nickel region than in the machineable glass covering. A plot of the calculated 1-D and 2-D surface temperature

rises (figure 4.9), indicates that the calibration method of fitting lines to the first and second sections of the curve would produce an incorrect point of intersection. This is discussed further in Chapter 6.

4.5 Use of a thermal radiation technique.

A simple method of radiative heating, which applied a step in heat flux to the whole surface of the sample, was employed in conjunction with the electrical discharge method. The advantage of this is that the lateral conduction effects, caused by using the finite width film itself to produce the heating, are removed. The system employed is shown in figure 4.10 . The element from a car cigarette lighter, powered by a 12 Volt battery, was used as a heat source, and a mechanically operated camera shutter was placed between it and the sample to be tested. A battery powered electrical analogue was used to apply 1 volt across the film. A thin coating of matt black paint was sprayed across the whole surface of the sample, to ensure a uniform absorption of heat. Heat was provided to the surface for a finite length of time (controlled by the camera shutter), and for each test, 3000 samples at 0.5ms/sample of the filtered and amplified signal from the analogue output were recorded on the DATALAB Transient recorder.

From equation 3.61, for a two-layered medium, with semi-infinite metal layer,

$$s^{1/2}\bar{T}_s = \frac{\bar{\dot{q}}_s}{(\rho_1 c_1 k_1)^{1/2}} \frac{(1 + A\exp -2a(s/\alpha_1)^{1/2})}{(1 - A\exp -2a(s/\alpha_1)^{1/2})}$$

So if $\dot{q}_s$ is a step, then

$$s^{1/2}\bar{T}_s = \frac{1}{s(\rho_1 c_1 k_1)^{1/2}} \frac{(1 + A \exp -2a(s/\alpha_1)^{1/2})}{(1 - A \exp -2a(s/\alpha_1)^{1/2})} \qquad 4.33$$

where $s^{1/2}\bar{T}_s$ is the output from the electrical analogue $= \bar{V}_a(s)$ (from equation 3.64).

Hence expanding the denominator gives

$$\bar{V}_a(s) = s^{1/2}\bar{T}_s = \frac{1}{s(\rho_1 c_1 k_1)^{1/2}} (1 + 2\sum_{m=1}^{\infty} A^m \exp -2a\,(s/\alpha_1)^{1/2}) \qquad 4.34$$

which can then be inverted to give

$$V_a(t) = \frac{1}{(\rho_1 c_1 k_1)^{1/2}} (1 + 2\sum_{m=1}^{\infty} A^m \operatorname{erfc} \frac{ma}{\sqrt{(\alpha_1 t)}}) \qquad (4.35)$$

At $t = o$, $V_a(t) = \frac{1}{(\rho_1 c_1 k_1)^{1/2}}$ and as $t \longrightarrow \infty$, then

$$V_a(t) \longrightarrow \frac{1}{(\rho_2 c_2 k_2)^{1/2}}$$

The expected analogue output signal is shown in figure 4.11. In practice, however, partly due to the slow opening time of the shutter, the application of this method was effectively limited to providing an alternative check (to wind tunnel testing) on the validity of the calibrations obtained by the pulsing method, as will be described in chapter 6.

CHAPTER 5

Thin Film Technology.

There are two commonly used techniques for depositing thin film resistance thermometers, namely by vacuum deposition, and by hand painting and firing a proprietary metallic suspension .

'Painted' films are formed by painting platinum, in the form of liquid bright paint (HANOVIA 05-X, Englehard Industries), in thin strips on the model, the surface of which must be smooth and highly polished. The model is then fired in an oven by bringing it to a temperature of about 650^{o}C (depending on the insulator) and held at that temperature for about 30 minutes. The painting and firing cycle may be repeated until the desired resistance of the gauge is achieved. Electrical leads may be connected by painting wider tags at either end of the film and by painting gold or platinum paint over them to reduce their resistances.

The main advantages in painting of thin film resistance thermometers lies in the ease of their application to curved surfaces and their

excellent adhesive nature. Against these however, the uniformity of the film thickness and area is very dependent on skill. A major limitation is that the insulating substrate must be capable of withstanding the high temperatures used in the firing process, and typically, such gauges have been painted on pyrex or quartz models. The well tried technique at Oxford uses machineable glass (CORNING 'MACOR') for the model material. This material has physical properties which render it suitable for this purpose, including the ease with which it can be machined and polished, good thermal insulation and its ability to withstand temperatures of up to 1000^{o}C without significant deformation. Detailed descriptions of thin film heat transfer gauge construction are given in HENSHALL and SCHULTZ (1959), VIDAL (1956), and SCHULTZ and JONES (1973).

Vacuum deposition, on the other hand, produces films whose areas and thicknesses can be accurately controlled by the use of masks. The adhesive qualities compared to those of painted films are poor: even when a thin chromium layer on insulators such as quartz or pyrex is used as a primary 'keying' coat, the adhesion of the vacuum deposited film is still inferior to that of the painted films.

Detailed descriptions of vacuum deposition methods are contained in HOLLAND (1970) and METCALF and DUMBRELL. Nickel is the material commonly used in sputtering techniques and it is also successful when used in an electron beam evaporator.

5.1 Requirements for validation of gauge use on two-layer composites.

There were two major requirements for an experimental program to validate the calibration technique discussed in chapter 4, for thin film gauges on two-layered media .

The first was the production of two-layer flat substrates, comprising a thin electrically insulating layer on a second layer, (not necessarily a metal but indeed any base). For the validation of the calibration method described in chapter4, it was necessary that the substrate surface could be instrumented (either by painting or vacuum deposition), with thin film gauges.

Further, it was necessary to know the values of $(\rho_1 c_1 k_1)^{1/2}$ for the insulating layer, $(\rho_2 c_2 k_2)^{1/2}$ for the metal and a, the thickness of the insulating layer, so that comparisons could be made between experimental values obtained and the manufacturers' values.

The second requirement was the development of a system whereby a metal model (circular cylinders in the cases to be described, or turbine blades for future use) could be coated with an electrically insulating layer and subsequently instrumented with thin film heat transfer gauges. Electron beam evaporation as discussed was considered to be less convenient due to the complexity of evaporating on to a curved surface.

Initially it was envisaged that it might be possible to satisfy both of these requirements simultaneously, by the use of commercially sputtered alumina (Al_2O_3) on a nickel-based turbine alloy. Attempts to paint surface thin film gauges proved unsuccessful however, since the films, after baking, were found to form a shorting circuit to the underlying metal. Furthermore, it was found that although a successful (i.e. "non-shorting") film could be produced, after some time a short developed. This was possibly caused by the film metal diffusing through the alumina layer. Electron micrographs revealed that the alumina was microporous. A cross section of a painted film on a substrate comprising about 20μm alumina on a nickel based turbine alloy (N86), is illustrated in figure 5.1 where the magnification is 4000 times. A surface view is shown in figure 5.2a with a magnification of 50, and in figure 5.2b with a magnification of 2000. At this magnification, the porosity of the alumina is immediately obvious, and the cross section further indicates that the pores may extend directly to the surface of the underlying metal.

5.2 Flat plate samples for method validation.

For the purposes of producing flat plate two-layer samples, nickel thin film gauges were evaporated onto thin insulating substrates, using an evaporation unit with an electron bombardment source of the ring cathode type (CRASWELL SCIENTIFIC RG 2A). A schematic diagram is shown in figure 5.3. The two substrates used were slices of machineable glass ceramic, of thickness approximately 190μm, and a high temperature polyimide (KAPTON, from Dupont de Nemours), of thickness 50μm. The inability of the substrates to withstand the high firing temperatures precluded the use of painted films; in the case of machineable glass, this was due to the thinness of the section. Evaporation was carried out at pressures of less than 2.0×10^{-5} torr, and adhesion was improved by heating the substrate up to about 200^{o}C, and by deposition of an initial layer of chrome. Films of widths 1 and 2mm, and with resistances between 20 and 90 Ω were formed .

Commercially evaporated films (DISA), consisting of evaporated nickel on Kapton of thickness 50μm were also obtained.

The thin layers of machineable glass and Kapton were then glued to slabs of 99.9% pure nickel, of thickness 6mm using Epotek H54E (Epoxy Technology Inc.). The adhesive between the layers was cured at 100^{o}C for about one hour, a small vice being used to compress the layers. This resulted in a glue layer of thickness 79μm, for the machineable glass, which was as thin as could be achieved, given that the glass layer was very fragile and could not be compressed very much. Discussion of the effect of the glue layer is given in chapter 6. The Kapton layer was compressed more highly and this resulted in a glue layer of only 25 μm. Electrical leads were attached using Epotek H20E.

The $\sqrt{(\rho ck)}$ values for machineable glass, Kapton, Epoxy and nickel were available from commercial literature and the values for machineable

glass and Kapton were also obtained using the $\sqrt{(\rho ck)}$ tester, described in chapter 4.

5.3 Insulator coating for use on circular cylinder models for wind tunnel tests.

The requirements for the production of an insulating layer which could easily be applied to circular cylinders and complex turbine blade profiles were very stringent.

It was intended to manufacture the cylinders and blades from an easily machineable metal, preferably mild steel or DURAL, or, at worst stainless steel. Experience showed that glueing sheets of Kapton instrumented with vacuum deposited films, to curved surfaces, was not practicable, since it was found that even moderate bending caused the metallic films to crack. Hence, painted surface thin film gauges appeared to be the most promising solution. The insulator coating was thus required to have a smooth or polishable surface, to be impervious to the platinum or gold paint used in painting the films, and capable of withstanding the temperatures of 650^{o}C used in the firing process.

A coat of commercially obtainable vitreous enamel on mild steel was found to satisfy the above requirements. Application of vitreous enamel coatings to steel, cast iron and aluminium to improve appearance and to protect the surface has wide commercial applications including an increasing use in microcircuitry.

Preferred enamelling steel has a carbon content of less than 0.07%; this reduces carbon boil defects which are caused by a reaction between the carbon and oxides in the glass metal system. Carbon monoxide and carbon dioxide, are produced by the reaction, and during the firing of the enamel, rise through the molten enamel leaving pinholes. This kind of

defect, if severe, would have precluded the use of an enamel as an electrical insulator. Such high grade enamelling quality steel is only produced commercially in sheet form, which is unsuitable for model construction. The preferred metal for model construction is machineable mild steel, which is readily available in suitable forms. Fortunately, however, a medium gloss ground coat enamel was obtained, which was suitable for application to EN1A, a mild steel, with a carbon content in the range 0.07% to 0.12%. A simple process of application outlined below, which was subsequently followed successfully during the course of this work, made the use of this enamel and type of steel particularly attractive, since elaborate 10-stage surface pre-treatment, which is common for most enamelling procedures was unnecessary. The enamelling process used was as follows;

(a) Thorough cleaning and degreasing of the surface with acetone, by immersion in an ultrasonic bath for about 5 minutes, followed by cleaning with an abrasive alkaline cleaner, for example, the proprietary fluid AJAX .

(b) Application of enamel with a compressed air-operated spray gun (Binks-Bullows type 630 gravity feed spray gun, with nozzles of .086 inches diameter, which was driven by a Motivair Airlink M13 compressor).

(c) Model then dried in a low temperature oven at 100^{o}C for 15 minutes

(d) Model fired in high temperature furnace at 820^{o}C for 15 minutes

(e) Model removed from furnace and left to cool in air

A photograph using a high resolution optical microscope, of a cross section of a sample of vitreous enamel on mild (EN1A) steel, at a magnification of 500 times, is shown in figure 5.4. An acoustic micrograph, at a microscope operating frequency of 370 MHz, at the focus of the enamel layer, and at a magnification of 500 times, of the cross

section is shown in figure 5.5. The enamel thickness is about 140μm and its structure can be clearly seen. There are small voids visible, and this illustrates why the thermal properties of such enamels are not reliably known, and cannot, as is the case with most deposited layers, be determined from bulk properties. There is good bond, with no voids at the enamel-steel interface. Since the typical width of a painted film (1mm) is approximately 50 times greater than the maximum void diameter, the enamel appears homogeneous over this width. Before the correct enamel-steel combination was obtained, early experiments with different enamels produced pin holes which extended from the surface of the enamel through to the steel, and thus did not provide an insulating layer. An acoustic micrograph at 4μm defocus, at a magnification of 500 times is shown in figure 5.6, and the grain boundaries of the steel and the enamel-steel interface are visible.

Mild steel circular cylinders, of diameter approximately 13mm, with central enamelled sections were successfully instrumented with thin film gauges (figure 5.7). Machined grooves were used to take the leads from the films and were filled with Araldite to retain a smooth contour.

An alternative two-layered cylinder was made by glueing a strip of Kapton instrumented with DISA thin film gauges, around a steel rod, using Epotek H54E (figure 5.8). This was accomplished using a silicon rubber mould of the cylinder to compress the glue layer.

CHAPTER 6

EXPERIMENTAL CALIBRATIONS

6.1 Calibrations from flat plate samples.

In order to validate the method of calibration of thin film gauges on two-layer substrates, developed theoretically in chapter 4, the temperature response to a step in heat transfer rate, of the substrate was obtained, by suddenly causing a current to flow through the thin films on the surface. The construction of the flat plate samples designed to verify the procedure, and the circular cylinder models have been described in chapter 5. The change in voltage across the film was recorded using a fast sampling transient recorder (DATALAB DL/2800)). The transient recorder was used in the pre triggering mode, such that 1096 samples were taken before the step in heat flux was applied. The transient recorder was then triggered by the sudden change in voltage across the resistance bridge in the current pulse unit, and 3000 samples were subsequently recorded.

6.1.1 Test on machineable glass.

A sample test was performed using a film on machineable glass i.e. a " semi-infinite" single layer substrate. The resultant unscaled surface

temperatures plotted against (time)$^{1/2}$ for pulses in air and glycerine are shown in figure 6.1.

Using the relationship

$$\sqrt{(\rho ck)}_{m.g.c.} = \frac{\sqrt{(\rho ck)}_{glycerine}}{1 - \frac{\Delta Vair/\sqrt{t}}{\Delta V_{gly}/\sqrt{t}}} \qquad 6.1$$

The corresponding temperature in air versus the temperature in glycerine is plotted in figure 6.2, and the slope $(\Delta Vair/\sqrt{t})/(\Delta Vgly/\sqrt{t})$ is used in equation 6.1 to give

$$\sqrt{(\rho ck)}_{machineable\ glass} = 2050\ J/K\ s^{1/2}m^2 \quad \pm 2.5\%$$

for this particular sample. This compares with a value of 1808 from a CORNING data sheet. Sample to sample variation has been reported by CONSIGNY et al (1981), possibly resulting from different firing cycles during film production.

The accuracy with which $\sqrt{(\rho ck)}$ is measured depends on the measurement of the voltage ΔV and the accuracy with which $\sqrt{(\rho ck)}$ of glycerine is known. As discussed in Chapter 4, ρ,c and k of glycerine have been measured and $\sqrt{(\rho ck)}$ is known to within ±2.0%.

The measurement of the voltage ΔV, depends on the resolution of the transient recorder, which is 1024 bits. In practice, a line of best fit was drawn to the air-glycerine curve over about one-fifth of the full scale of the transient recorder, so the accuracy is approximately $\frac{1}{200}$ or 0.5%. There is thus a combined accuracy of ± 2.5%.

The calibration technique was subsequently applied to determine $\sqrt{(\rho ck)}$ of quartz, which exhibits far less sample-to-sample variation in

properties. A value of 1560 $J/Ks^{1/2}m^2$ was obtained, which compares very well with the value of 1530 $J/Ks^{1/2}m^2$ from various sources (SCHULTZ and JONES,(1973)). In addition, the variation of $\sqrt{(\rho ck)}$ of machineable glass with temperature was measured by applying the pulse calibration to a sample placed inside an oven, which was allowed to "soak" at various temperatures. The variation of $\sqrt{(\rho ck)}$ with temperature was calculated to be

$$\sqrt{(\rho ck)}_T = (1 + .0012(T - 20^{\circ}C))\sqrt{(\rho ck)}_{20^{\circ}C}$$

The variation in $\sqrt{(\rho ck)}$ is thus appreciable if the temperature rise is significant. Such would be the case for a model fabricated entirely from this material, during the course of a run using the I.L.P.T., in situations where the surface temperature rose by 50°C. As will become clear in Chapter 7, however, the rise in surface temperature for a multi-layered model is generally far less than the corresponding temperature rise for a model made entirely from an insulator. Correction for thermal variation in $\sqrt{(\rho ck)}$ is therefore generally small.

6.1.2 Calibrations on two-layered substrates.

Temperature signals from thin film gauges on the two-layered substrates which were subjected to the sudden imposition of a constant current were recorded on the transient recorder and subsequently transferred to the PDP 11/34A mini-computer. Two films of width 2mm, and one of width 3mm on 50μm Kapton, bonded with 25μm Epotek to pieces of machineable glass ceramic, thickness 4mm, were tested. The first object was to determine if a value of $\sqrt{(\rho ck)}$ for the Kapton layer could be obtained which compared well with manufacturer's quoted values.

An air-glycerine test was performed using a film of 2mm, and the corresponding temperature vs √time traces for air and glycerine are shown in figures 6.3(a) and (b). The sampling rate was 10μs so the "switch"

point is not seen in such a short timescale, and there are no effects due to two-dimensional conduction of any significance.

The slope of the line obtained by plotting the temperature in air against the temperature in glycerine (figure 6.4), produced a value of 560 J/K $s^{1/2}m^2$, which compared with the manufacturer's value of 489 J/K $s^{1/2}$. Again note that there is sample-to-sample variation in the properties, as with machineable glass ceramic.

The temperature-/time trace at a sampling rate of 1ms/sample is shown in figure 6.5, for the 2mm film. The effects of 2-D conduction in the second section of the curve can be clearly seen, and this indicates the difficulty in applying the calibration method, which is based on the 1-D surface temperature. To overcome this problem, a modified method of calibrating was used.

If it is assumed that the effects of 2-D conduction in the insulating layer are negligible, at least up to the time of the switch point, then the calibration curve follows the 1-D surface temperature up to this point. A line of best fit may then be drawn to the first section of the curve and its slope calculated. For samples where the thermal properties of the second layer are known to a reasonable degree of precision, as is certainly the case for mild steel and, to a somewhat lesser extent, for machineable glass, the second line can be fitted to the second section of the curve (after the switch point). The second line is fitted so that it is tangential to the curve in the region where the switch point is expected to occur, and such that its slope is in the ratio

$$\frac{\text{slope 1}}{\text{slope 2}} = \frac{\frac{1}{\sqrt{(\rho_1 c_1 k_1)}}}{\frac{1}{\sqrt{(\rho_2 c_2 k_2)}}}$$

where $\sqrt{(\rho_1 c_1 k_1)}$ has been determined from an air-glycerine test, and $\sqrt{(\rho_2 c_2 k_2)}$ is considered already known.

The $\sqrt{(\rho ck)}$ of Epotek H54E is typically 630 J/K $s^{1/2}m^2$,(see Table 1) hence for the purposes of this experiment and for comparison between experiment and theory, a layer comprising 50μm Kapton and 25μm Epoxy can be considered as equivalent to 75μm Kapton, since the individual values of ρ, c and k are fairly close.

The application of this modified procedure is illustrated in figure 6.6, where lines have been drawn to the experimental calibration curve from the 2mm film on the Kapton-Machineable glass substrate, in the ratio

$$\frac{\text{slope 1}}{\text{slope 2}} = \frac{1/560}{1/2050} .$$

The resulting point of intersection of these lines is found at a $\sqrt{\text{time}}$ of 0.267 $s^{1/2}$, which from equation 4.8 gives a value of 4.5×10^{-5} fro the parameter $\frac{a}{k_1} = \frac{\text{thickness of kapton}}{\text{thermal conductivity}}$. The accuracy of this procedure was tested easily, since using a value of 0.155 for k_1 of Kapton (the manufacturer's value, see Table 1), the experimental thickness a, was calculated to be 70μm. This compared very satisfactorily with the measured value of 75μm, given the uncertainty in the properties of the actual kapton used, and those of the Epoxy layer.

In order to check the validity of the assumption that the response is effectively 1-D up to the switch point, the finite difference scheme mentioned in chapter 4 and described in Appendix 1 was applied to calculate the full 2-D response for a film of width 2mm on 75μm Kapton bonded to 4mm machineable glass. This corresponded to the conditions for this first practical test. Following the notation used in Appendix 1, for the numerical solution 11 steps were taken in the x-direction of the

Kapton, $\Delta x_1 = 7.5\mu$, i.e. $\Delta\eta_1 = 2.37 \times 10^{-2}$, and 39 in the machineable glass ceramic, $\Delta x_2 = 102.56\mu$, i.e. $\Delta\eta_2 = 0.1107$. 65 steps were taken in the lateral direction from the centreline ($\Delta y_1 = \Delta y_2 = 80.0\mu$, $\Delta\xi_1 = \frac{80}{\sqrt{\alpha_1}}$, and $\Delta\xi_2 = \frac{80}{\sqrt{\alpha_2}}$), with 13 points covering the 1mm half-width of the film. (The time step was such that $|r|_{max} \leq \frac{1}{2}$, the stability limit). This numerically predicted temperature response is shown in figure 6.7, where it is compared with the exact analytic solution for the 1-D surface temperature, and with the experimental calibration. The values used for ρ, c, and k of Kapton and machineable glass are those given in table 1. These are the manufacturer's values, which give a value of 489 J/k $s^{1/2}m^2$, for $\sqrt{(\rho ck)}$ of Kapton, and 1808 for $\sqrt{(\rho ck)}$ of machineable glass, rather than the experimentally calibrated values of 560 and 2050 respectively, since it was necessary to know each property individually for the predictions. From figure 6.7, there is very good agreement between the predicted 2-D temperature and the calibration, and the assumption that the process is 1-D until at least after the switch point can be seen to be valid. The predicted curve before the switch point is slightly steeper than the experimental curve, and since this depends on $\frac{1}{\sqrt{(\rho ck)}}$, it indicates that the experimentally determined value for $\sqrt{(\rho ck)}$ is probably more accurate than that calculated using the quoted values.

A plot of the temperature-time distribution is shown in figure 6.8, at a time of 1.6 seconds, and a corresponding plot of the temperature contours in both regions at this time is shown in figure 6.9. These clearly show, both that the step in heat transfer has, at this time, still not appreciably penetrated to the back wall (i.e. there are no " backwall" effects to compensate partially for the lateral conduction

effects), and that the heat has diffused appreciably in the lateral direction at the surface of the substrate. The lateral diffusion from the film at the surface is further illustrated in figure 6.10, which compares the surface temperature distribution at t = 0.135 seconds and t = 1.65 seconds.

The most important conclusion to be drawn from this is that the modified form of calibration which relies on the process remaining 1-dimensional up to the switch point can be applied successfully in this case.

Repeat calibrations using a second film of width 2mm resulted in completely repeatable results.

A plot of a temperature-√time trace from a film of 3mm on the same substrate is shown in figure 6.11 and it can be seen that the 2-D effects are considerably reduced.

Note that the modified calibration procedure could not be applied to the case of 350 μm machineable glass on nickel discussed in chapter 4, since there is a considerable departure from the 1-D response well before the switch point, because of lateral conduction, This is due to the fact that nickel is an excellent conductor and acts as a heat sink, producing strong 2-D effects, whereas conversely machineable glass is a good insulator.

The two-layer substrates comprising 190μm machineable glass, bonded with 79μm Epotek to nickel, produced anomalous results, which were subsequently explained by the presence of large air bubbles in the glue layer, resulting from the difficulty of compressing the machineable glass, as discussed in Chapter 5.

6.2 Calibrations of circular cylinder models.

The experiments to be described in chapter 7 required the use of two-layered circular cylinder models. It was intended to use a stainless steel rod of diameter 12.7mm with an instrumented machinable glass insert, (figure 6.12) in the isentropic light piston tunnel at O.U.E.L. to obtain baseline heat transfer rate, using the standard heat transfer gauges and processing methods. The results were to be compared firstly with a correlation obtained by LOWERY and VACHON (1975) for stagnation point heat transfer to circular cylinders. Secondly, the results could be compared with those obtained from two-layer circular cylinders, (using the calibration and processing methods developed in chapters 3 and 4.).

6.2.1 Calibration of machinable glass model.

A standard air-glycerine test was performed using one of the thin film gauges and the resulting value for $\sqrt{(\rho ck)}$ of Machineable glass obtained was 1859 J/K $s^{1/2}m^2$. The value from this sample of machineable glass actually agrees well with the quoted value.

6.2.2. Calibration of two-layered cylinders.

Two rods of mild steel, and diameter 13mm, with central enamelled sections (figure 6.13a and b) were instrumented with thin film gauges.

A piece of Kapton with vacuum deposited DISA films was wrapped around a third cylinder (figure 6.14) of mild steel diameter 12.9mm, and glued to it using EPOTEK H54E. The different models used are summarised in the following table.

CYLINDER	material	film	film width
1	Enamel on mild steel	platinum, gold tags	2mm
2	enamel on mild steel	platinum film and tags	2mm
3	Kapton on mild steel	nickel film, gold tags	2mm

The $\sqrt{(\rho ck)}$ of the enamel was obtained using the standard air-glycerine test described in chapter 4. An example of the two temperature curves obtained, in air and glycerine for cylinder 1, where the sampling rate was 2μs/sample, is shown in figure 6.15 a and b.The slope of the line obtained in plotting T_{air} vs $T_{glycerine}$ was found to be 1.63 with a correlation coefficient of 0.99, which gave a value of 1468 J/K $s^{1/2}m^2$ for $\sqrt{(\rho ck)}$ enamel.

6.2.3 Determination of switch point.

The calibration function requires a knowledge of $\sqrt{(\rho_1 c_1 k_1)}$ of the insulating layer, a factor $\frac{a}{k_1}$, where a is the thickness of the insulating layer, and k_1 is the thermal conductivity and $\sqrt{(\rho_2 c_2 k_2)}$ of the base, which is usually a metal. The constant $\frac{a}{k_1}$ can be determined from equation 4.8 given $\sqrt{(\rho_1 c_1 k_1)}$, $\sqrt{(\rho_2 c_2 k_2)}$ and the point of intersection of the two

lines fitted to the temperature response of the film when a step in heat transfer rate is applied at the surface. As discussed, with reference to the flat plate samples, the accurate determination of the switch point depends upon several factors, in particular the effects of lateral conduction.

It was decided to use two complementary methods to obtain maximum accuracy for the point of intersection. Firstly, the current pulse unit, (the "$\sqrt{(\rho ck)}$ tester") was used to provide a step in heat transfer rate at the surface . The resulting temperature response was plotted against $(\text{time})^{1/2}$ and the calibration described was applied, modified to take account of the lateral conduction, assuming that the process remains one-dimensional up to at least the time of the " switch" point. A line of best fit was drawn to the first part of the curve and its slope determined. Given that $\sqrt{(\rho_1 c_1 k_1)}$ and $\sqrt{(\rho_2 c_2 k_2)}$ are known, ($\sqrt{(\rho_1 c_1 k_1)}$ from the standard air-glycerine test and $\sqrt{(\rho_2 c_2 k_2)}$ from a quoted value in the case of mild steel, then the second line can be fitted with a slope such that the equation

$$\frac{\text{slope line 1}}{\text{slope line 2}} = \frac{\sqrt{(\rho_2 c_2 k_2)}}{\sqrt{(\rho_1 c_1 k_1)}}$$

holds.

The temperature versus $(\text{time})^{1/2}$ response is shown for cylinder 1 in figure 6.16, where this method was adopted. The value of $\sqrt{(\rho_1 c_1 k_1)}$ for enamel was determined to be 1468 J/K $s^{1/2}m^2$ and $\sqrt{(\rho_2 c_2 k_2)}$ mild steel is 14,190 J/K $s^{1/2}m^2$. A line of best fit was drawn to the curve between 0.03

and 0.16 $s^{1/2}$ and the slope calculated. The second line was fitted tangentially after the switch point with slope such that

$$\frac{\text{slope line 1}}{\text{slope line 2}} = \frac{\sqrt{(\rho_2 c_2 k_2)}_{\text{steel}}}{\sqrt{(\rho_1 c_1 k_1)}_{\text{enamel}}}$$

The switch point or point of intersection of the two lines was found to occur at $0.20s^{1/2}$. This resulted in a value of 0.0001393 for the constant $\frac{a}{k_1} = (\frac{\text{thickness of enamel}}{\text{thermal conductivity}})$. The value of k for enamel is not known, but if it assumed to be similar to that for quartz, i.e. k = 1.36, then this suggests that the enamel is of thickness 189.5 μm. A plot of the experimental response is compared with the predicted 1-D temperature and the numerically predicted 2-D temperature, in figure 6.17. The predictions were obtained using the values of ρ, c and k for quartz as an approximation to the values of these properties of enamel and assuming that the enamel is 190 μm thick. This is a reasonable assumption for the purposes of prediction since $\sqrt{(\rho ck)}$ of quartz is typically 1530 $J/Ks^{1/2}m^2$, which compares with a value of 1468, determined experimentally for the enamel. The solution domain measured 12mm by 12mm, very closely approximating the true circular region of diameter 12.7mm, since within the time scale of interest, backwall or sidewall effects should not be significant. It can be seen from figure 6.17, that it is again valid to assume that the process remains one-dimensional up to at least the time of the switch point, and thus the application of the modified calibration procedure is justified.

The same procedure was followed for the second enamelled cylinder and for the Kapton covered steel cylinder. A value of 0.0004362 was obtained for the constant $\frac{a}{\bar{k}_1}$ of the Kapton-steel model, which using a value of 0.155 W/mK for the thermal conductivity of Kapton, produced a value of 67μm for the combined thickness of the Kapton and Epoxy. This compares well with the measured value.

6.3 Thermal radiation technique.

As a complementary technique, the thermal radiation method described in chapter 4, was employed. It was shown (chapter 4, equation (4.35)), that if the heat transfer rate to the surface of a two-layered composite was constant (as provided by radiant heating), then the analogue output $V_a(t)$ is given by

$$V_a(t) = \frac{1}{(\rho_1 c_1 k_1)^{1/2}} \left(1 + 2 \sum_{m=1}^{\infty} A^m \operatorname{erfc} \frac{ma}{\sqrt{(\alpha_1 t)}} \right)$$

In chapter 3, equation 3.78 , it was shown that if the analogue output is represented as a series of steps, then

$$\dot{q}_s(t) = \frac{1}{\alpha} \frac{k_a}{V_o} (\rho_1 c_1 k_1)^{1/2} \sum h\,(N-n)\tau\,(v(n\tau)-v(n-1)\tau)$$

where $h(t) = 1 + \sum_{m=1}^{\infty} (-1)^m A^m \operatorname{erfc} \frac{ma}{\sqrt{(\alpha_1 t)}}$, for a two-layered substrate,

and $h(t) = u(t)$ (unit step function) for a single-layered substrate.

If the parameters $\sqrt{(\rho_1 c_1 k_1)}$ and $\frac{a}{\bar{k}_1}$ have been correctly obtained, then by processing the analogue output in the computer program which will be used in chapter 7, for obtaining true heat transfer rate from a two-layered medium, the input heat transfer rate, i.e. $\dot{q}_s$ as a step should be obtained. The value of $\frac{a}{\bar{k}_1}$ can then be refined to obtain the best reconstructed $\dot{q}_s$.

The analogue output from a single layered (quartz) substrate is shown in figure 6.18, and as expected, the signal, which represents the heat transfer rate is approximately constant, with a slight falling off due to the small surface temperature increase.

The analogue output from the film signal produced by radiant heating on an enamelled cylinder is shown in figure 6.19. Using the value of $(\rho_1 c_1 k_1)^{1/2}$ obtained from the pulse calibration (1468 J/K $s^{1/2}m^2$) and $\frac{a}{\bar{k}_1}$ = 0.001393 from the point of intersection, the actual reconstructed heat transfer rate is shown in figure 6.20, which provides a good indication that the empirically obtained constants are accurate, since it is approximately constant. The effects of using incorrect values of $\frac{a}{\bar{k}_1}$ are shown in figure 6.21., where the reconstructed signals for values of $\frac{a}{\bar{k}_1}$ = 0.0001393, (the correct value used), and $\frac{a}{\bar{k}_1}$ ± 10%, (which correspond to values of 0.00015323 and 0.00012537 respectively) are plotted. Errors of +10% and -10% can be seen to produce errors of approximately -8% and +8%

in the reconstructed heat transfer rate respectively. The serious errors incurred in the reconstructed heat transfer rate, when errors of approximately ± 30% in $\frac{a}{\bar{k}_1}$ are taken, are shown in figure 6.22.

Hence, a thermal radiation technique may be used to check the value of the pulse-calibrated constant $\frac{a}{\bar{k}_1}$, by reconstructing the heat transfer rate signal from the analogue output.

CHAPTER 7

HEAT TRANSFER RATE TO CIRCULAR CYLINDERS

7.1 Use of cylinders to measure heat transfer rate in isentropic light piston tunnel.

After calibration of the multi-layered model cylinders, stagnation point heat transfer measurements were made in subsonic hot flow using the I.L.P.T. The analysis developed in chapters 3 and 4 was then applied to the processing of the output signal from the heat transfer gauges.

The objective of the experiment was to test the accuracy with which the heat transfer rate could, in practice, be measured using gauges on multi-layered models, coupled with the analysis procedure outlined in chapters 3 and 4.

The accuracy was determined by comparing values of heat transfer rate obtained using this technique, with the corresponding results obtained from;

(a) standard techniques (films on a semi-infinite ceramic model) and

(b) from the value predicted by a widely accepted correlation of circular cylinder heat transfer measurements.

Numerous studies including those by KESTIN and MAEDER (1956 and 1961), VAN DER HEGGE ZIJEN (1957), PIERCY and RICHARDSON (1928) and LOWERY and VACHON (1975) have been conducted over the last forty years into the analysis of forced convection heat transfer from circular cylinders in cross flow. Particular attention has been given to the effects of the influence of turbulence on the stagnation point heat transfer rate. LOWERY and VACHON (1975) measured the effect of turbulence intensity, Tu, on the stagnation point heat transfer to a circular cylinder. Based on a large number of results, they presented the correlation equation

$$\frac{Nu}{Re^{1/2}} = 1.01 + 2.624\left[\frac{Tu\ Re^{1/2}}{100}\right] - 3.07\left[\frac{Tu\ Re^{1/2}}{100}\right]^2 \qquad 7.1$$

for $0 < TuRe^{1/2} < 64$, where Tu is defined as $\frac{(\bar{u'^2})^{1/2}}{U}$, and

u' = fluctuating component of freestream velocity

U = mean freestream velocity.

7.2 The Isentropic Light piston Tunnel.

A schematic diagram of the I.L.P.T. is given in figure 7.1. The theory behind its use is given in JONES et al (1973), and details of the Oxford facility are given in SCHULTZ et al (1977), and NICHOLSON (1981).

A short duration (typically 0.4 seconds) hot flow provided by this facility is produced by compressing the test gas in the " pump" tube (figure 7.1) from an initial set level, subsequently referred to as $P_{initial}$. The sequence of operation is briefly as follows:

At the start of the run, valves are opened allowing gas from the high pressure reservoir to flow into the "pump" tube driving the piston forward and isentropically compressing the gas to a pressure referred to

as $\bar{P}$, in the region ahead of the piston. When the desired gas pressure, and thus temperature, have been attained, the fast acting valve is opened, allowing the warm test gas to flow through the working section, out through a second throat, and finally exhausting to a large capacity dump tank. The piston velocity can be maintained constant by matching the volumetric flow rates into and out of the tube. With a constant piston velocity, a steady flow of heated gas at constant total pressure, passes through the working section until the piston reaches the end of the "pump" tube, ending the run.

Departures from the ideal analysis are discussed by JONES et al (1973). The piston in the I.L.P.T. has significant mass and cannot instantly respond to the opening of the fast acting slide valve. Unless compensated for, the effect of this is to cause oscillations in the piston velocity and the test gas pressure. JONES et al (1973) describe a method of compensating for this, which utilises a second high pressure reservoir which is connected only during the compression phase. The purpose of this is to ensure that (at the instant the working section valve opens), the piston velocity is equal to that required for 'matched' running.

For the purposes of the present study a turbulence generating grid, which is normally inserted to provide about 4% turbulence, was removed and the background turbulence level was assumed to be less than 0.2%, as reported by NICHOLSON (1981).

The position of the cylindrical rods in the cascade working section is shown in figure 7.2. The cylinder was placed upstream of a cascade of turbine rotor blades, and the experiments were performed during a break in the normal cascade testing performed in the tunnel. The rod was held fixed in the tunnel sidewall at either side, by lockable collars, which

allowed the model to be rotated until the film coincided with the stagnation point, and then clamped (as shown in figure 7.3).

The on-line computer based instrumentation and data acquisition system is described by OLDFIELD et al (1978). A highly interactive computer suite (TOPSY) which calculates the run parameters from the overall calibrations and sampled data is described in BAINES (1983) For these test a maximum of 10 channels was scanned at 3ms intervals for 0.6 seconds.

The upstream total pressure P_o was measured by a Kistler type 7031 gauge pressure transducer, connected via 25cm of 0.5mm hypodermic tubing to a pitot tube.

The sidewall static pressure was measured differentially using National Semiconductor Transducers type LX1620D. The low pressure port of this transducer was connected to a reference tank (maintained at a pressure slightly below the run-time static pressure), whilst the high pressure port was connected, via hypodermic tubing, to an array of sidewall static tappings (pneumatically averaged).

The calibration and use of such pressure instrumentation is well established and is extensively dealt with in NICHOLSON (1981).

A compression ratio $\frac{\bar{P}}{P_{initial}}$ of 3.15 was used, which resulted in a total temperature of 405K from an initial ambient temperature of 293 K. With the turbulence grid removed, the pressure drop between the pump tube and working section is minimal, and $\bar{P}$ is only marginally greater than P_o. Thus the typical mean temperature ratio $\frac{T_{air}}{T_{model\ (initial)}}$ was 1.39, calculated assuming isentropic (adiabatic) compression. As the total period allowed for these tests was very brief, the total temperature of the gas was not measured directly. From DANIELS (1978) and JONES et al (1973), however, the temperature error due to a non-adiabatic compression

is small, typically 0.5% in 150K, for the moderate pressure ratios used in this study.

7.3 Heat transfer measurements

7.3.1 Data Acquisition.

Two independent data acquisition systems were used to record the output signals from the heat transfer analogue circuits. The first system, with a maximum sampling rate of 3ms, was based on the PDP 11/34A computer. The second comprised a "stand-alone" transient recorder (Datalab model DL2800) with a maximum simultaneous sampling rate on up to 8 channels of 2MHz. The transient recorder data was transferred to the O.U.E.L. VAX 11/780 for processing.

The existing processing method for measuring the heat transfer rate to machineable glass models, as described in Chapter 4, was used to determine the baseline heat transfer rate to the machineable glass cylinder. Since the standard processing, which scales the analogue output to give actual heat transfer rate for the one-layer gauges was not applicable for the two-layered cylinders, all the computer sampled and transient recorder sampled analogue data were processed on the VAX, using a suite of computer programs written by the author, and based on the theory given in chapters 3 and 4.

7.3.2 Heat transfer rate processing.

From equation 3.78, assuming that the output of the analogue is a series of steps, then

$$\dot{q}_g(t) = \frac{k_a}{\alpha v_0} (\rho_1 c_1 k_1)^{1/2} \sum h(N-n)\tau \, (v(n\tau) - v(n-1)\tau)$$

where h(t) is the gauge step calibration function, as defined in chapter 3. k_a is the analogue calibration constant = $\frac{\sqrt{r}}{\sqrt{c}}$ and v_o is the pre-set film voltage, which for these experiments was set to be 0.25 volts. For two-layered gauges it was shown that

$$h(t) = 1 + 2 \sum (-1)^m A^m \operatorname{erfc} \frac{ma}{\sqrt{(\alpha_1 t)}}$$

For a single-layered gauge, h(t) = u(t), the unit step. A computer program HTRANS2, was written to calculate the heat transfer rate from the analogue output. For maximum flexibility of the program, the section which generates the gauge calibration function h(t), which is gauge specific, was written as a series of subroutines, so that the appropriate h(t) for one, two, or multilayer gauges could be called up. The constants to be entered in the heat transfer program are α the temperature coefficient of resistance of the film, k_a, v_o, $\frac{a}{k_1}$, $\sqrt{(\rho_1 c_1 k_1)}$ and $\sqrt{(\rho_2 c_2 k_2)}$.

7.3.3 Surface temperature recalculation.

The procedure outlined in chapter 4 for calculation of the surface temperature can be applied for any heat transfer gauge.

From 4.9

$$\bar{\dot{q}}_s = F(s)\,\bar{T}_s = \frac{k_a\,F(s)\,\bar{v}_a(s)}{V_o\,\alpha\,\sqrt{s}}$$

so

$$\bar{T}_s = \frac{k_a\,\bar{v}_a(s)}{v_o\,\alpha\,\sqrt{s}} \qquad (7.1)$$

If the transformed signal from the analogue is considered to be the sum of a series of steps such that

$$\bar{v}_a(s) = \sum_{n=1}^{N} a_n \frac{e^{-st_n}}{s} \qquad (7.2)$$

then $$\bar{T}(s) = \frac{1}{s^{3/2}} \frac{k_a}{\alpha v_o} \sum_{n=1}^{N} a_n e^{-st_n} \qquad (7.3)$$

and $$T = \frac{k_a}{\alpha v_o} \sum_{n=1}^{N} a_n H(t - n\tau) (t - n\tau)^{1/2} \qquad (7.4)$$

where $a_n = v(n\tau) - v(n-1)\tau$

For $t = N\tau$

$$T(N\tau) = \frac{k_a}{\alpha v_o} \sum_{n=0}^{N} a_n ((N-n)\tau)^{1/2} \qquad (7.5)$$

Thus the surface temperature can be calculated within the same program loop as the heat transfer rate.

7.4 Results.

(i) Machineable glass cylinder.

The scaled heat transfer rate obtained from the transient recorder sampled analogue output for run 4957 is shown in figure 7.4. The transient recorder-sampled data, for this and all runs to be described, was low pass-filtered at 2KHz. The output signal has been processed using

the program HTRANS2, with a simple kernel function for h(t) = u(t), the unit step. For comparison, the heat transfer rate obtained from the slow-sampled (computer sampled) analogue output data is shown in figure 7.5, after it has been scaled using existing routines for processing the computer acquired data. As can be seen there is excellent agreement between the fast- and slow- sampled data.

As stated in section 7.1, the measured values of the heat transfer rate to the cylinder stagnation point were compared with the correlation of Lowery and Vachon (1975);

For Tu = 0 , $\frac{Nu}{Re^{1/2}} = 1.01$

Since $Nu = \frac{hl}{k}$, where h refers here to the heat transfer coefficient, l is a characteristic body length (= diameter for a cylinder), and k is the local thermal conductivity of the freestream,

$\dot{q} = h\Delta T$, then

$\dot{q} = 1.01 \frac{\Delta T}{D} k (Re)^{1/2}$, where D is the diameter of the cylinder.

To determine the Reynolds number, least squares line fits are applied to all the pressure measurements by TOPSY, and a fitted value at a user defined time in the run is obtained from the processed results sheet.

The extrapolation procedure which consists of plotting the heat transfer rate against the recalculated surface temperature and extrapolating back to zero temperature rise to obtain the heat transfer rate to an isothermal model was not used, since it was shown by DOORLY (1983), to be unreliable for highly fluctuating heat transfer rate measurements. Instead, his alternative method was used and the application to these tests will be described.

For run 4957, at a time of 0.135 seconds into the run , the inlet Mach number was 0.417 and the Reynolds number 1.0857 x 10^5. The recalculated surface temperature for this run is plotted in figure 7.6 . The ambient model temperature was given by the run sheet to be 289.4 K and the gas temperature 398.2 K. The surface temperature rise of the model at t = 0.135 seconds was found to be 16K by averaging over a short time interval, centred on 0.135 seconds. The upstream total and static pressure traces for the run are shown in figure 7.7, illustrating the rapid tunnel start-up times and flow constancy. The thermal conductivity of air is given by the correlation (valid within the temperature range of interest)

$$k = .0047 + (7 \times 10^{-5} \times T) \qquad \text{(from LOFTUS (1982))}$$

which for T = 398.2 gives a value of 3.257×10^{-2}, so the predicted heat transfer rate for an isothermal model with a reduced driving temperature of ((398.2-289.4)-16) is given by

$$\dot{q}_{isoth} = \frac{1.01 \times (398.2 - 289.4 - 16)}{12.7 \times 10^{-3}} \times 3.257 \times 10^{-2} \times (1.0857 \times 10^5)^{1/2}$$

This yields $q_{(isoth)} = 78.4\ kW/m^2$, as the predicted heat transfer rate for a surface temperature rise of 16K.

From figure 7.4, the measured heat transfer rate at t = 0.135 seconds was found to be 77.0 kW/m^2, which is in excellent agreement with that predicted by LOWERY and VACHON's correlation. The same procedure applied to a repeat run for the machinable glass cylinder produced a measured heat transfer rate of 77.5 kW/m^2 which compared with a predicted value of 79.5 kW/m^2.

A plot of $\frac{Nu}{Re^{1/2}}$ against time is shown in figure 7.8, and it agrees well with the correlation of Lowery and Vachon. The Nusselt number, Reynolds number and Mach number were calculated point by point in the

run. Since the runs were not totally compensated (i.e. there were inevitably slight oscillations in the test gas pressure), the total temperature also oscillated slightly and was also calculated point by point from

$$\frac{\bar{P}}{P_{init}} = \left[\frac{T_{tot}}{T_{amb}} \right]^{3.5}$$

By plotting $\frac{Nu}{Re^{1/2}}$, figure 7.8 clearly shows that the slight oscillations in the heat transfer rate signal, which were visible in figure 7.4, have been largely removed.

Note that a further correction to the measured surface heat transfer rate should be made for the thermal variation in substrate properties $\sqrt{(\rho ck)}$. As discussed in Chapter 6, the variation of $\sqrt{(\rho ck)}$ for machineable glass ceramic was measured in the course of this work, and it was found that, within the temperature range $15^{\circ}C < T < 70^{\circ}C$, the almost linear variation can be described by

$$\sqrt{(\rho ck)}_T = (1 + 0.0012)(T - 20^{\circ}C)\sqrt{(\rho ck)}_{20^{\circ}C}$$

Since the analogue output signals are multiplied by the factor $\sqrt{(\rho ck)}$, the measured heat transfer rate at the processing time t_m, i.e. $\dot{q}_{t_m}$, should be corrected to $\dot{q}'_{t_m}$, according to the relation

$$\dot{q}'_{t_m} = \dot{q}_{t_m} (1 + 0.0012(T_{t_m} - 20^{\circ}C)).$$

This correction amounts to 2% for the trace in figure 7.4, giving a corrected value of 78.5 kW/m^2 (instead of $77kW/m^2$), or almost exactly the predicted level of 78.4 kW/m^2. When applied to the repeat run, the corrected heat transfer rate is $79.1kW/m^2$, compared with the predicted value of 79.5 kW/m^2. The agreement between the corrected measured heat flux, and that predicted is thus well within the expected accuracy of

this technique, although the extreme closeness of the agreement may, in this case, be slightly fortuitous.

7.4.2 Results from two-layered cylinders

Figure 7.9 shows the scaled but uncorrected output signal measured by a battery powered analogue, and sampled by the transient recorder at a sampling rate of 200μs for a typical run, 4956. As was expected, owing to the presence of the metal layer, the signal falls off considerably when compared with the actual heat transfer rate which would be obtained from a one-layer substrate. The correction for the two-layers was done using the program HTRANS2 with the two-layer kernel, where

$$h(t) = 1 + 2\Sigma (-1)^m A^m \operatorname{erfc} \frac{ma}{\sqrt{(\alpha_1 t)}}$$

with the appropriate values of the calibration constants, $\frac{a}{k_1}$, $(\rho_1 c_1 k_1)^{1/2}$ and $(\rho_2 c_2 k_2)^{1/2}$. The kernel function, h(t), for this case is shown in figure 7.10. The actual heat transfer rate, which is the output of HTRANS2 is plotted shown in figure 7.11, where it is superimposed on the unprocessed analogue output, (or the " single layer output"), to show the effect of the correction. The re-calculated surface temperature is plotted in figure 7.12. A measured surface temperature is often noisy, and the simultaneous recording of the voltage across the thin film (to measure the surface temperature), with the signal from the analogue connected to the film, often adds undesirable "noise" to the analogue signal. For comparison between a measured and a reconstructed surface temperature trace therefore, the measured temperature from an independent repeat run is shown in figure 7.13. As can be seen, apart from the electronic noise, there is very good agreement between the reconstructed trace of 7.12, and the measured trace of 7.13, allowing for the slight difference in run-to-run conditions.

The finite difference scheme described in the appendix may be used to calculate the surface heat flux from the measured surface temperature. This procedure is not as accurate as using an electrical analogue directly to perform the calculation, since errors in the surface temperature measurement result in greatly increased errors in the calculated surface heat flux. Even with the elimination of all the spurious "noise" from the temperature signal, the problem of "digitisation" errors produced in the A/D conversion remains. This could be satisfactorily overcome with the use of high resolution A/D converters, as mentioned earlier, but these have not yet proved economic for widespread adoption. To illustrate the magnification in noise (whether electrical interference or digitisation), a sample calculation of surface heat flux from the measured surface temperature was performed. With the surface temperature trace of figure 7.13, input as the time-varying boundary condition on x = 0, and 11 steps taken through the 190μm enamel layer, and 50 steps through a 6mm nickel base, with a zero flux condition on the backwall, the calculated surface heat flux is plotted in figure 7.14. The signal is almost entirely obscured by noise. Smoothing of the temperature trace to reduce the electronic noise, prior to the numerical calculation greatly helps. Applying a 21 point Hanning type smoothing function, results in the reduced noise trace of figure 7.15. The heat flux calculated from this temperature trace is shown in figure 7.16. The noise is still appreciably greater than that from the analogue, fig 7.16b

Following the same calculation as for the machineable glass model, for the sample run 4956 considered, at a processing time, t_m, of 0.135 seconds, the model temperature rise (from the reconstructed surface temperature trace) T_{t_m}, was found to be 14.0 K, figure 7.12. The corresponding predicted heat transfer rate for an isothermal model with a reduced driving temperature of 113.7-14.0 is given by

$$\dot{q}_{isoth} = \frac{1.01}{13x10^{3}} (113.7-14.0) \times 3.31510^{-2} x (1.0825x10^{5})^{1/2} = 84.5 kW/m^{2}$$

This compares well with a measured value of 82.7 kW/m^{2}, the measured value being approximately 2.2% low.

A plot of $Nu/(Re^{1/2})$ against time for this run is shown in figure 7.17, and gives good agreement with the predicted value of 1.01 of Lowery and Vachon. Unfortunately, time did not permit the measurement of the variation on the property $\sqrt{(\rho ck)}$ of the enamel with the rise in model temperature. A crude estimate, based on the measured behaviour of machineable glass ceramic, would suggest that the measured heat transfer rate should be corrected by +1 to +2%, for a 14K rise in surface temperature. If this were so, near perfect agreement would again be obtained between measured and predicted values. Although the enamel coating is essentially "glass like", there is not sufficient justification for using the same value as that obtained for machineable glass ceramic. Instead, a similar process to that described in Chapter 6 should be performed to determine the variation in $\sqrt{(\rho ck)}$ of the enamel.

As mentioned, the electrical analogue was powered by a battery, because the signal from a mains powered analogue was found to suffer from "pick up". The effects of "pick-up" had serious consequences when the analogue output signal was processed to give the actual heat transfer rate, as will be seen by consideration of figures 7.18 and 7.19. The scaled but uncorrected mains analogue signal for run 4949 is shown in figure 7.18 and is superimposed on the battery powered analogue signal in figure 7.19, from run 4950. The uncorrected signals are very similar in level, except for the mains "pickup". After correction however, as shown in figure 7.20, there is a significant difference in level between the two, with the mains powered result being higher than the battery powered result. This is caused by the convolution of the extra area under the graph of the uncorrected signal for 4949, with h(t) in the processing

program. For this reason, it was essential to use a battery powered analogue to prevent the corrected signal from being artificially high.

In later processing, it was found that, for many of the early runs, the starting transient had not been captured (i.e. the transient recorder channel had saturated) and so the results could not be accurately processed. Although the high starting transient only lasts for typically 20ms, its effect on the subsequent processed mean heat transfer decays slowly. The scale of the effect is illustrated with reference to figure 7.21, where a 20kW pulse lasting 20ms was imposed in a computational experiment. It can be seen that even at a typical processing time of 0.135 seconds, the initial pulse would contribute 2kW. Thus if the effect of saturation was to reduce the heat transfer transient by only 20kW, then the apparent heat transfer at 0.135 seconds after processing would be 2kW low, an error of 2.5% in a typical measured value of 80kW.

Since the unprocessed heat transfer signal decays rapidly to a low level (typically to 20 kW/sq.m), the desire to record this low level accurately, conflicts with the necessity of fully capturing the transient. As the importance of the initial transient was not at first appreciated, some of the early runs suffered from saturated initial readings, with possibly up to 40 kW effective "saturation" error in the initial 20 ms. transient.

A similar problem was encountered with the computer sampled data, which was sampled at 3.0ms. per sample for 200 readings. Although the channels were not saturated, the slow sampling of the computer failed, in some cases to define the correct shape of the transient. In general, the area under the transient was underestimated. This also resulted in processed heat transfer rates which were lower than those measured using the transient recorder. In other cases, agreement was very good, as shown in figure 7.22.

The results from typical runs for each model will now be summarised in a table.

Model	Run	Predicted $\dot{q}$ kW/sq.m	Measured $\dot{q}$ kW/sq.m	Mean error	Error when corrected for thermal variation in $\sqrt{(\rho ck)}$
MGC	4957	79.5	77.5	-2.2%	-0.2%
	4958	78.4	77.0		
Enamel 1	4950	82.1	78.3	-4.5%	not corrected
	*****				
Enamel 2	4956	84.5	82.7	-3.5%	not corrected
	4953	83.18	79		
Kapton/ steel	4961	68.1	70.5	+4.2%	not corrected
	4963	67.3	70.7		

**** Repeat run not available.

The results of the wind tunnel tests thus demonstrated that the theoretical analysis of Chapters 3 and 4, and the multi-layered model construction method described in Chapter 5, can successfully be applied. the processing of the heat transfer signals is relatively uncomplicated, and provided due care is exercised, it should be possible to obtain results sufficiently accurate for research work.

CHAPTER 8

CONCLUSIONS

Summary.

The theoretical analysis developed in Chapters 3 and 4 has identified a new, accurate, and computationally efficient method for determining the surface heat flux to a multi-layered model turbine blade. This method allows the existing successful technique, whereby electronic analogue circuitry is used in conjunction with thin film surface thermometers on a model made from a thermal insulator, to measure the surface heat flux, to be extended for application to multi-layered models.

A method for calibrating the thermal properties of the multi-layered system, using the pulse calibration technique has been developed theoretically. The problem of lateral conduction errors in the calibration process has been theoretically and computationally addressed,

and a method for adapting the calibration procedure to counteract these errors is described.

The results of practical tests on coatings applied by vacuum deposition, adhesion with an epoxy, and enamelling, together with tests on films applied by electron beam deposition and hand painting and firing, have identified the most suitable system for experimentation. This involves the use of hand painted films on an enamelled coating applied to a mild steel base.

Radiant, and wind tunnel testing of multi-layered cylindrical models has confirmed that the method is both practical and accurate. Although tests have not yet been performed using an actual turbine blade profile, the analytical processing, calibration, and practical problems have been examined in considerable detail. It is thus concluded that surface heat transfer rate may be determined using a thin film gauge on an insulator coating, applied to a metal turbine rotor blade, with sufficient ease and accuracy to enable detailed measurements to be made under the actual, highly unsteady conditions which occur in an engine.

Detailed Conclusions.

The use of multi-layered model turbine blades has been shown (in Chapter 2), to be highly desirable. The major advantage is that the base, (usually metal), may be chosen to satisfy the requirements, both of easy model manufacture, and the strength to withstand high rotational speeds. Furthermore, a full covering of insulator, (rather than using "plug" type insulating inserts) is convenient both for instrumentation versatility and ease, and minimum flowfield disturbance.

The mathematical problem of analysing the transient response of a thin film gauge on a two-layered substrate has been considered in Chapter

3. Solutions are given for the case of a semi-infinite base layer, and for a finite metal base layer. The first solution is given in a form particularly suited for efficient computation. This form has also subsequently been used in the analysis of the output signal from an electronic heat transfer analogue circuit, connected to a thin film on a multi-layered model.

The second solution allows the effects of the backwall to be investigated. The times at which there are appreciable effects due to finite model thickness have been considered for several test cases of practical importance.

The application of the theoretical analysis to allow the existing, successful technique, (which employs electronic analogue circuitry to extract the heat flux measured by a surface thin film thermometer gauge) to be used for multi-layered substrates has been considered in Chapter 4. It has been shown that a numerical correction may efficiently (and for practical applications, accurately) be applied to the signal from the analogue, to compensate for the presence of the base layer. Associated with the use of a deposited insulating coating (whether enamelled or vacuum deposited) is the uncertainty in the thermal properties of the coating. The theoretical analysis (described in Chapter 4), showed that the standard pulse calibration technique may be applied to determine the required thermal properties. Knowledge of these parameters, and of the film response is required, whether analogue circuitry or numerical techniques are employed to extract the measured heat flux.

The problem of the errors caused by lateral conduction using the pulse calibration procedure have been addressed both analytically (for the simple case) and computationally (for the multi-layered substrates.)

The numerical experiments indicated that lateral conduction may cause significant errors in practical applications.

Suitable multi-layered systems, both for experimental validation of the calibration technique, and for wind tunnel testing, were successfully developed, as described in Chapter 5. The results of the development tests clearly indicated that the use of painted thin film gauges on an enamelled coating was the most suitable form. The smooth surface of the enamel provides a good "key" for the painted films and does not cause flow disturbances. In addition, complicated model shapes can be readily and economically machined, given the selection of mild steel as the recommended base metal, and the full coating with the enamel also allows greatest convenience for instrumentation purposes.

The results from Chapter 6 showed that the calibration procedure can be adapted successfully to counteract 2-D effects. The process whereby this is achieved is convenient and justifiable by numerical experimentation. At present, however, it is necessary to use the 2-D numerical calculations as a check for specific applications.

The results of the radiant tests in Chapter 6 were shown to provide a good check on the accuracy of the calibration constants obtained from the pulse calibrations. These were useful as an independent (of the wind tunnel) test, to indicate the dependence of the accuracy of the heat transfer results on the determination of the calibration constants.

The wind tunnel tests described in Chapter 7, demonstrated the successful application of the technique to measure heat transfer rate, to an accuracy well within 5%. The tests also served to identify some of the problems of using the technique in practice, such as the effects of electronic noise on the analogue output signal and the necessity of capturing the initial transient at the start of the run. It was shown

that these difficulties could be surmounted with a reasonable degree of ease.

Suggestions for future work.

The major objective should be the testing of the new technique on a turbine blade. In regions of very thin blade walls, such as trailing edges, it may be necessary to consider the effect of the finite backwall on the new processing methods. Further consideration of the effects of lateral conduction in the blade, which may occur in regions of high radii of curvature, during actual wind tunnel testing, may also be necessary. If either of these effects are found to be significant, the possibility of using a thicker coating of enamel should be considered, which would delay the effects of the finite backwall, and also the onset of the effects of lateral conduction. The variation in thermal property $\sqrt{(\rho ck)}$ of the enamel with the rise in surface temperature of the model should also be determined to achieve higher levels of measurement precision.

APPENDIX 1

Considering the unsteady heat conduction equation with $\alpha = 1$,

$$\frac{\partial T}{\partial t} = \frac{\partial^2 T}{\partial x^2} + \frac{\partial^2 T}{\partial y^2} \qquad (1)$$

the simplest finite difference replacement, often referred to as the classic explicit (C.E.) scheme, consists of replacing (1) by a forward difference in time, and central differences in space. If $T^{n}_{m,\iota}$ is used to denote $T(m\Delta x, \iota\Delta y, n\Delta t)$, $\Delta t = k$, $\Delta x = \Delta y = h$, and

$$\delta_x^2 T^n_{m,\iota} = T^n_{m+1,\iota} - 2T^n_{m,\iota} + T^n_{m-1,\iota}$$

$$\delta_y^2 T^n_{m,\iota} = T^n_{m,\iota+1} - 2T^n_{m,\iota} + T^n_{m,\iota-1}$$

$$r = \frac{k}{h^2}$$

Then from the Taylor series expansion of $T(x,y,t)$ it may be shown that the simple scheme

$$T^{n+1}_{m,\iota} = [\, 1 + r(\delta_x^2 + \delta_y^2)]\, T^n_{m,\iota} + O(k^2 + kh^2) \qquad (2)$$

approximates (1) with a truncation error $O(k + h^2)$. The approximation is consistent with (1) for all h, k and a von Neumann stability analysis shows that it is stable for $0 < r \leq \frac{1}{4}$. (The convergence of the finite difference solution to the solution of the continuous equation is ensured by the Lax equivalence theorem, as h,k -> 0, ref. ISAACSON and KELLER (1966) and RICHTMYER and MORTON (1967)).

For multi-layered regions, it is very convenient to split equation (2) in the x and y directions, according to the so-called locally one-dimensional (L.O.D.) method developed by Russian numerical analysts (ref. LAPIDUS and PINDER (1982), and MITCHELL and GRIFFITHS, (1980) among others.)

In this method, equation (1) is written as the pair of equations

$$\frac{1}{2}\frac{\partial T}{\partial t} = \frac{\partial^2 T}{\partial x^2} \qquad (3a)$$

$$\frac{1}{2}\frac{\partial T}{\partial t} = \frac{\partial^2 T}{\partial y^2} \qquad (3b)$$

and in solving over one complete time step, (3a) is used to advance from $t = nk$ to $t = (n + \frac{1}{2})k$ and (3b) to advance from $t = (n + \frac{1}{2})k$ to $t = (n+1)k$, i.e.

$$\frac{1}{2}\left[\frac{T_{m,\iota}^{n+1/2} - T_{m,\iota}^{n}}{k/2}\right] = \delta_x^2\left[\frac{T_{m,\iota}^{n}}{h^2}\right]$$

$$\frac{1}{2}\left[\frac{T_{m,\iota}^{n+1} - T_{m,\iota}^{n+1/2}}{k/2}\right] = \delta_y^2\left[\frac{T_{m,\iota}^{n+1/2}}{h^2}\right]$$

or

$$T_{m,\iota}^{n+1/2} = \left(1 + r\delta_x^2 \right) T_{m,\iota}^{n}$$

.....(4)

$$T_{m,\iota}^{n+1} = \left(1 + r\delta_y^2 \right) T_{m,\iota}^{n+1/2}$$

The composite form of (4)

$$T_{m,\iota}^{n+1} = \left(1 + r\delta_y^2 \right) \left(1 + r\delta_x^2 \right) T_{m,\iota}^{n}$$

is equivalent to (2) with the addition of the perturbation term $r^2\delta_x^2\delta_y^2$, which is the same order as the truncation error. For $0 \leq r < \frac{1}{2}$, however, (4) is stable.

A.2. Testing numerical scheme in 1-D.

The calculation of the 1-D response of a multi-layered substrate comprising 350μm of machineable glass on 5.85mm nickel (figure A.1) is now considered as a test problem.

The equations to be solved are

$$\frac{\partial T_1}{\partial t} = \alpha_1 \frac{\partial^2 T_1}{\partial x_1^2} \qquad (5)$$

$$\frac{\partial T_2}{\partial t} = \alpha_2 \frac{\partial^2 T_2}{\partial x_2^2} \qquad (6)$$

where subscript 1 refers to the machineable glass and 2 to the nickel.

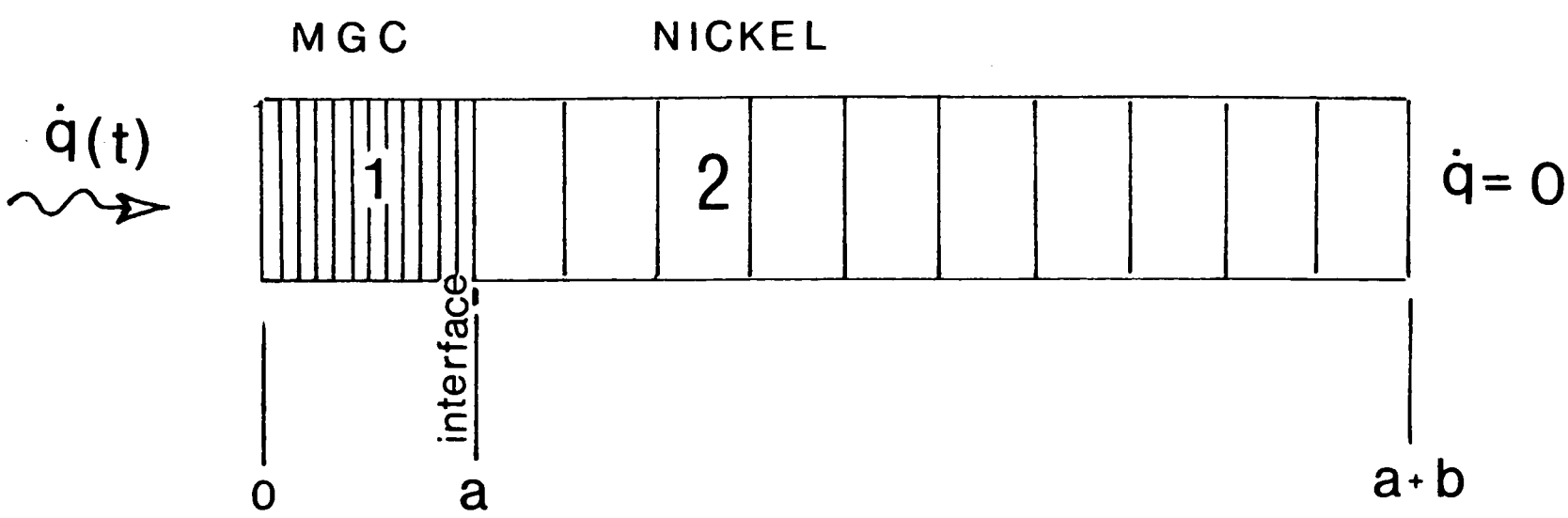

A-1

It is useful to scale the spatial dimension by division by $\sqrt{\alpha}$ in each region, to remove the constant from the equation. The advantage of this is that although the computation proceeds in " actual " time, the heat flux is scaled by division by $\sqrt{(\rho ck)}$, which is often a very convenient form.

Thus if $\eta_1 = \dfrac{x_1}{\sqrt{\alpha_1}}$

and $\eta_2 = \dfrac{x_2}{\sqrt{\alpha_2}}$

then (5) and (6) become

$$\frac{\partial T_1}{\partial t} = \frac{\partial^2 T_1}{\partial \eta_1^2} \qquad (7)$$

$$\frac{\partial T_2}{\partial t} = \frac{\partial^2 T_2}{\partial \eta_2^2} \qquad (8)$$

which are solved with the boundary conditions

On $x = 0$ $\quad \dot{q} = 0.1*\sqrt{(\rho ck)_1}$, i.e. $-k_1 \dfrac{\partial T}{\partial x_1} = 0.1\sqrt{\rho c k_1}$

$$\Rightarrow \frac{\partial T}{\partial \eta_1} = \frac{-\dot{q}}{k_1}\sqrt{\alpha_1} = \frac{-\dot{q}}{\sqrt{(\rho ck)_1}} = -\dot{q}^* = -0.1$$

on the interface $x = a$ $\quad T_1|_a = T_2|_a$

and $$k_1 \frac{\partial T_1}{\partial x}\Big|_a = k_2 \frac{\partial T_2}{\partial x}\Big|_a \Rightarrow \frac{\partial T_1}{\partial \eta_1}\Big|_a = \frac{\sqrt{\alpha_1}}{\sqrt{\alpha_2}} \frac{k_2}{k_1} \frac{\partial T_2}{\partial \eta_2}\Big|_a$$

and at the backwall $x=a+b$,

$$\left.\frac{\partial T_2}{\partial x}\right|_{a+b} = 0 \quad \Rightarrow \quad \left.\frac{\partial T_2}{\partial \eta_2}\right|_{a+b} = 0$$

Replacing boundary conditions by finite difference equivalents and letting

$T(1)$ denote T_1 at $x = 0$

$T(a)$ T at $x = a$, since $T_1 = T_2$ at this point

$T(L)$ T_2 at $x = a + b$, where $L = a + b$

then the boundary condition on $x = 0$ becomes

$$\frac{T(2) - T(0)}{2h_1} = -\dot{q}^* \qquad \text{where } h_1 = \Delta\eta_1 \text{ and } T(0) \text{ is a}$$

fictitious point outside the boundary

$$\Rightarrow \qquad T(0) = \dot{q}^* . 2h_1 + T(2)$$

The boundary conditions on $x = a$ become

$$T(a) = \left[\frac{1}{h_1} + \frac{\sqrt{\alpha_1}}{\sqrt{\alpha_2}}\frac{k_2}{k_1}\cdot\frac{1}{h_2}\right]^{-1}\left[\frac{T(a-1)}{h_1} + \frac{\sqrt{\alpha_1}}{\sqrt{\alpha_2}}\frac{k_2}{k_1}\frac{T(a+1)}{h_2}\right] \qquad (9)$$

The boundary condition on $x = a + b$ gives,

$$\frac{T(L+1) - T(L-1)}{2h_2} = 0$$

$$\Rightarrow \qquad T(L+1) = T(L-1)$$

Thus the new temperature (i.e. at the next time level) is calculated at each point in region (1), bar the interface, and likewise, the new temperature is calculated in region (2). Finally the temperature at the new time level at the interface is calculated from (9), before starting the next time iteration.

Note that the one-sided finite difference replacement of the temperature gradient at the interface has a truncation error of O(h), which is greater than that of the overall scheme, so the error is increased.

The numerically calculated, and analytical solutions for 350 μm machineable glass ceramic on 5.85mm nickel are compared in figure A.2 where $\Delta h_1 = 1.89 \times 10^{-2}$, and $\Delta h_2 = \Delta h_1$. The time step k was chosen as 8.8×10^{-5}. The very small discrepancy between the two is of the order of the truncation error, h.

— *350 μM M.G.C. ON 5.85 MM NICKEL: EXACT SOLUTION*
o *350 μM M.G.C. ON 5.85 MM NICKEL: NUMERICAL SOLN. (C.E. SCHEME, H:1.889E-2)*

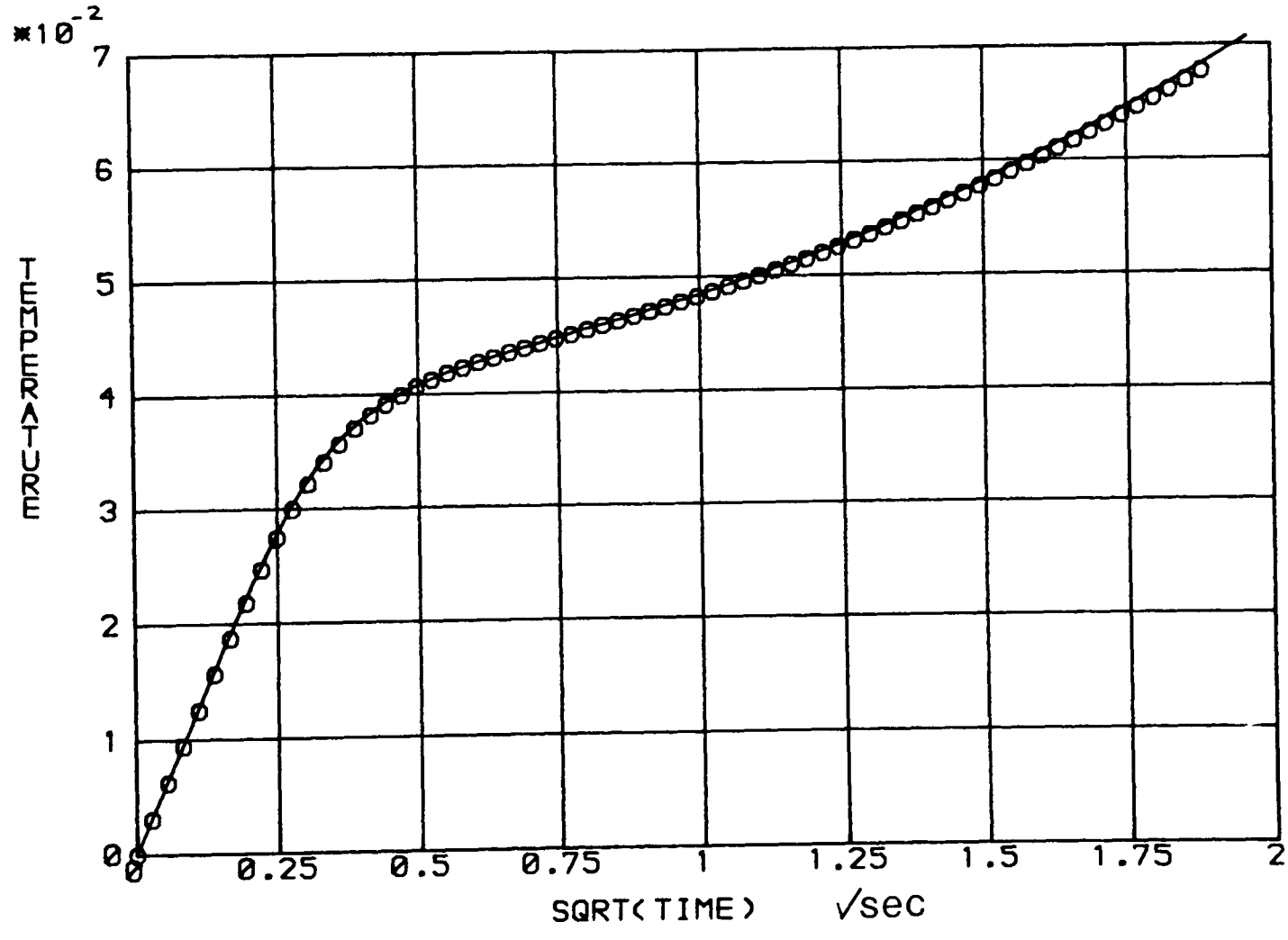

A-2

A.3 Two-dimensional solution.

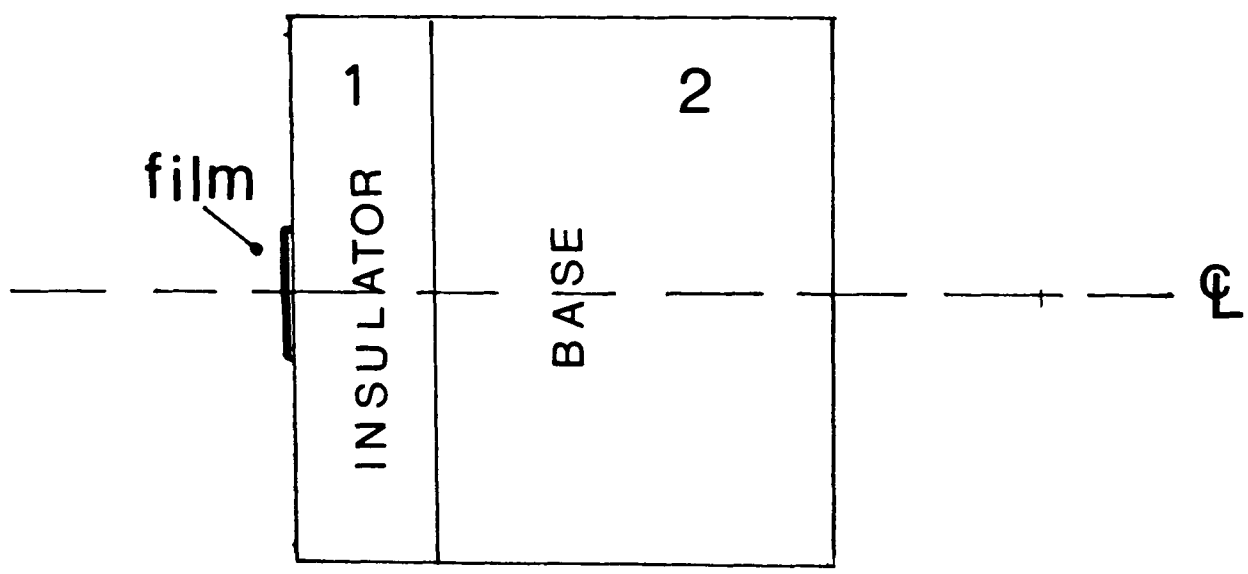

A-3

In two dimensions, symmetry allows the computation to be restricted to only half of the rectangular region, figure A.3 . A simplified computational grid, together with the boundary conditions is shown in figure A.4.

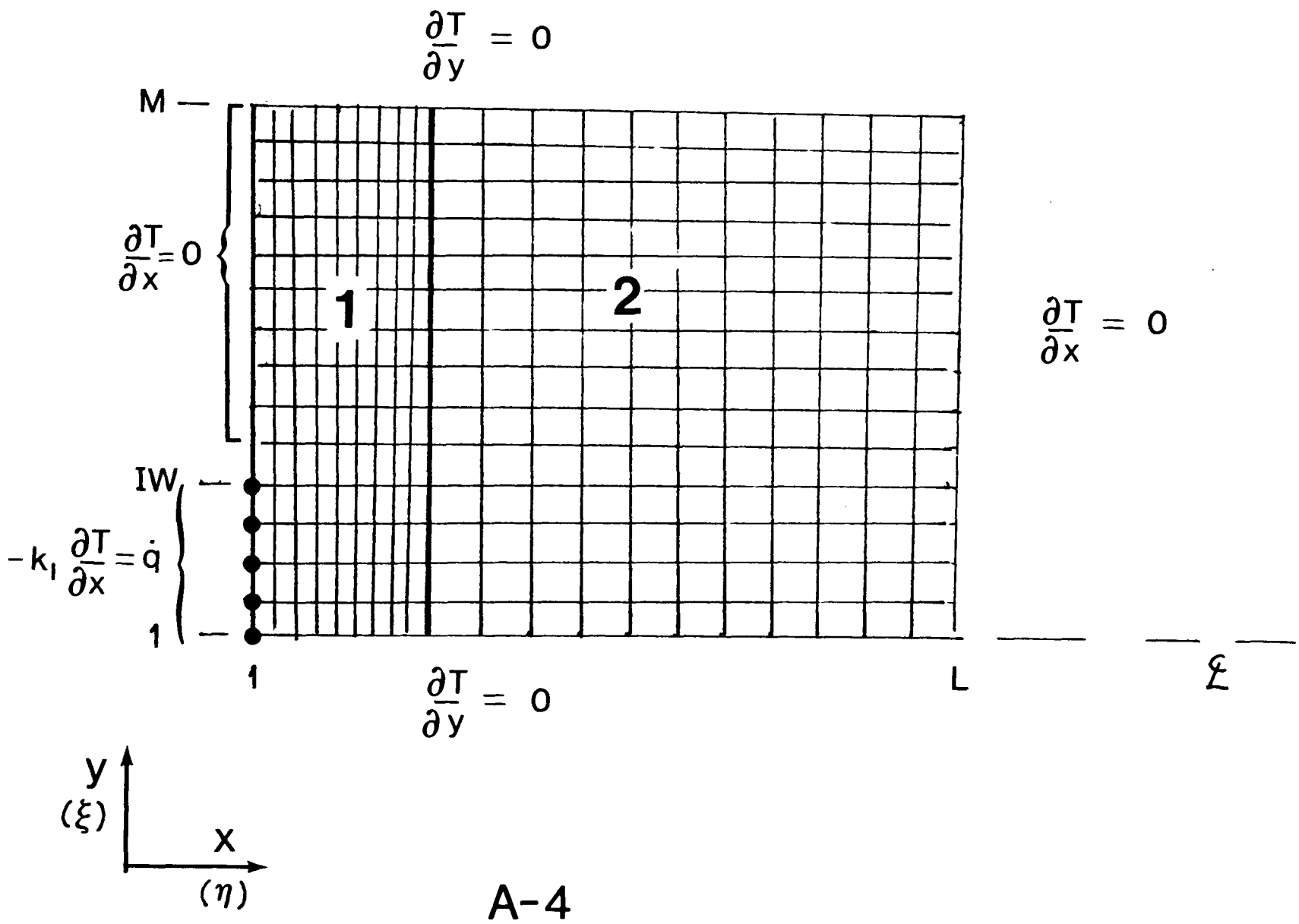

A-4

The half-film is represented by IW points on the first x line. Clearly, it is advantageous to use different x-steps in the two regions; (indeed if $\Delta\eta_1 = \Delta\eta_2$, effectively, $\Delta x_1 = \frac{\sqrt{\alpha_1}}{\sqrt{\alpha_2}} \Delta x_2$, so the step sizes are automatically different). For the grid points on the interface to match, it is necessary that

$$\Delta y_1 = \Delta y_2 .$$

So if the y directions are likewise scaled by division by $\sqrt{\alpha}$,

$$\Delta\xi_1 = \frac{\Delta y_1}{\sqrt{\alpha_1}} \quad ; \quad \Delta\xi_2 = \frac{\Delta y_2}{\sqrt{\alpha_2}}$$

thus for grid matching $\frac{\Delta\xi_1}{\Delta\xi_2} = \frac{\sqrt{\alpha_1}}{\sqrt{\alpha_2}}$.

With different x and y steps, the finite difference equations (4) take the form

$$T_{m,\iota}^{n+1/2} = [\, 1 + r_{x_1} \delta_x^2 \,]\, T_{m,\iota}^{n} \qquad \text{in region (1)}$$

$$T_{m,\iota}^{n+1/2} = [\, 1 + r_{x_2} \delta_x^2 \,]\, T_{m,\iota}^{n} \qquad \text{in region (2)}$$

$$T_{m,\iota}^{n+1} = [\, 1 + r_{y_1} \delta_y^2 \,]\, T_{m,\iota}^{n+1/2} \qquad \text{in region (1)}$$

$$T_{m,\iota}^{n+1} = [\, 1 + r_{y_2} \delta_y^2 \,]\, T_{m,\iota}^{n+1/2} \qquad \text{in region (2)}$$

where $r_{x_1} = \frac{\Delta t}{(\Delta\eta_1)^2}$, and $r_{x_2} = \frac{\Delta t}{(\Delta\eta_2)^2}$, $r_{y_1} = \frac{\Delta t}{(\Delta\xi_1)^2}$, $r_{y_2} = \frac{\Delta t}{(\Delta\xi_2)^2}$.

Thus the computation proceeds at each step by first sweeping in x i.e. η, across both regions, applying the boundary conditions required in this direction, and then sweeping separately in y, i.e. ξ, in each region, applying the boundary conditions. The mean film temperature is calculated by integrating over the IW points covering the film, using Simpson's rule applied by partitioning the interval into groups of 3 consecutive points. (Clearly the accuracy depends on the number of points used to define the film.)

REFERENCES

ABRAMOWITZ, M. and STEGUN, I.A.,

Handbook of Mathematical Functions, Dover Publications Inc., New York, 8th ed. 1972.

AINLEY, D.G.,

" The High Temperature Turbo-jet Engine."

Jnl. R. Aeronautical Soc., 60, 1956, 549

BAINES, N.C.,

O.U.E.L. Report no 1462/83, 1983.

BARRY, B., FOREST, A.E., and WHITE, A.J.,

"Measurements of Heat Transfer Coefficients on Gas Turbine Components. Part 1."

A.S.M.E. Paper no. 82-GT-174.

BAYLEY, F.J. and TURNER, A.B.

"Bibliography of Heat Transfer Instrumentation."

Aero. Res. Council R+M, 3512, 1968.

BAYLEY, F.J. and PRIDDY, W.J.,

"Effects of free-stream turbulence intensity and frequency on heat transfer to turbine blading."

A.S.M.E. Paper no. 80-GT-79 (New Orleans 1980).

BEACOCK, R.J., HORTON, F.G., KIRKER, T.J. and WHITE, A.J.

"Measurement of Heat Transfer Coefficients on Gas Turbine Components. Part 2."

A.S.M.E. Paper no. 82-GT-175

CONSIGNY, H. and RICHARDS, B.E.,

"Short Duration Measurements of Heat Transfer Rate to a Gas Turbine Rotor Blade."

A.S.M.E., Paper no. 81-GT-146.

DANIELS, L.C.,

D. Phil Thesis, Oxford University, 1978.

DOORLY, D.J.

D. Phil thesis, Oxford University 1983.

DOORLY, D.J. and OLDFIELD, M.L.G.,

"Simulation of the Effects of Shock Wave Passing on a Turbine Rotor Blade."

A.S.M.E.,Paper no. 85-GT-112, to be presented, Houston, Texas, March 1985.

DOORLY, D.J., OLDFIELD, M.L.G. and SCRIVENER, C.T.J.,

"Wake-Passing in a turbine rotor cascade."

AGARD-PEP 65th Symposium, May 1985, Bergen, Norway.

DRING, R.P., JOSLYN, H.D., HARDIN, L.W. and WAGNER, J.H.,

"Turbine Rotor-Stator interaction."

A.S.M.E. Paper no. 82-GT-3

DUNN, M.G.

"Measurement of heat flux and pressure in a turbine stage."

A.S.M.E. Paper no. 84-GT-175.

DUNN, M.G. and STODDARD, F.J.,

"Measurement of Heat Transfer Rate to a Gas Turbine Stator."

A.S.M.E. Paper no. 78-GT-119

DUNN, M.G. and HAUSE, A.

"Measurement of Heat Flux and Pressure in a Turbine Stage."

Mechanical Engineering, Vol. 104, 1982.

EPSTEIN, A.H. and GUENETTE, G.R.

" The M.I.T. Blowdown Facility."

A.S.M.E. Paper no. 84-GT-116.

GIERE, A.C.,

"Transient Heat Flow in a Composite Slab- constant flux, zero flux boundary conditions."

Applied Scientific Research, Section A, Vol. 14, no.3, 1964-5

GODEFROY, J-C.

" Thin Film Transducers for Temperature and Heat Flux Measurements.""

La Recherche Aerospatiale, 1981-2, pp 9-19

HENSHALL, B.D. and SCHULTZ, D.L.,

"Some notes on the use of resistance thermometers for the measurement of heat transfer rates in shock tubes."

ARC CP No. 408, 1959.

HODGE, J.,

Gas Turbines, Vol. I - 'Cycles and Performance Estimation',

Butterworths, London 1955.

HODSON, H.P.,

D. Phil Thesis, Cambridge University, 1983

HODSON, H.P.,

"Boundary Layer and Loss Measurements on the rotor of an Axial Flow Turbine."

A.S.M.E. Paper no. 83-GT-4, Pheonix, Arizona, March 1983.

HOLLAND, L.

"Vacuum deposition of thin films."

London, Chapman and Hall, 1970.

HUFF, R.G.,

"Convective Heat Transfer Coefficients from a Solution of the Conduction Equation for a Wall separating Two Fluids, one having an Oscillating Temperature."

NASA TN D-5520, 1969

HUFF, R.G.

"Experimental Evaluation of an Oscillating Temperature Technique for Obtaining Convective Heat Transfer Coefficients."

NASA TM X-1980, 1970

ISAACSON, E. and KELLER, H.B.,

"Analysis of Numerical Methods."

Wiley, New York, 1966.

JONES, T.V.,

"Heat Transfer, Skin Friction, Total Temperature and Concentration Measurements."

In "Measurement of Unsteady Fluid Dynamic Phenomena" ed. B.E.Richards, McGraw-Hill, V.K.I., 1977.

JONES, T.V., SCHULTZ, D.L., OLDFIELD, M.L.G. and DANIELS, L.C.,

"A New Transient Facility for the Measurement of Heat Transfer Rates."

A.G.A.R.D., CP-229, " High Temperature Problems in Gas Turbine Engines". Ankara, 1979.

JONES, T.V., SCHULTZ, D.L. and HENDLEY, A.,

"On the flow in an isentropic light piston tunnel."

ARC, R and M, 3731, 1973.

KESTIN, J. and MAEDER, P.

"Influence of turbulence on transfer of heat from cylinders."

NACA TN 4018, March 1956.

LAPIDUS, L. and PINDER, G.F.,

"Numerical Solution of Partial Differential Equations in Science and Engineering."

Wiley Interscience, New York, 1982.

LOFTUS, P.J.

D.Phil thesis (1982), Oxford University.

LOWAN, A.N.,

"On some problems in the diffraction of Heat."

Phil. Mag. 29, 1940 93-99.

LOWERY, G.W. and VACHON, R.I.,

"The effect of turbulence on heat transfer from heated cylinders."

Int. J. Heat and Mass Transfer, Vol 18, pp 1229-1242, 1975.

MAULARD, J.

"Les fluxmetres thermique a temperature superficielle pour tubes a choc."

Rech. Aer. No. 126, Sept. 1968, p. 39.

MAULARD, J.

" Etude du fluxmetre a temperature superficielle pour mesures dans les tubes a choc."

ONERA NT 139, 1969.

MAULARD, J.

" Calibration method used at ONERA for hotshot and shock tube heat transfer transducers." Proc. 3rd Int. Congr. Instr. Aerosp. Simul. Facilities, I.E.E.E./G-AES May, 1969, p.96

MARTIN, B.W., BROWN, A., and GARRETT, S.E.,

"Heat Transfer to a PVD Rotor Blade at High Subsonic Passage Throat Mach Numbers."

AGARD CP-229, High Temperature Problems in Gas Turbine Engines, Ankara, 1977, Paper 32.

METZGER, D.E. and MAYLE, R.E.,

"Gas Turbine Engines"

Mech. Engineering, Vol. 105, no. 6, June 1983.

MEYER, R.F.

"A heat flux meter for use with thin film surface thermometers."

NRC Canada, Aero. Rep. LR-279, 1960.

MEYER, R.F.,

"Further comments on analogue networks to obtain heat flux from surface temperature measurements."

NRC Canada, Aero. Rep. LR-375, 1963

MICHARD, J.,

"Mesures de Flux de Chaleur sur Aubes Fixes de Turbines."

Office National d'Etudes et de Recherches Aerospatiales,

T.P. No. 871, 1970.

MITCHELL, A.R., and GRIFFITHS, D.F.,

"The finite difference Method in Partial Differential Equations."

John Wiley and Sons, New York, 1980, Wiley Interscience.

NICHOLSON, J.H.

D. Phil thesis (1981), Oxford University.

NORTON, R.J.

D. Phil thesis, (1981), Oxford University.

OLDFIELD, M.L.G., JONES, T.V. and SCHULTZ, D.L.,

"On-line Computer for Transient turbine Cascade Instrumentation."

I.E.E.E. Transactions on Aerospace and Electronic Systems, Vol. AES-14, No. 5, pp 738-749 Sept. 1978.

OLDFIELD, M.L.G., BURD, H.J. and DOE, N.G.

"Design of wide-bandwidth analogue circuits for heat transfer instrumentation in transient tunnels."

Proc. 14th ICHMT Symposium on Heat and Mass Transfer in Rotating Machinery., Dubrovnik, August 1982.

OWEN, J.M.

"On the computation of heat transfer coefficients from imperfect temperature measurements."

Jnl. Mech. Eng. Science, 21(5), 1979.

PAULON, J., PORTAT, M., GODEFROY, J.C. and SZECHENYI, E.

"Les Capteurs Ultraminces appliques aux mesures dans les turbomachines."

ONERA T.P. 1981-38

PFEIL, H., HERBST, R. and SCHROEDER, T.,

"Investigation of the Laminar-Turbulent Transition of Boundary Layers Disturbed by Wakes."

A.S.M.E. Paper no. 82-GT-124.

PIERCY, N. and RICHARDSON, E.

"The variation of velocity amplitude close to the surface of a cylinder moving through a viscous fluid."

Phil. Mag. 6, 970-977, 1928.

RUDEY, R.A. and GRAHAM, R.W.,

" A Review of NASA Combustor and Turbine Heat Transfer Research."

A.S.M.E., 84-GT-113

SCHAFER, H.J., KOCH, B. and PFEIFER, H.J.,

" Application of LDV techniques to high speed combustion flow."

ICIASP Record 1977 pp. 31-39.

SCHULTZ, D.L. and JONES, T.V.

"Heat Transfer Measurements in Short Duration Hypersonic Facilities."

A.G.A.R.D., AG-165, 1973.

SCHULTZ, D.L., JONES, T.V., OLDFIELD, M.L.G. and DANIELS, L.C.,

"Measurement of the Heat Transfer Rate to Turbine Blades and N.G.V.'s in a Transient Cascade."

6th International Heat Transfer Conference, Toronto,

Paper EC-12, 1978.

SHHADOCK, R.

3rd Year Project, Oxford University, 1978.

SPENCE, D.A.

" Two heat diffusion problems with shock tube applications."

RAE Tech. Note Aero 2637, 1959.

TURNER, A.B.

"Local Heat Transfer Measurements on a Gas Turbine Blade."

Jnl. Mech. Eng. Science. 13(1), 1971

VAN DER HEGGE ZIJEN, B.,

"Heat transfer from horizontal cylinders to a turbulent air flow."

Appl. Scient. Res. A7 205-223, 1957.

VIDAL, R.J.

"Model Instrumentation Techniques for Heat Transfer and Force Measurements in a Hypersonic Shock Tunnel."

Cornell Aero. Lab. Rep. No. AD-917-A-1, Feb., 1956.

TABLE 1

MATERIAL	density, ρ kg/m^3	specific heat capacity J/kg K	thermal cond. W/m K	$\sqrt{(\rho ck)}$ $J/Ks^{1/2}m^2$
m.g.c.	2520	774.6	1.675	1808
Kapton	1420	1090	0.155	489.8
mild steel	7820	473.1	54.4	14186
nickel	8900	450	84	18342
quartz	2220	775	1.36	1529
epoxy	1150	1700	0.2	625

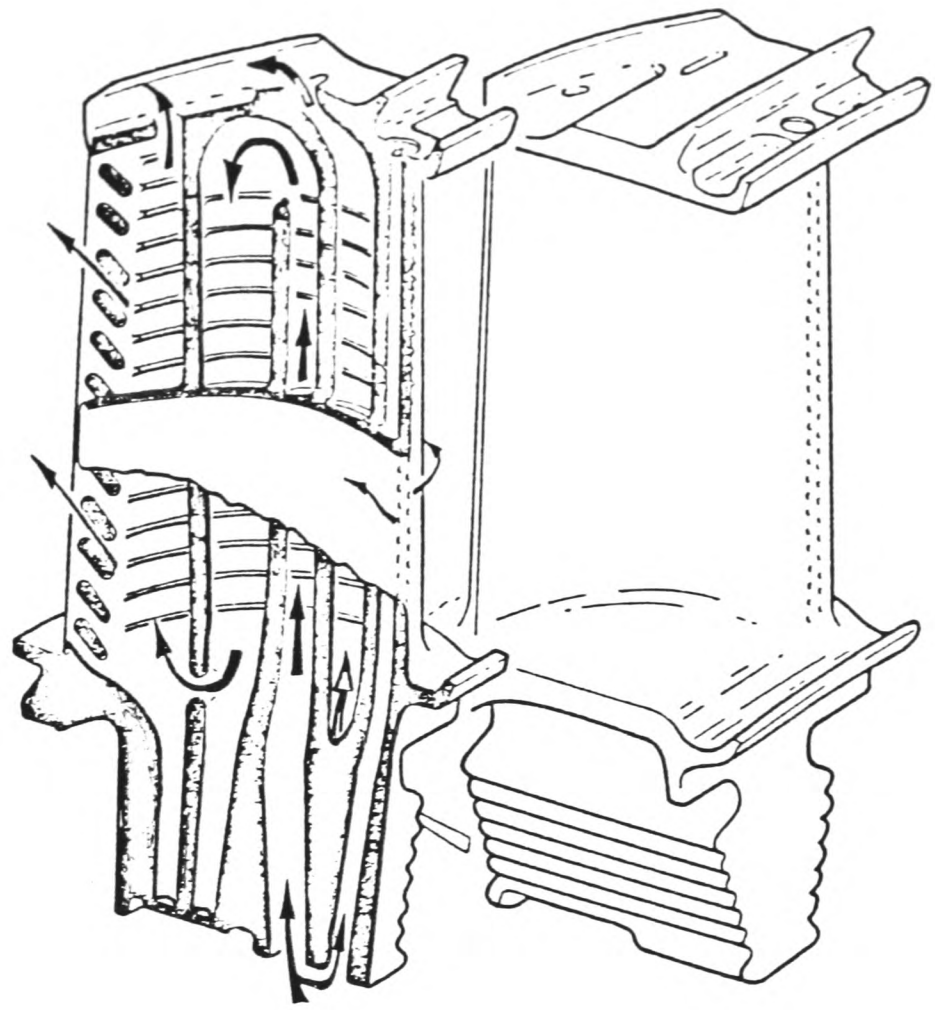

Fig. 1.1a A modern cooled turbine rotor blade.

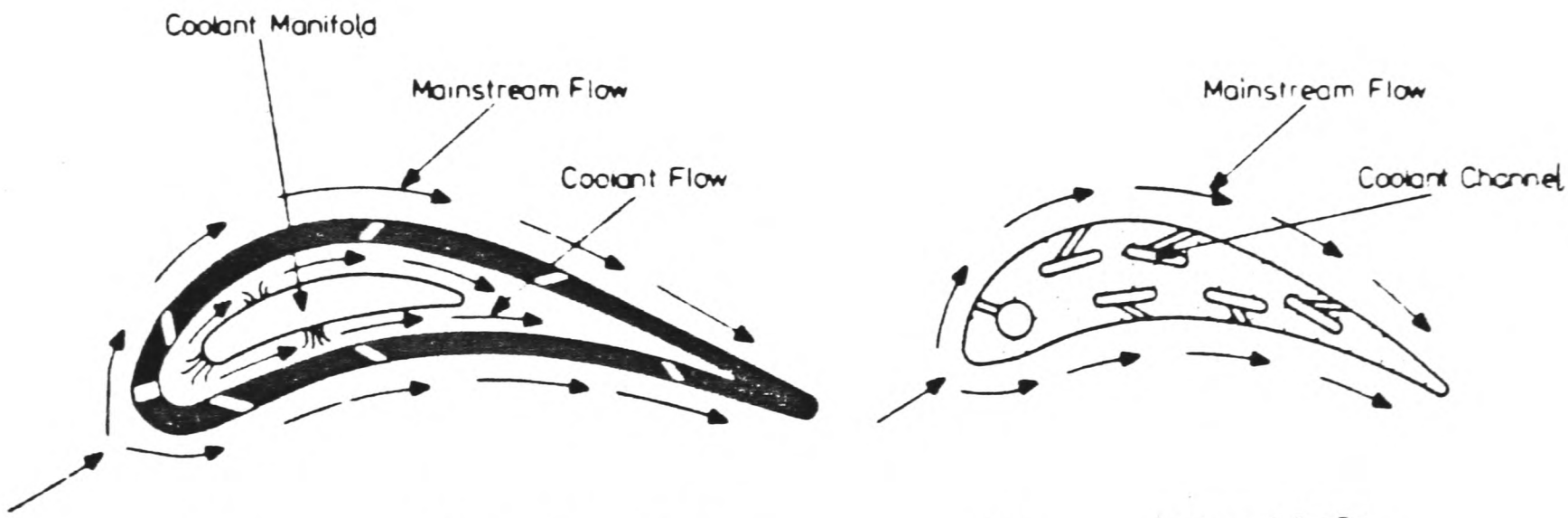

(1) nozzle guide vane. (2) rotor blade.

FIG. 1.1b Flow configurations in cooled turbine blades.
from Hay, Lampard and Benmansour, A.S.M.E. 82-GT-147

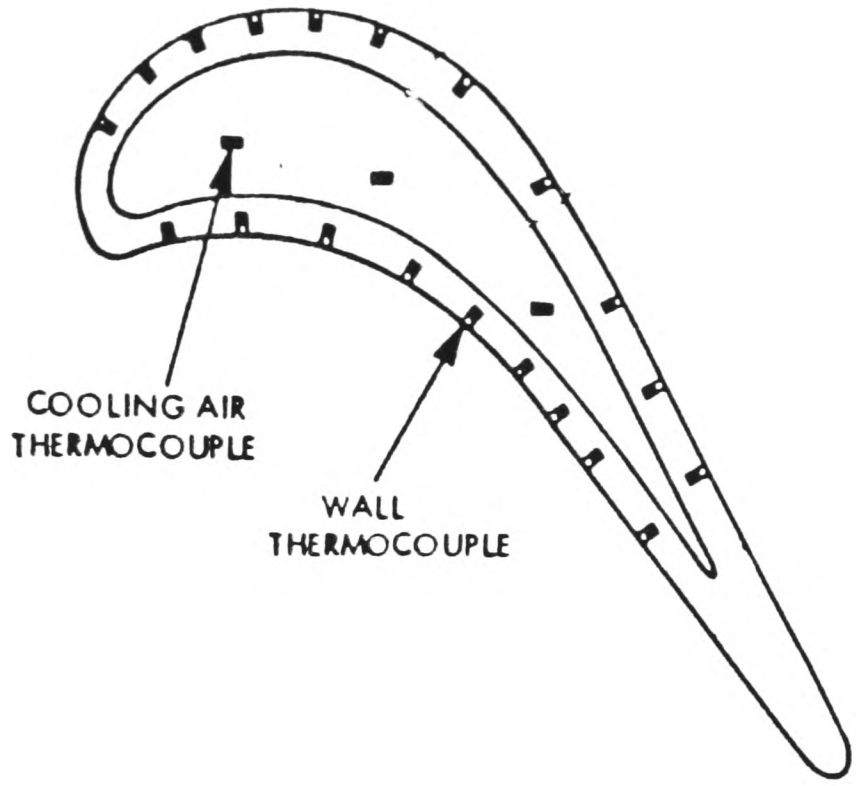

FIG. 2.1 Schematic of test aerofoil, from Barry, Forest and White, A.S.M.E., 82-GT-174.

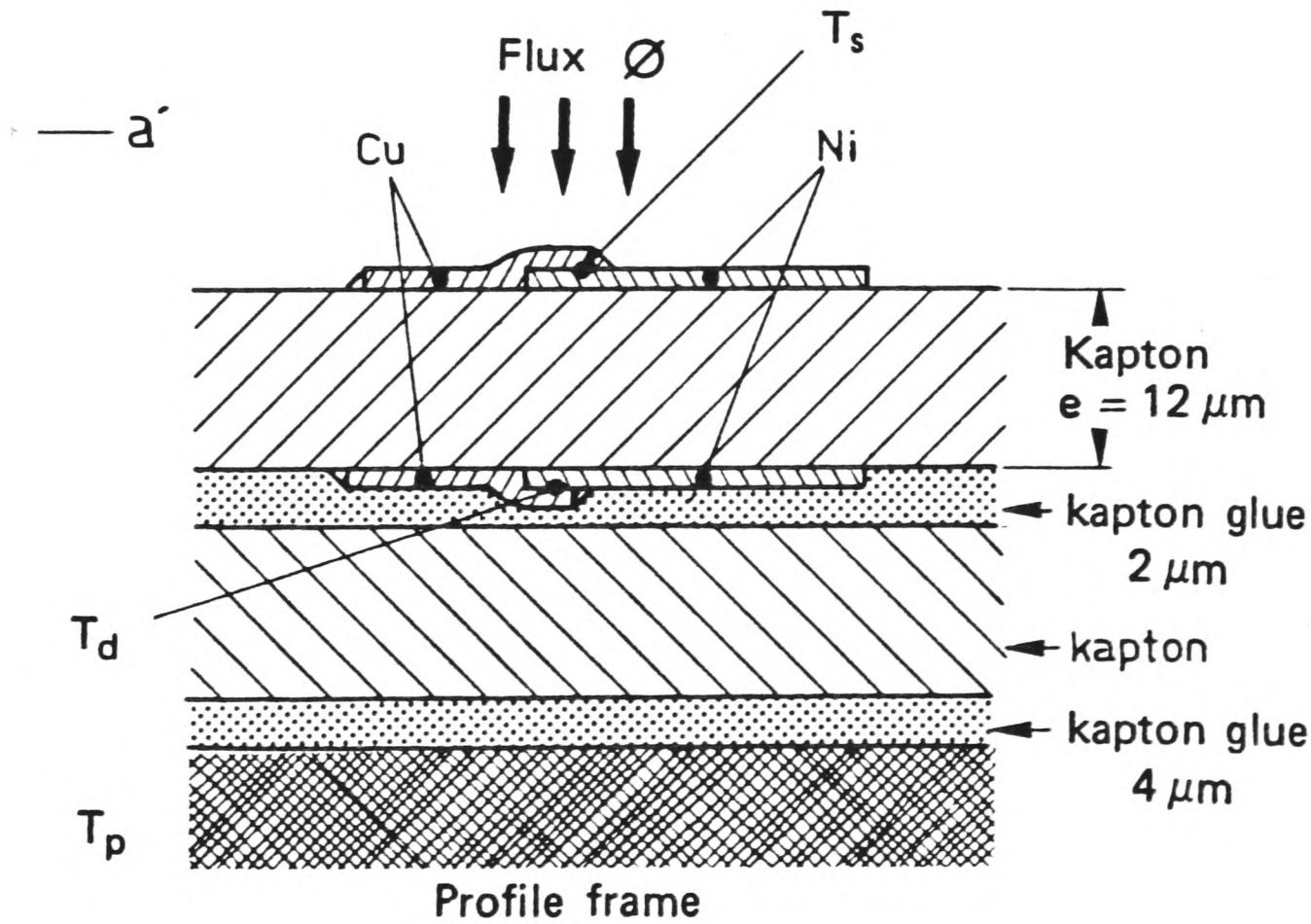

FIG. 2.2 Thin film fluxmeter, from PAULON et al, O.N.E.R.A., T.P. 1981-38.

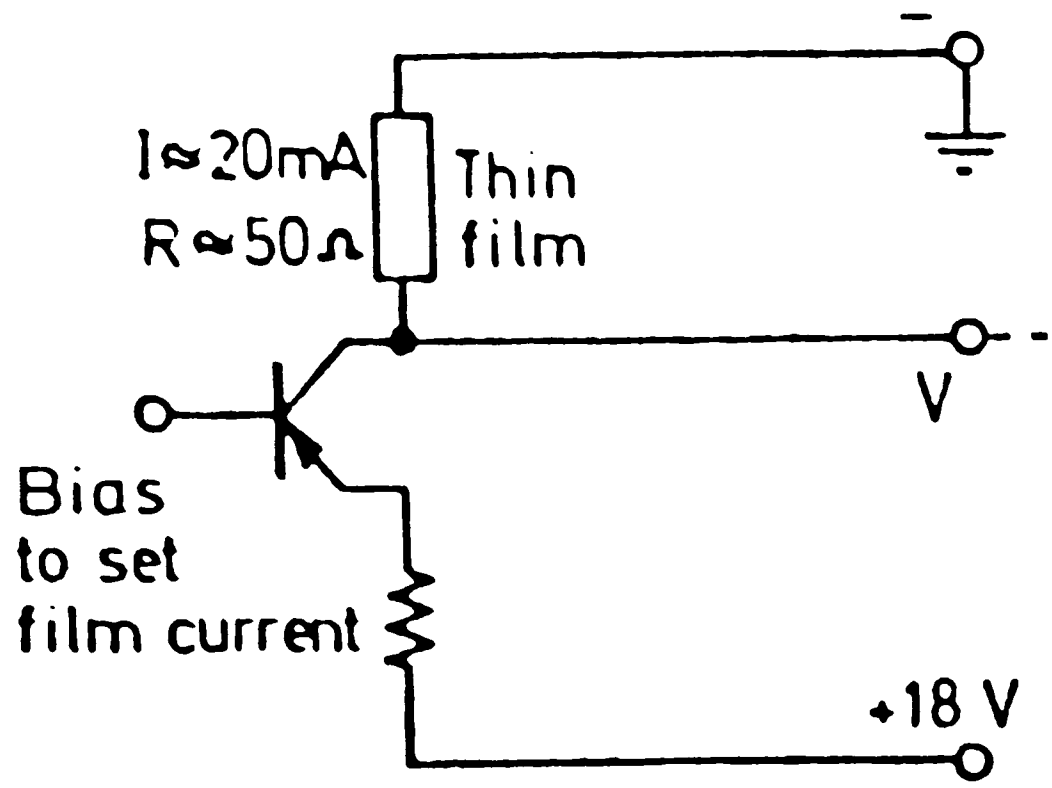

FIG. 3.1 Thin film resistance thermometer.

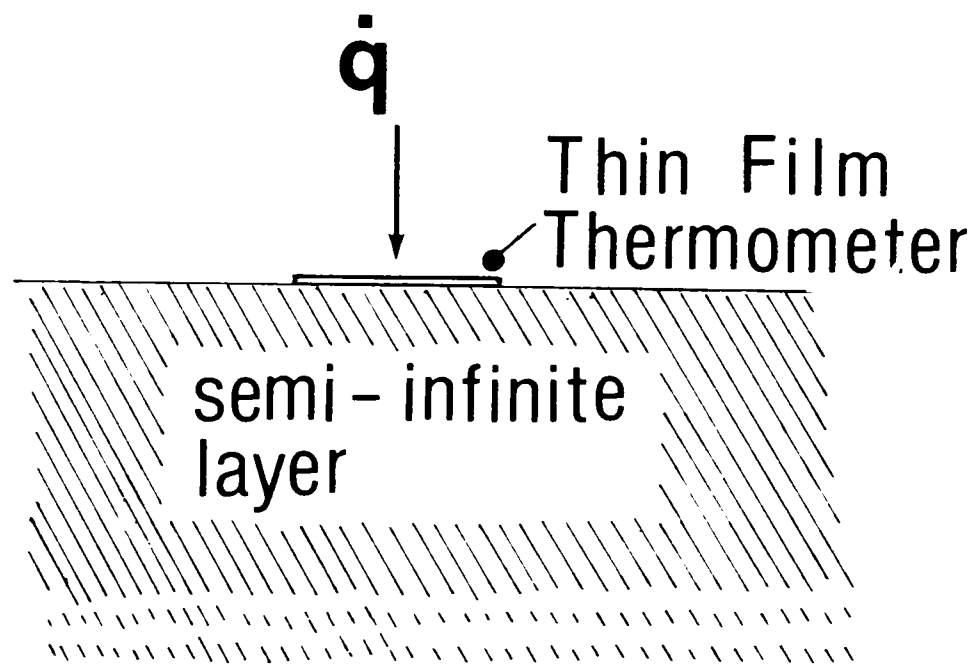

FIG. 3.2 Thin film gauge on single layer semi-infinite substrate.

(a) THERMAL

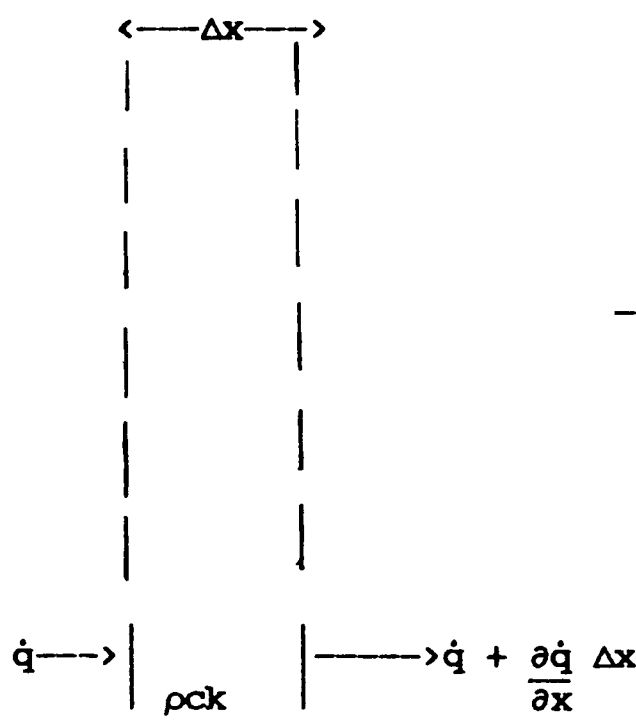

Rate of gain of energy in element Δx

$$= -\frac{\partial \dot{q}}{\partial x}\,\Delta x$$

which by conservation of energy

$$= \rho c\,\Delta x\,\frac{\partial T}{\partial t}$$

Then $$\frac{\partial \dot{q}}{\partial x} = \rho c\,\frac{\partial T}{\partial t}$$

and from $$\dot{q} = -k\,\frac{\partial T}{\partial x}$$

Combining the above equations

gives the diffusion equation

$$\frac{\partial^2 T}{\partial x^2} = \frac{\rho c}{k}\,\frac{\partial T}{\partial t}$$

(b) ELECTRICAL

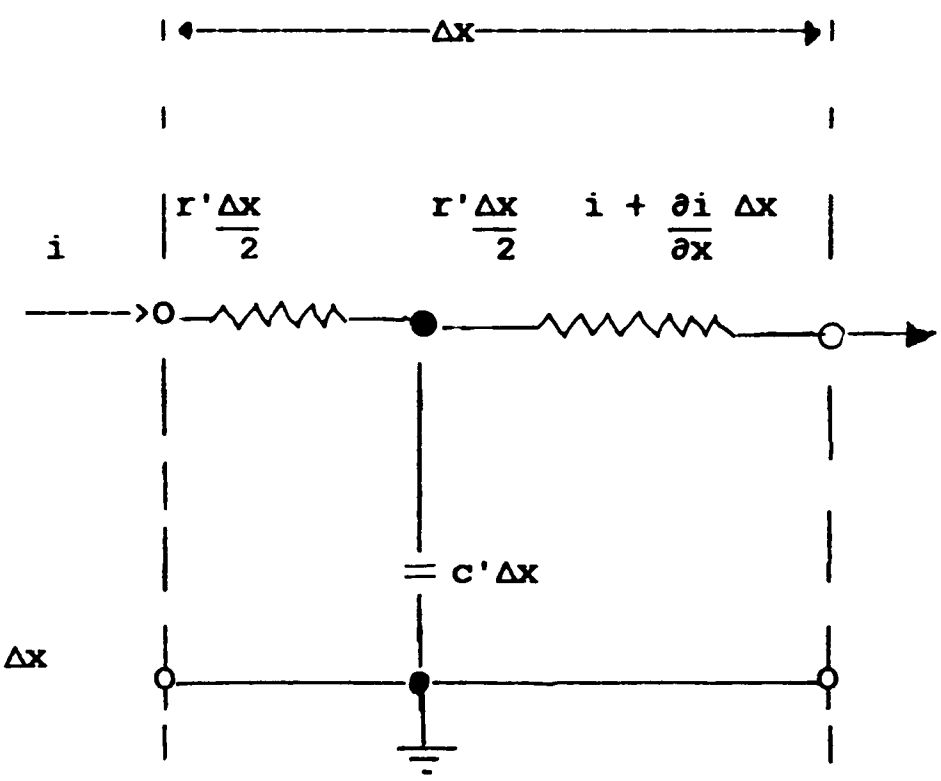

Rate of gain of charge in element Δx

$$= -\frac{\partial i}{\partial x}\,\Delta x$$

by conservation of charge

$$= c'\,\Delta x\,\frac{\partial V}{\partial t}$$

Then $$\frac{\partial i}{\partial x} = -c'\,\frac{\partial V}{\partial t}$$

Ohm's law gives

$$i = \frac{1}{r'}\,\frac{\partial V}{\partial x}$$

combining the above gives

the transmission line equation

$$\frac{\partial^2 V}{\partial x^2} = r'c'\,\frac{\partial V}{\partial t}$$

FIG 3.3

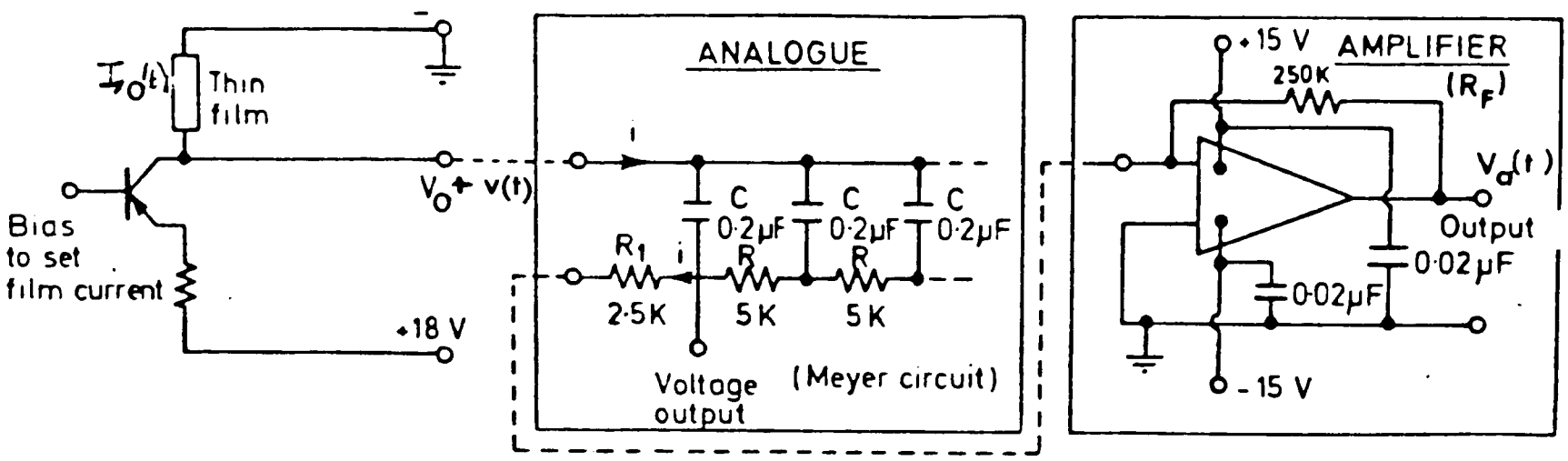

FIG. 3.4 Typical electrical analogue circuit for thin film use.

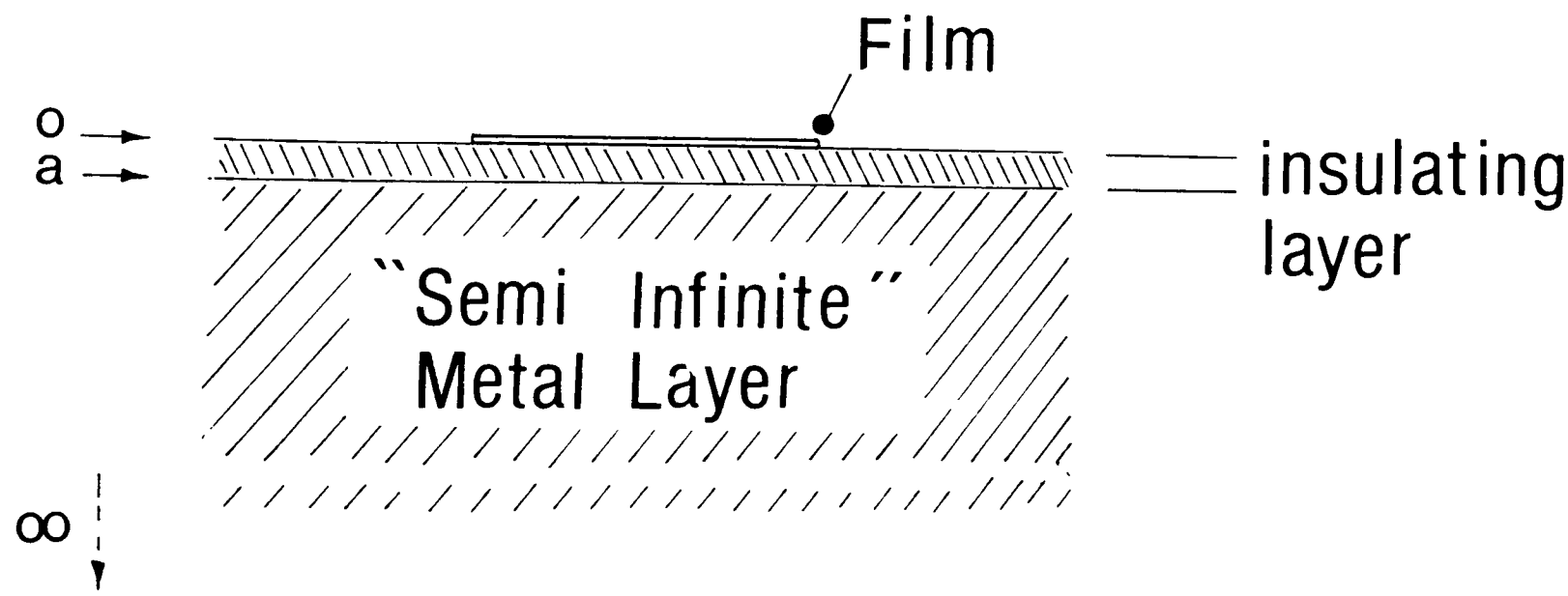

FIG. 3.5 Thin film gauge on two-layered substrate with semi-infinite metal layer.

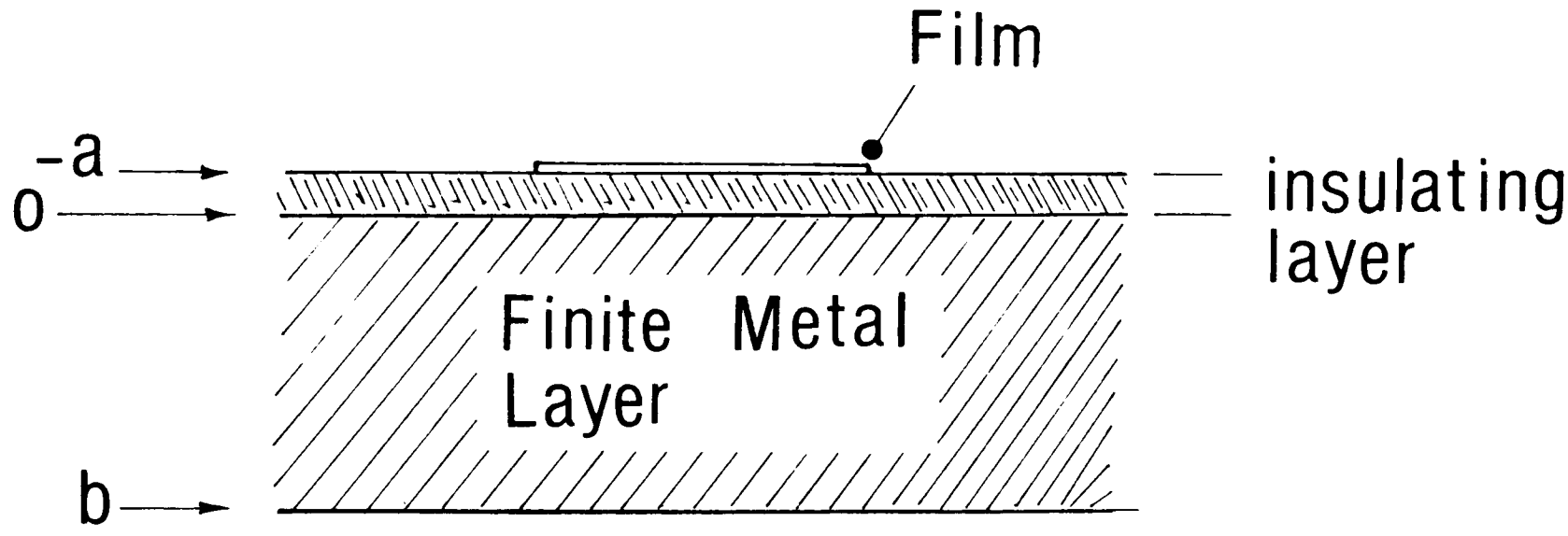

FIG. 3.6 Thin film on two-layered substrate with finite metal layer.

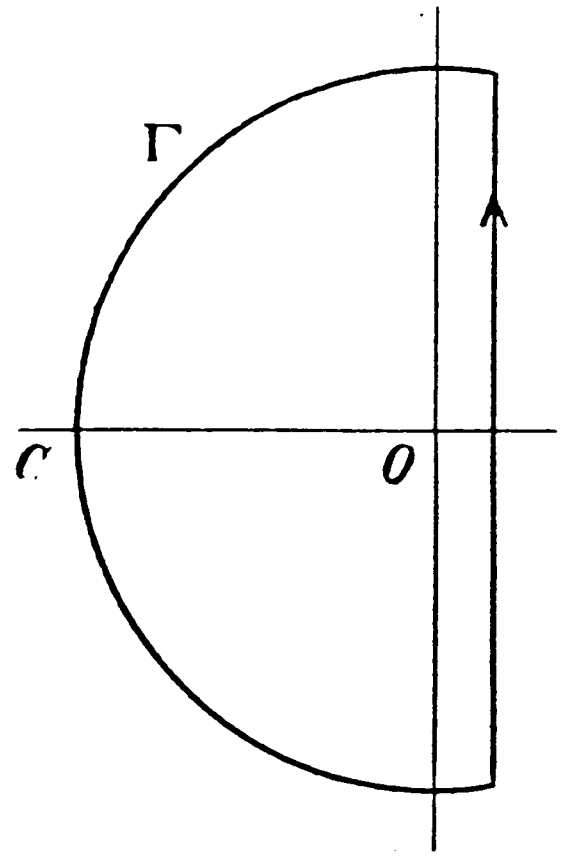

FIG. 3.7 Contour for transform inversion.

FIG 3.8 20 μm Al_2O_3 on 3mm Nickel

a

20 μ Al_2O_3 on 3mm Nickel : Roots of $k_1 \sin a\beta \cos \lambda b\beta + \lambda k_2 \cos a\beta \sin \lambda b\beta = 0$

Eigenvalues β_n

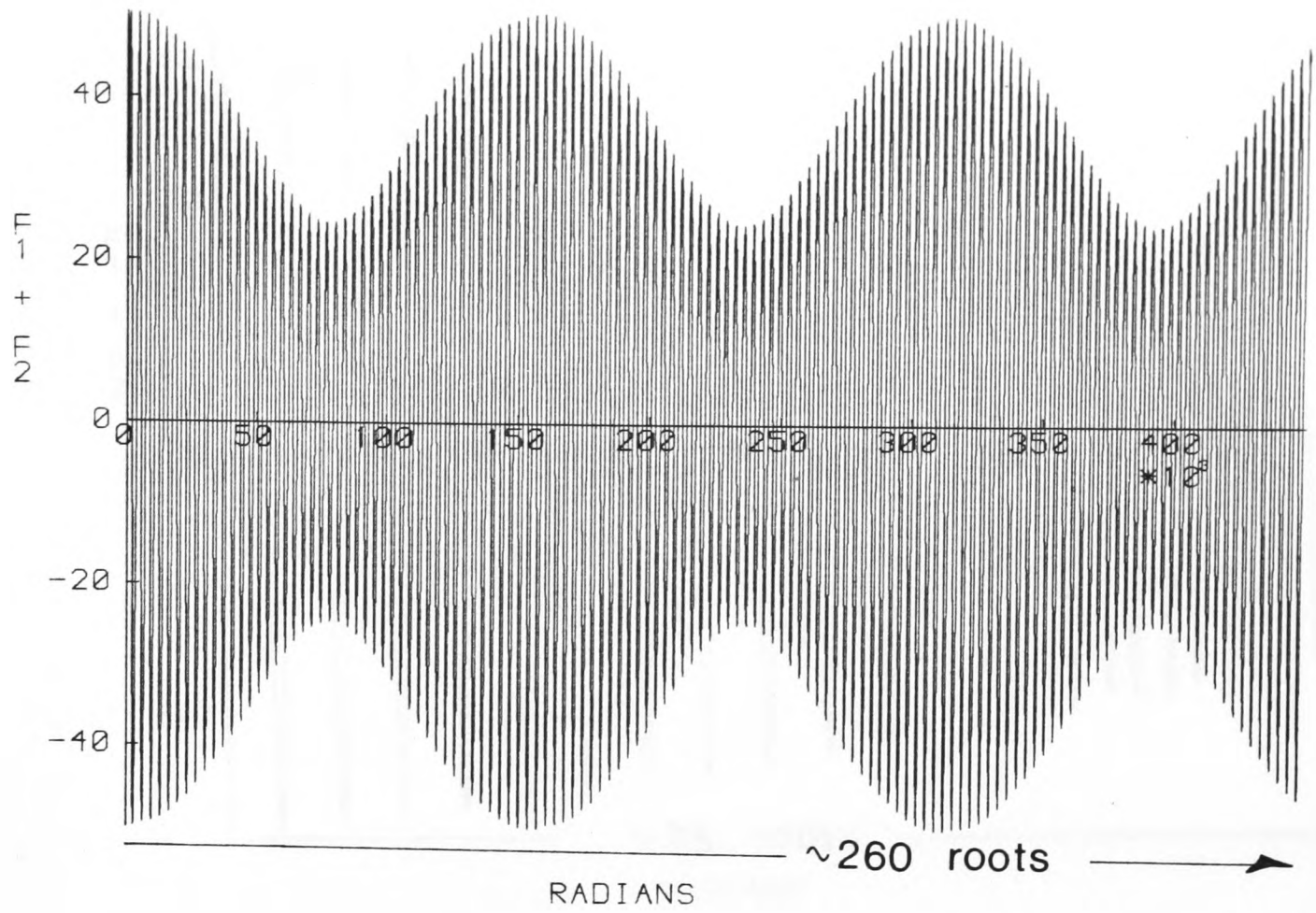

b

20 μ Al_2O_3 on 3mm Nickel : $k_1 \sin a\beta \cos \lambda b\beta + \lambda k_2 \cos a\beta \sin \lambda b\beta = 0$

First 3 roots

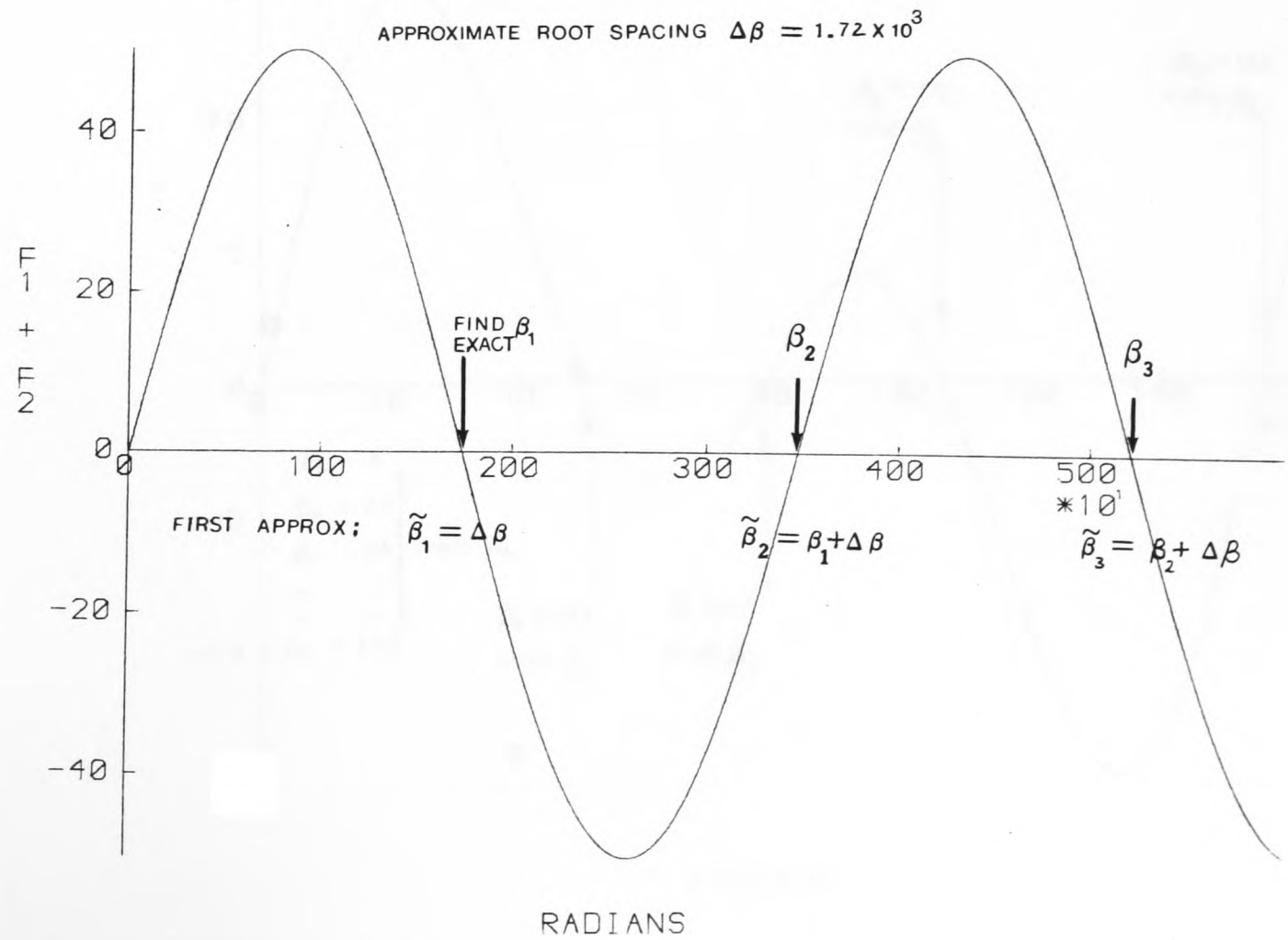

FIG 3.9 200 μm Quartz on 3mm Nickel (FINITE BACKWALL) ROOT FINDING PROCEDURE

a *200μm quartz on 3 mm Nickel* $k_1 \sin a\beta \cos \lambda b\beta + \lambda k_2 \cos a\beta \sin \lambda b\beta = 0$

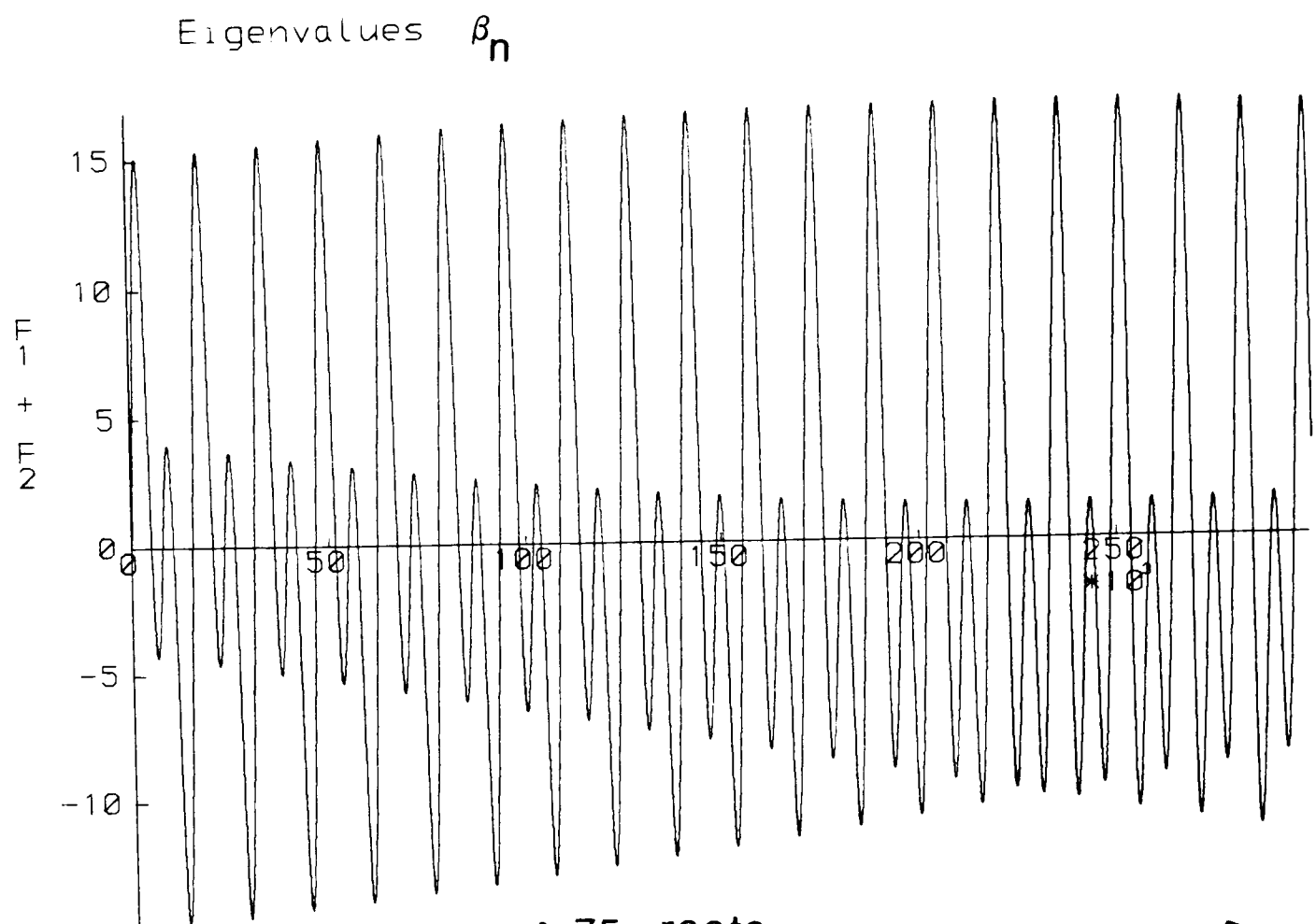

b *200 μm quartz on 3 mm Nickel, roots of :* $k_1 \sin a\beta \cos \lambda b\beta + \lambda k_2 \cos a\beta \sin \lambda b\beta = 0$

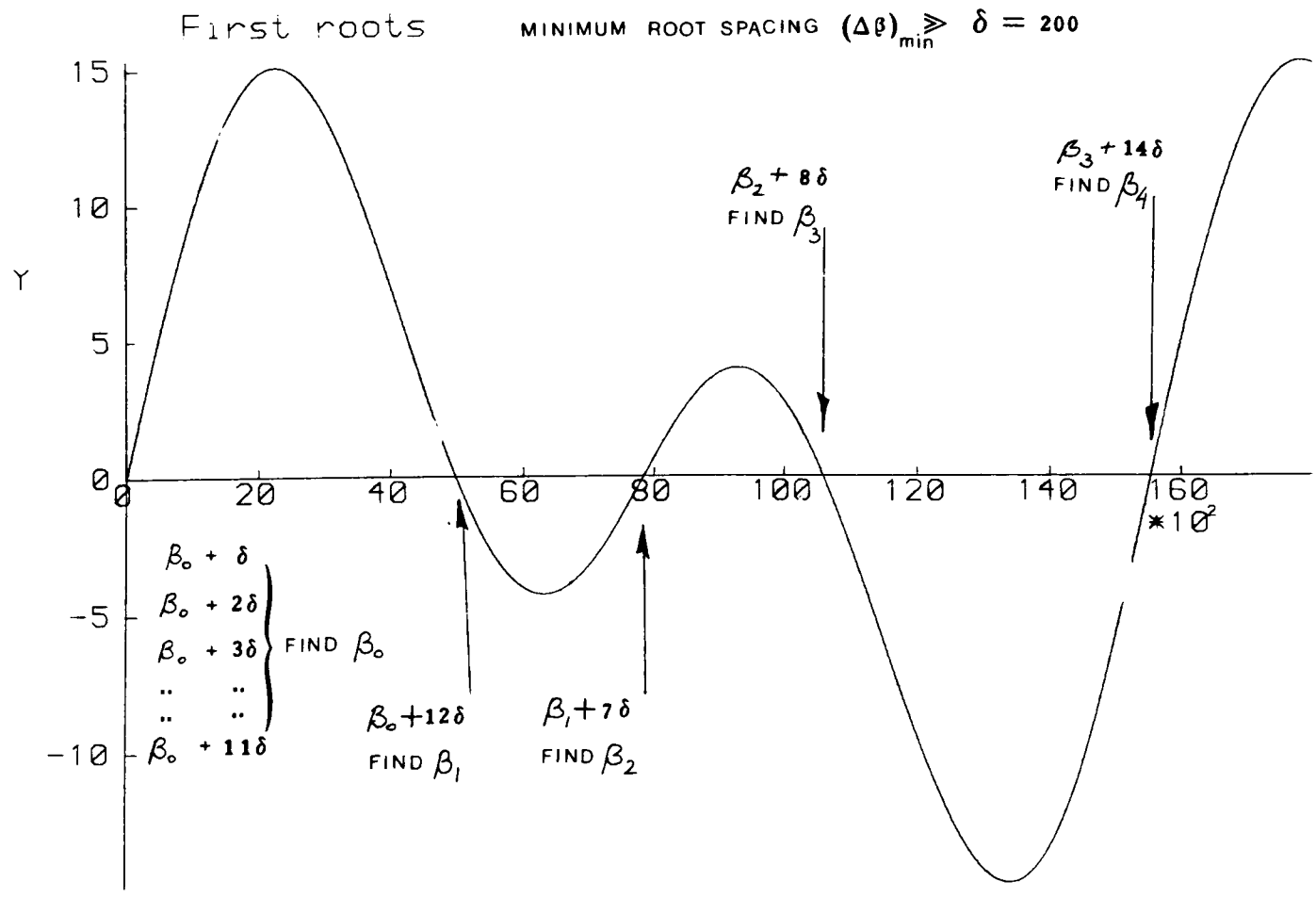

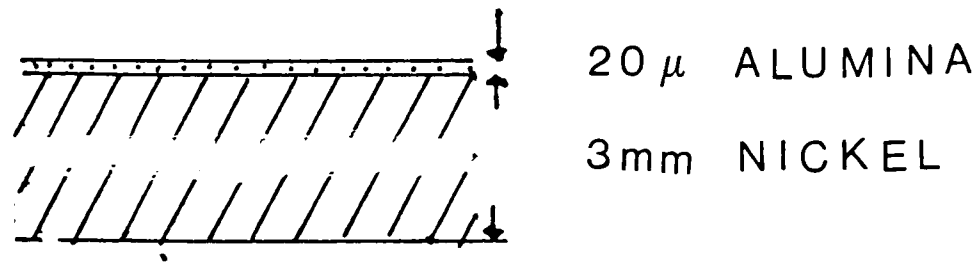

FIG. 3.10

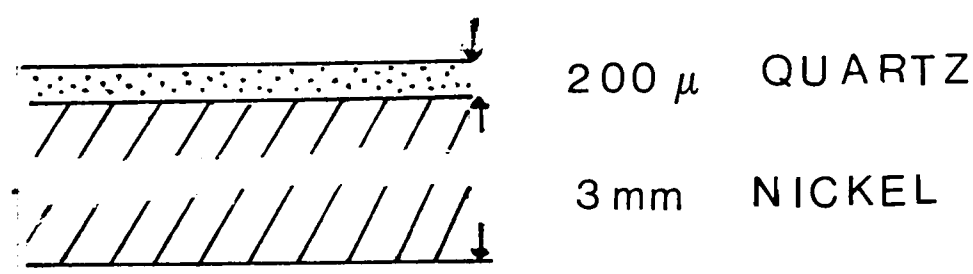

FIG. 3.11

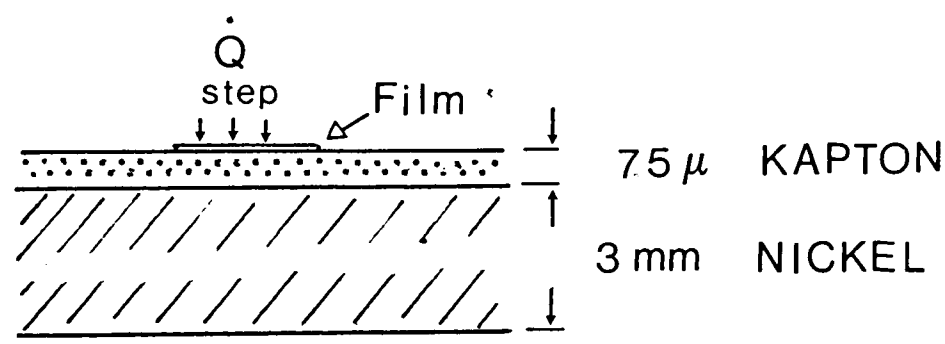

FIG. 3.12

FIG. 3.13 20 μm Al_2O_3 on Nickel Base

a: 20 μm Al_2O_3 on 3mm Nickel base (0 - 500ms)

b: 20 μm Al_2O_3 on infinite Nickel base (0 - 500ms)

SURFACE TEMP.

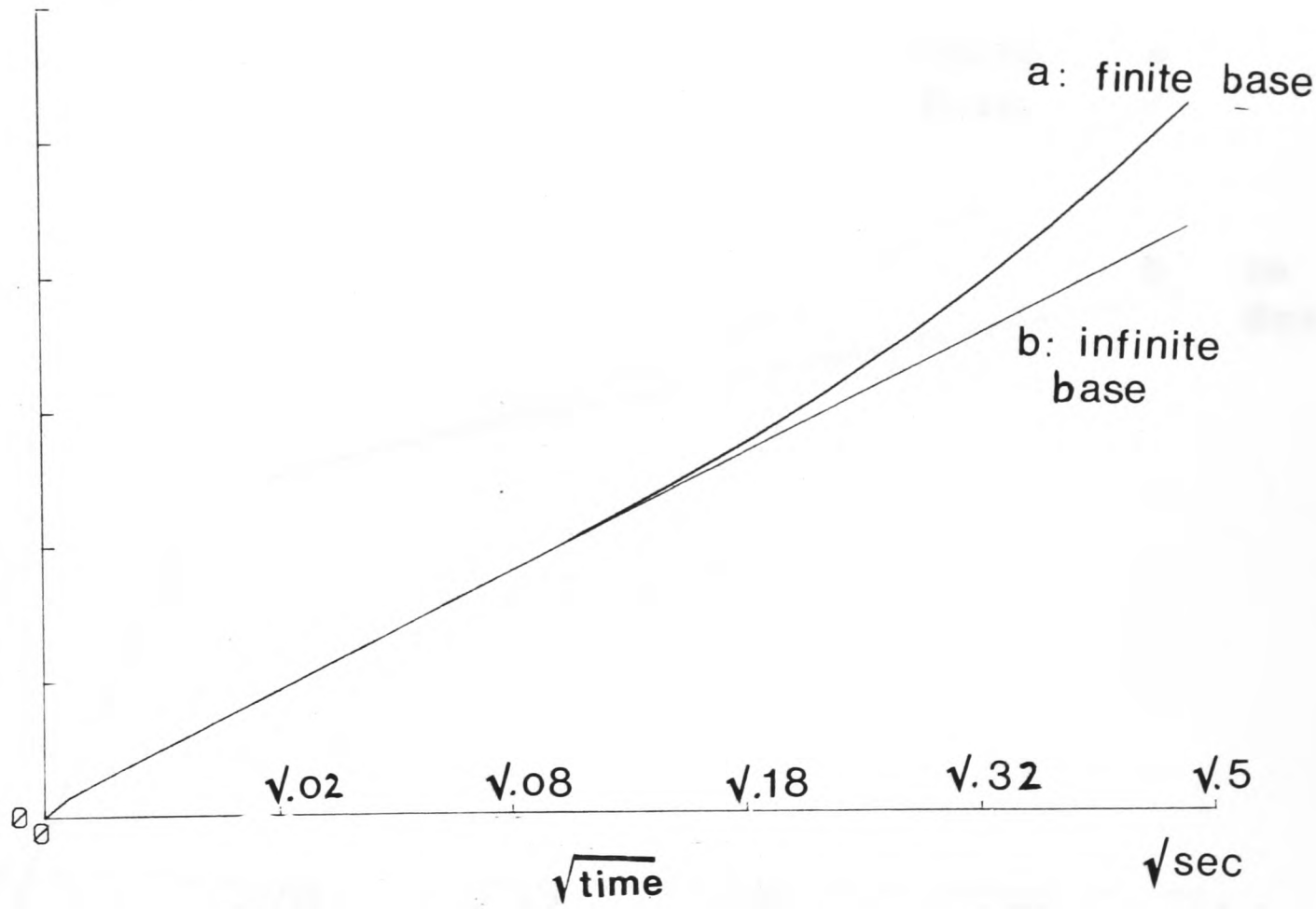

FIG 3.14 200 μm Quartz on Nickel

a: *200 um quartz on 3 mm Nickel*

b: *200 um quartz on an infinite Nickel base*

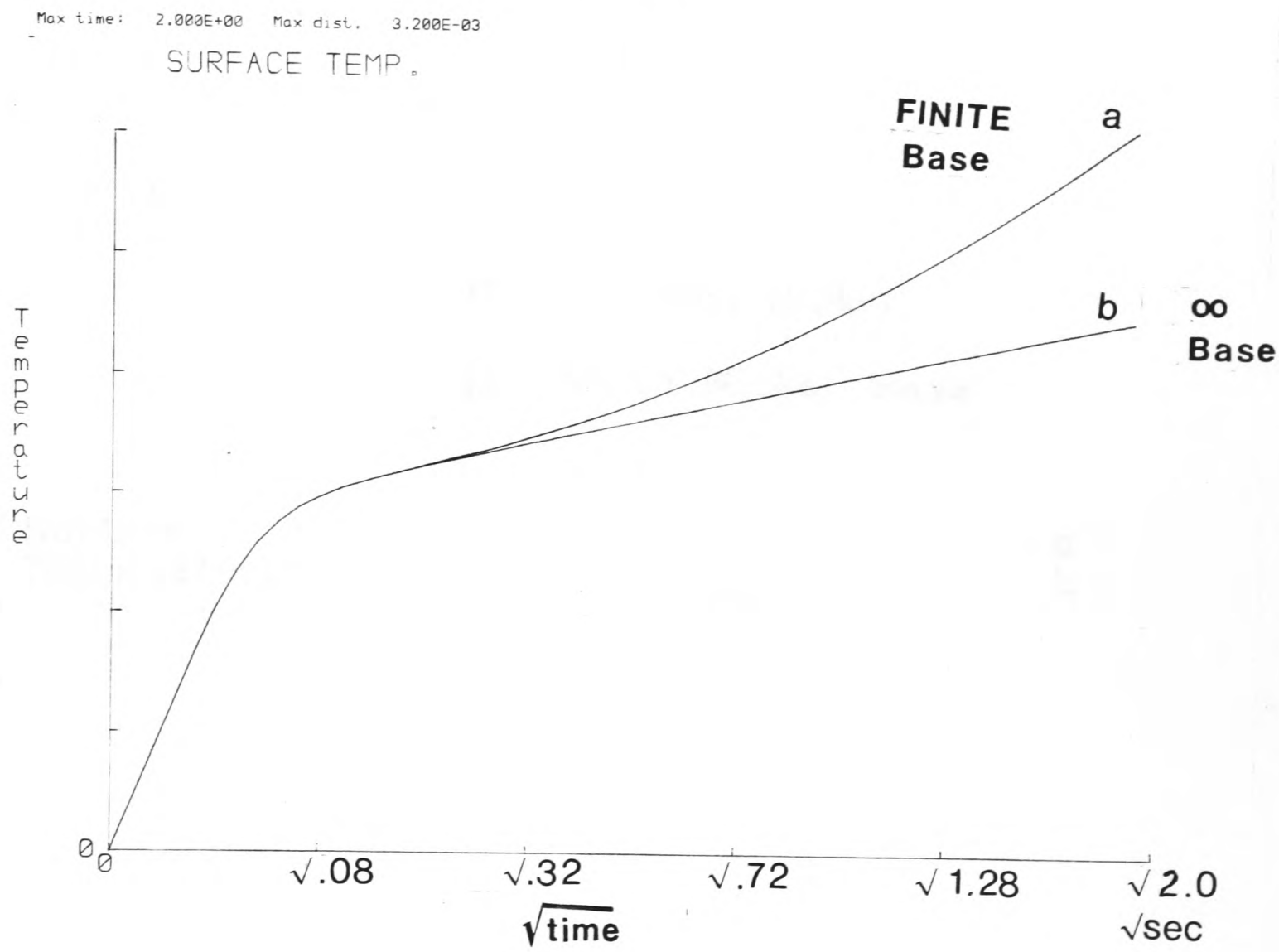

75μm Kapton

a: on 3mm Nickel

b: on ∞ Nickel Base

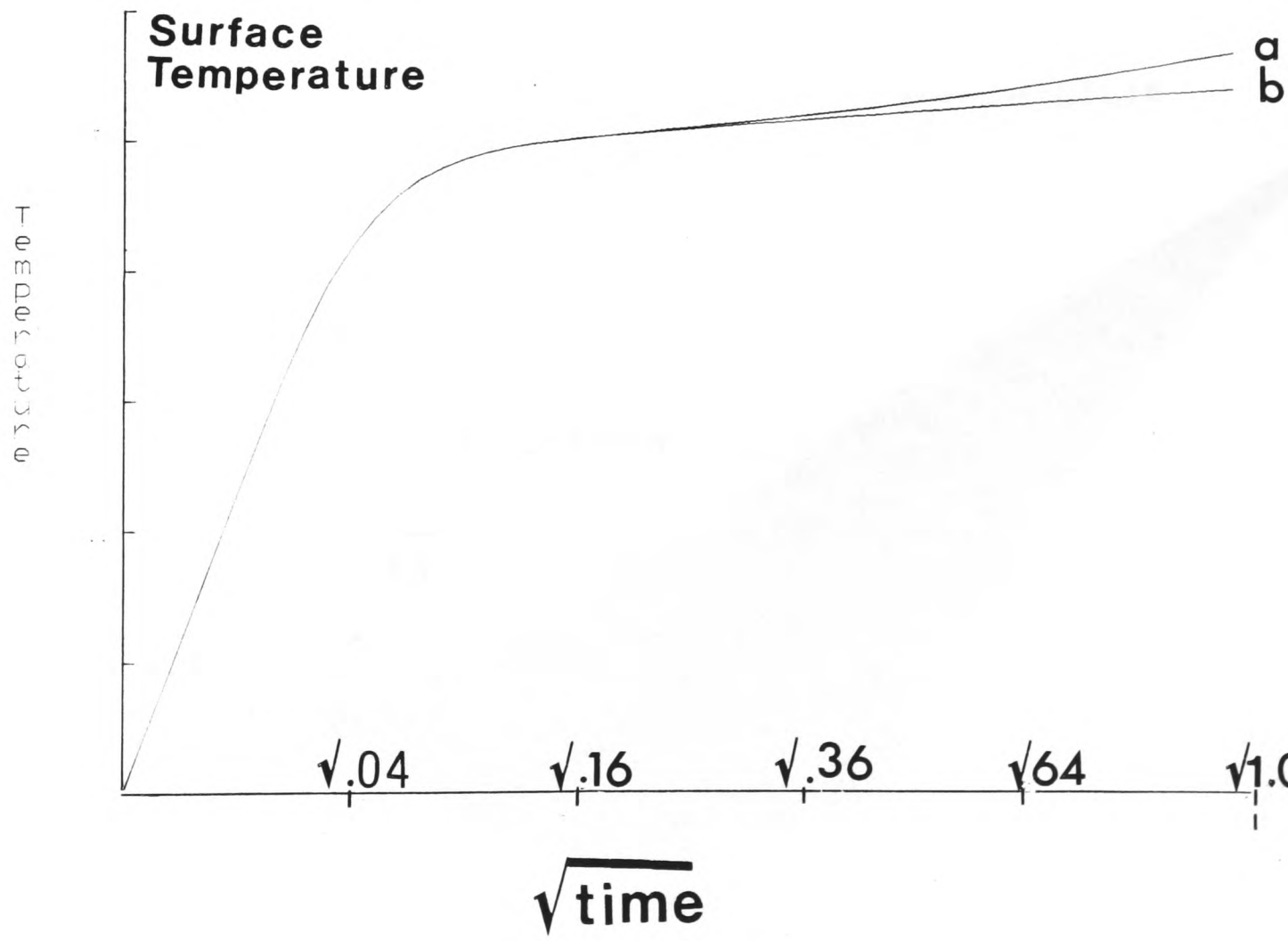

FIG 3.15

Fig 3-16 20 μm Al_2O_3 on ∞ Nickel Base

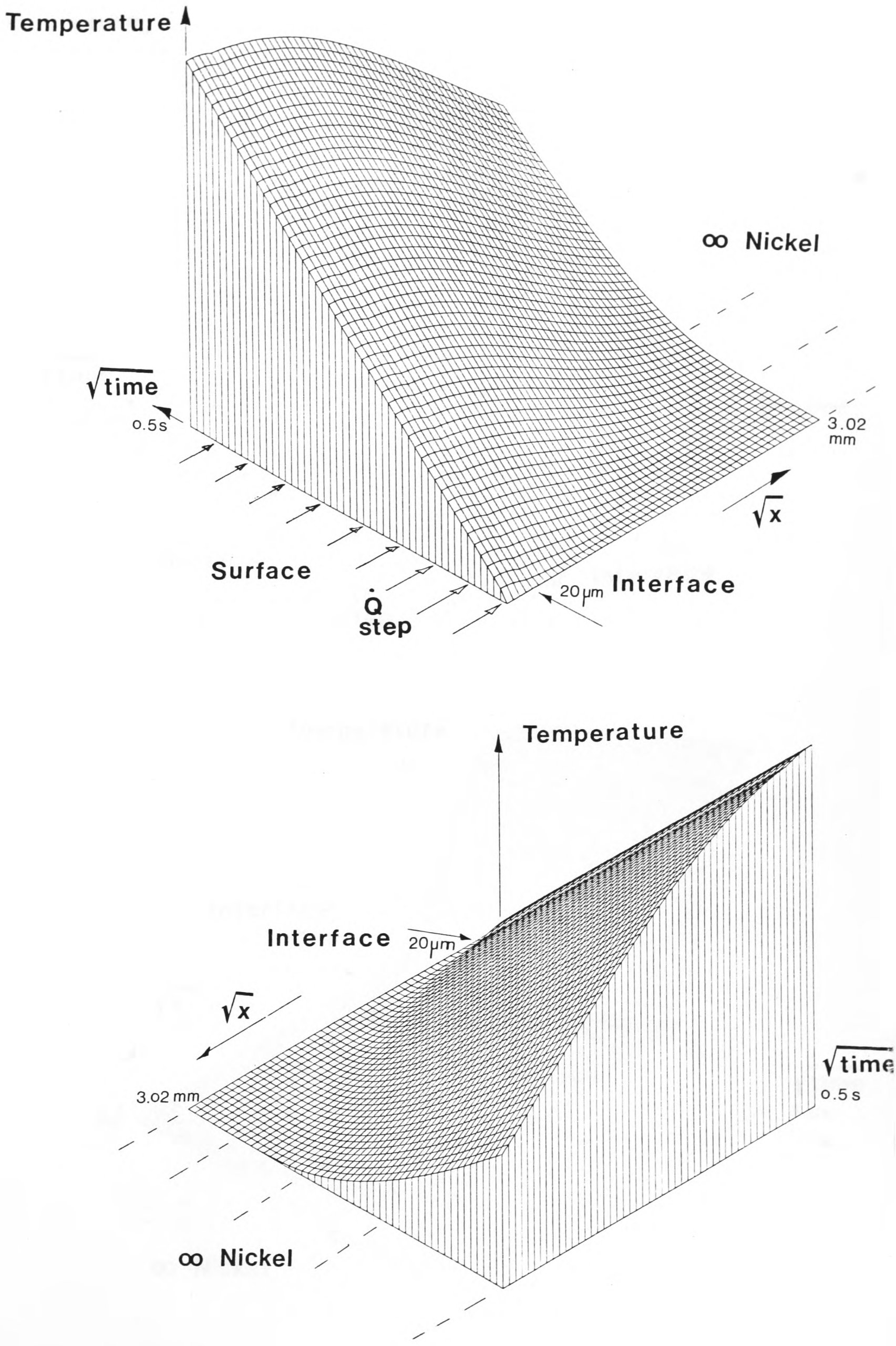

Fig 3-17 200 μm Quartz on ∞ Nickel Base

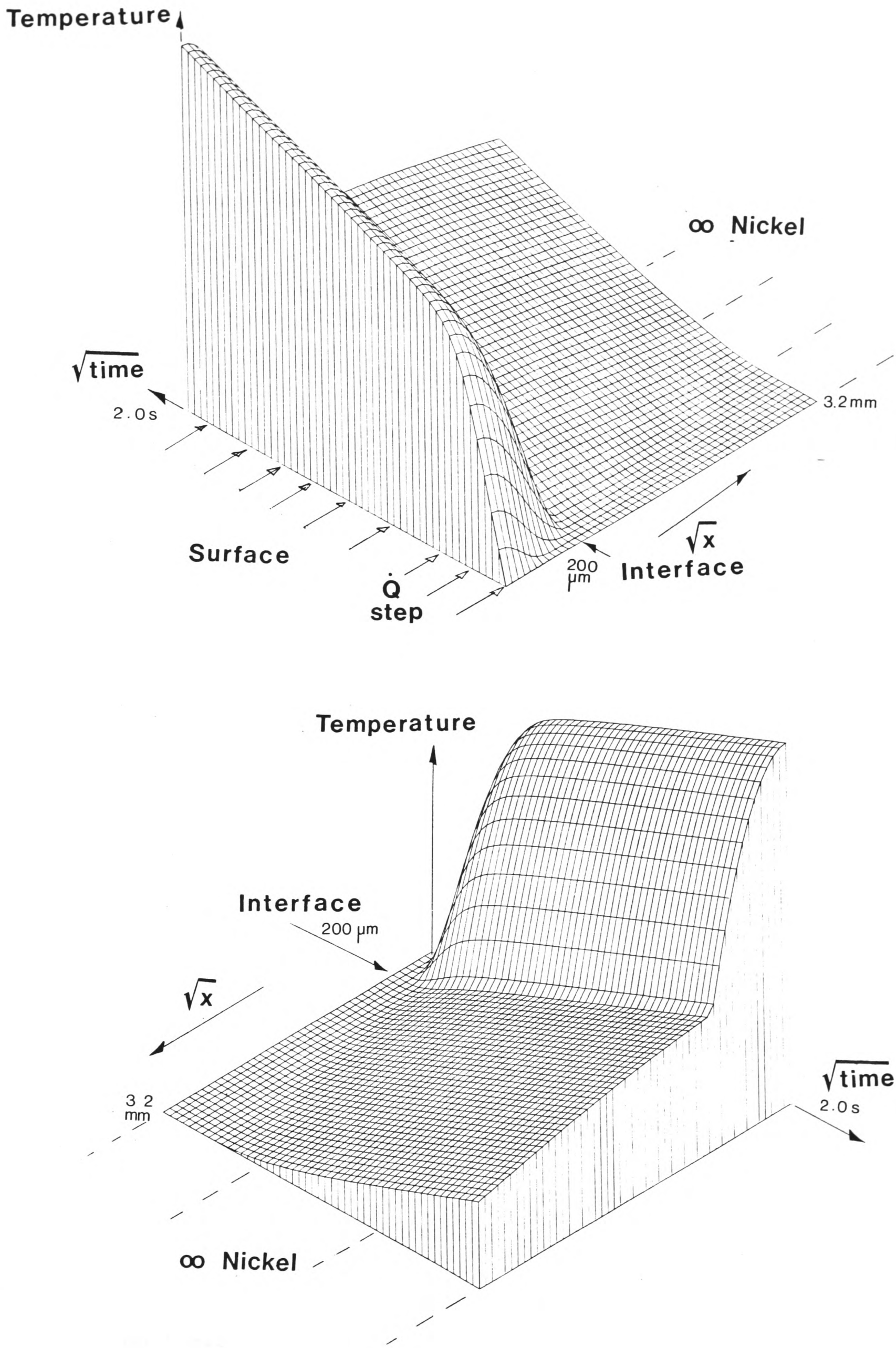

FIG 3-18 75 μm KAPTON on ∞ Nickel Base

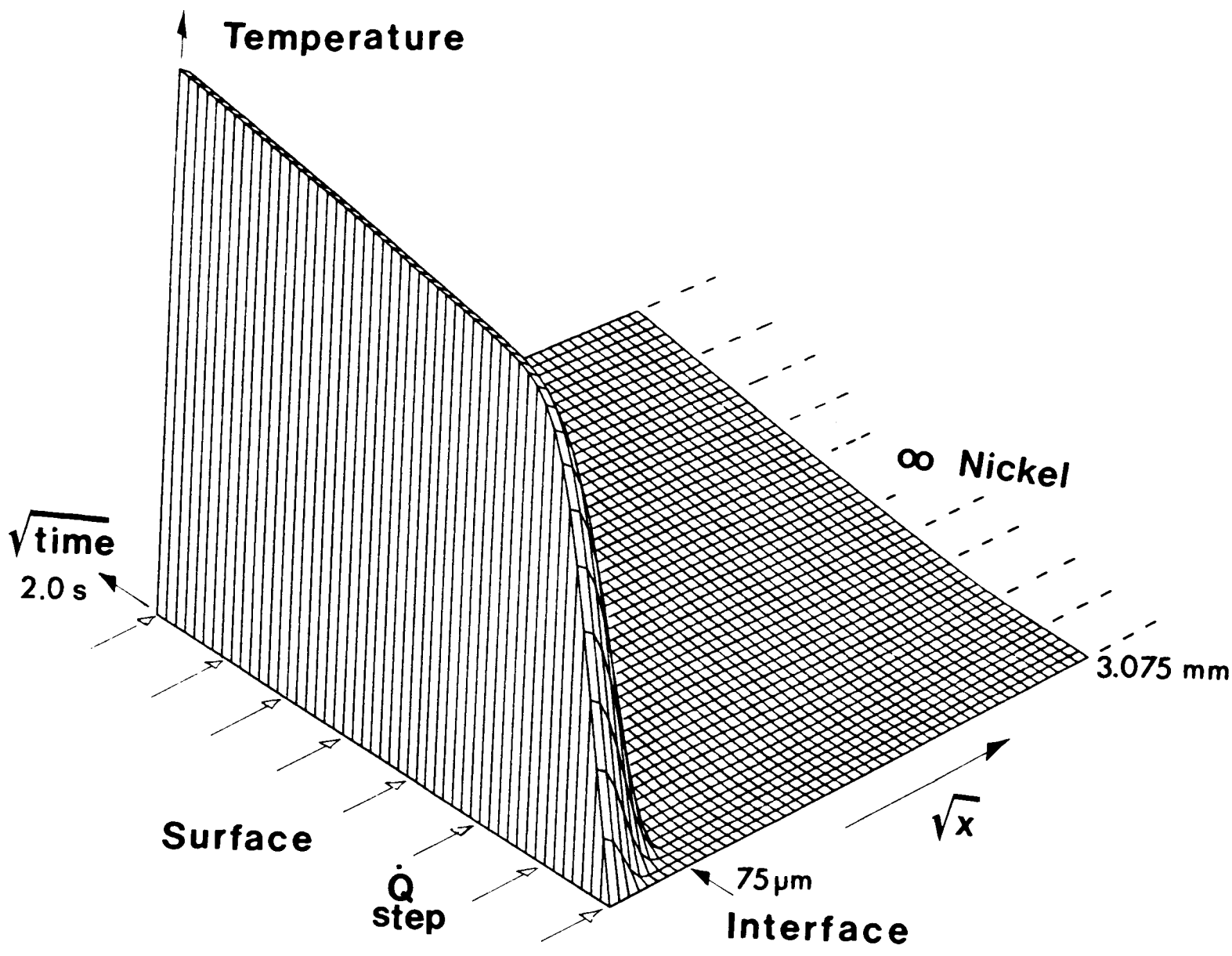

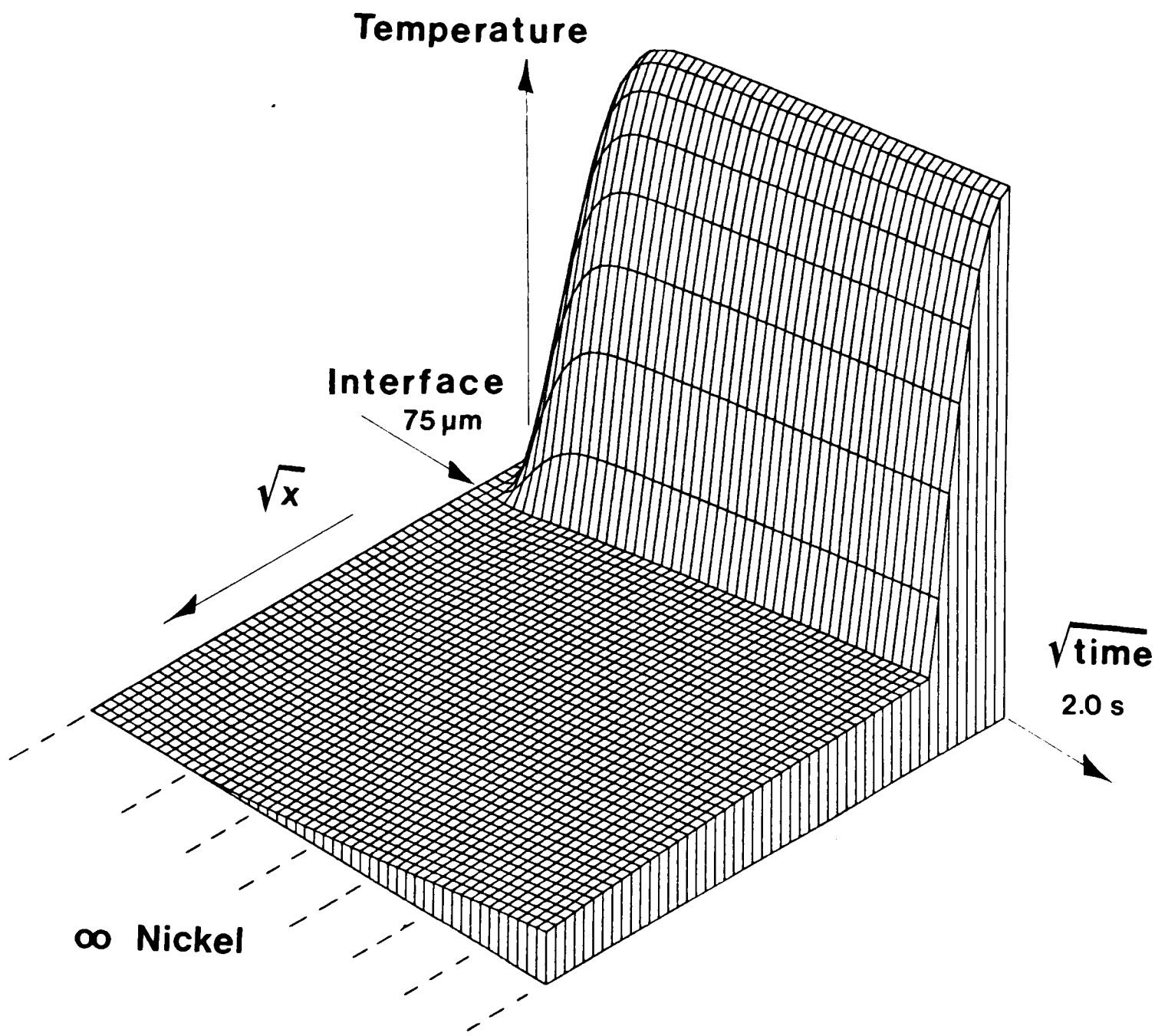

FIG 3-18 75 μm KAPTON on ∞ Nickel Base

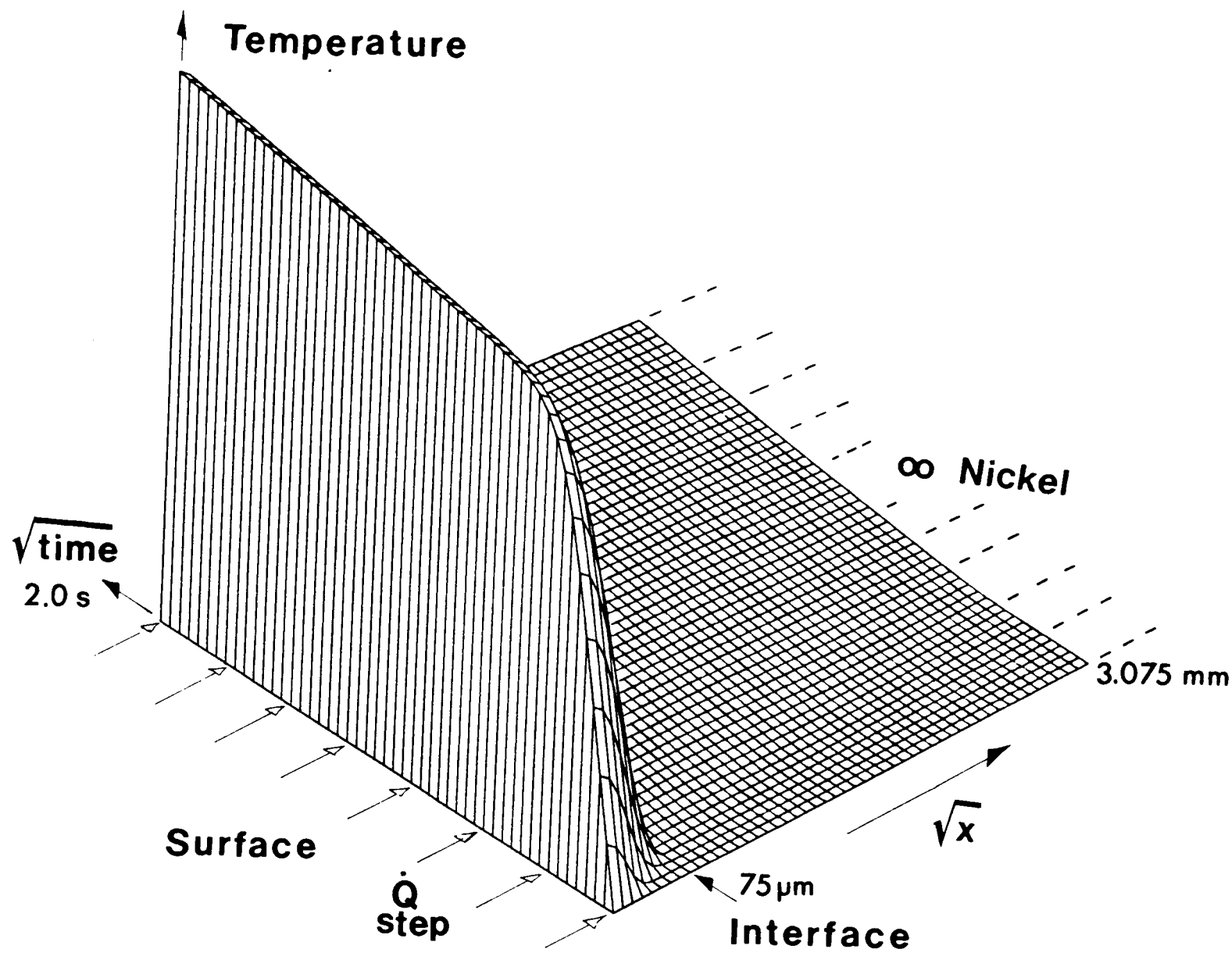

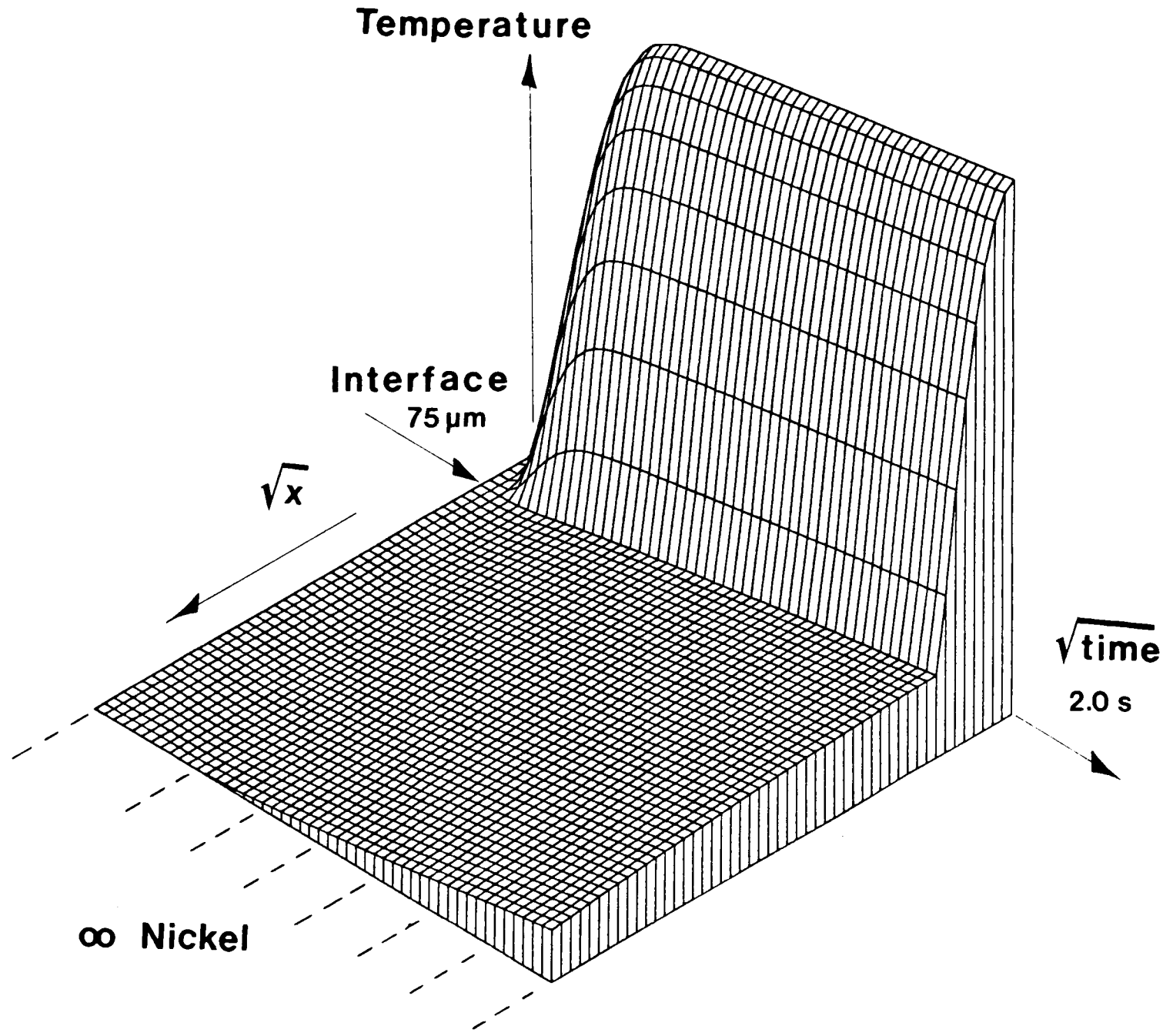

Fig 3-19 20 μm Al_2O_3 on 3mm Nickel

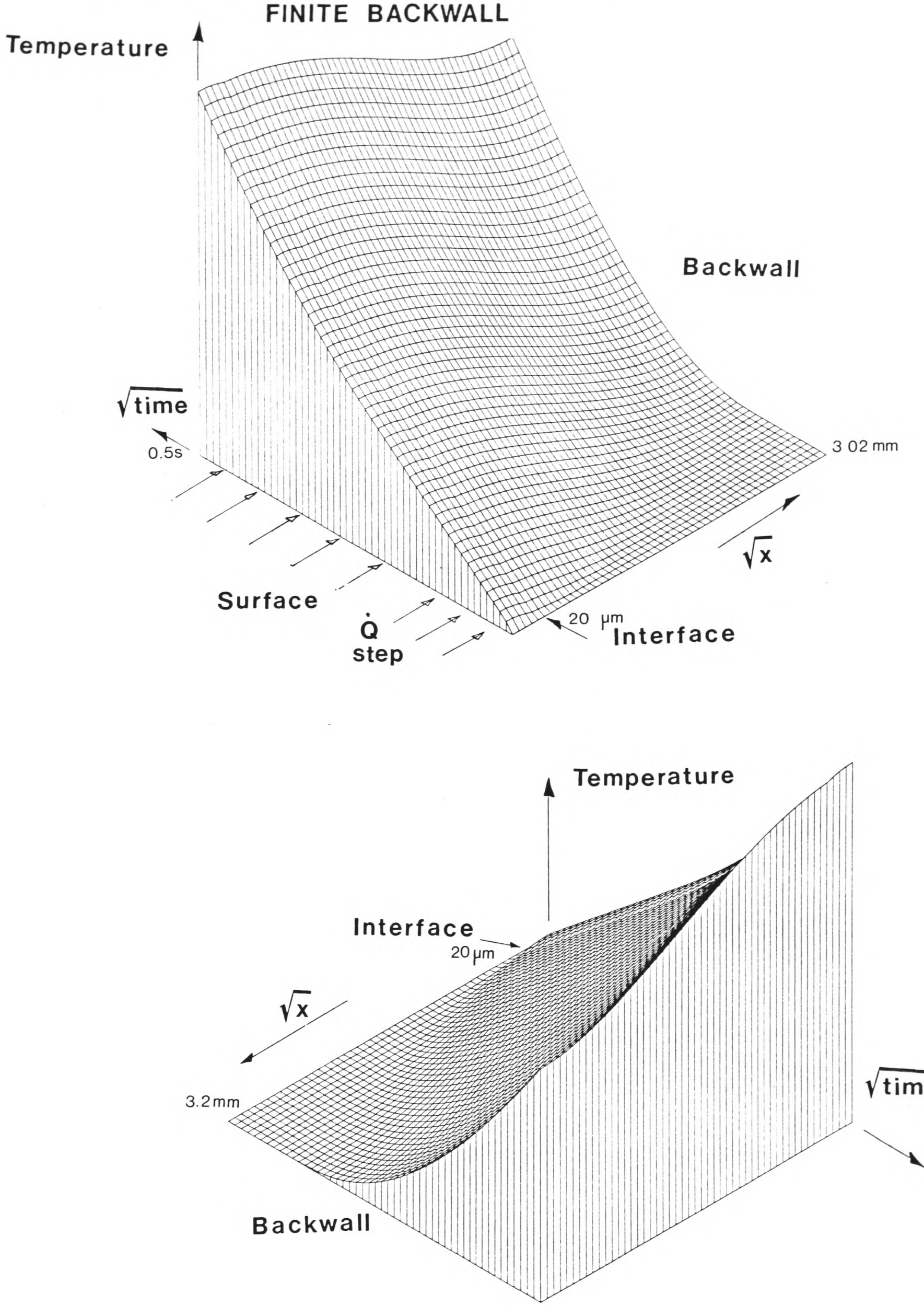

FIG 3-20: 200 μm Quartz on 3mm Nickel
(FINITE BACKWALL)

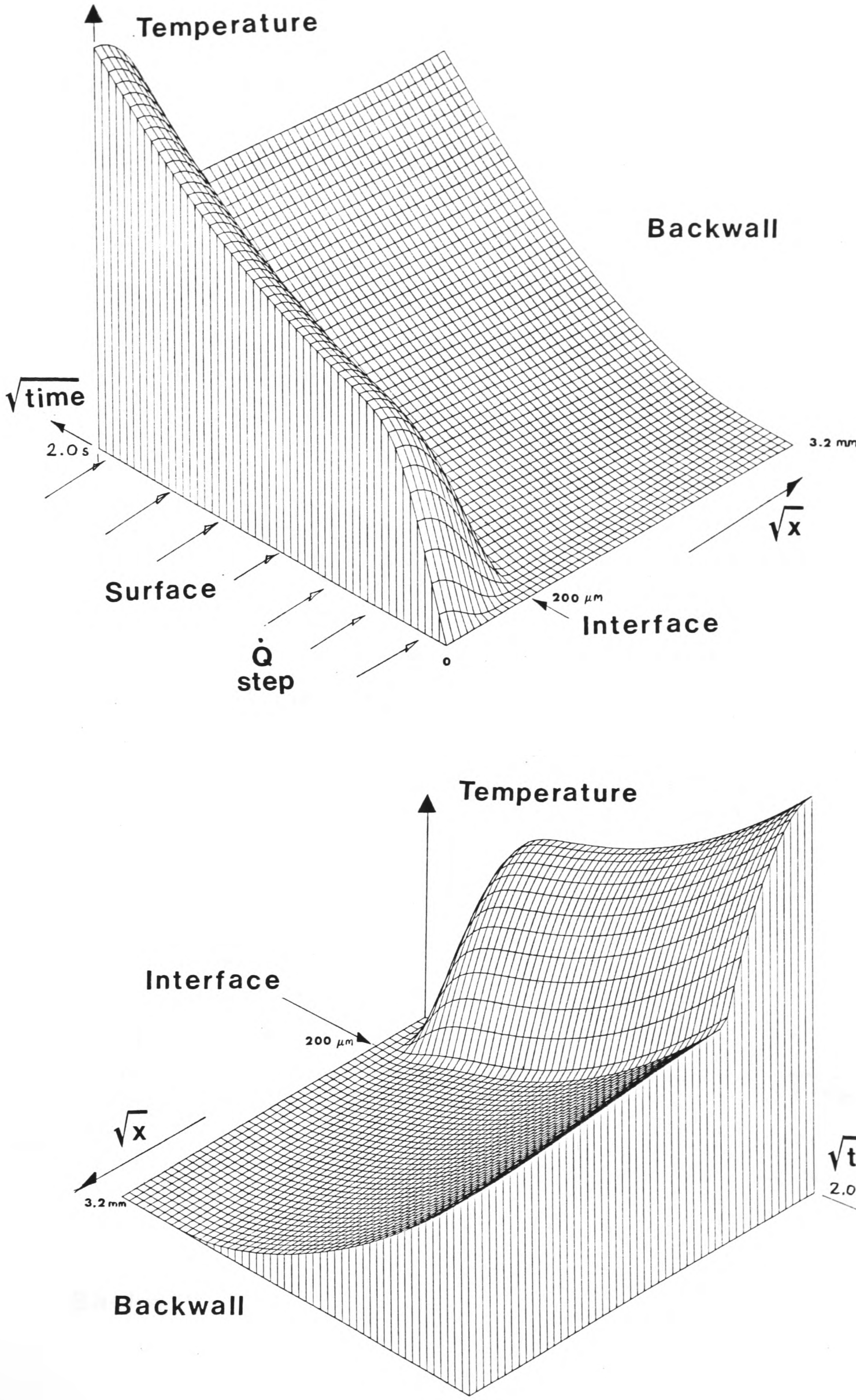

Fig 3-21 75 μm KAPTON on 3 mm Nickel

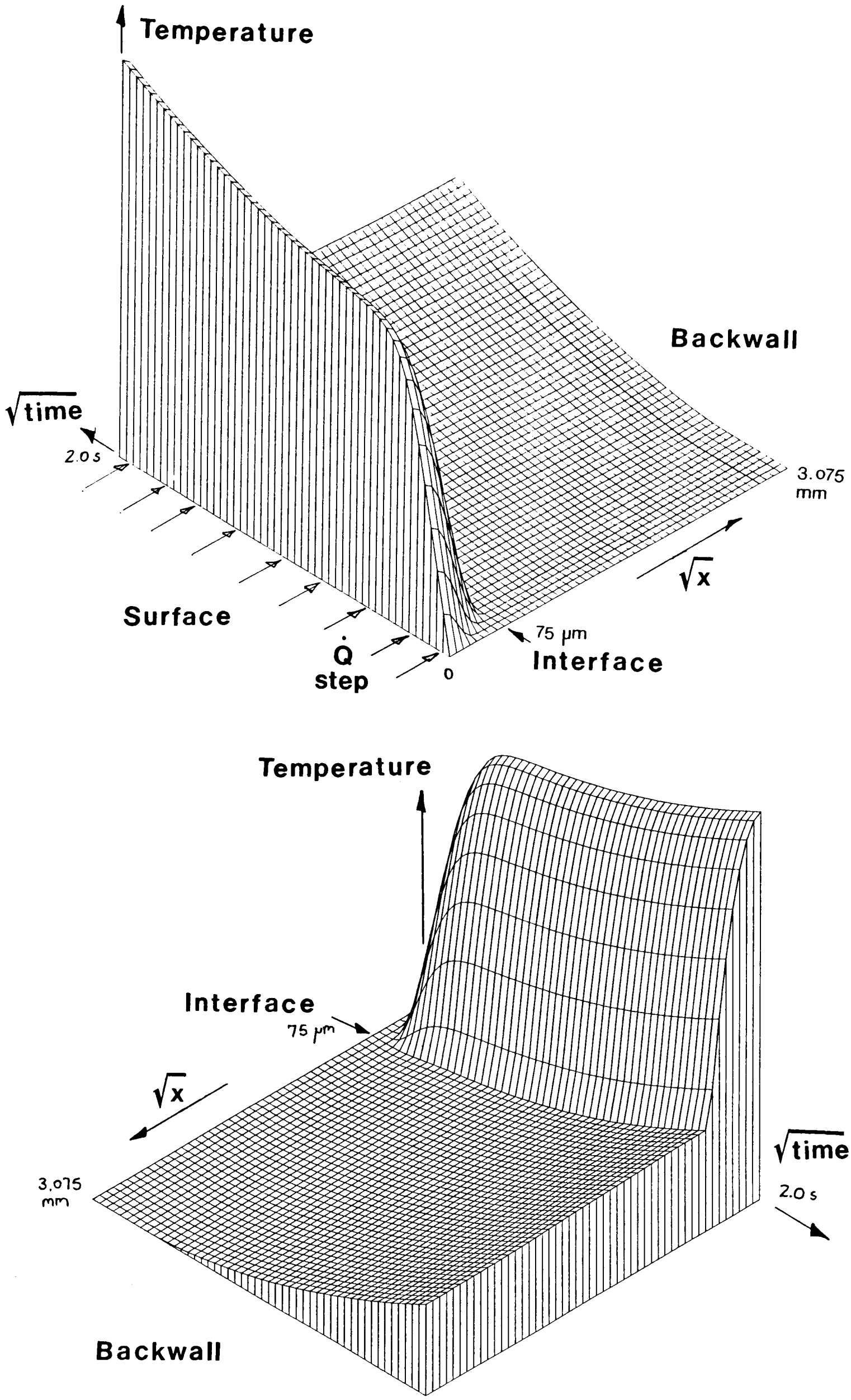

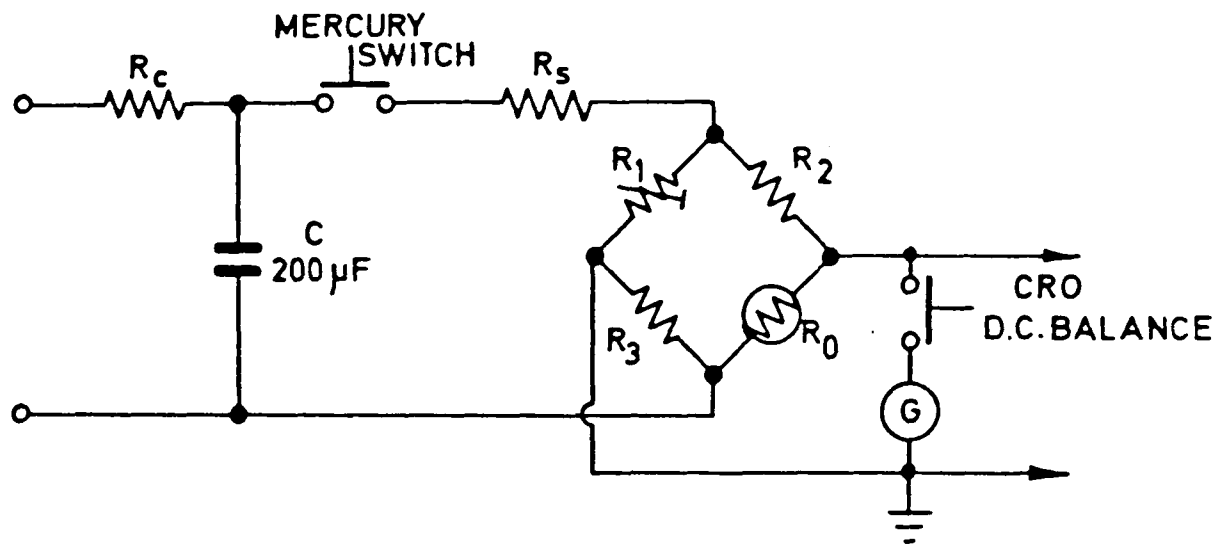

$C(R_s + R_2 + R_0) \sim 0.1$ sec

R_0 = FILM RESISTANCE

R_2, R_3 = FIXED BRIDGE RESISTANCES

R_1 = 4 DECADE VARIABLE RESISTANCE

R_s = SERIES RESISTANCE

FIG. 4.1 Simple circuit for measurement of $\sqrt{(\rho ck)}$. From Schultz and Jones (1973).

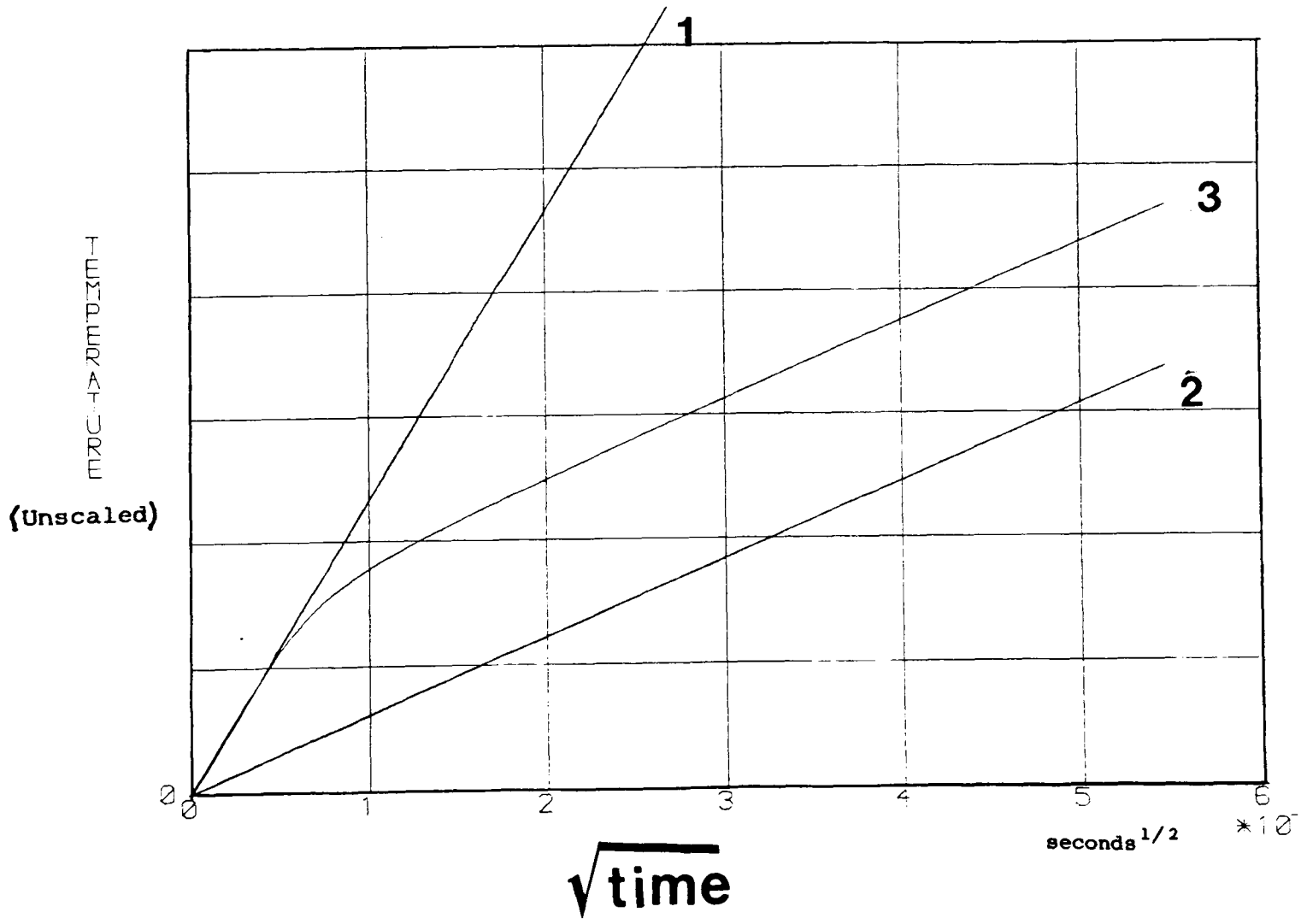

FIG. 4.2
Predicted surface temperature signals for step in heat transfer rate.
1 Insulator alone
2 metal alone
3 Insulator coated metal.

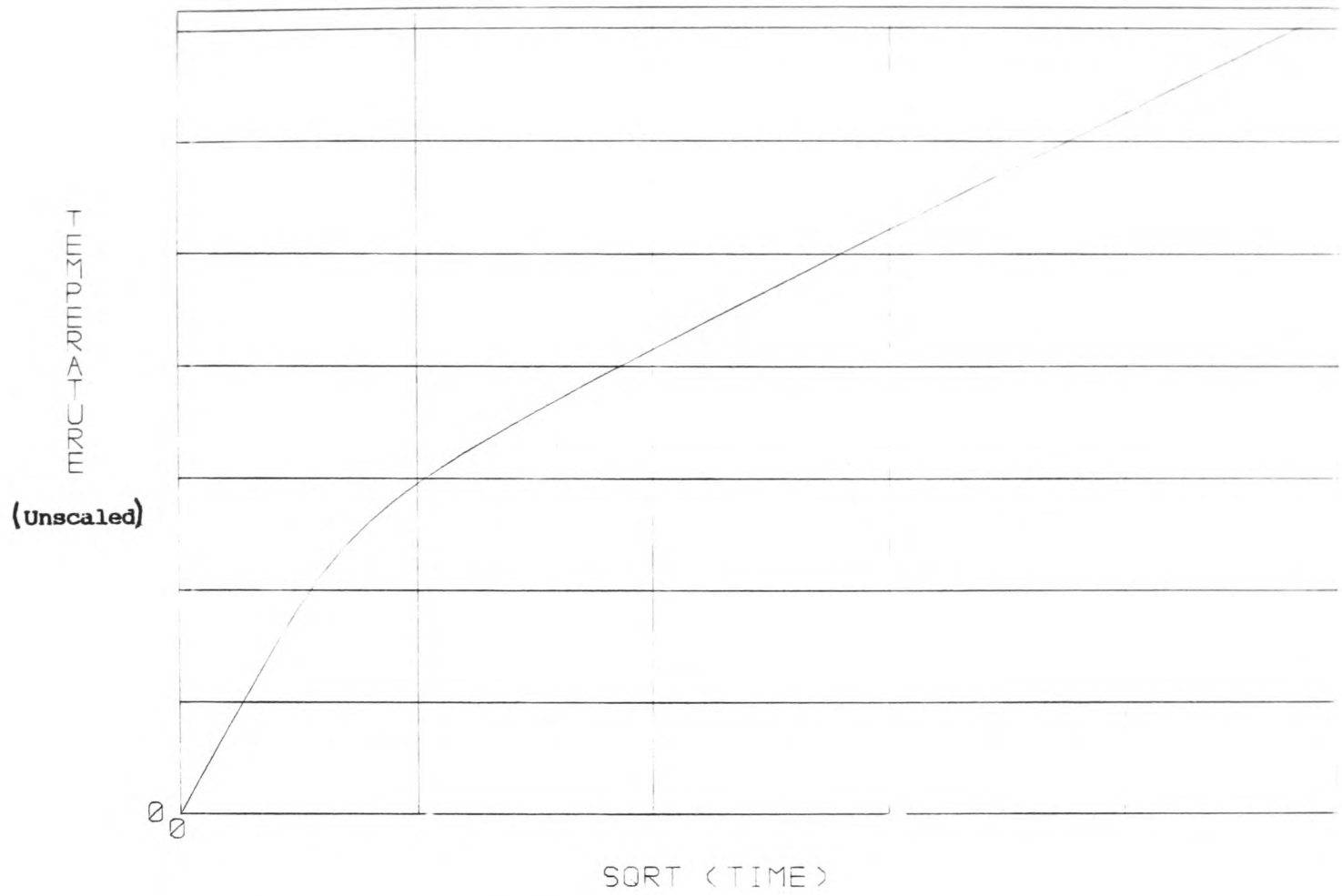

FIG. 4.3 Typical predicted surface temperature response for thin film gauge on two-layered substrate, to a step in surface heat transfer rate.

FIG. 4.4

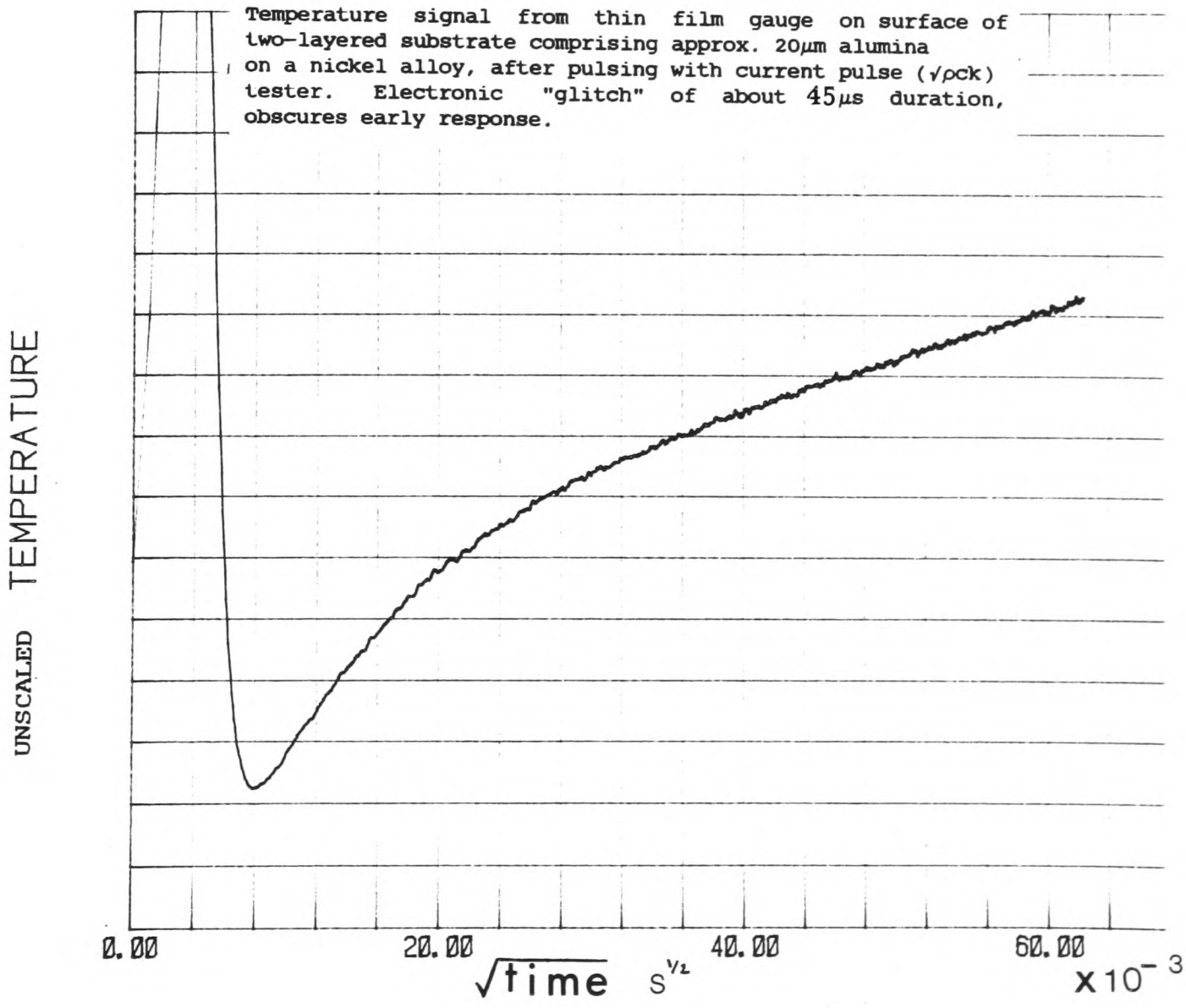

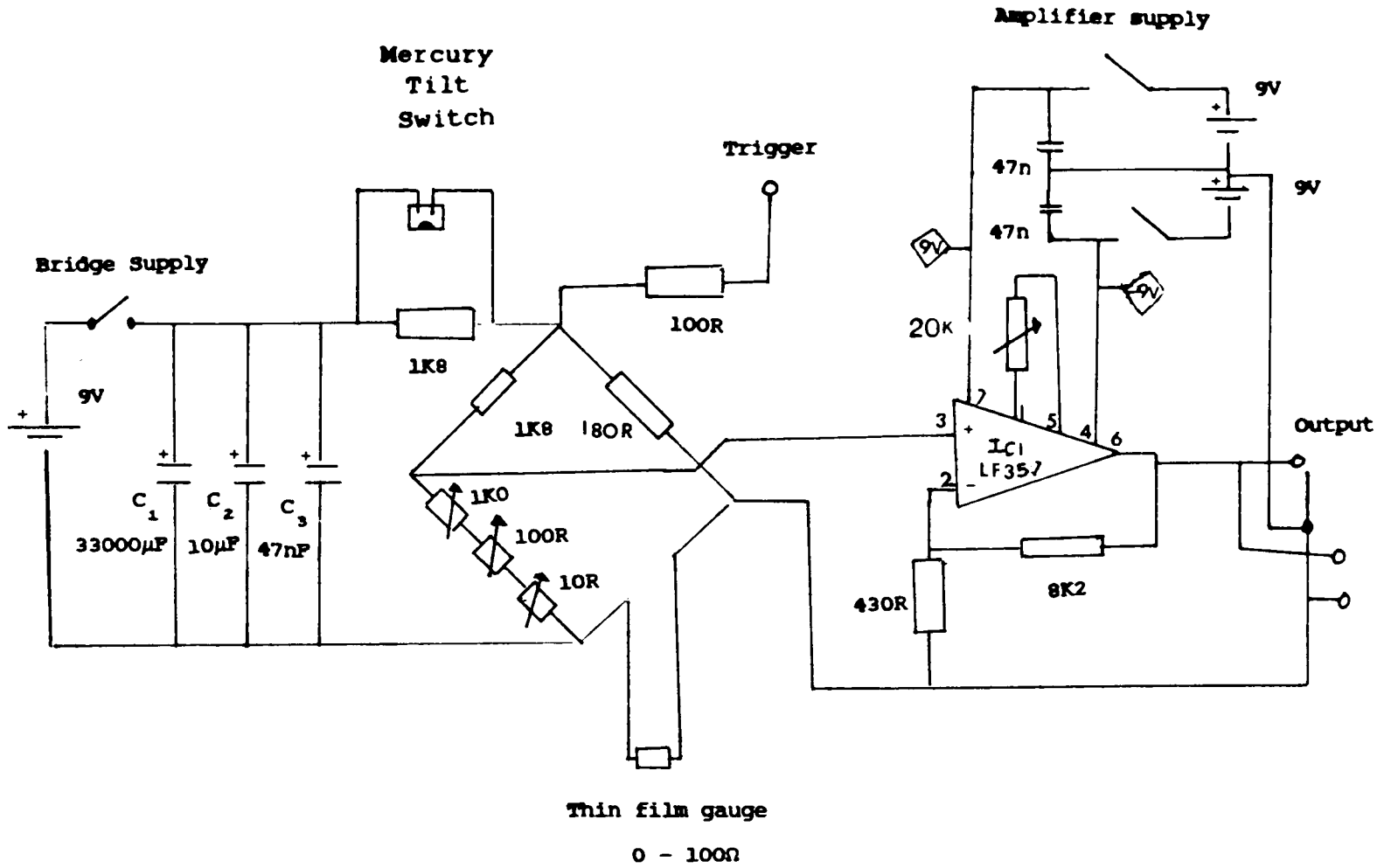

FIG. 4.5 Fast response √(ρck) circuit.

2-D Temperature for 2mm Film

2-D temperature for 1mm Film

1-D temperature on machineable glass ceramic

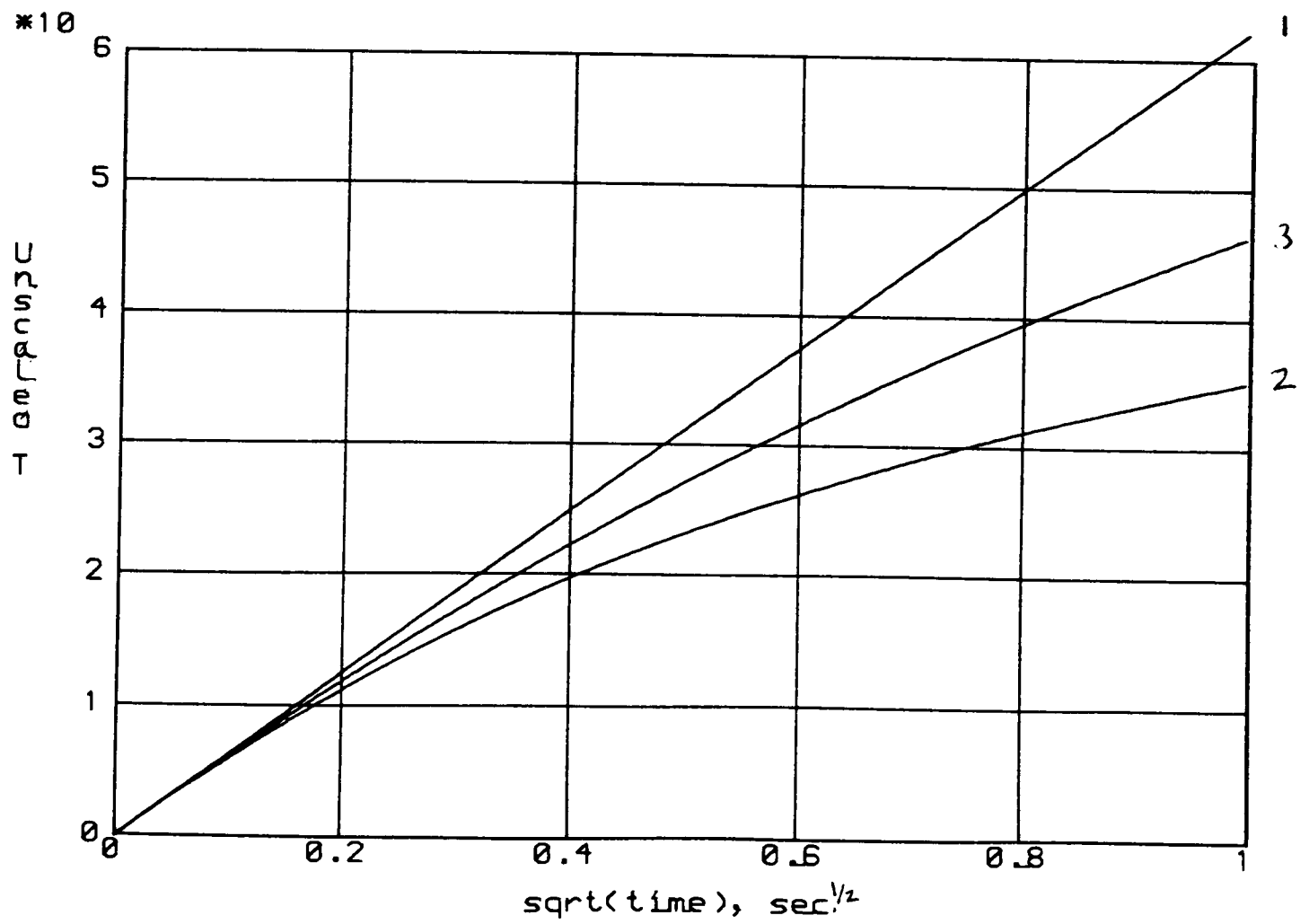

FIG. 4.6 1-d surface temperature for film on machineable glass. 1
2-d surface temperature, film width 1mm 2
2-d surface temperature, film width 2mm. 3

FIG. 4.7 Mean film temperature for 2mm wide film nickel.

- High accuracy explicit scheme: H = 2.7e-2, 9 pts cover film half-width
O Exact analytical solution.

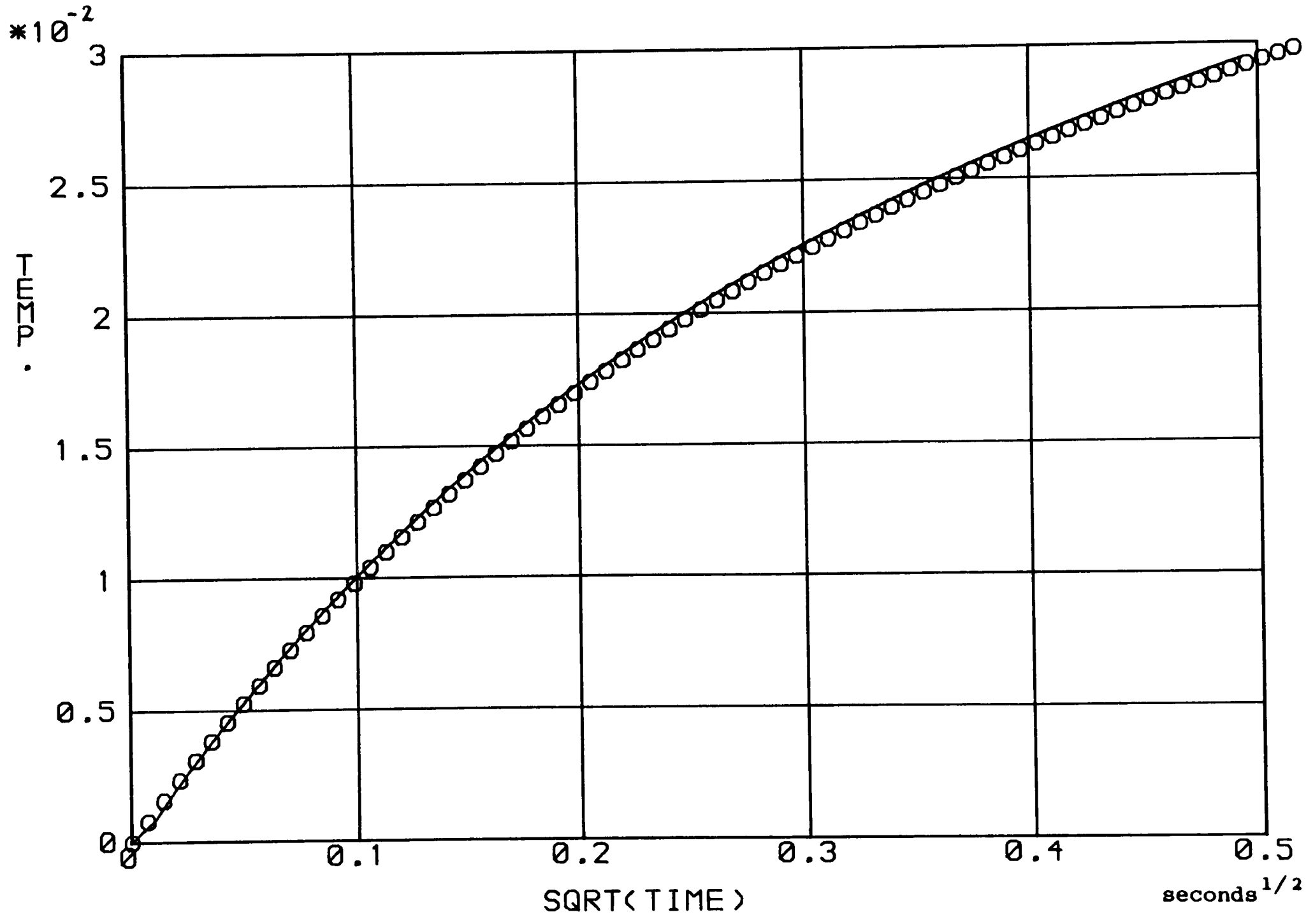

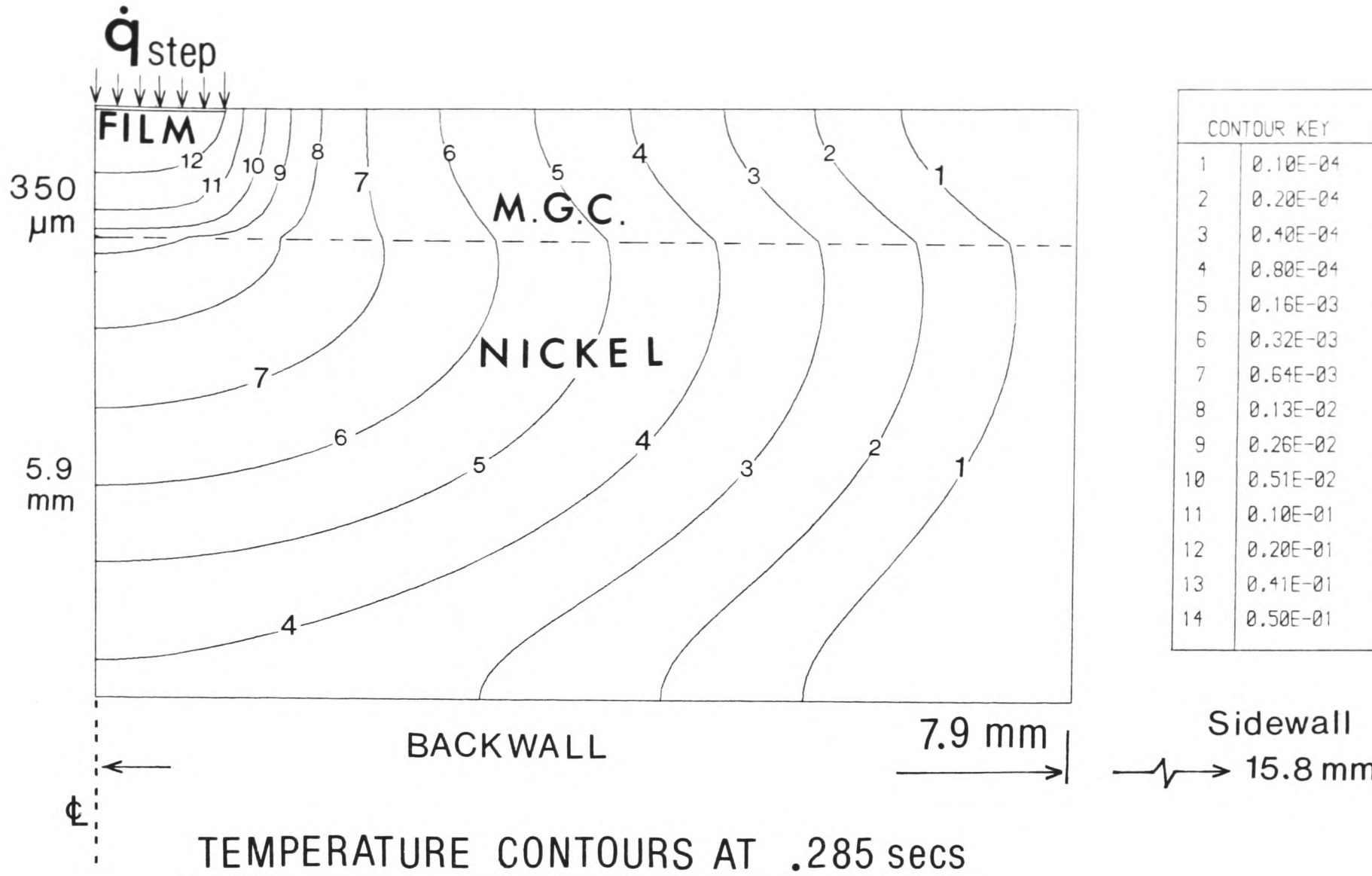

TEMPERATURE CONTOURS AT .285 secs

Fig. 4.8

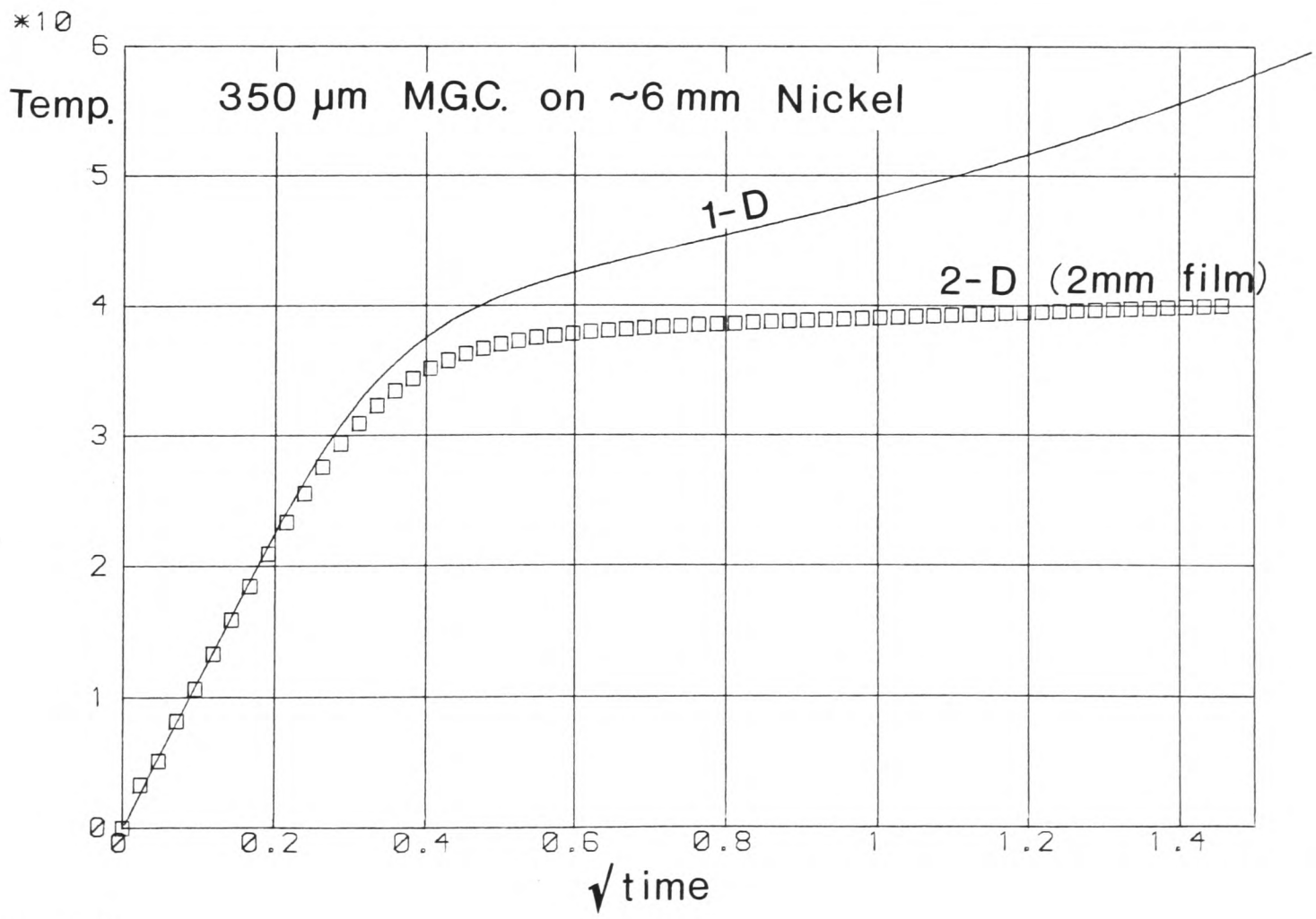

Fig. 4.9

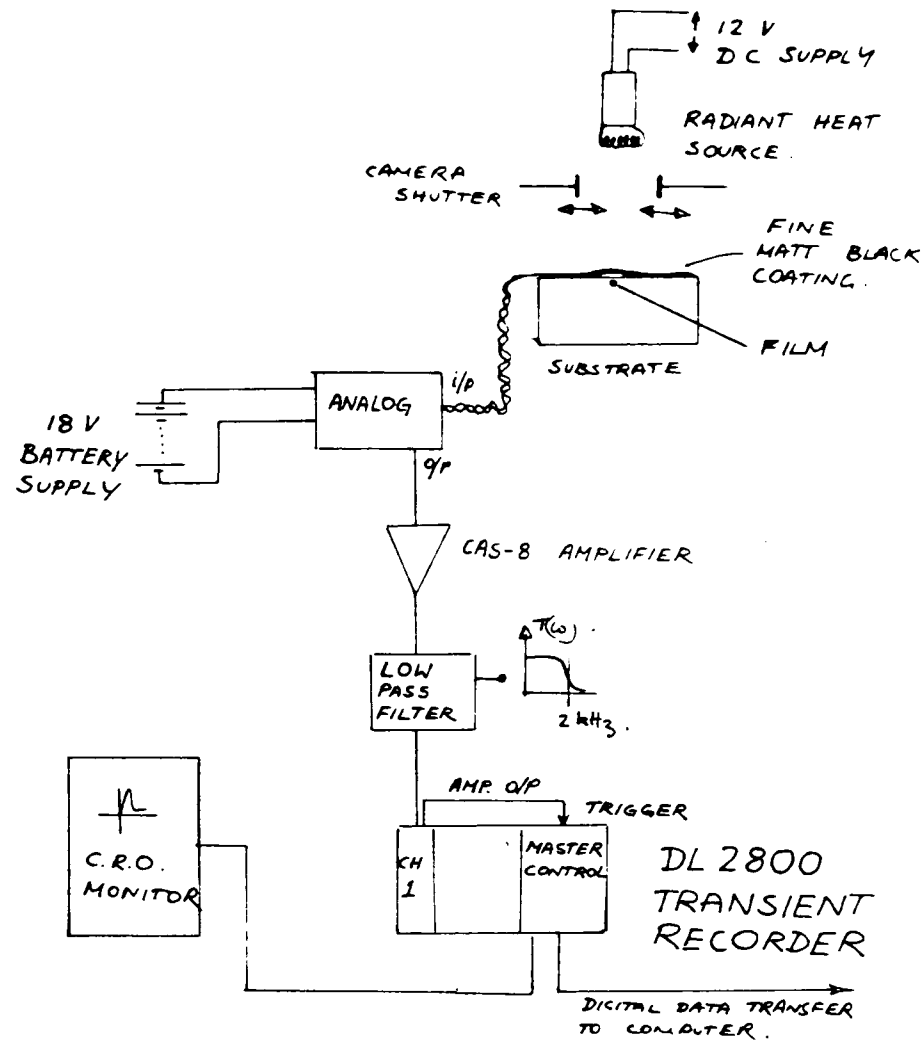

FIG. 4.10 Radiant heating system.

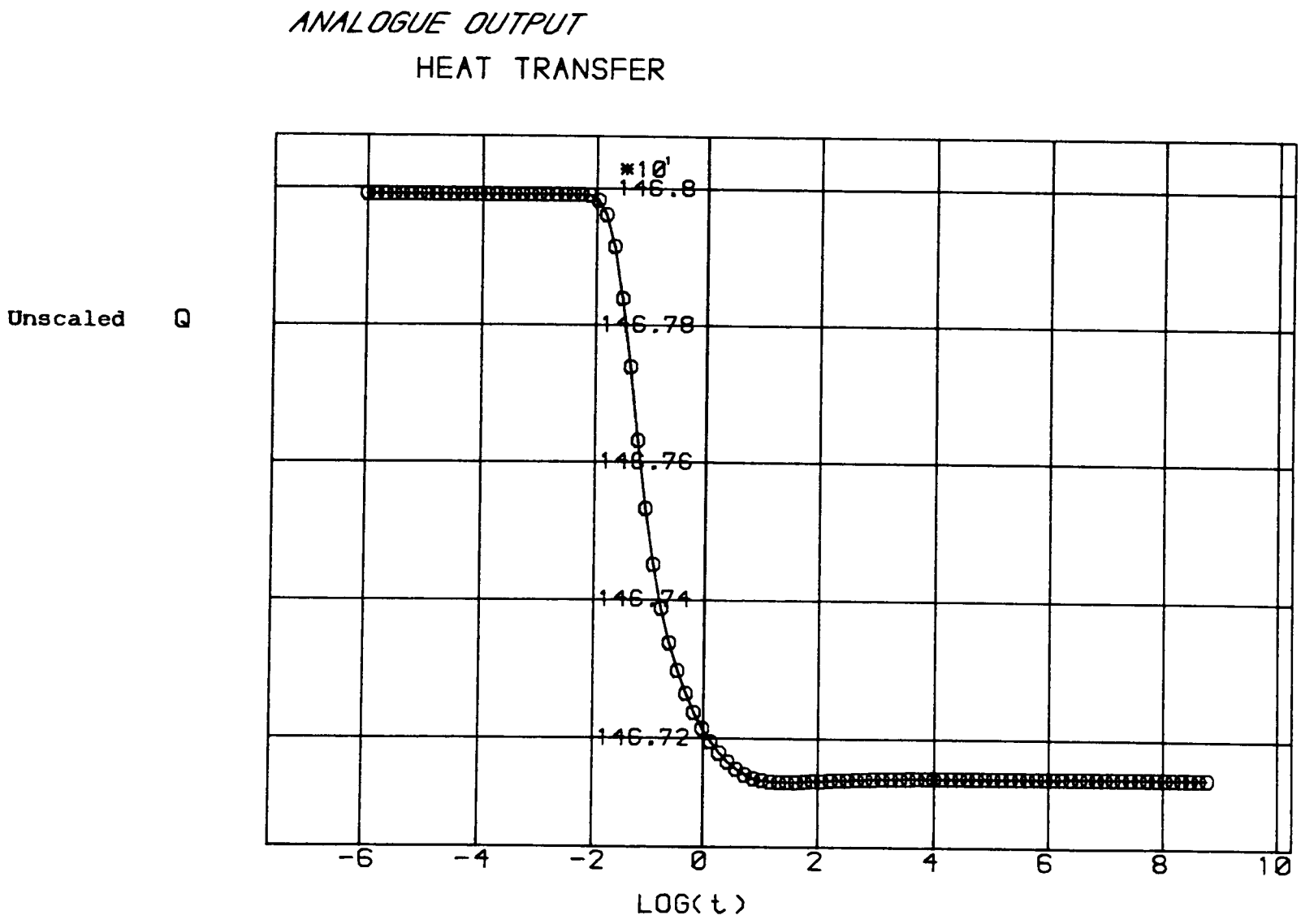

FIG. 4.11 Predicted analogue output signal from radiant testing of film on two-layered substrate.

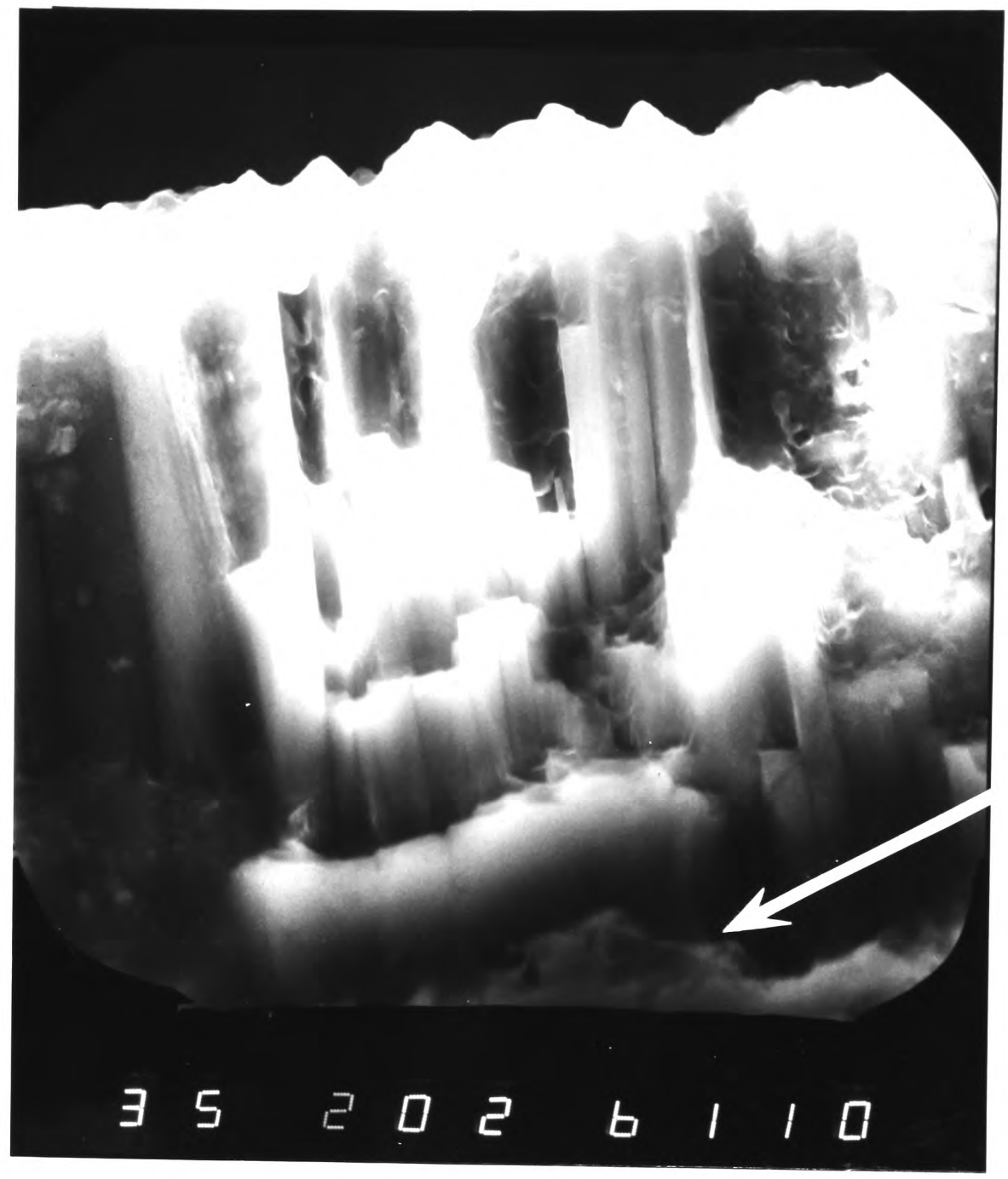

FIG. 5.1 Electron micrograph of a cross section of a painted film, on a substrate comprising 20μm alumina on a nickel based turbine alloy. Magnification 4000 x

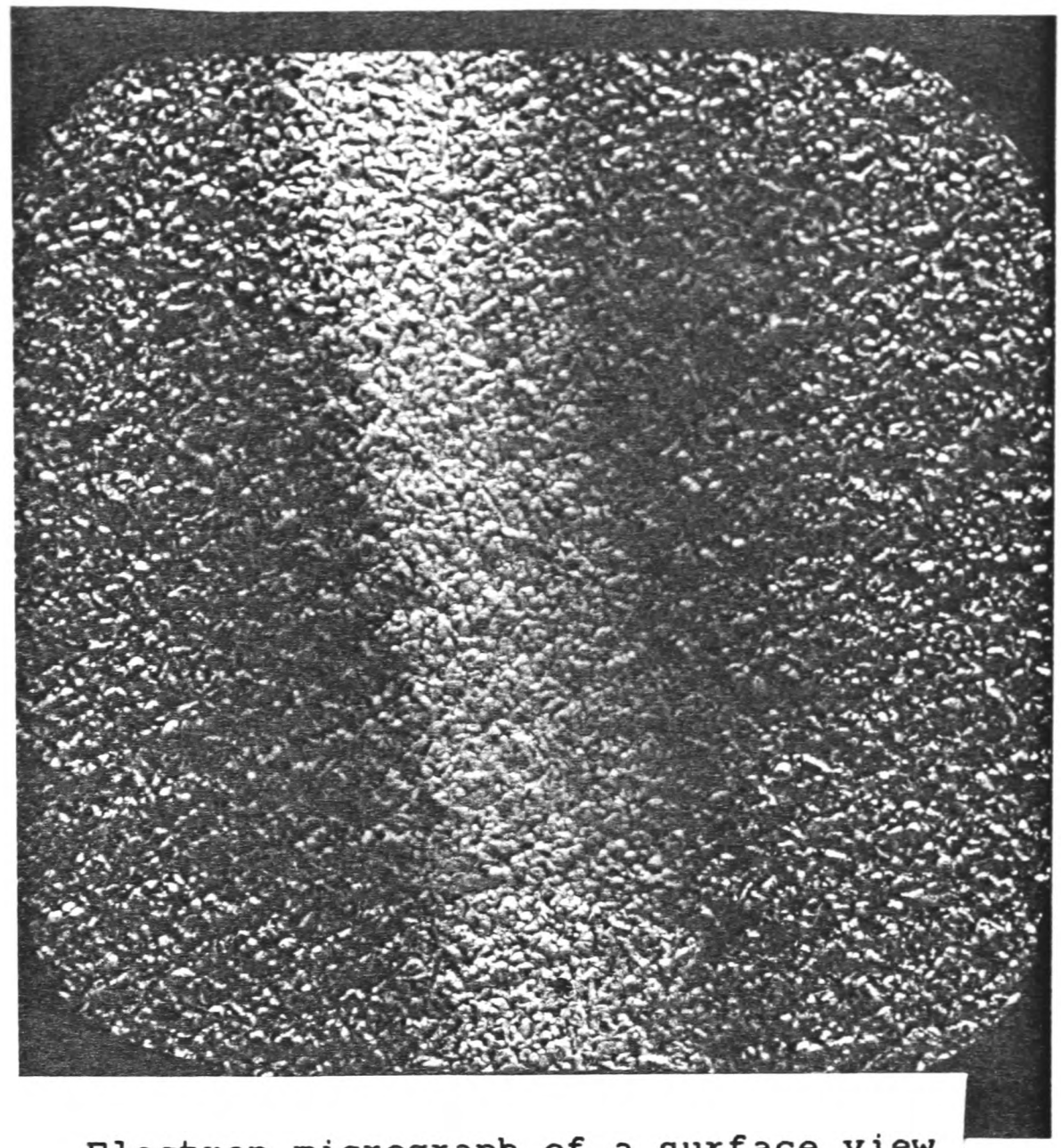

FIG. 5.2a Electron micrograph of a surface view of a painted film on alumina, magnification 50 x.

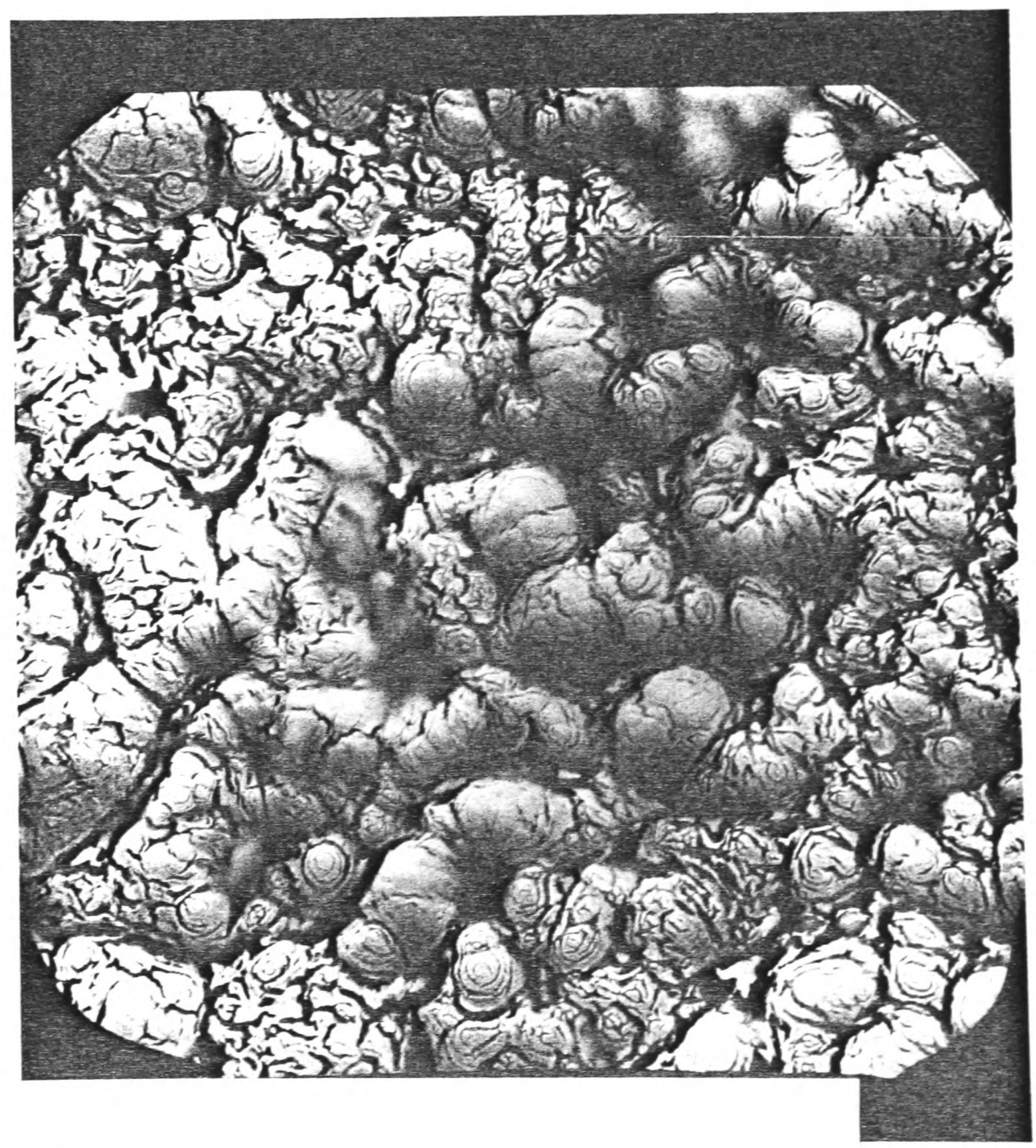

FIG. 5.2b Surface view of film, magnification 2000 x.

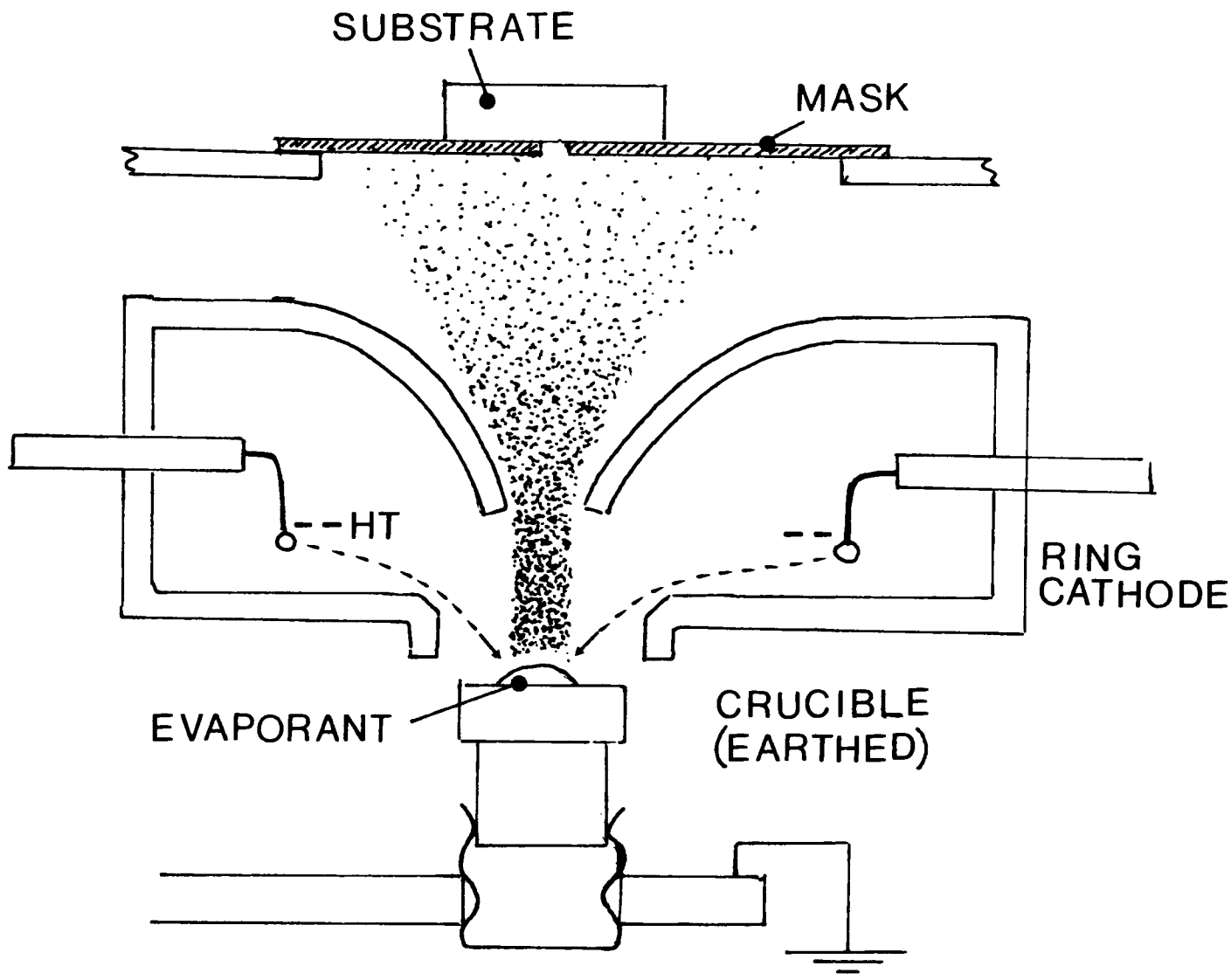

FIG. 5.3 Schematic of evaporation unit.

The evaporator has a circular refractory metal cathode, which is held at a high negative potential, enclosed in a stainless steel, geometrically designed case. This gives a fixed-focus position for the electrons emitted from the cathode, which are accelerated by the potential difference between it and the earthed crucible containing the evaporant. The filament is heated and the evaporation rate is adjusted by regulating the accelerating potential and filament current to control electron emission.

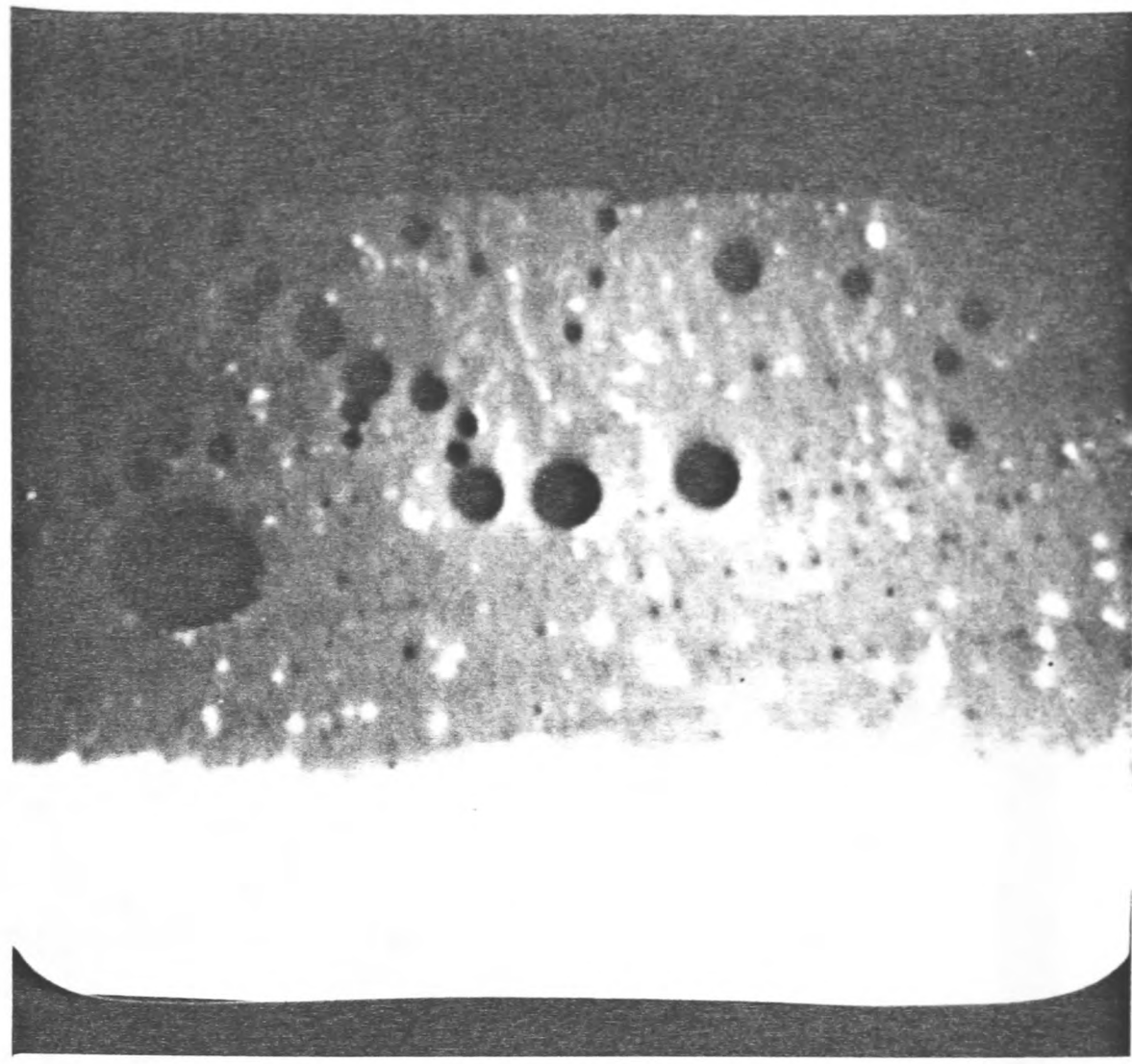

FIG. 5.4 Photograph from optical microscope of cross section of a substrate comprising vitreous enamel on mild steel, magnification 500 x.

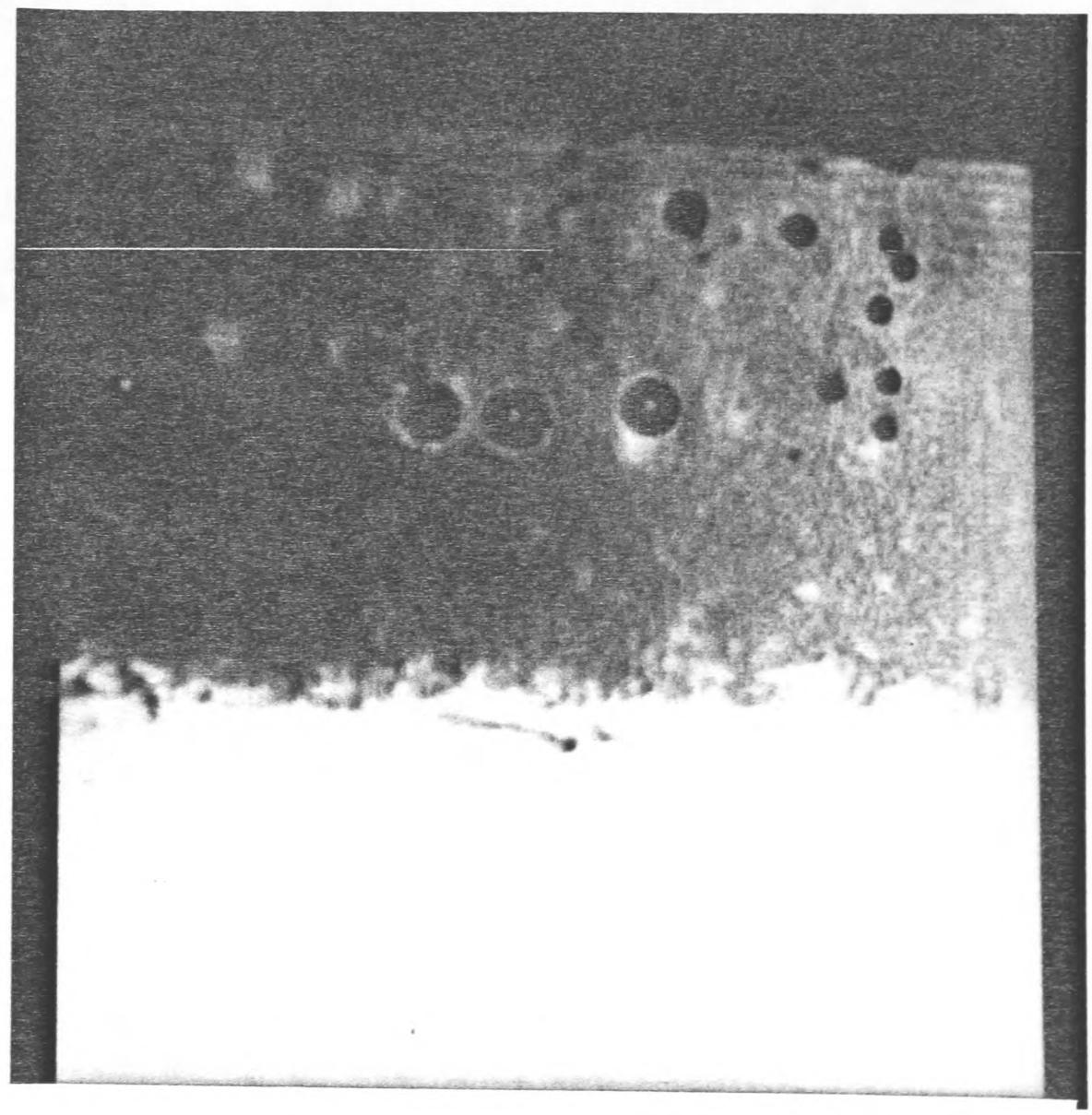

FIG 5.5 Acoustic micrograph, microscope operating frequency of 370MHz, of cross section of vitreous enamel on steel, at focus of enamel magnification 500x.

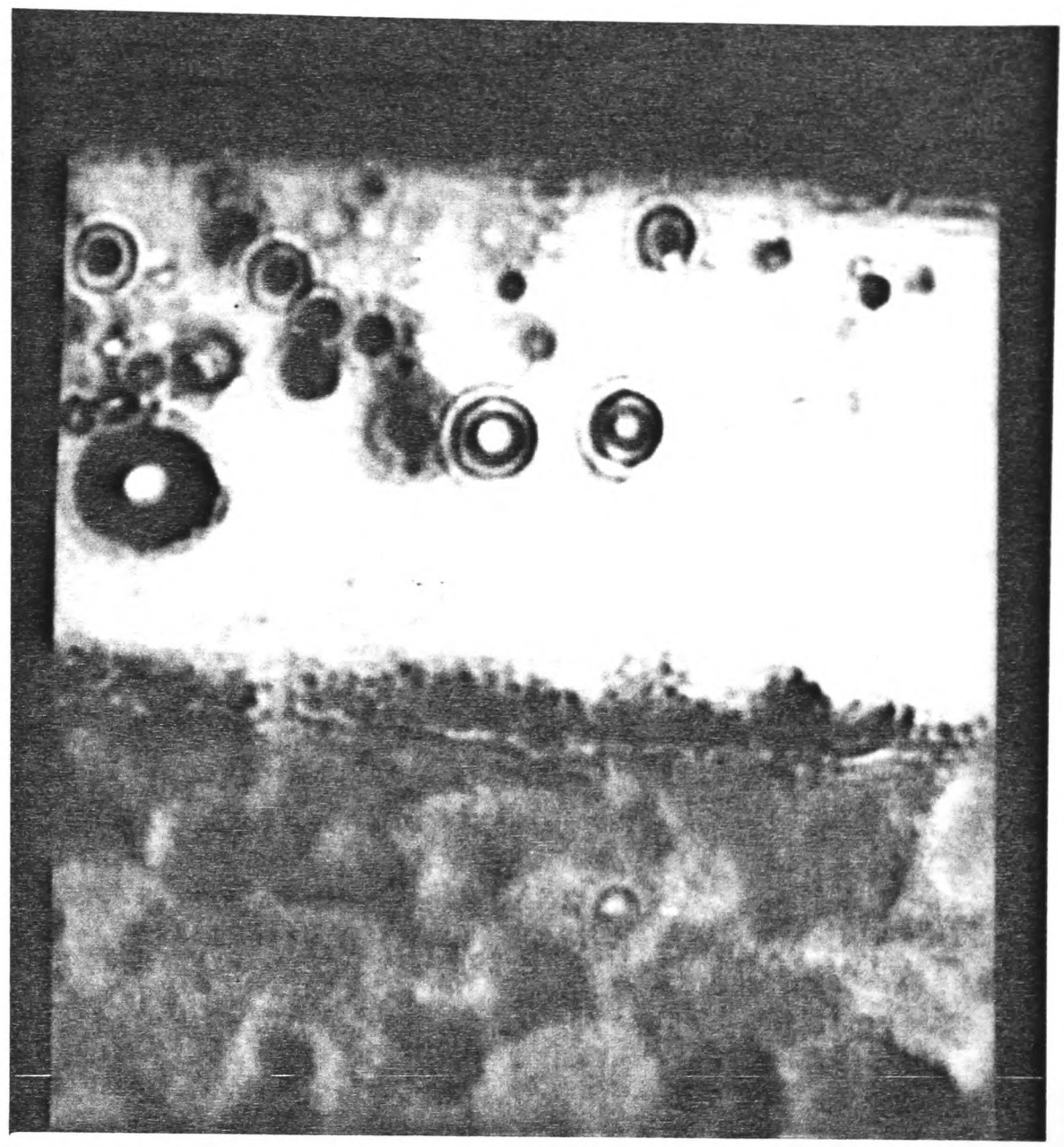

FIG 5.6 Acoustic micrograph, at 10μm defocus, magnification 500x showing enamel-steel interface and grain boundaries in steel.

FIG 5.7 Central enamelled section of mild steel cylinder, with painted platinum film and tags.

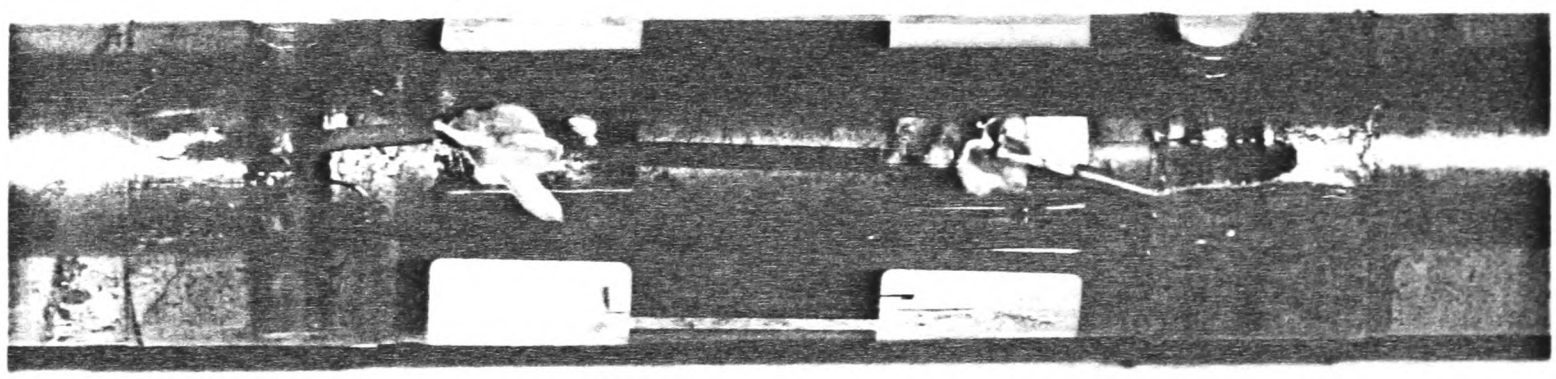

FIG 5.8 Kapton covered section of mild steel cylinder with evaporated gold films.

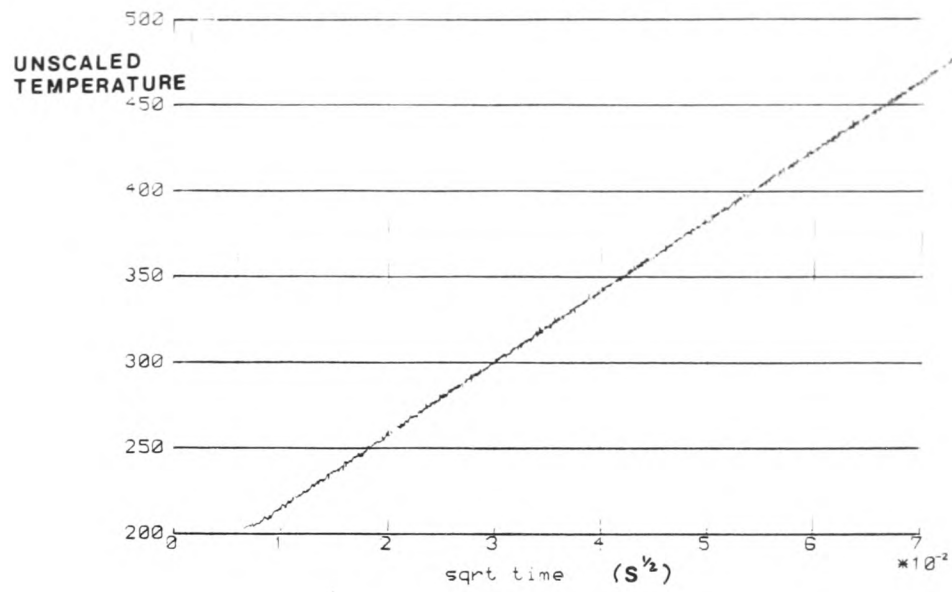

6.1a **Temperature response in air, of film on machineable glass against √time.**

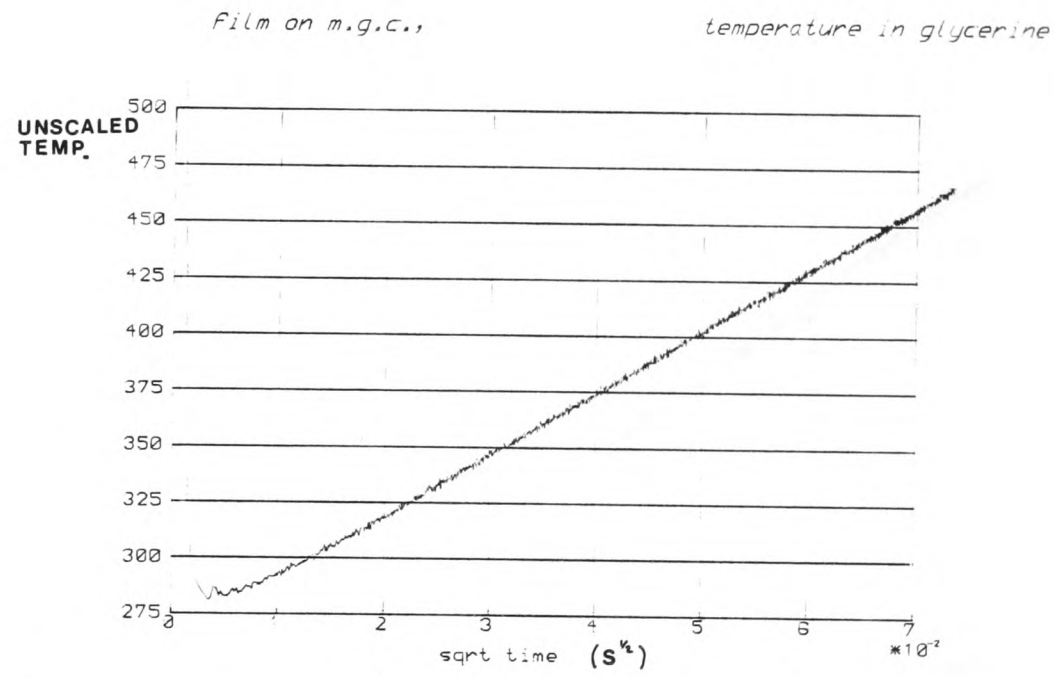

6.1b **Temperature response in glycerine, of film on machineable glass.**

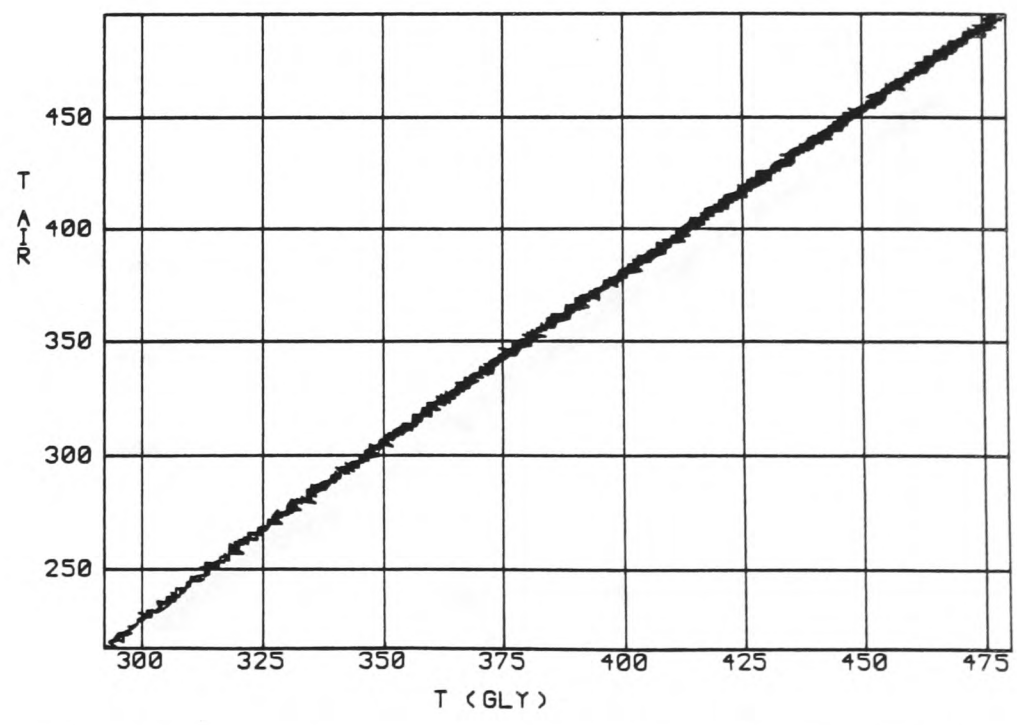

6.2 *Temperature in air versus temperature in glycerine for M.G.C.*

FIG 6.3a

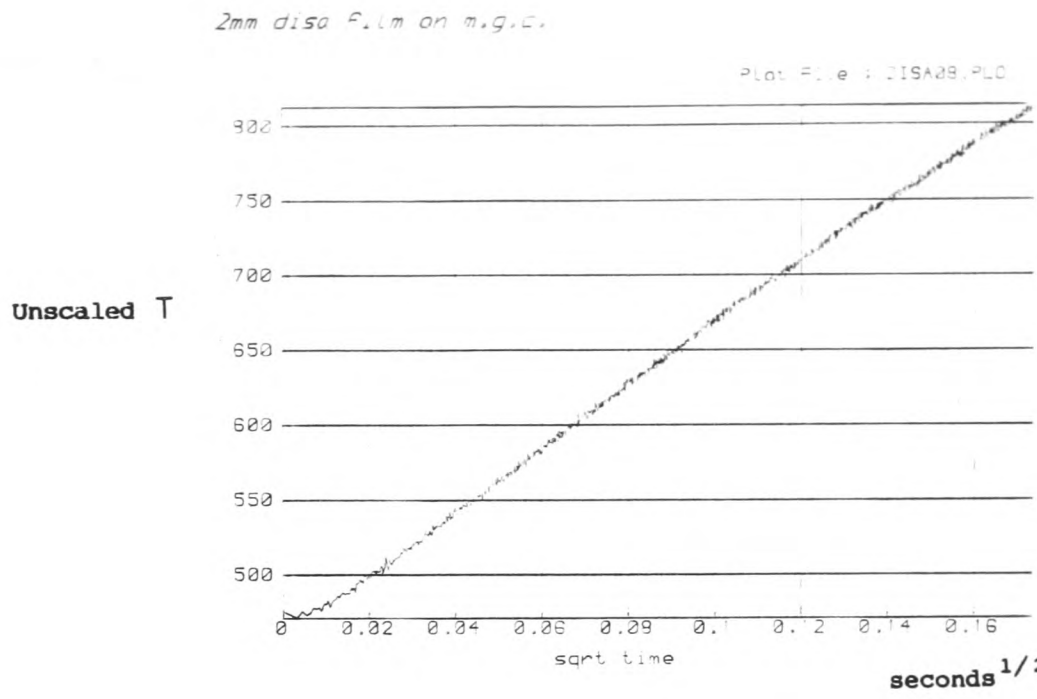

6.3 b

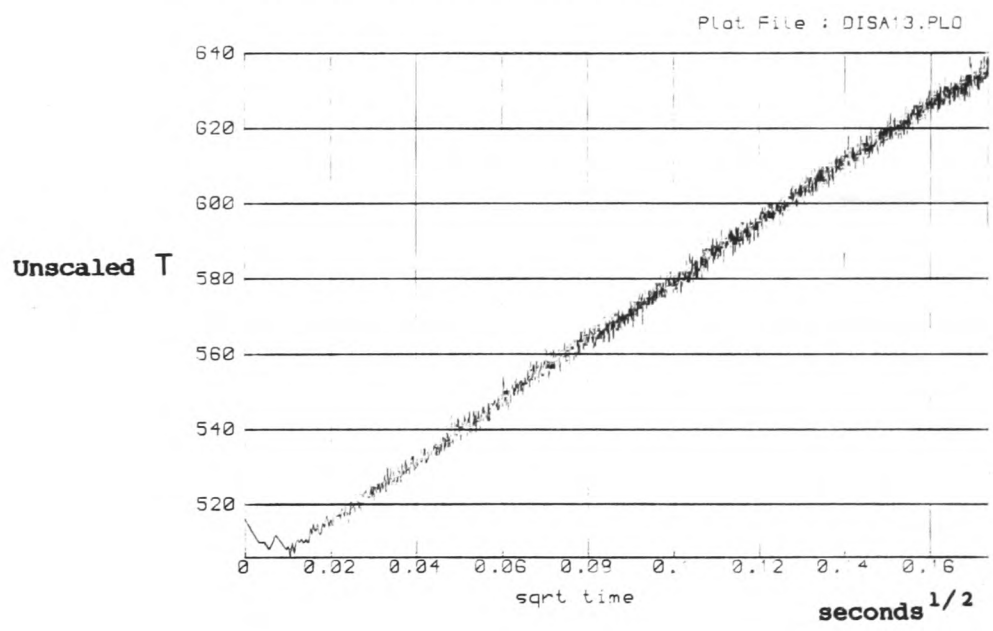

6.4

Temperature in air versus temperature in glycerine

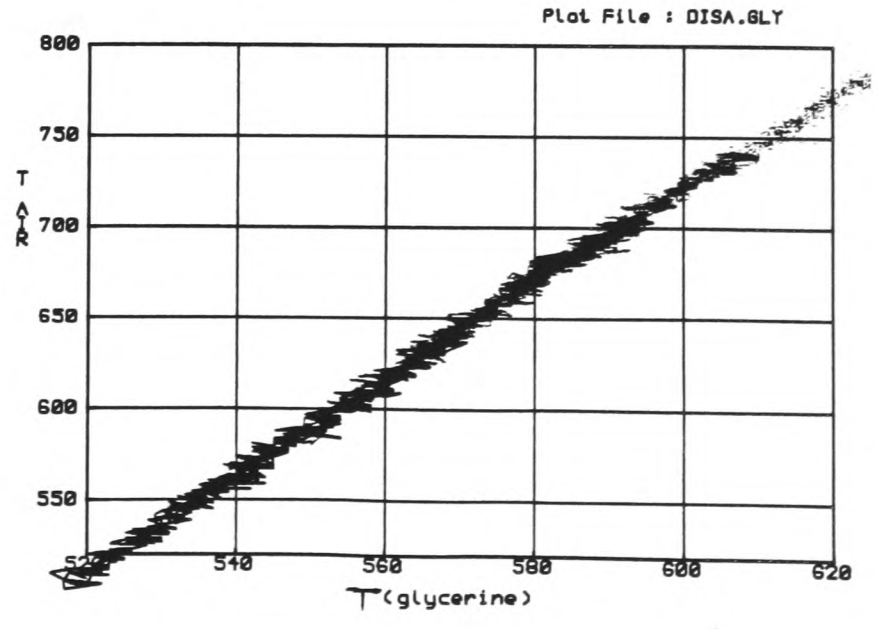

FIG. 6.5 **Surface temperature response from a 2mm film on a Kapton/machineable glass substrate.**

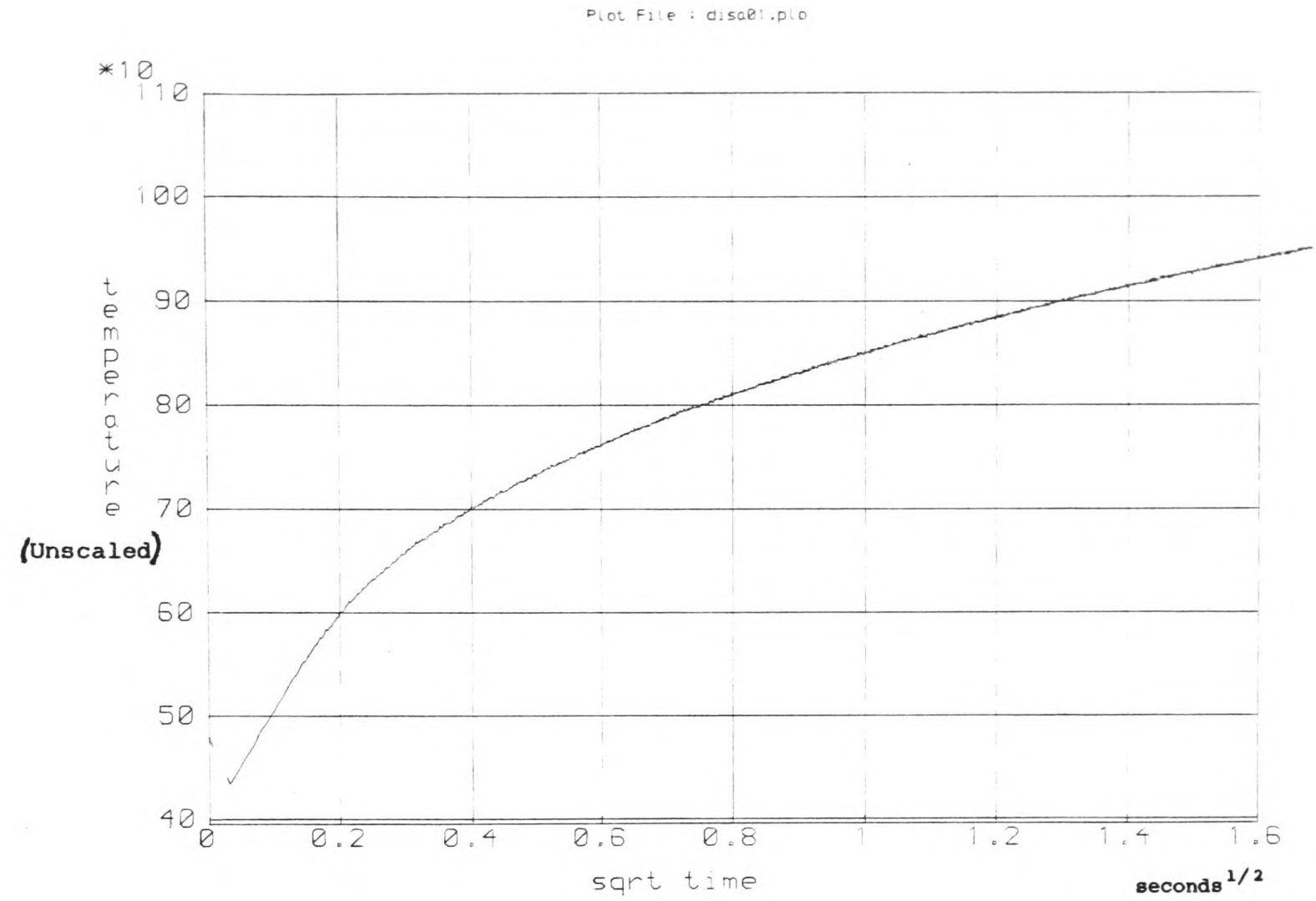

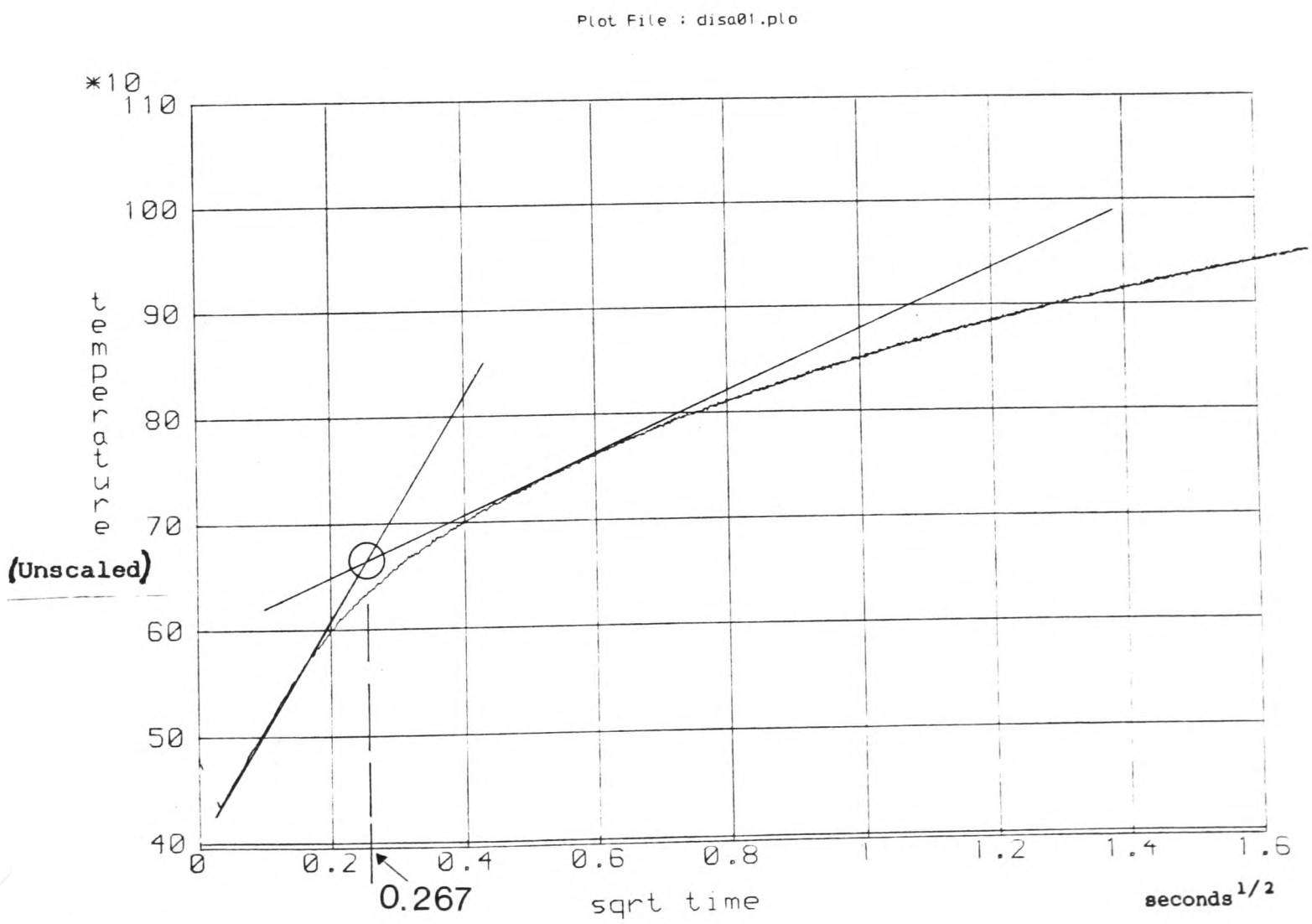

FIG. 6.6 **Application of calibration procedure.**

DISA FILM, 2MM wide on 75um kapton on m.g.c.

⊖⊖⊖ 1-D ANALYTIC SOLN.

□□□ 2-D NUMERICAL SOLN.

——— MEASURED RESPONSE

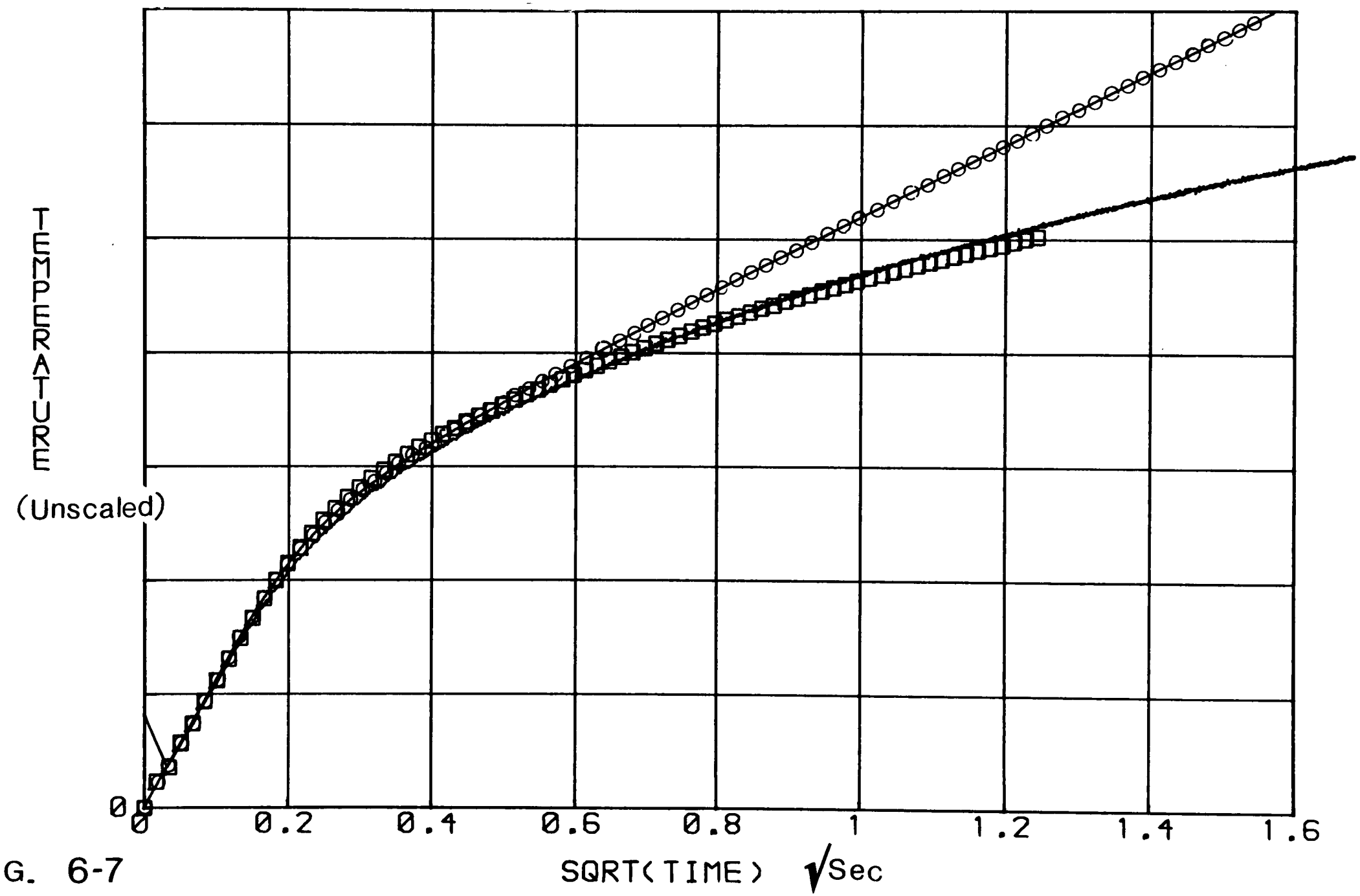

FIG. 6-7

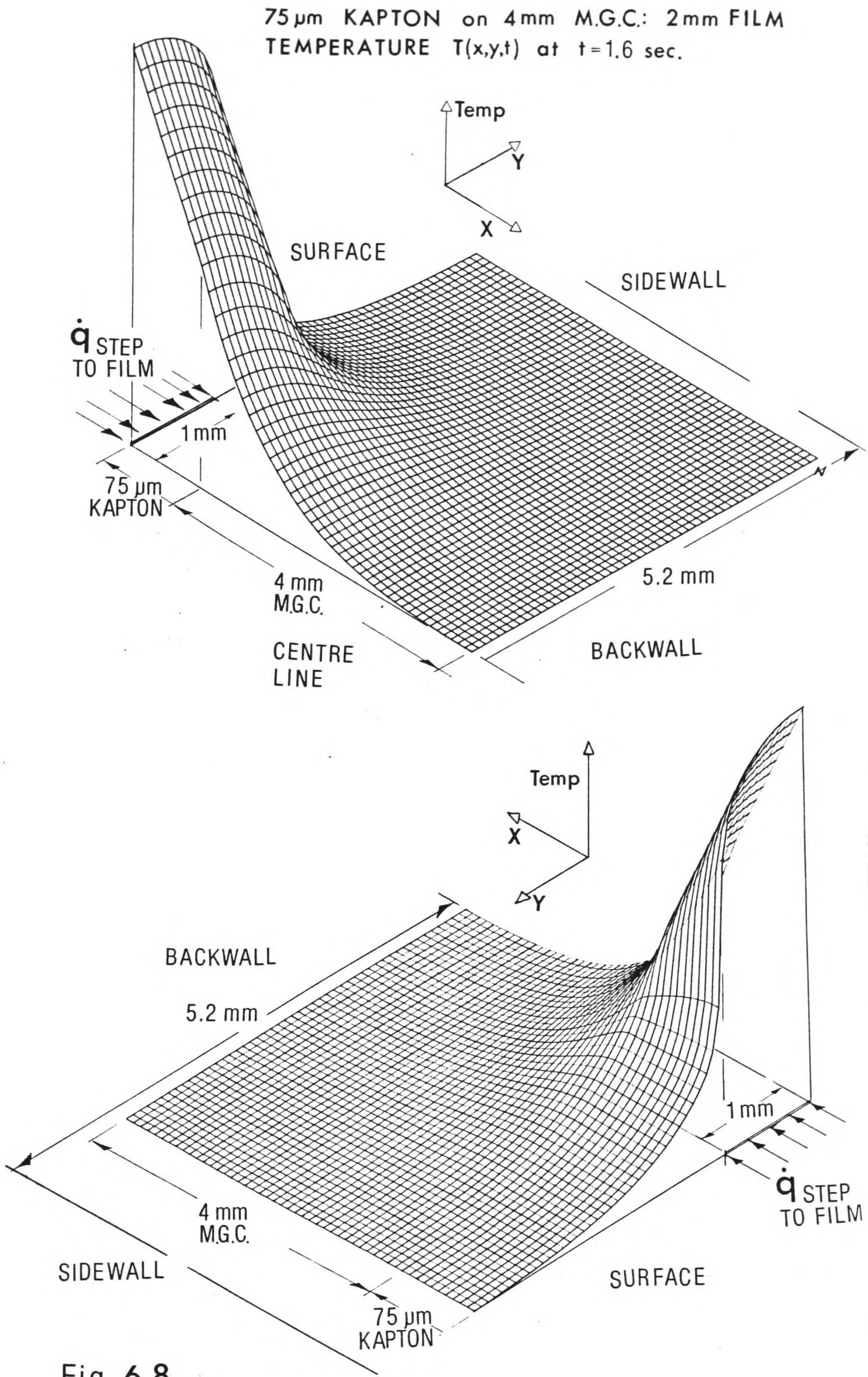
75 μm KAPTON on 4mm M.G.C.: 2mm FILM
TEMPERATURE T(x,y,t) at t=1.6 sec.
Temp
Y
X
SURFACE
SIDEWALL
q̇ STEP TO FILM
1 mm
75 μm KAPTON
4 mm M.G.C.
CENTRE LINE
5.2 mm
BACKWALL
Temp
X
Y
BACKWALL
5.2 mm
1 mm
q̇ STEP TO FILM
4 mm M.G.C.
SIDEWALL
75 μm KAPTON
SURFACE

Fig. 6.8

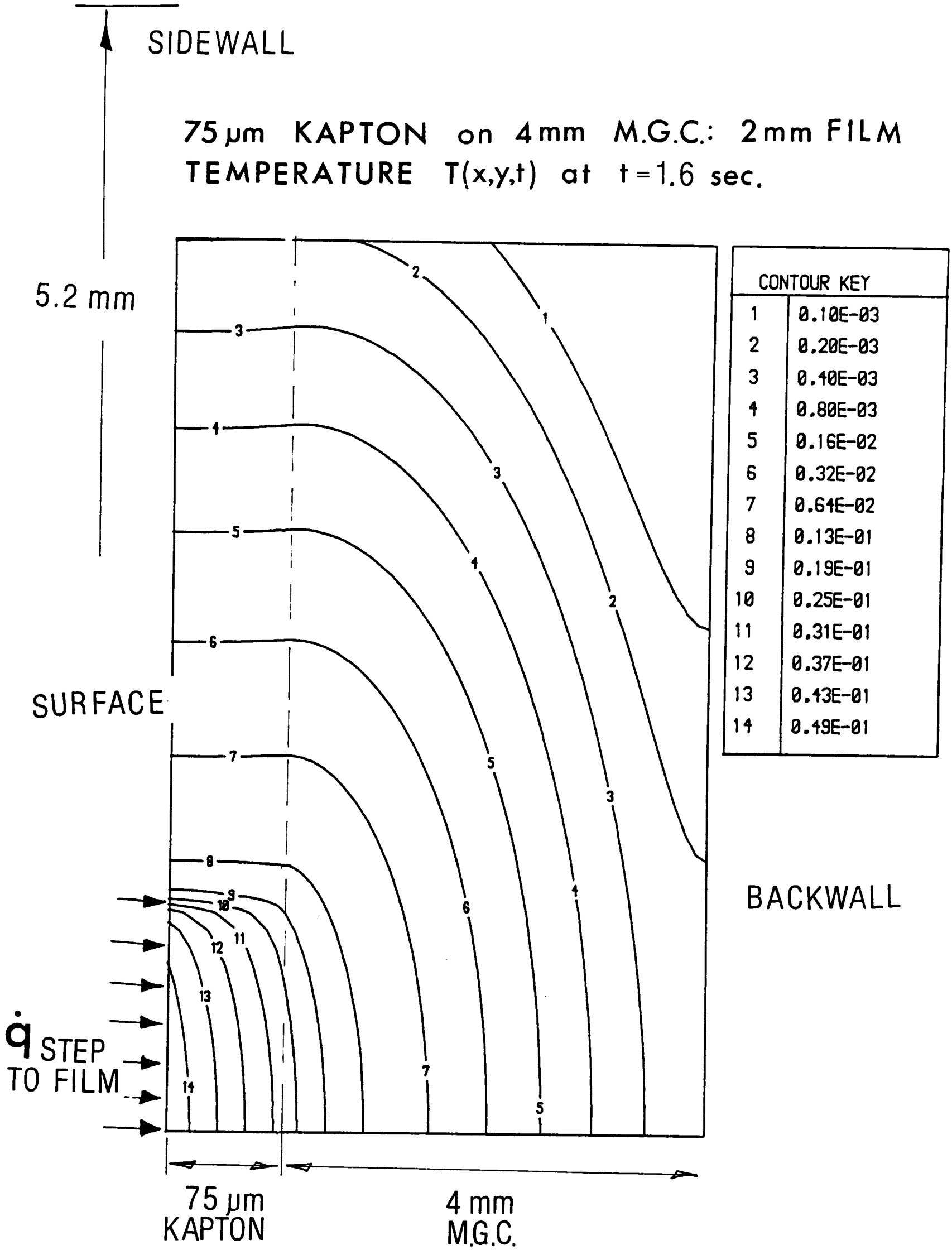
SIDEWALL
75 μm KAPTON on 4 mm M.G.C.: 2 mm FILM
TEMPERATURE T(x,y,t) at t = 1.6 sec.
5.2 mm
SURFACE
CONTOUR KEY
1 0.10E-03
2 0.20E-03
3 0.40E-03
4 0.80E-03
5 0.16E-02
6 0.32E-02
7 0.64E-02
8 0.13E-01
9 0.19E-01
10 0.25E-01
11 0.31E-01
12 0.37E-01
13 0.43E-01
14 0.49E-01
BACKWALL
q̇ STEP TO FILM
75 μm KAPTON
4 mm M.G.C.
CENTRE LINE

FIG 6.9

\+ SURFACE TEMPERATURE AT SQRT(TIME) = 0.367 SECS$^{1/2}$

o SURFACE TEMPERATURE AT SQRT(TIME) = 1.29 SEC$^{1/2}$

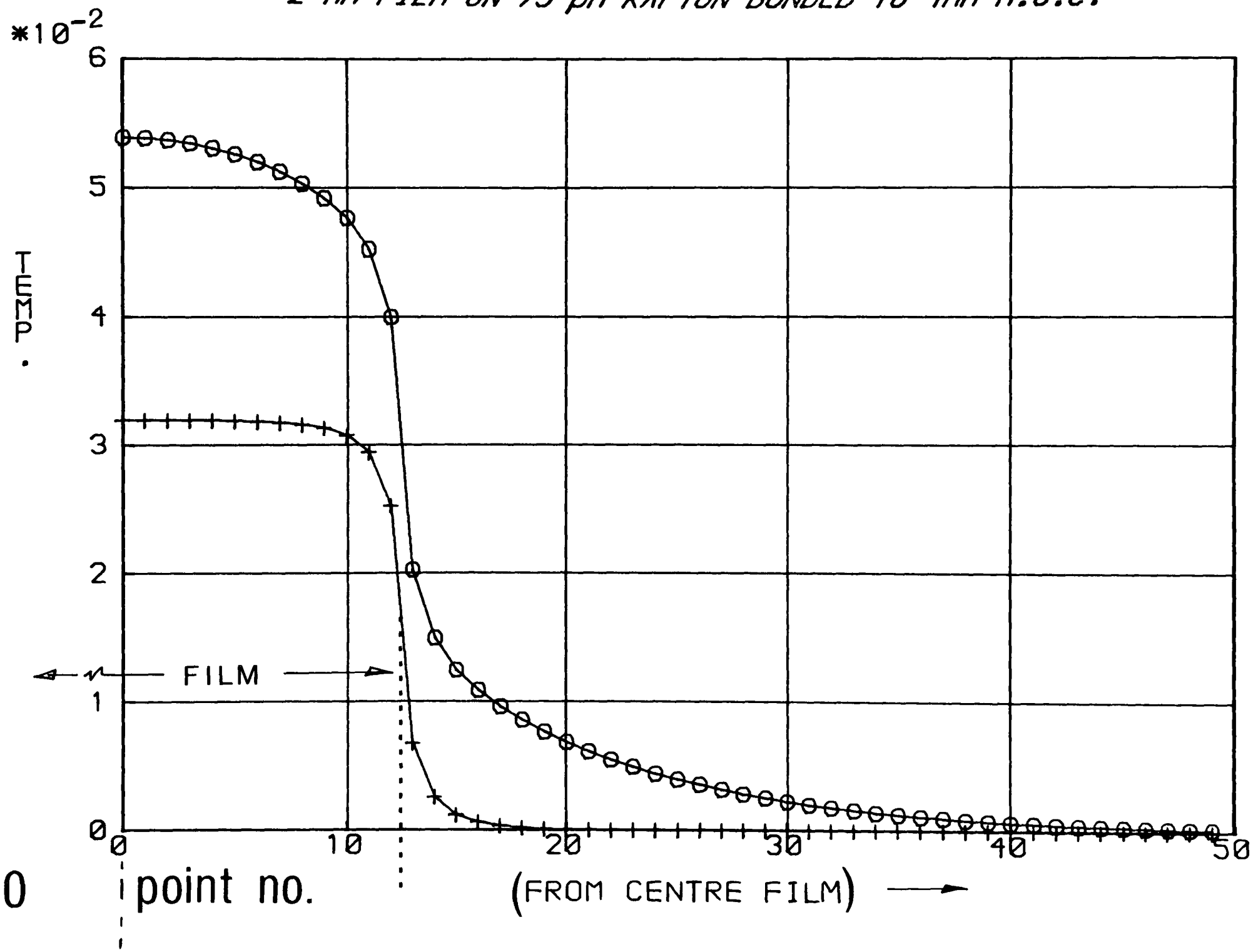

3mm DISA Film on m.g.c.

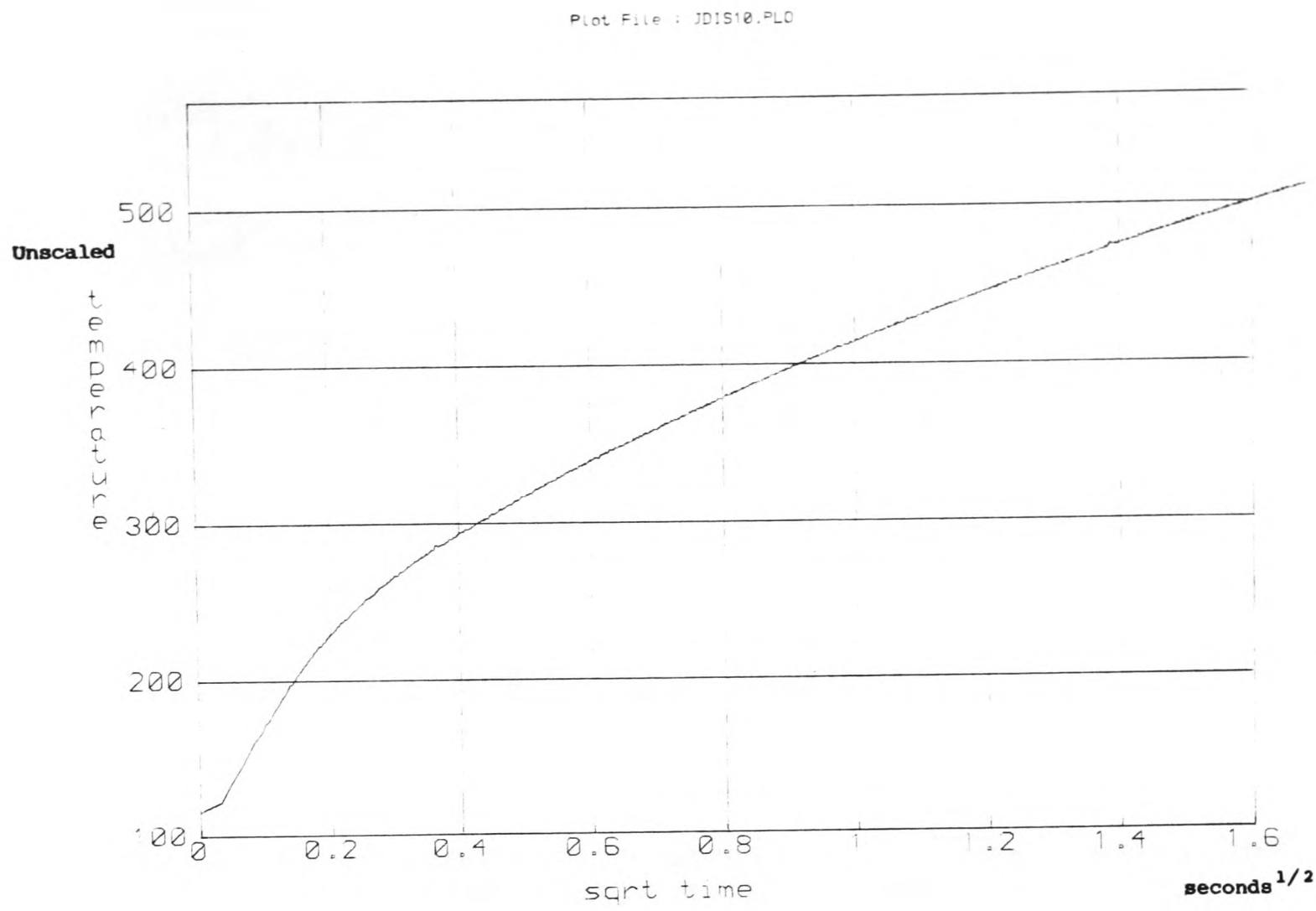

FIG. 6.11 Surface temperature trace from 3mm wide film on substrate comprising 75μm Kapton on machineable glass ceramic.

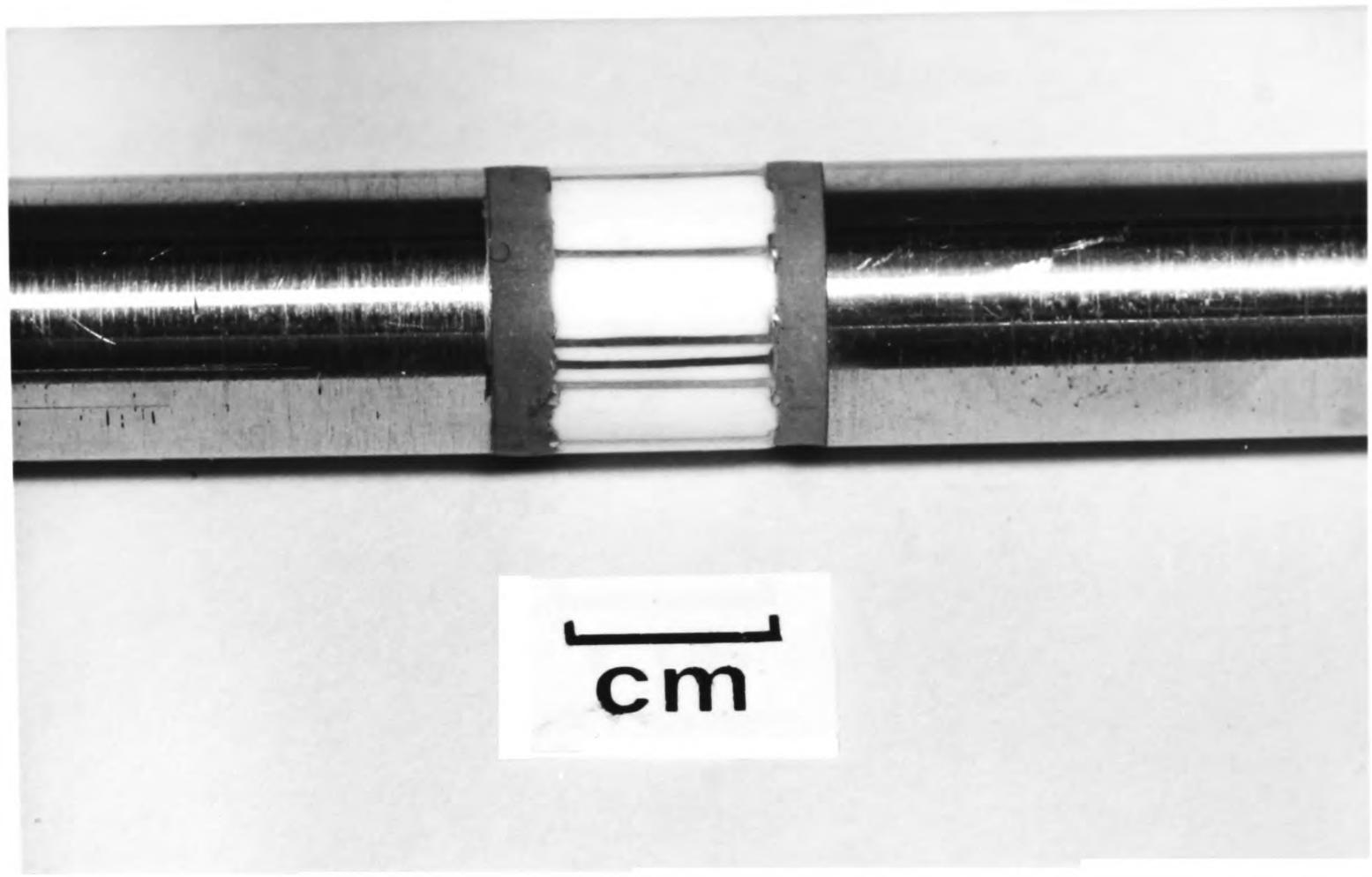

FIG. 6.12 Cylinder with machineable glass insert, and painted platinum thin films.

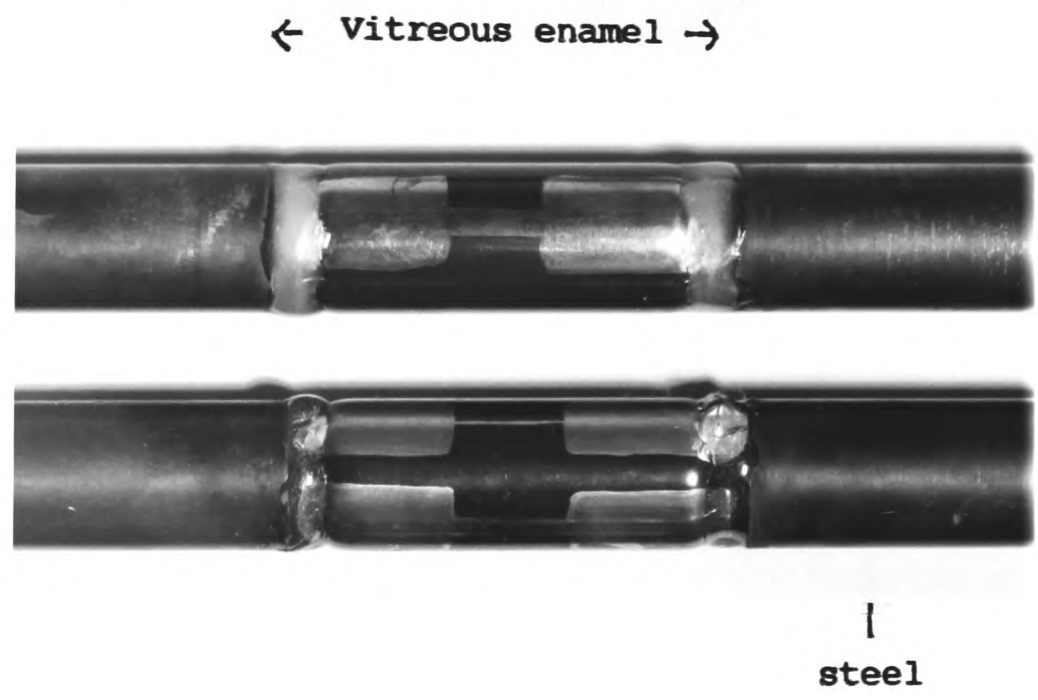

FIG. 6.13a

FIG. 6.13b

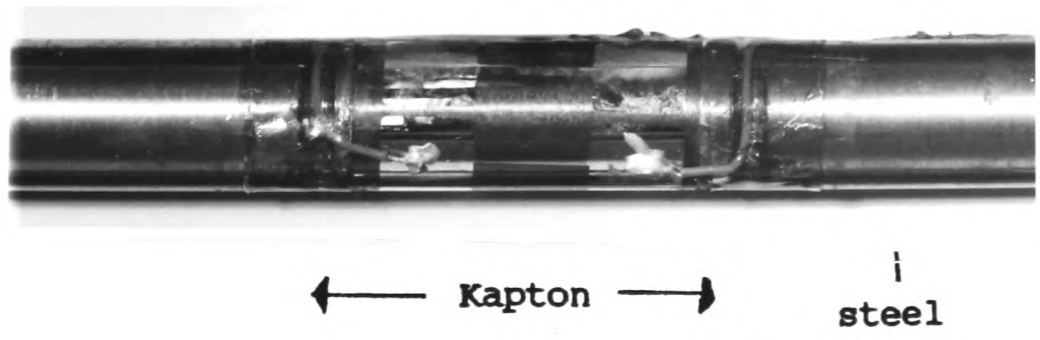

FIG. 6.14

FIG. 6.15a

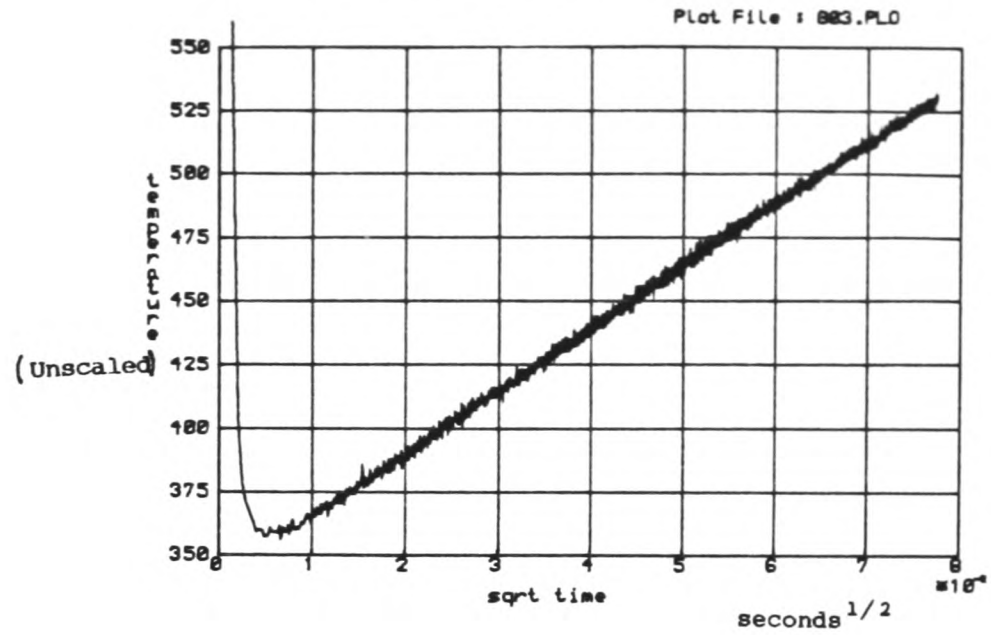

FIG. 6.15b

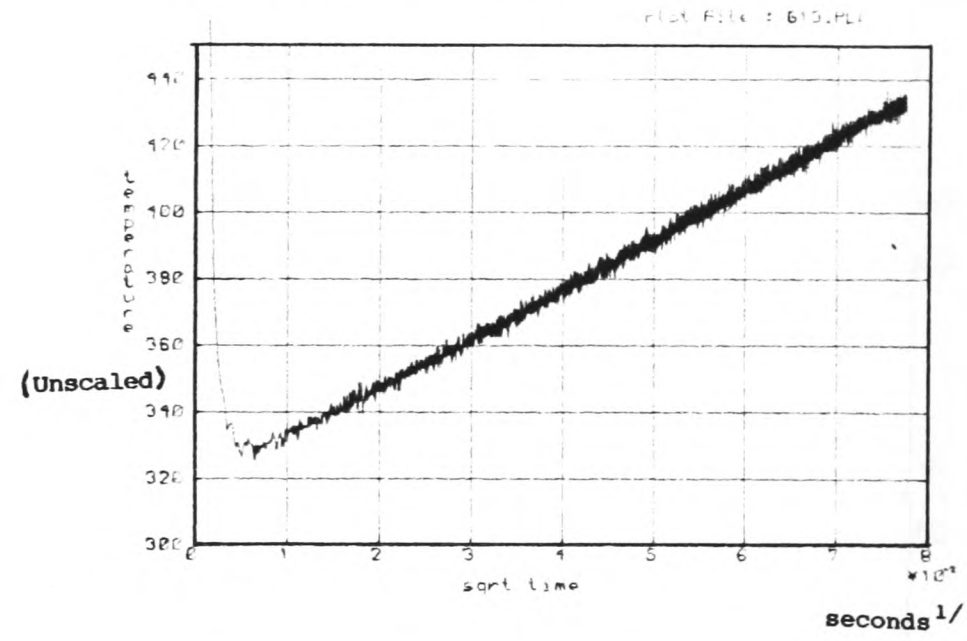

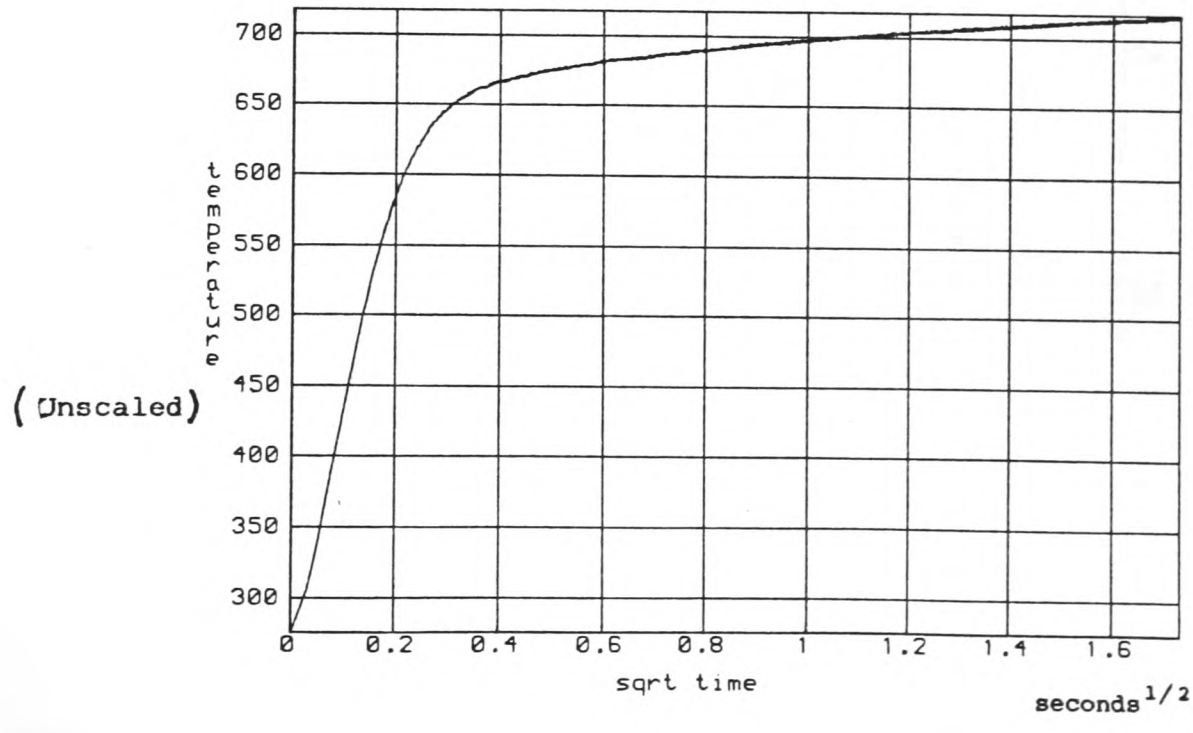

6.16 Surface temperature response for film on enamel/steel cylinder, in air.

KEY

— EXPERIMENTAL CALIBRATION OF FILM ON ENAMEL.

△ EXACT 1-D SEMI-INFINITE SOLUTION.

○ NUMERICAL SOLN.: 2 MM FILM

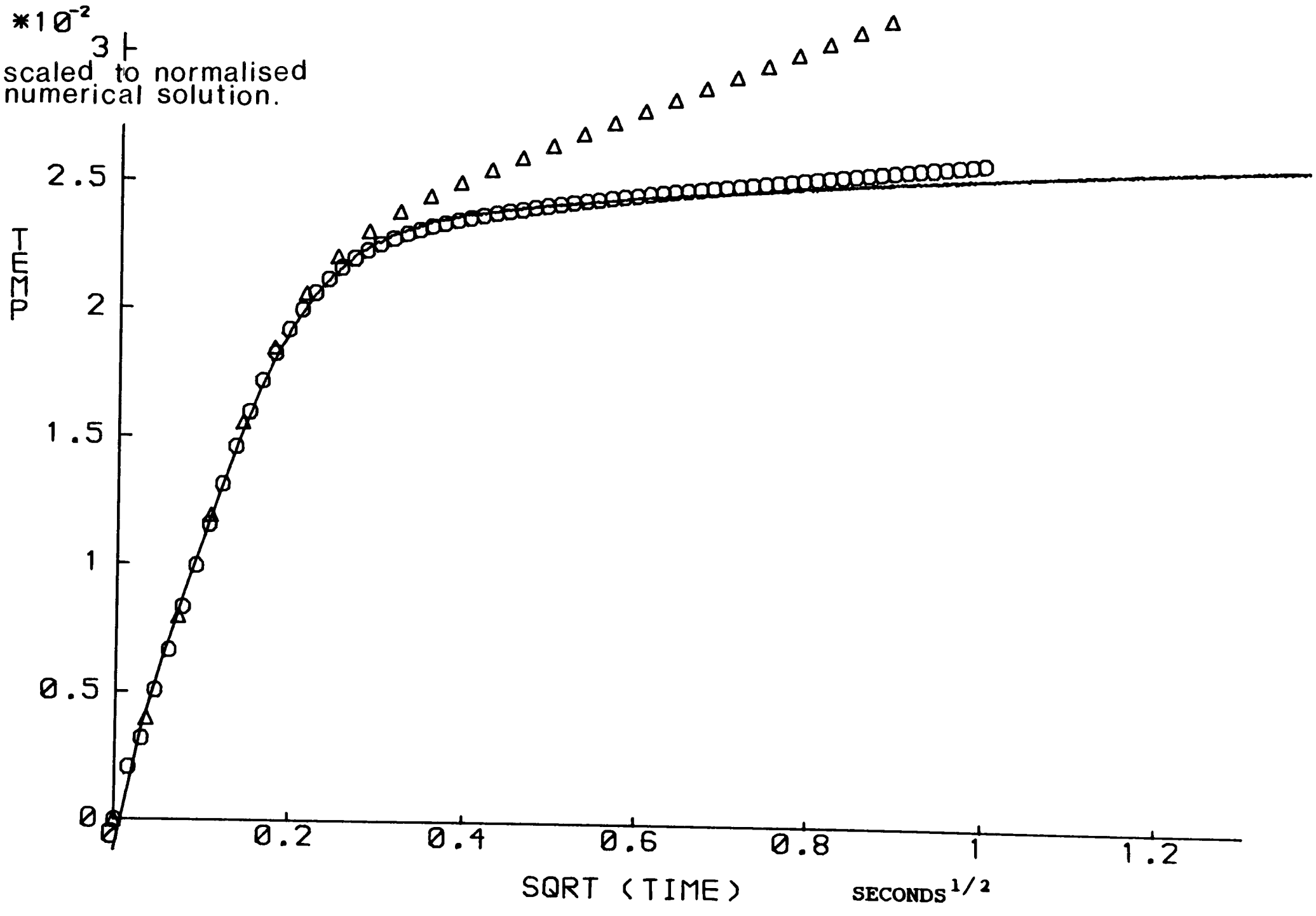

FIG. 6.18 Analogue output from radiant test for film on quartz.

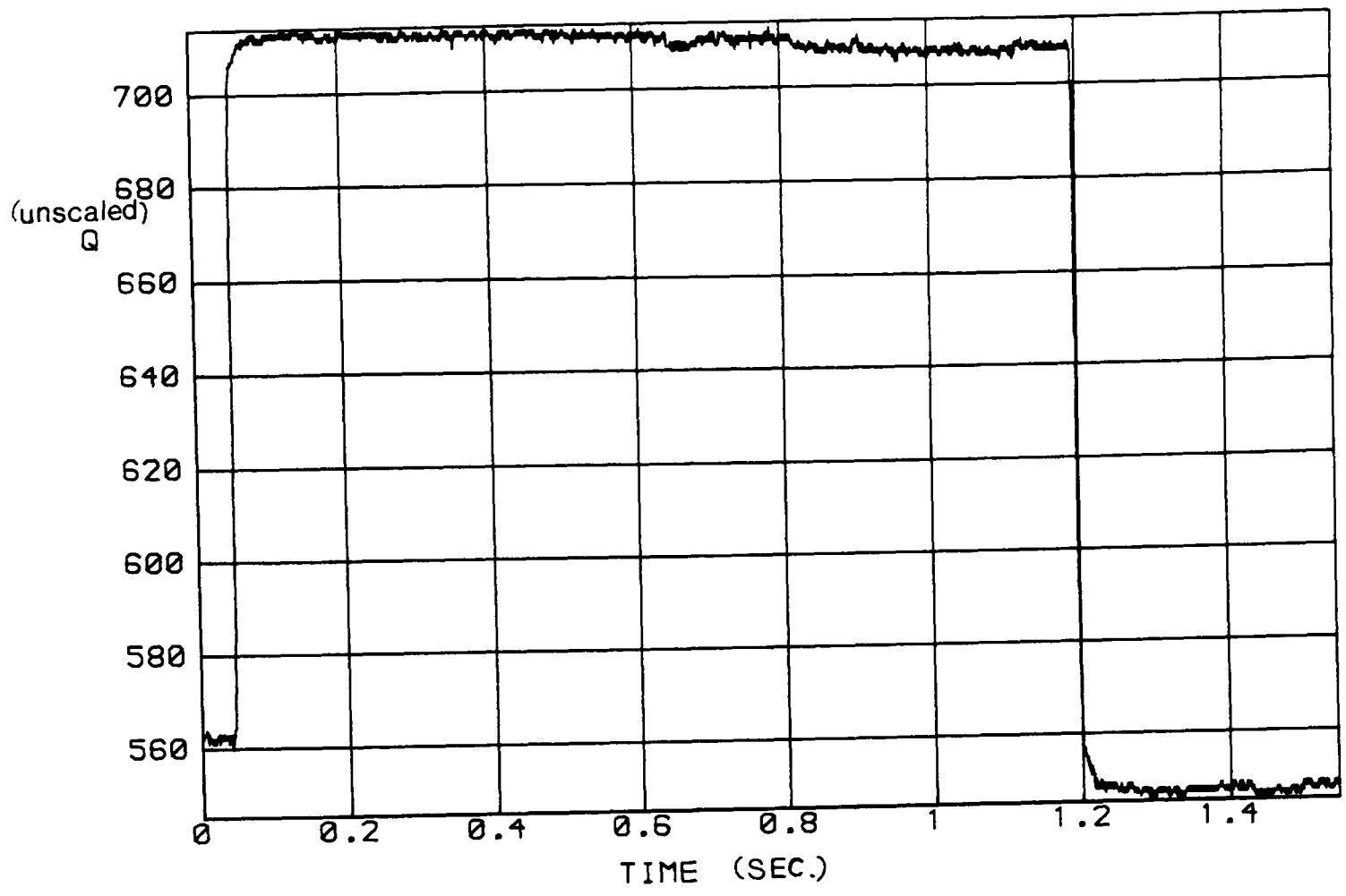

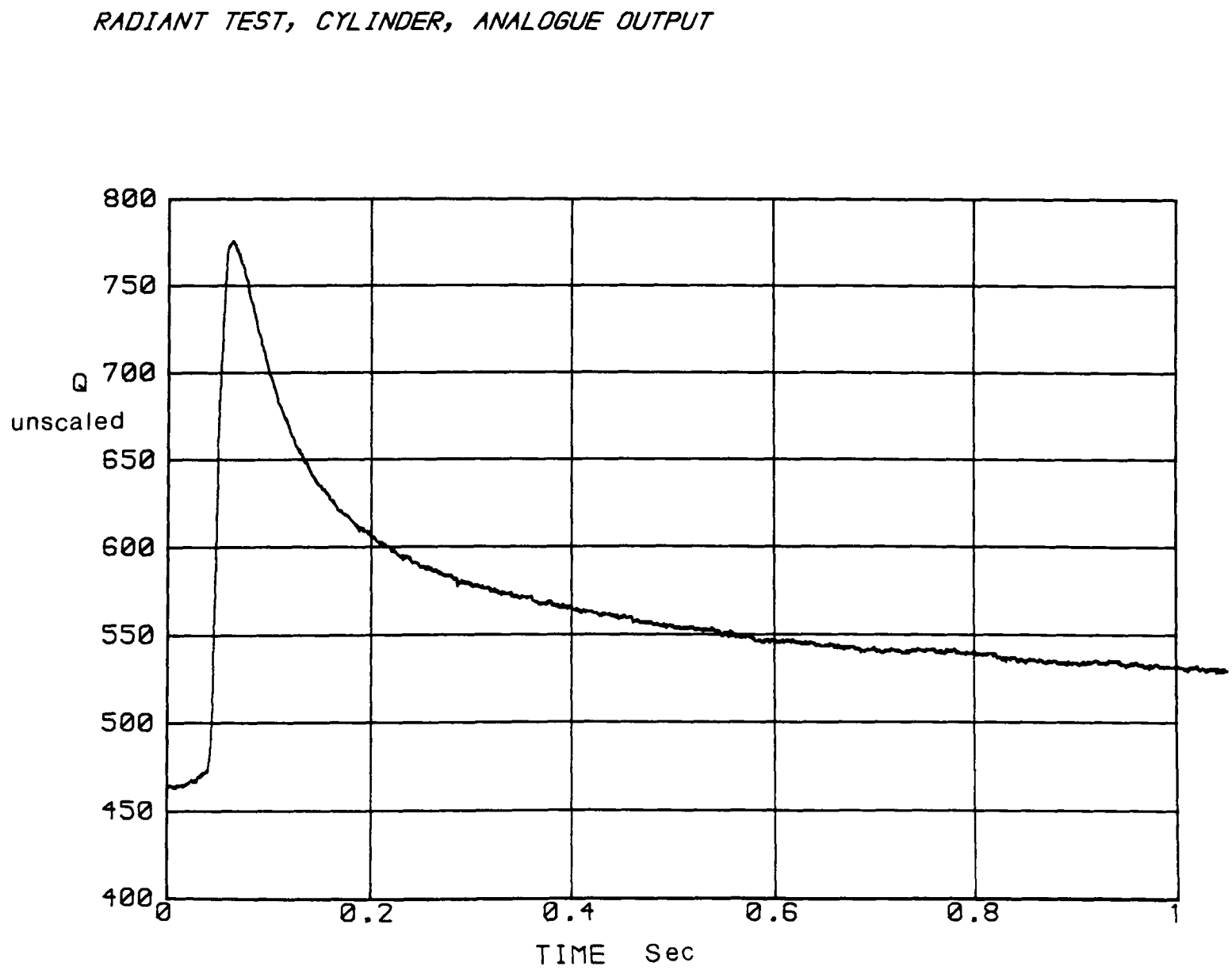

FIG. 6.19 Analogue output from radiant test for film on enamel/steel cylinder.

Radiant test on cylinder, a/k = 0.0001393

FIG. 6.20 Reconstructed heat transfer rate for enamel/steel cylinder.

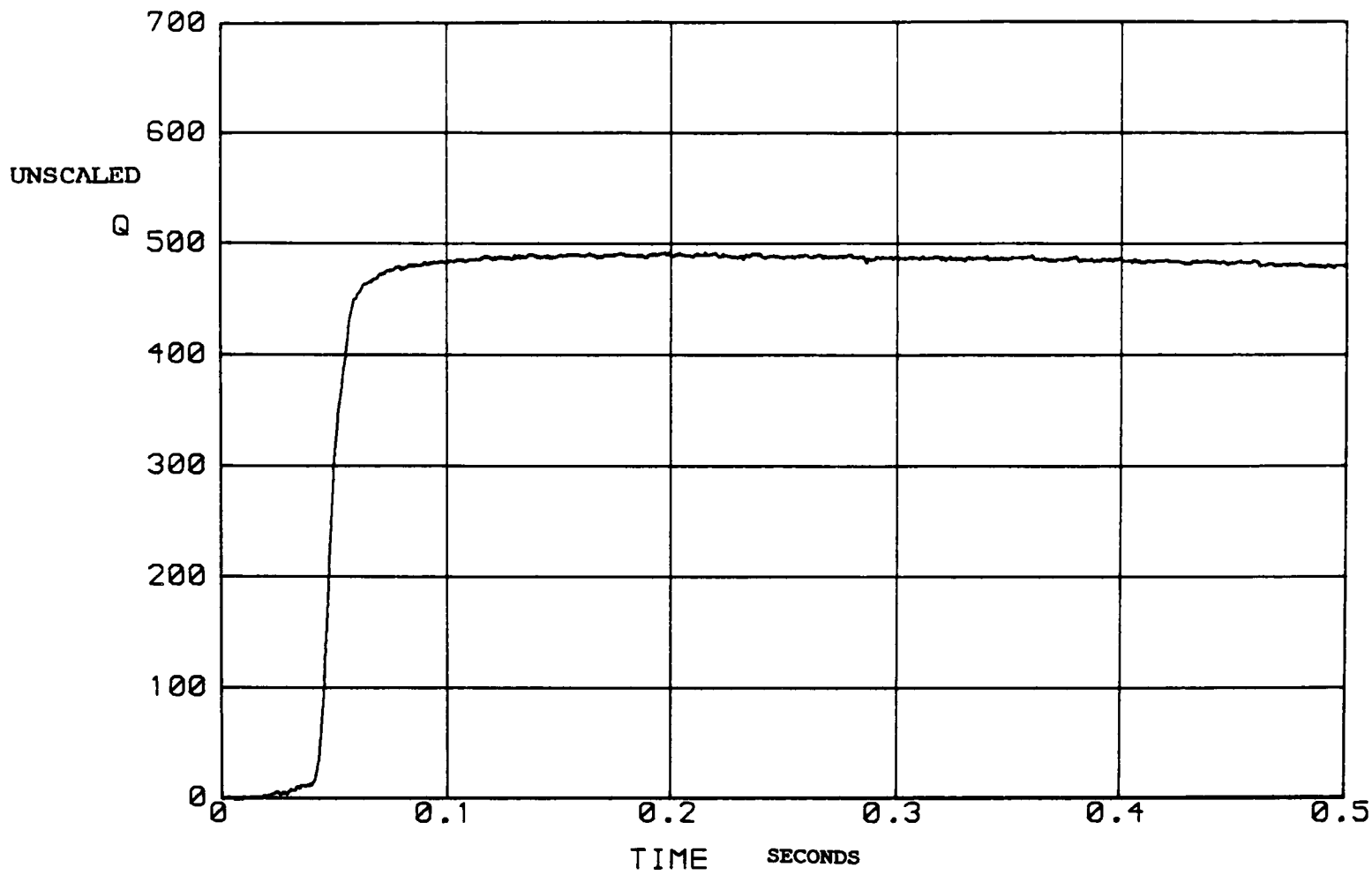

+10% *a/k = 0.00012537* ■

-10% *a/k = 0.00015323* ●

RADIANT TEST ON CYLINDER, a/k = 0.0001393 ▲

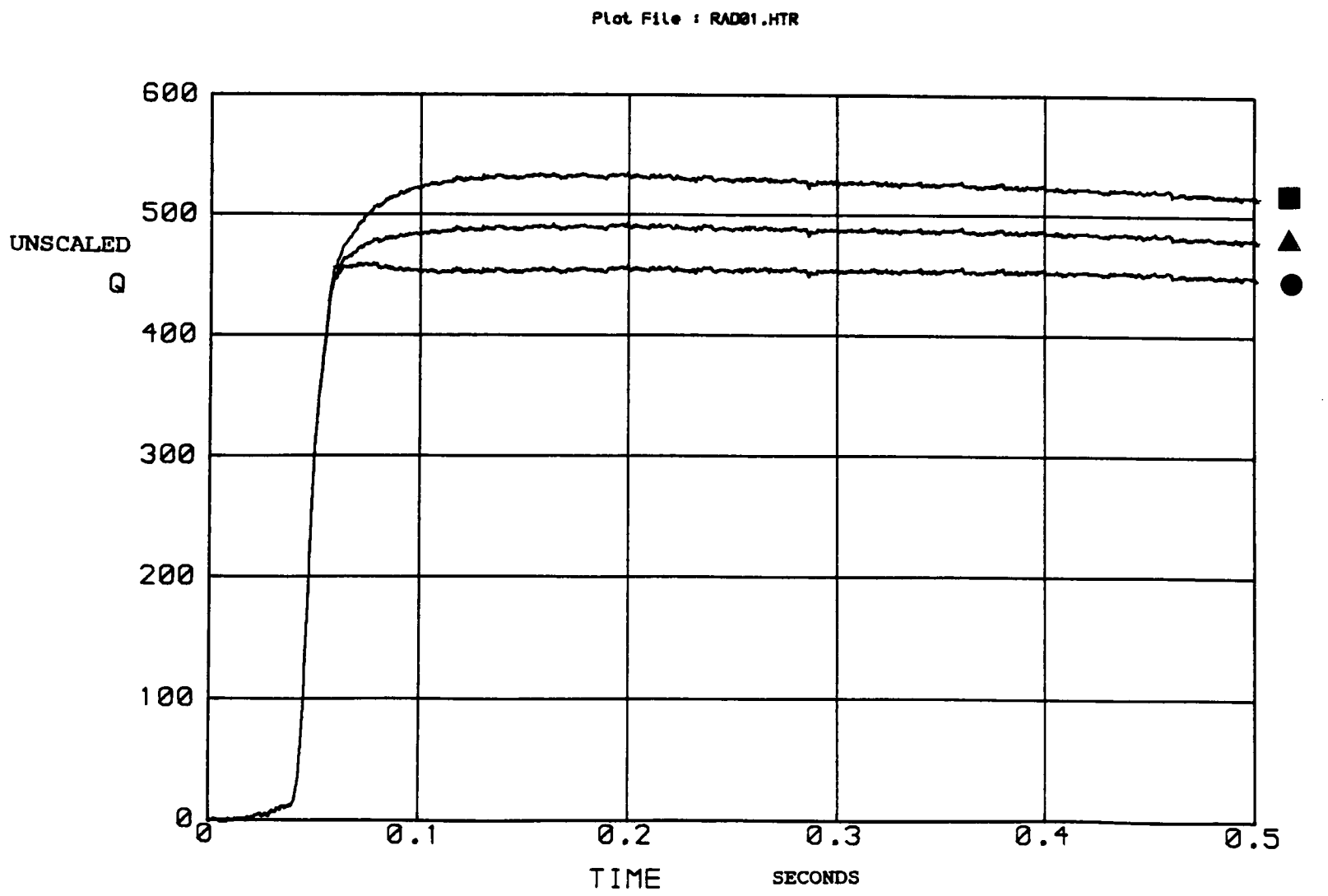

FIG. 6.21 Reconstructed heat transfer rate with varying values of a/k

A/K = 0.00009 ■

A/K = 0.0001800 ●

Radiant test on cylinder, a/k = 0.0001393 ▲

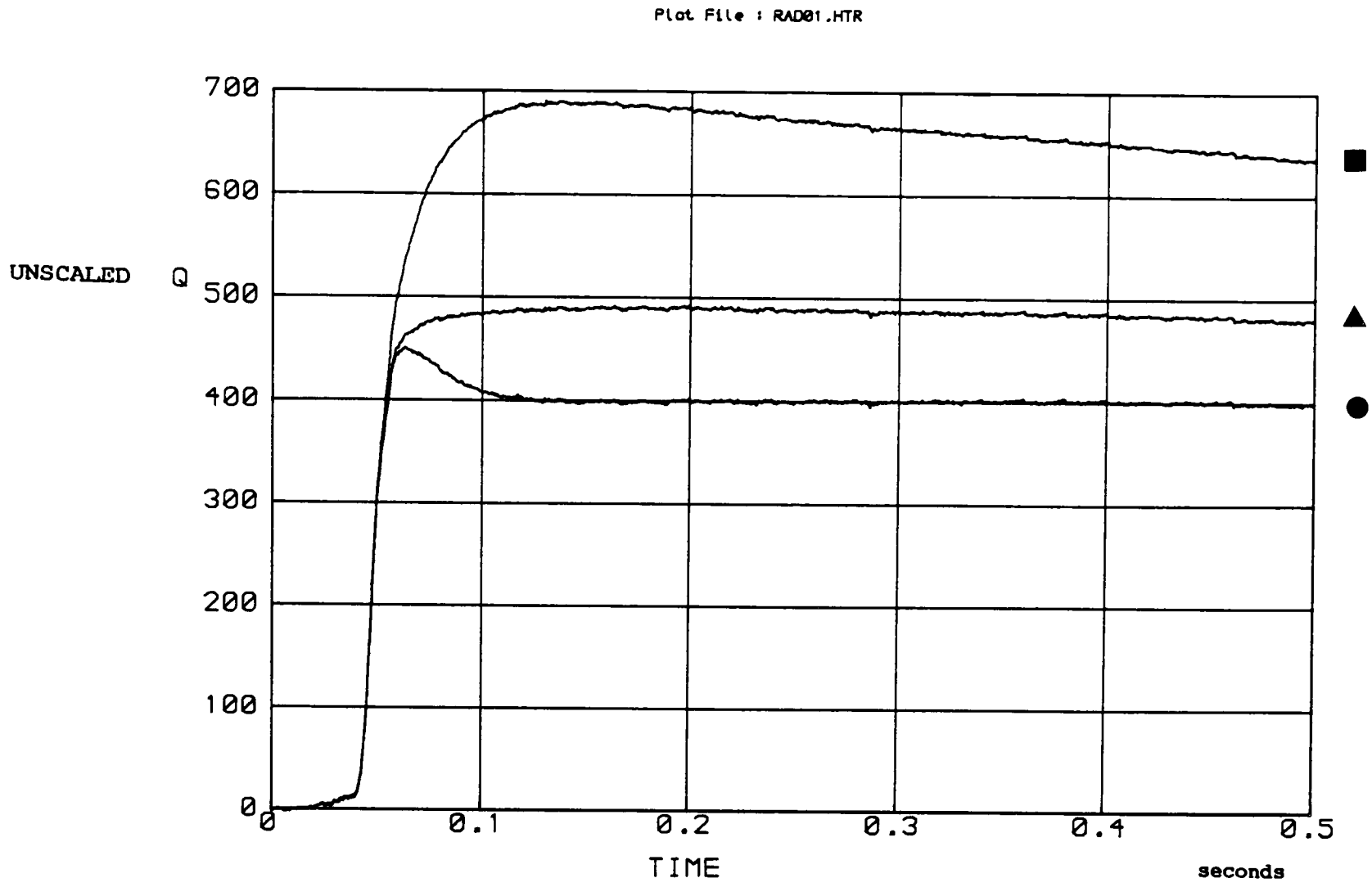

FIG 6.22 Reconstructed heat transfer rate.

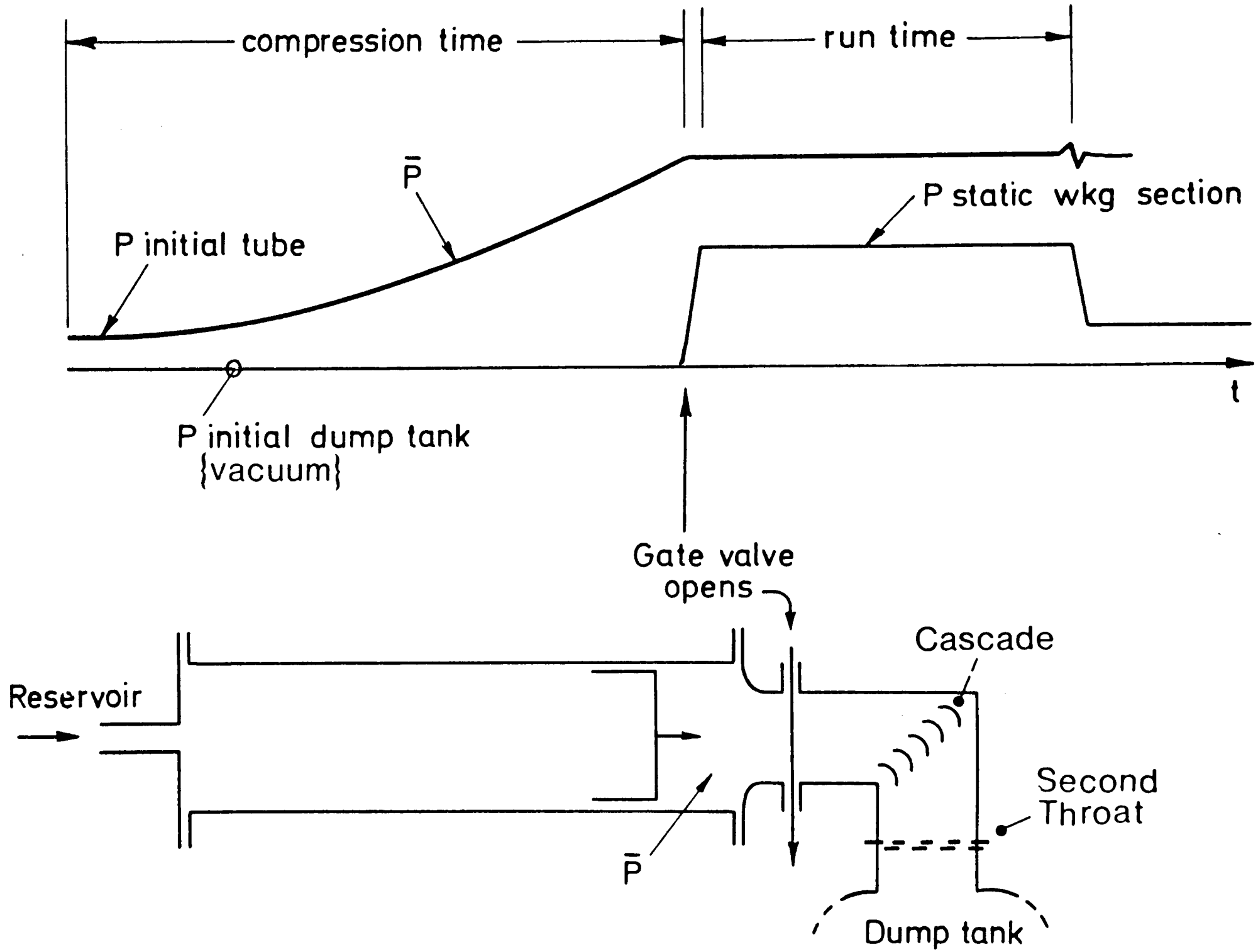

FIG. 7.1 Schematic of Isentropic Light Piston Tunnel

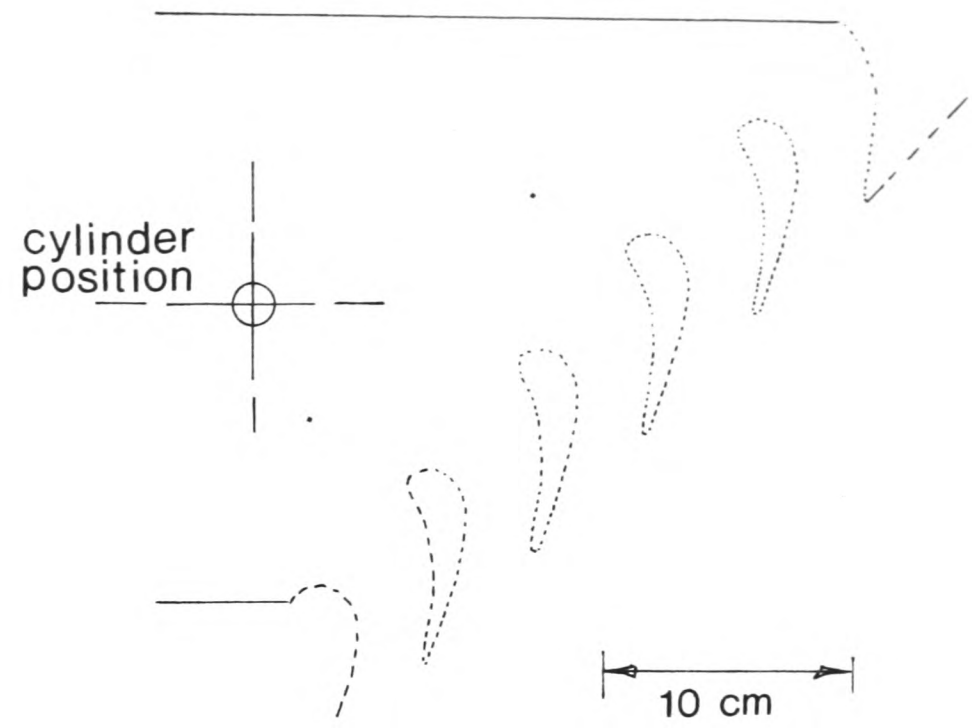

FIG. 7.2 Schematic of cascade showing position of circular cylinder.

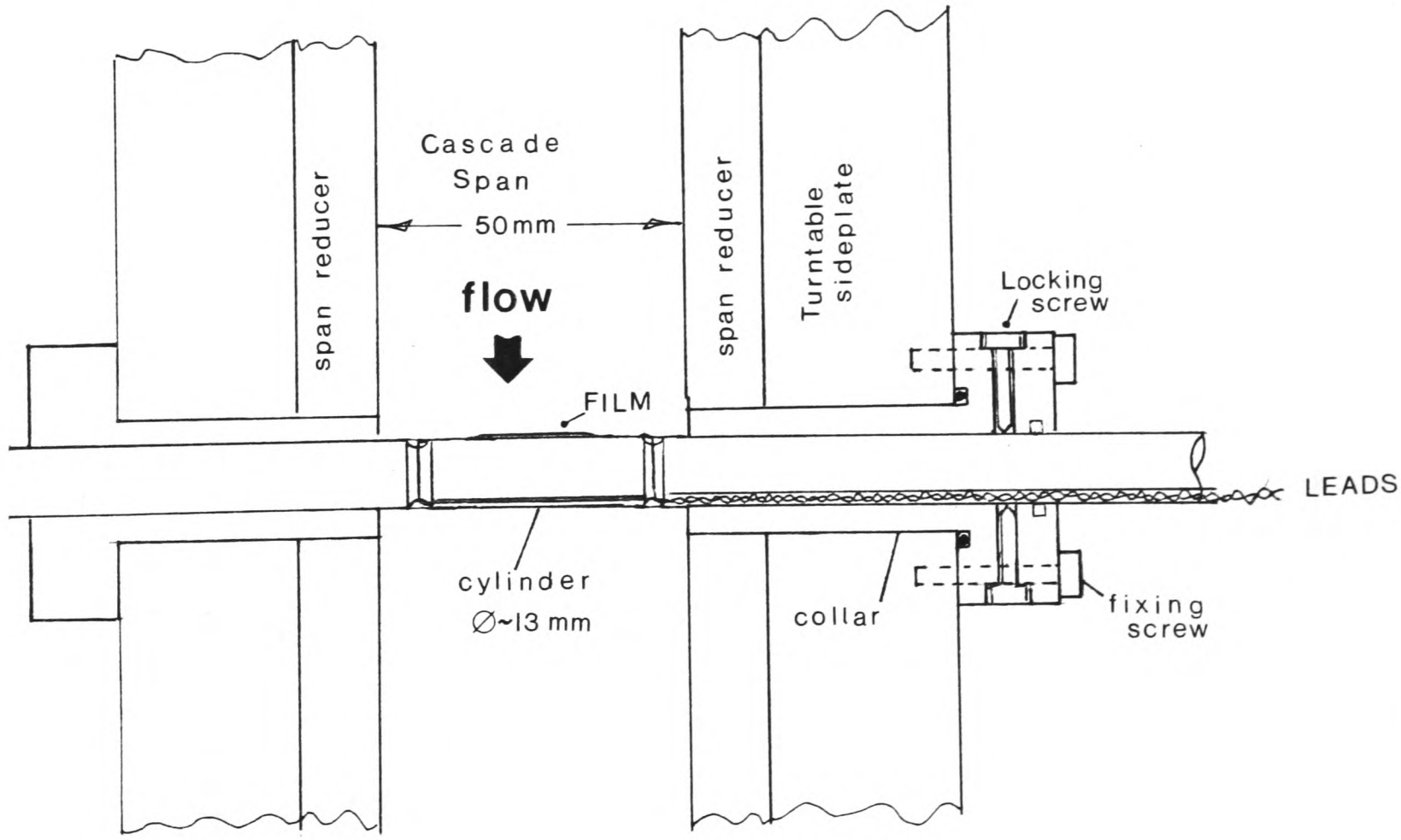

FIG. 7.3 Locking system for cylinder in I.L.P.T.

RUN 4957, MACHINEABLE GLASS CYLINDER

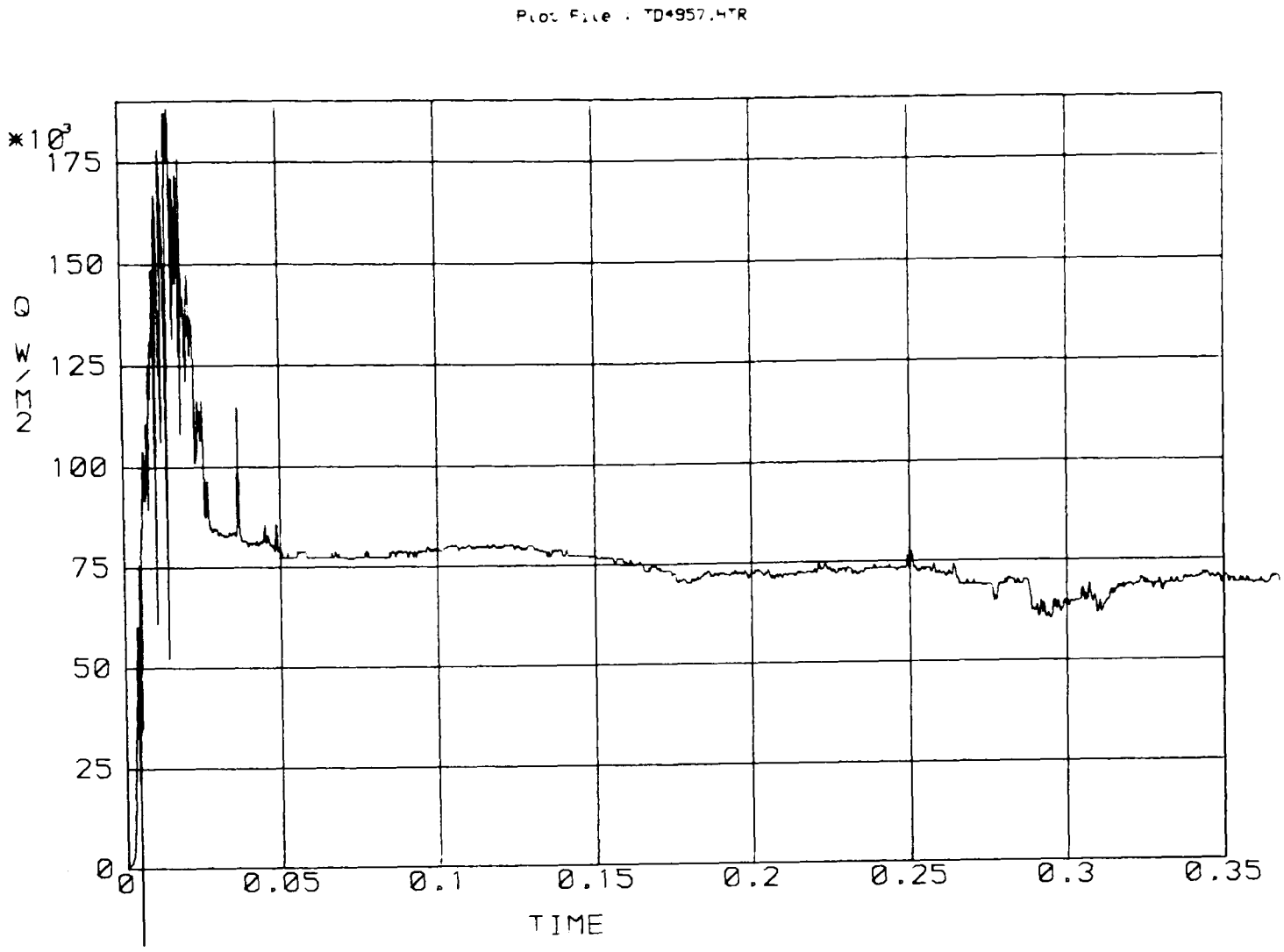

FIG. 7.4 Stagnation point heat transfer rate for machineable glass cylinder, sampled by transient recorder.

RUN 4957, COMPUTER-SAMPLED ANALOGUE O/P

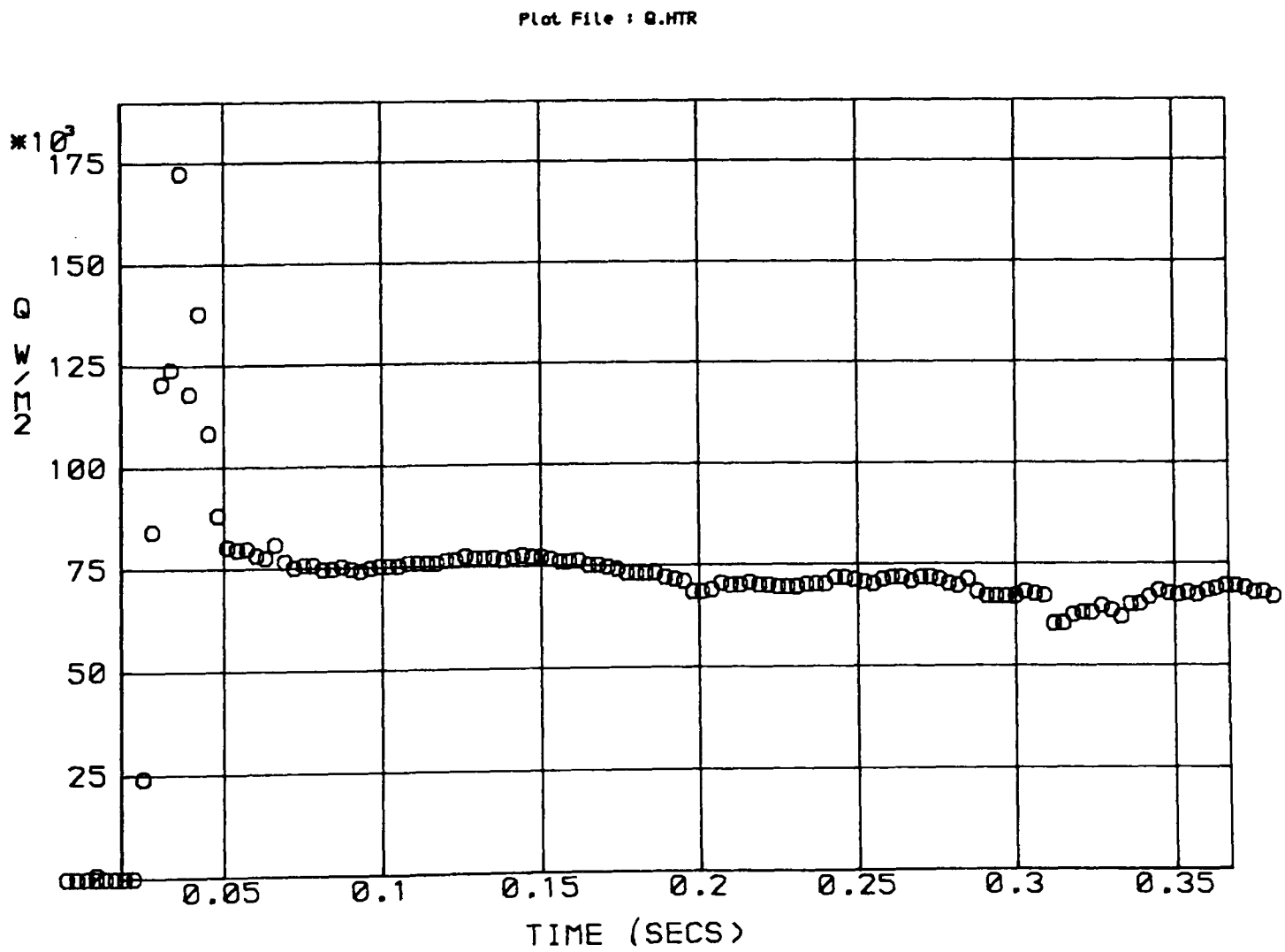

FIG. 7.5 Stagnation point heat transfer rate for machineable glass cylinder, sampled by computer.

RUN 4957, MACHINEABLE GLASS CYLINDER, SURFACE TEMPERATURE

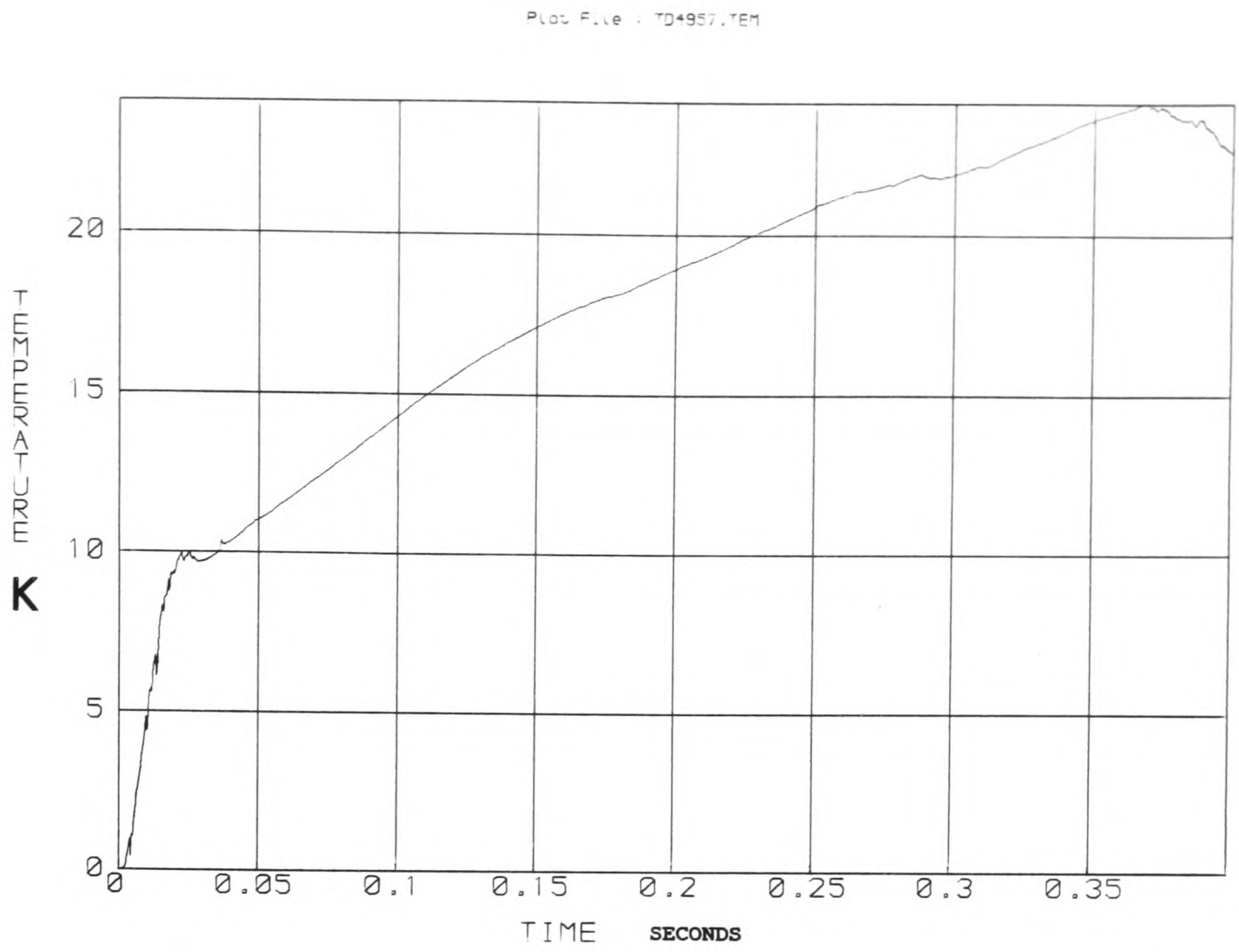

FIG. 7.6 Reconstructed surface temperature for machineable glass cylinder.

b UPSTREAM STATIC PRESSURE

a TOTAL PRESSURE FOR RUN 4957

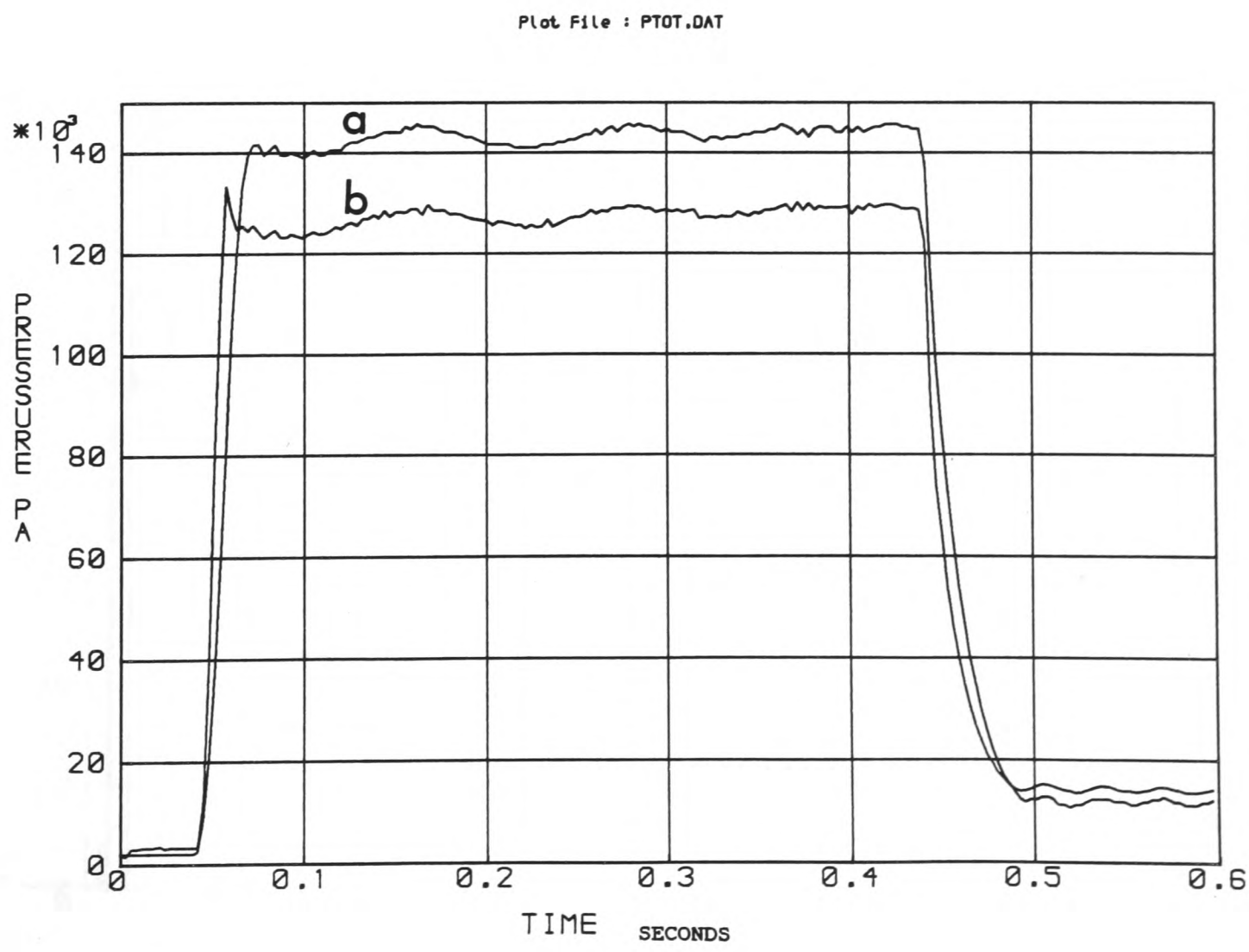

FIG. 7.7 Upstream total and static pressures.

MACHINEABLE GLASS CYLINDER

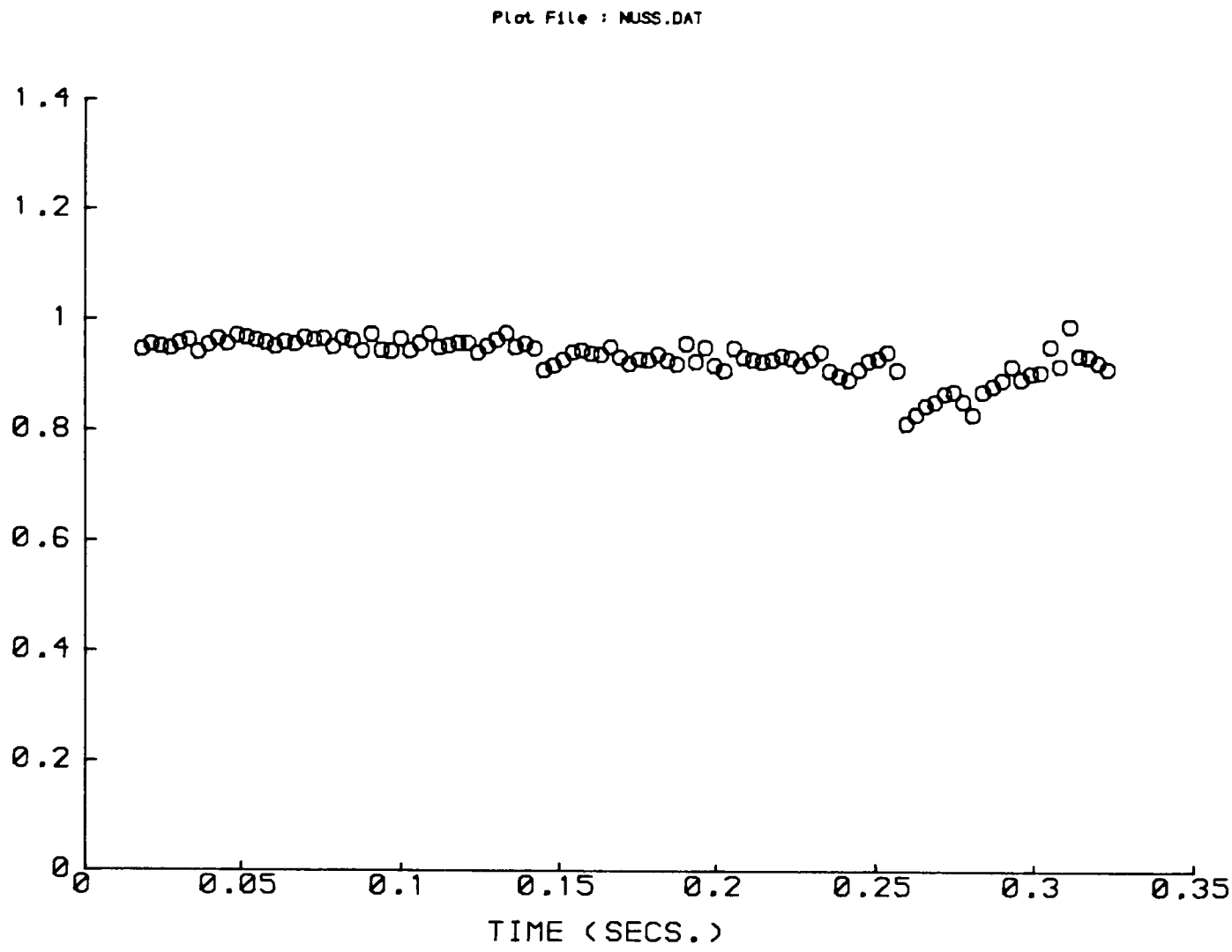

FIG. 7.8 Plot of $Nu/Re^{1/2}$ for machineable glass cylinder, run 4957

RUN 4956, ANALOGUE OUTPUT

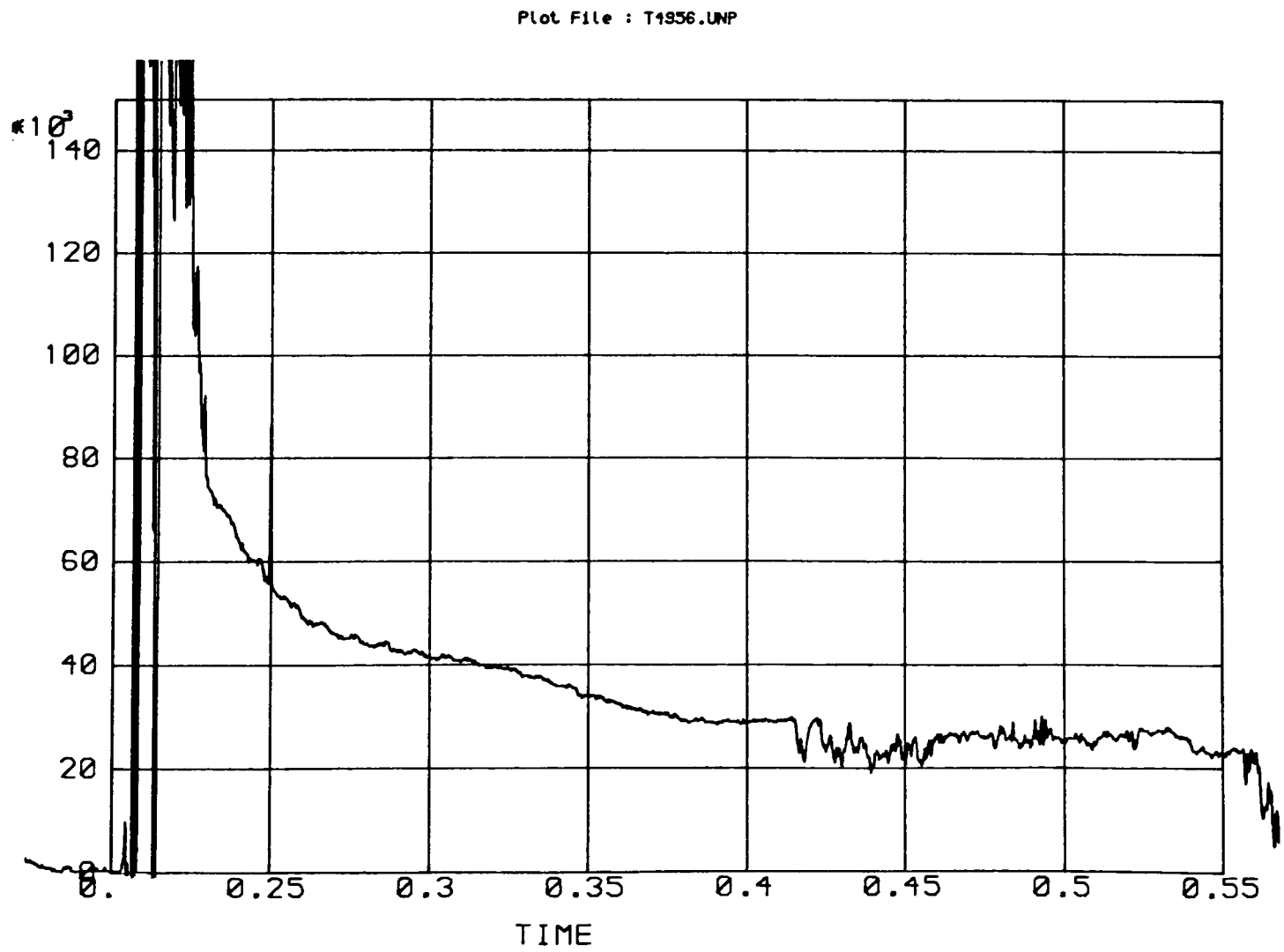

FIG. 7.9 Analogue output for enamel/steel cylinder, run 4956.

h(t),

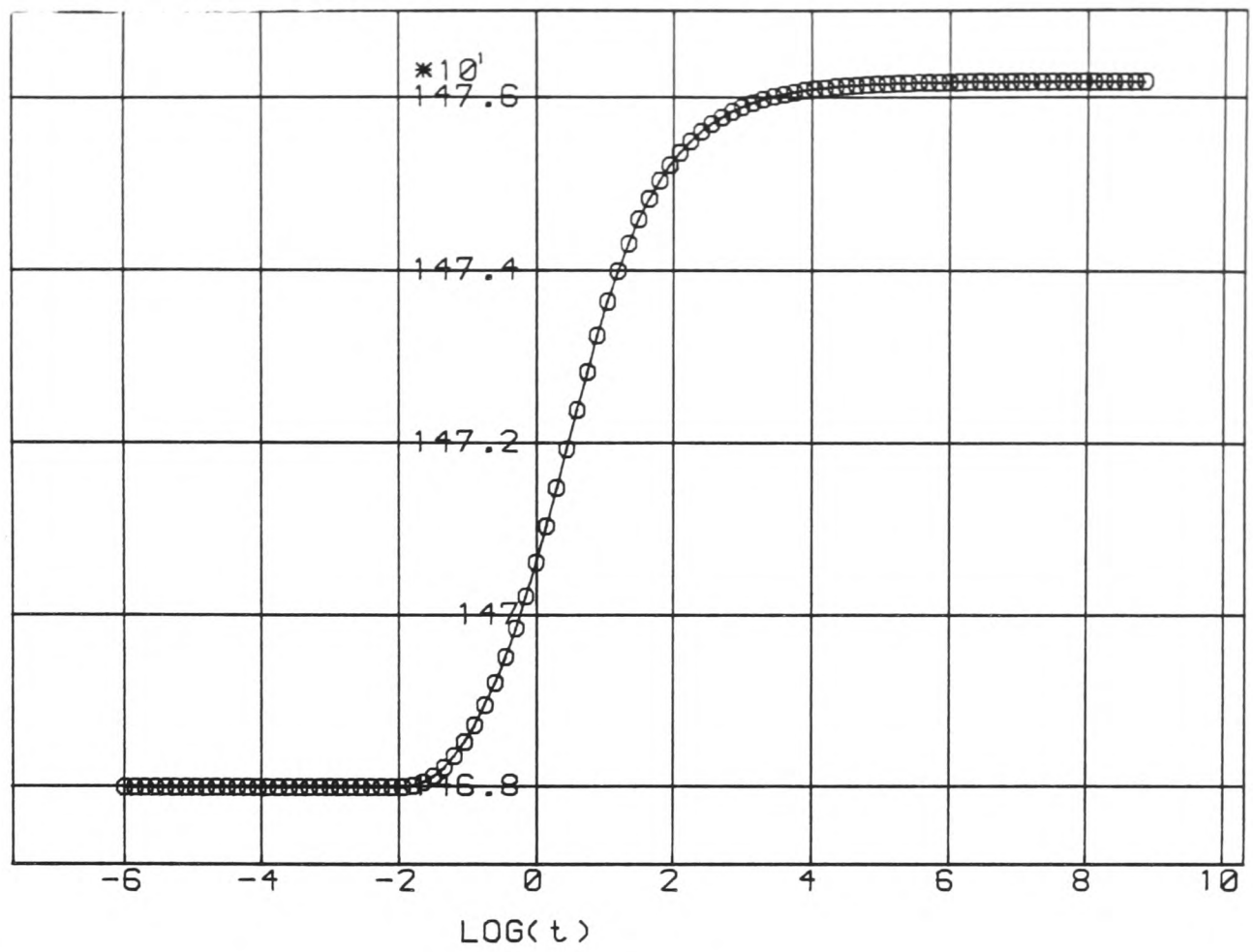

FIG. 7.10 Kernel function h(t) for enamel/steel cylinder model.

RUN 4956, UNCORRECTED ANALOGUE OUTPUT a

RUN 4956, CORRECTED HEAT TRANSFER RATE b

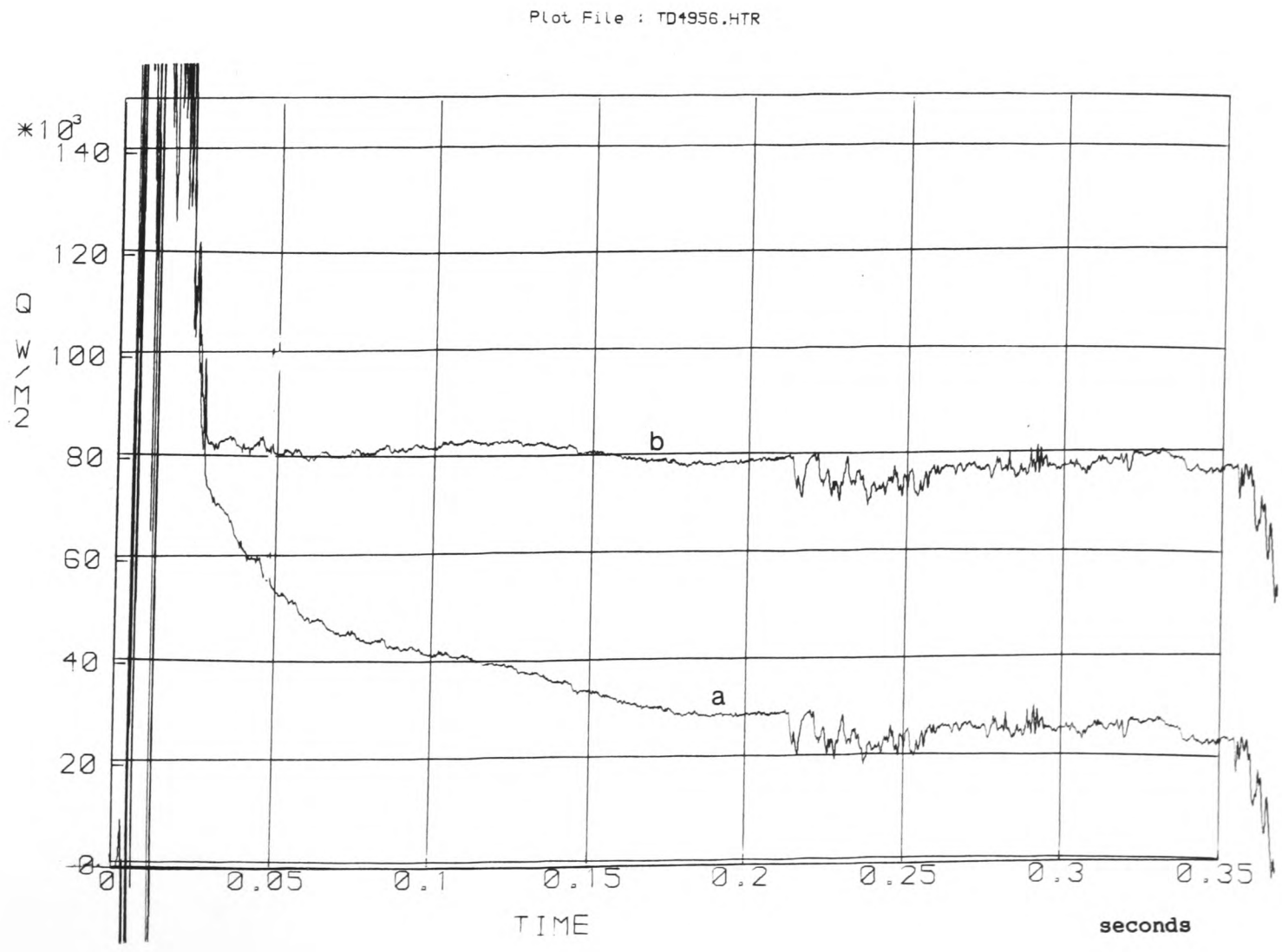

FIG. 7.11 Uncorrected analogue output signal and corrected heat transfer rate for enamel/steel cylinder, run 4956.

RUN 4956, SURFACE TEMPERATURE

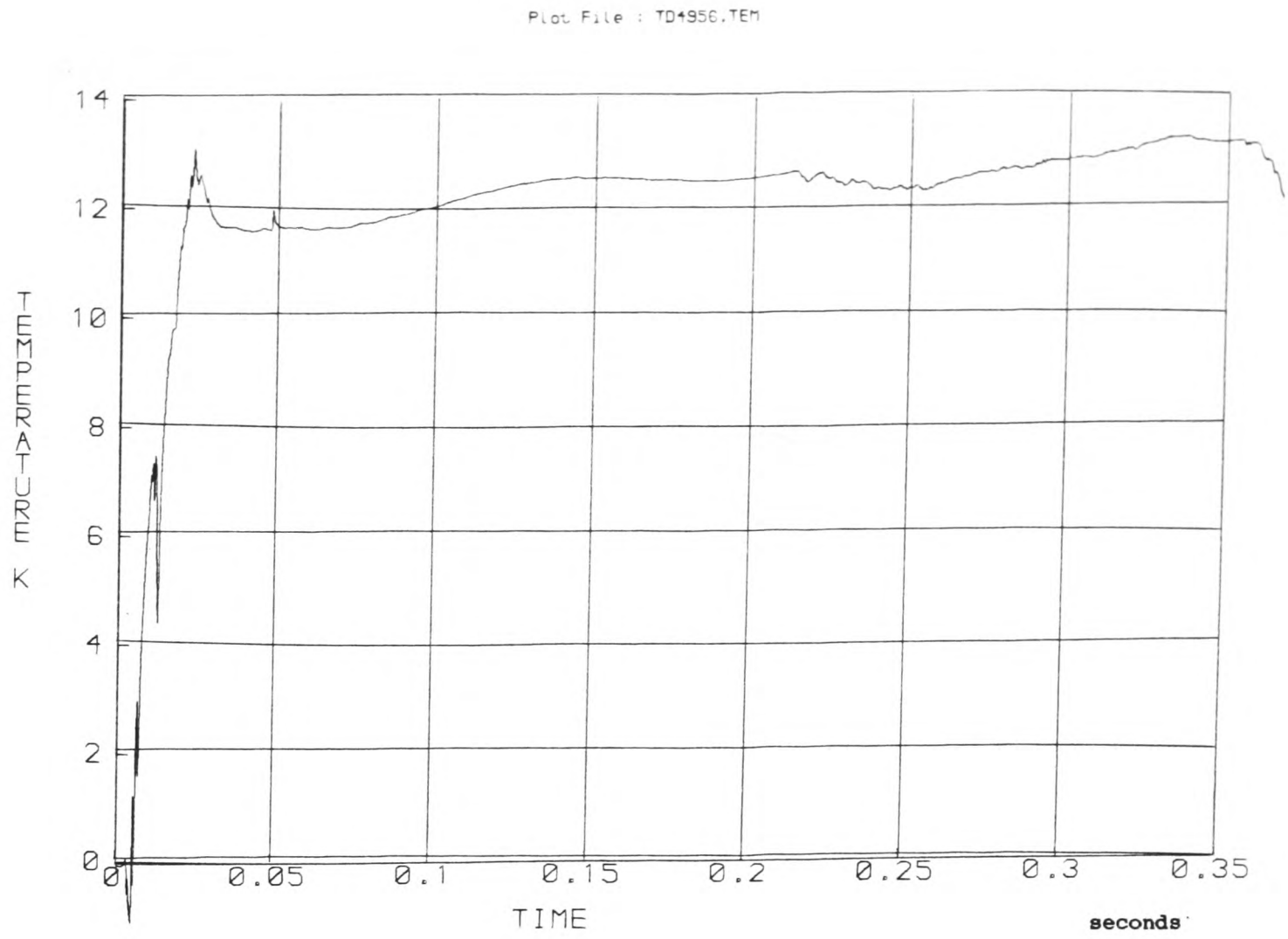

FIG. 7.12 Reconstructed surface temperature for run 4956.

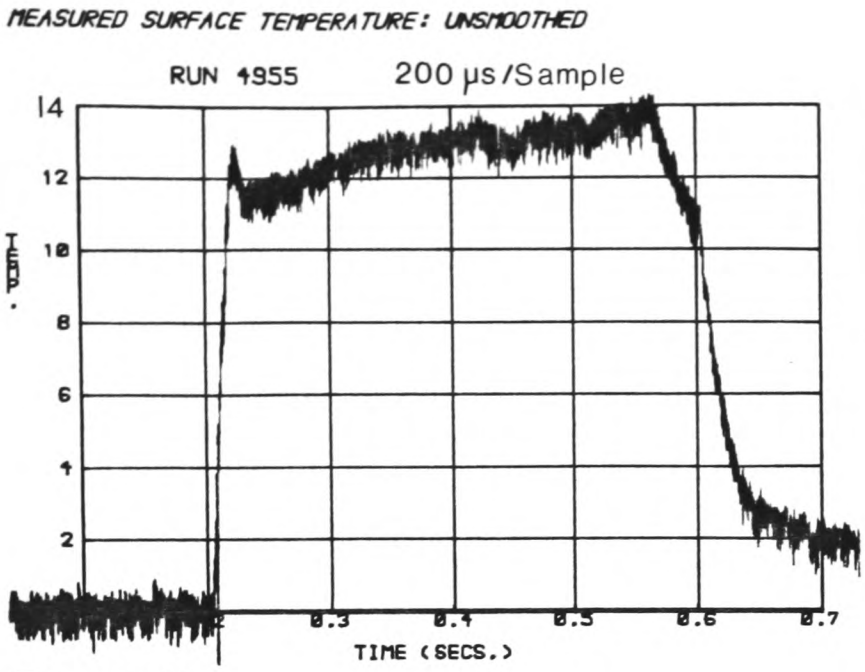

Fig. 7-13

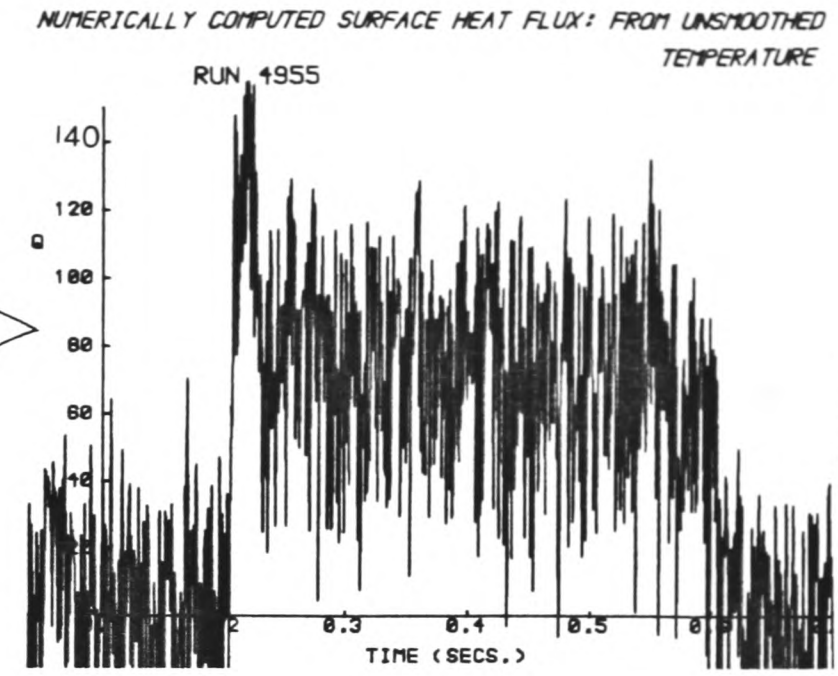

Fig. 7-14

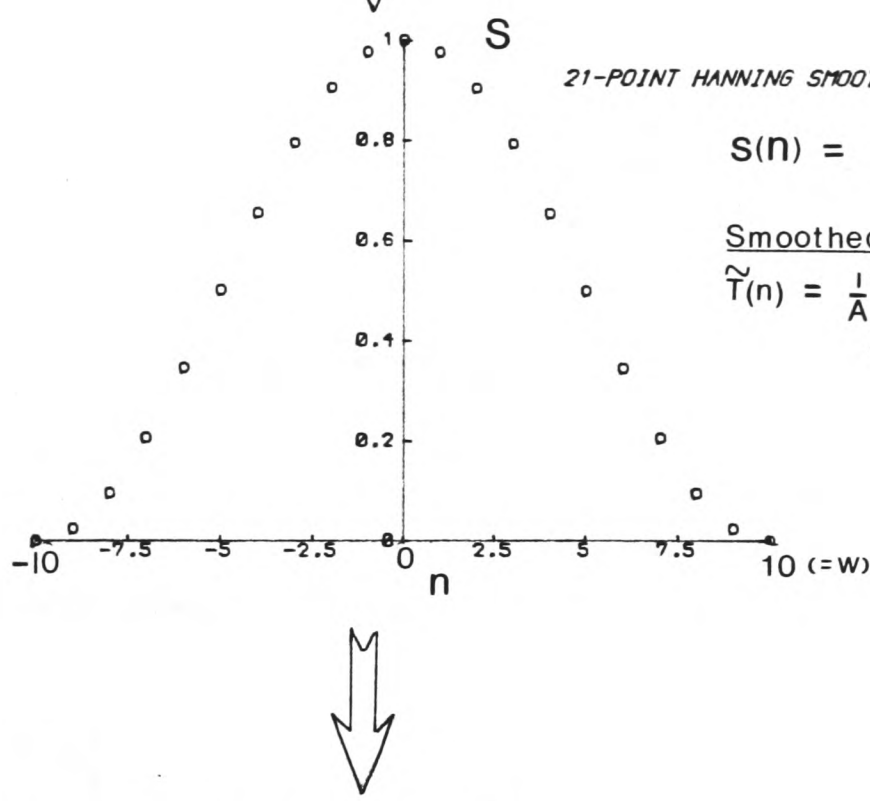

$$s(n) = \frac{1}{2}\left\{1 + \cos\left(\frac{\pi n}{W}\right)\right\} \qquad -W \le n \le W$$

Smoothed Temperature :

$$\tilde{T}(n) = \frac{1}{A}\sum_{j=n-W}^{j=n+W} [\,T(j)\,S(j-n)\,] \quad , \quad A = \sum_{j=-W}^{W} S(j)$$

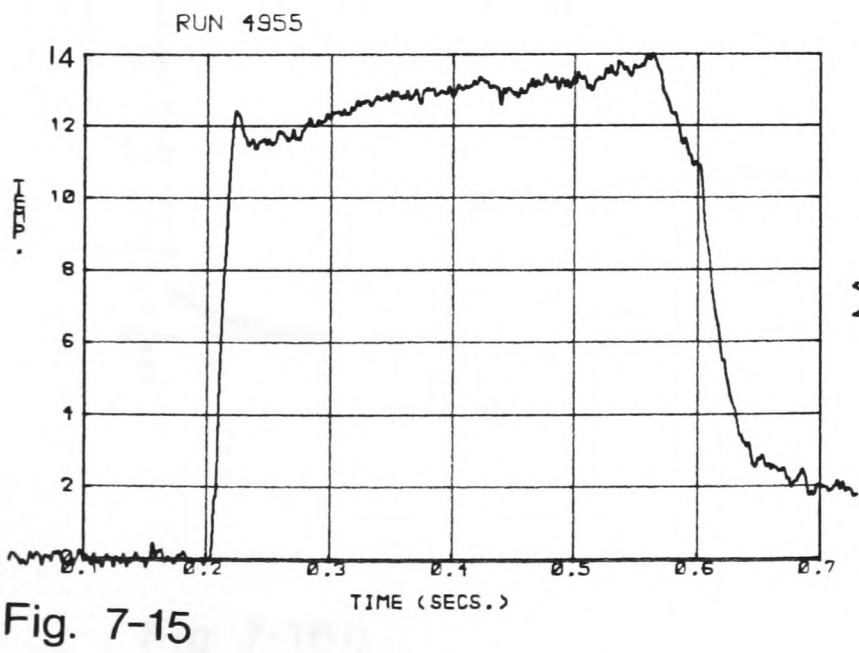

Fig. 7-15

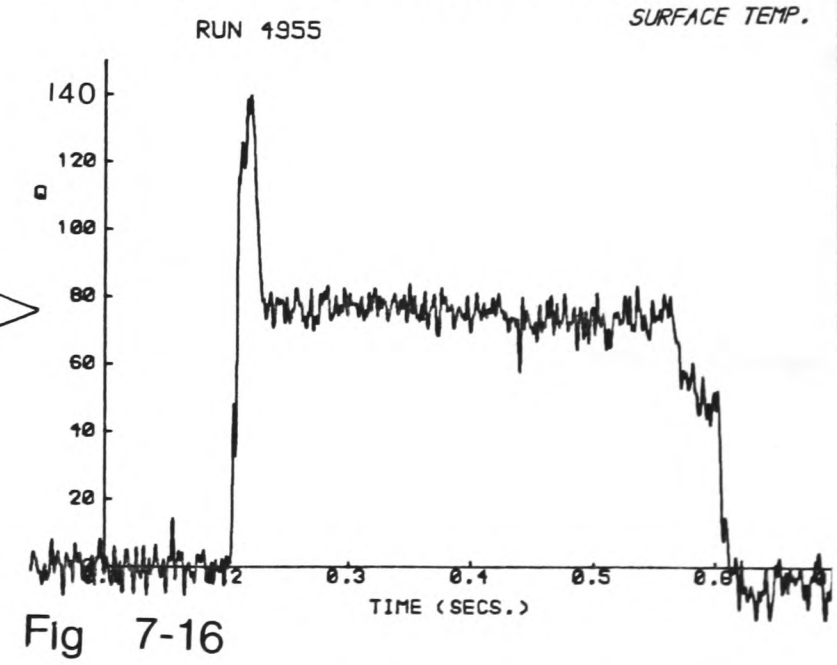

Fig 7-16

Numerical Calculation of Surface Heat Flux from Measured Surface Temperature: Application of Smoothing

● PROCESSED ANALOG O/P SIGNAL (RUN 4955 - FROM TRANSIENT RECORDER DATA)

—— NUMERICALLY CALCULATED SURFACE HEAT FLUX FROM MEASURED SURFACE TEMP. RUN 4955

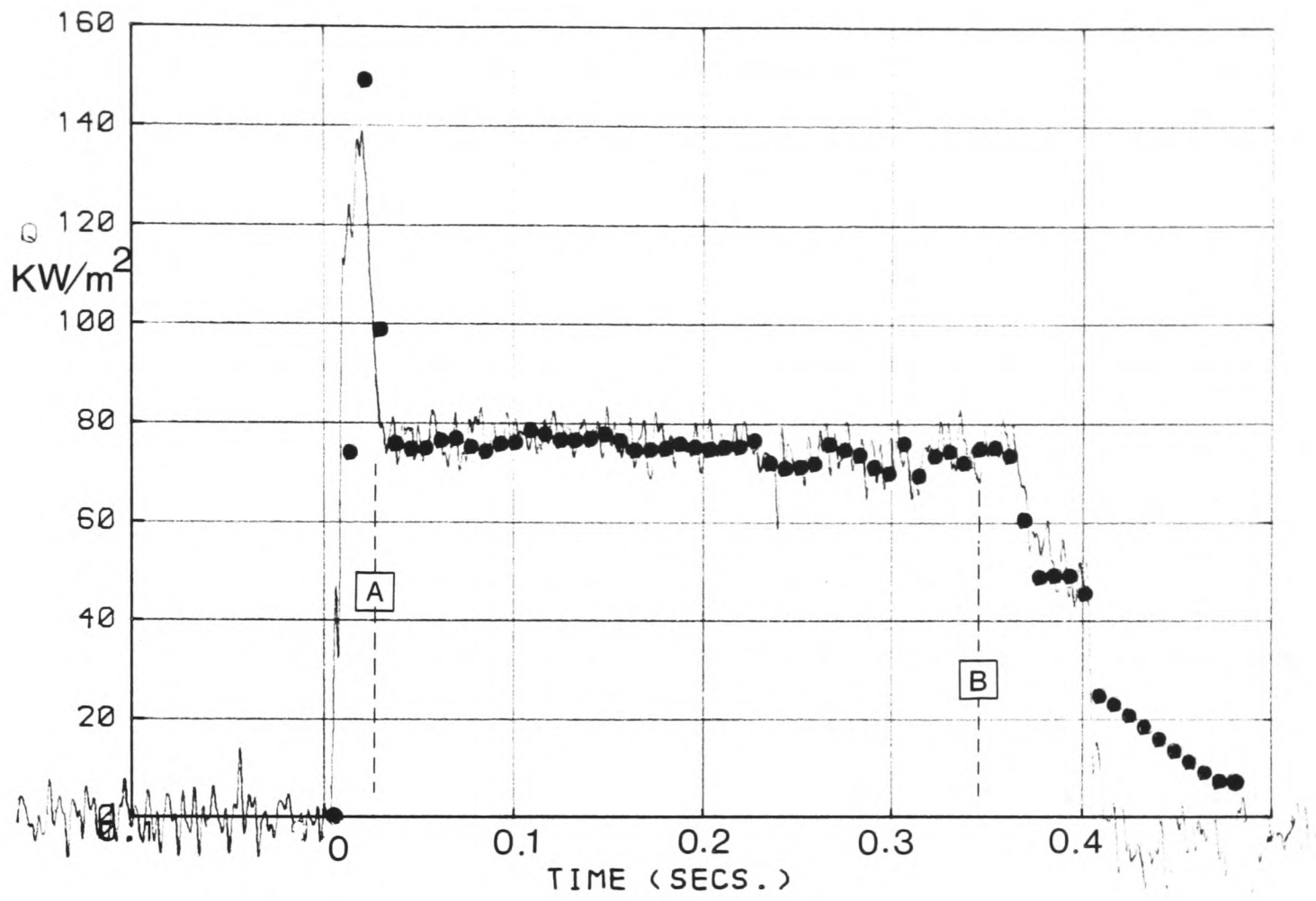

A: TEMPERATURE DISTRIBUTION AT .02 sec

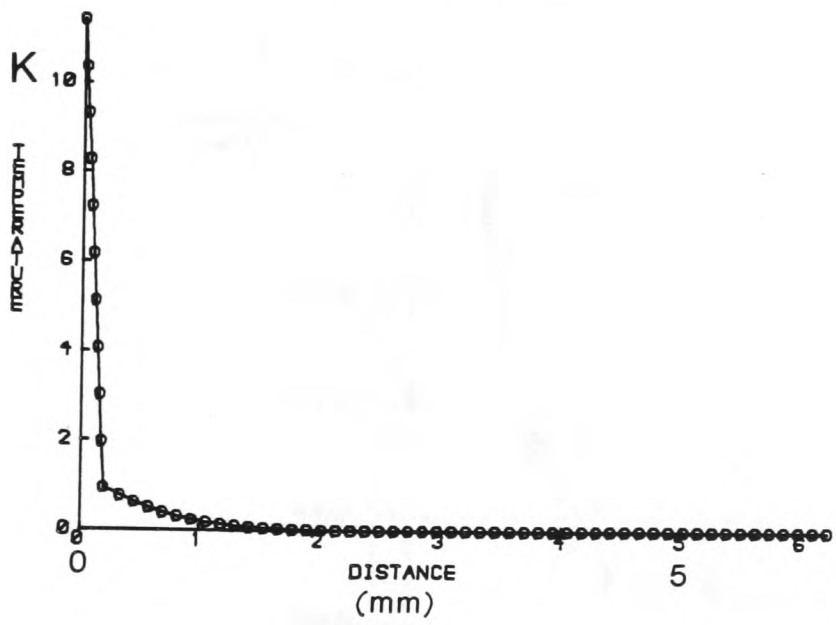

B: TEMPERATURE DISTRIBUTION AFTER .34 sec

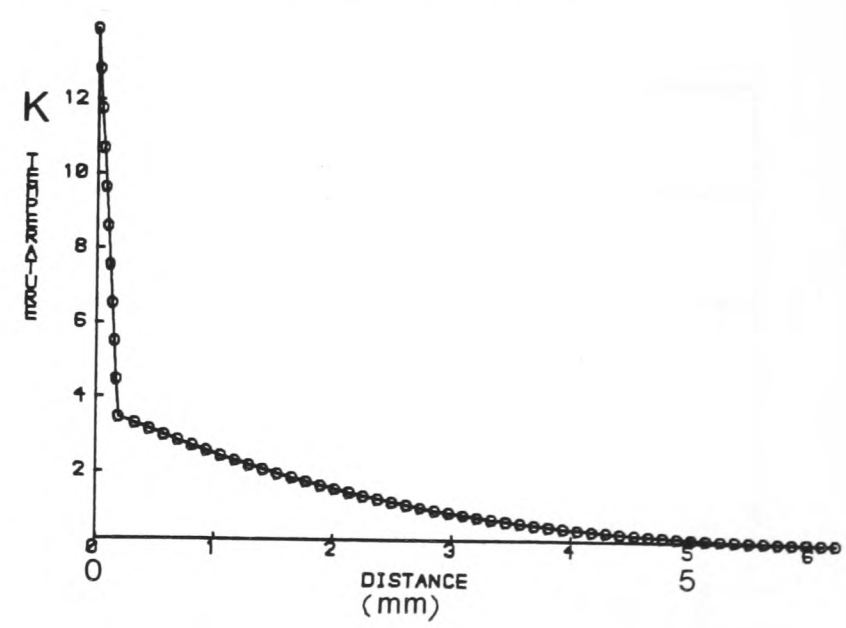

Fig 7-16b

RUN 4956, NUSSELT/SQRT (RE)

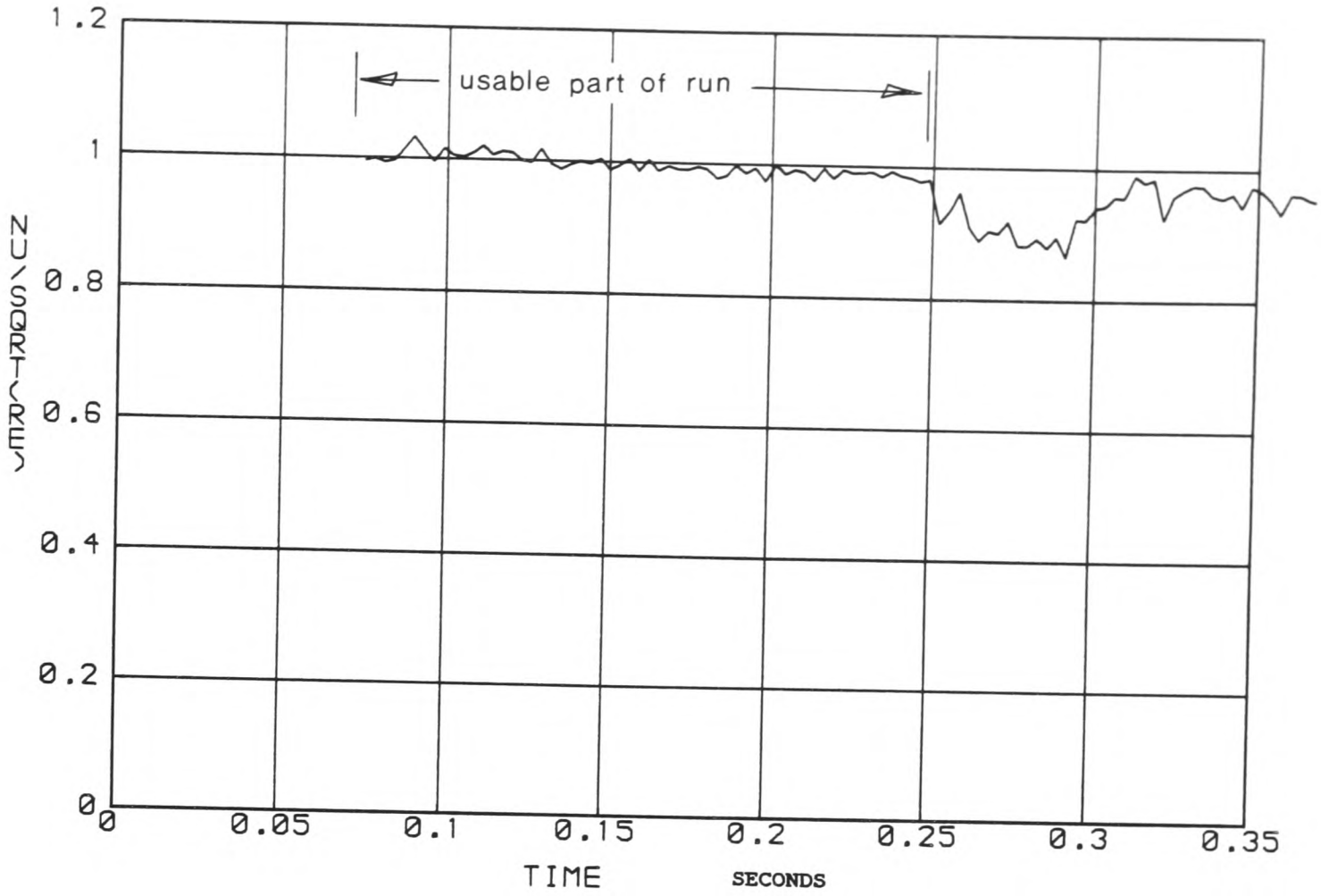

FIG. 7.17 Plot of $Nu/Re^{1/2}$ for enamel/steel cylinder, run 4956.

RUN 4949, MAINS ANALOGUE

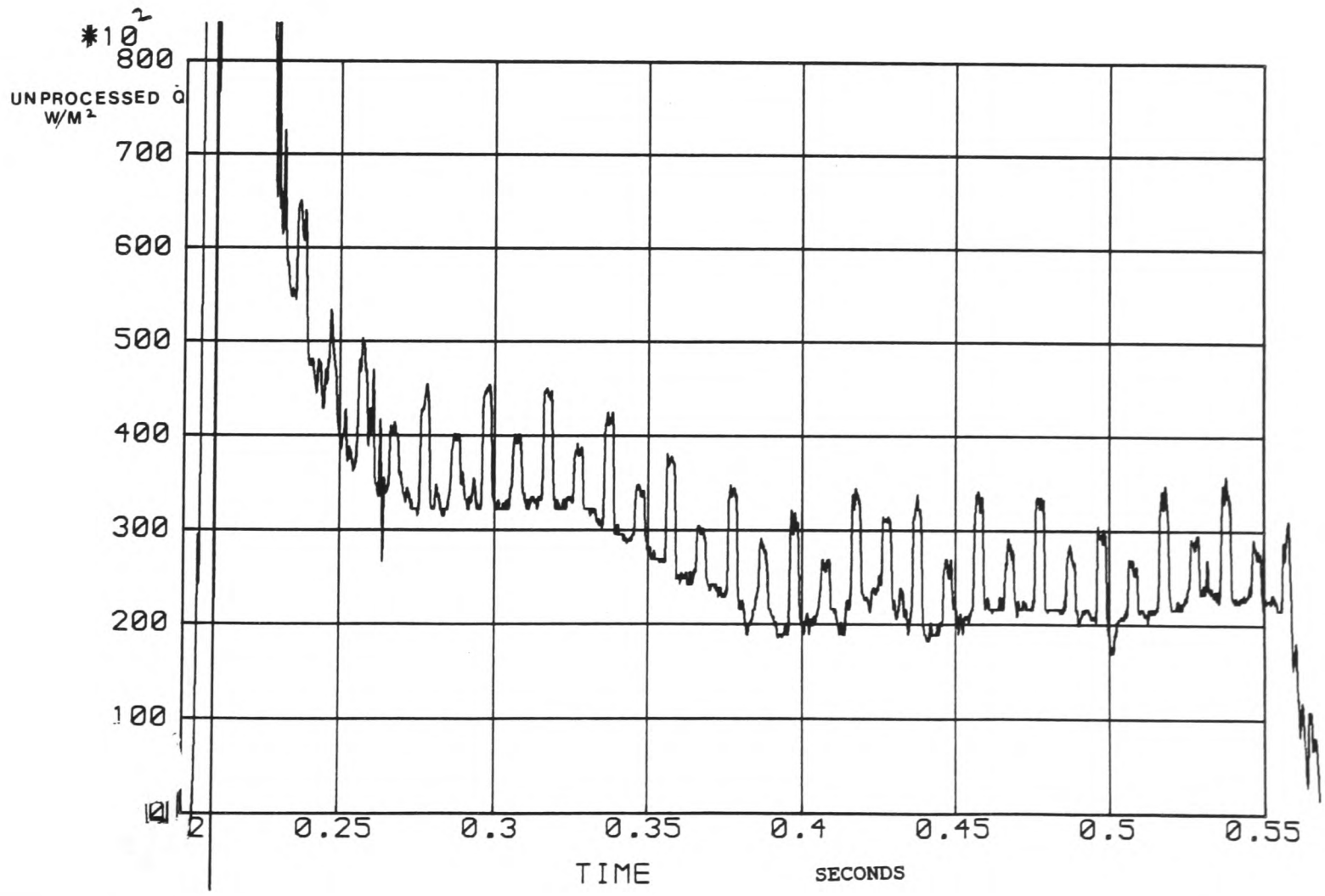

FIG. 7.18 Mains powered analogue output for run 4949, enamel/steel cylinder, showing "pick-up"

a *RUN 4949, MAINS ANALOGUE*

b *RUN 4950, ENAMEL/STEEL CYLINDER, BATTERY ANALOGUE OUTPUT*

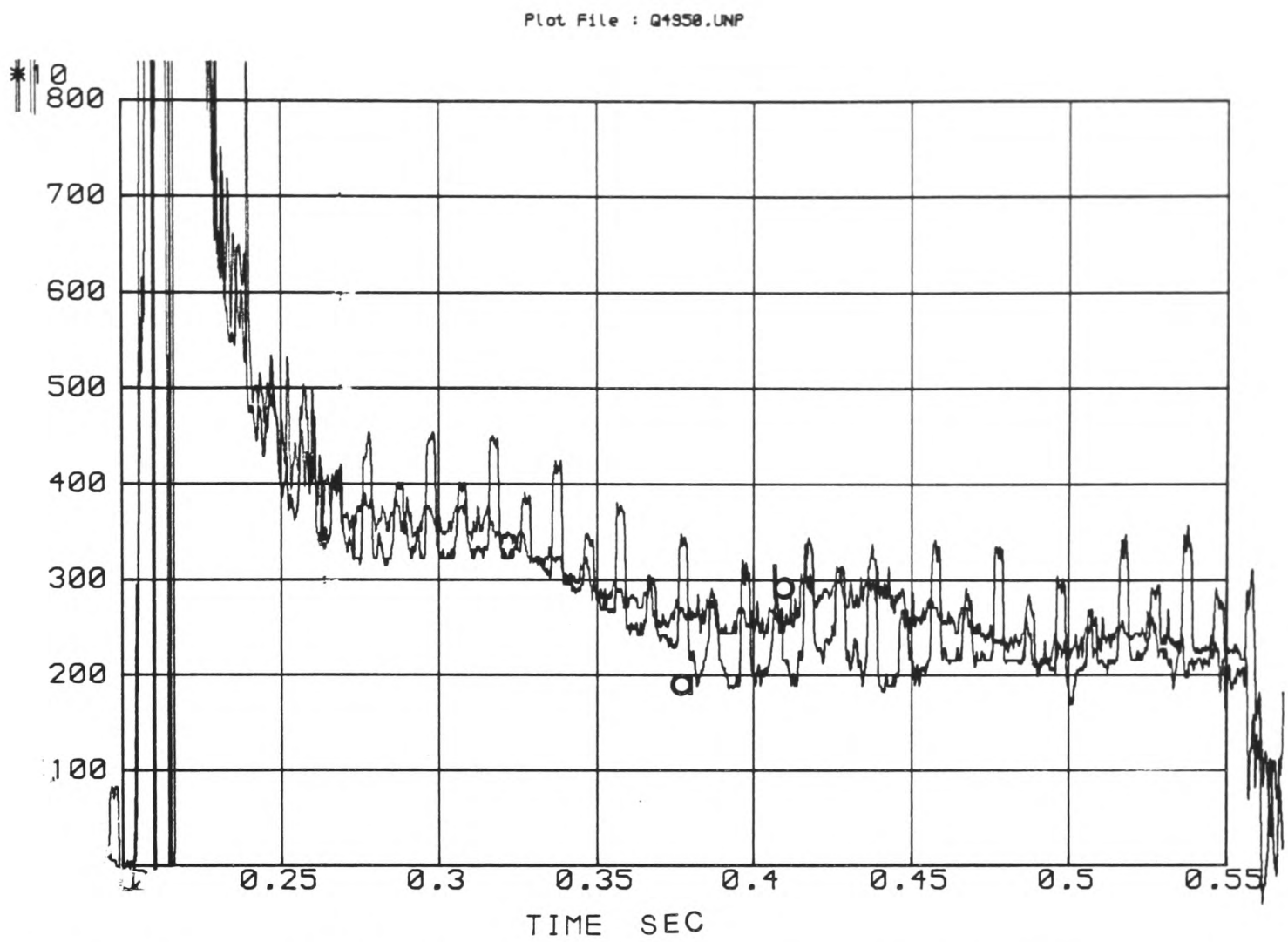

FIG. 7.19 Superimposed analogue output for run 4949 (mains analogue) and run 4950 (battery analogue),for enamel/steel cylinder.

a *RUN 4949*

b *RUN 4950, HEAT TRANSFER RATE*

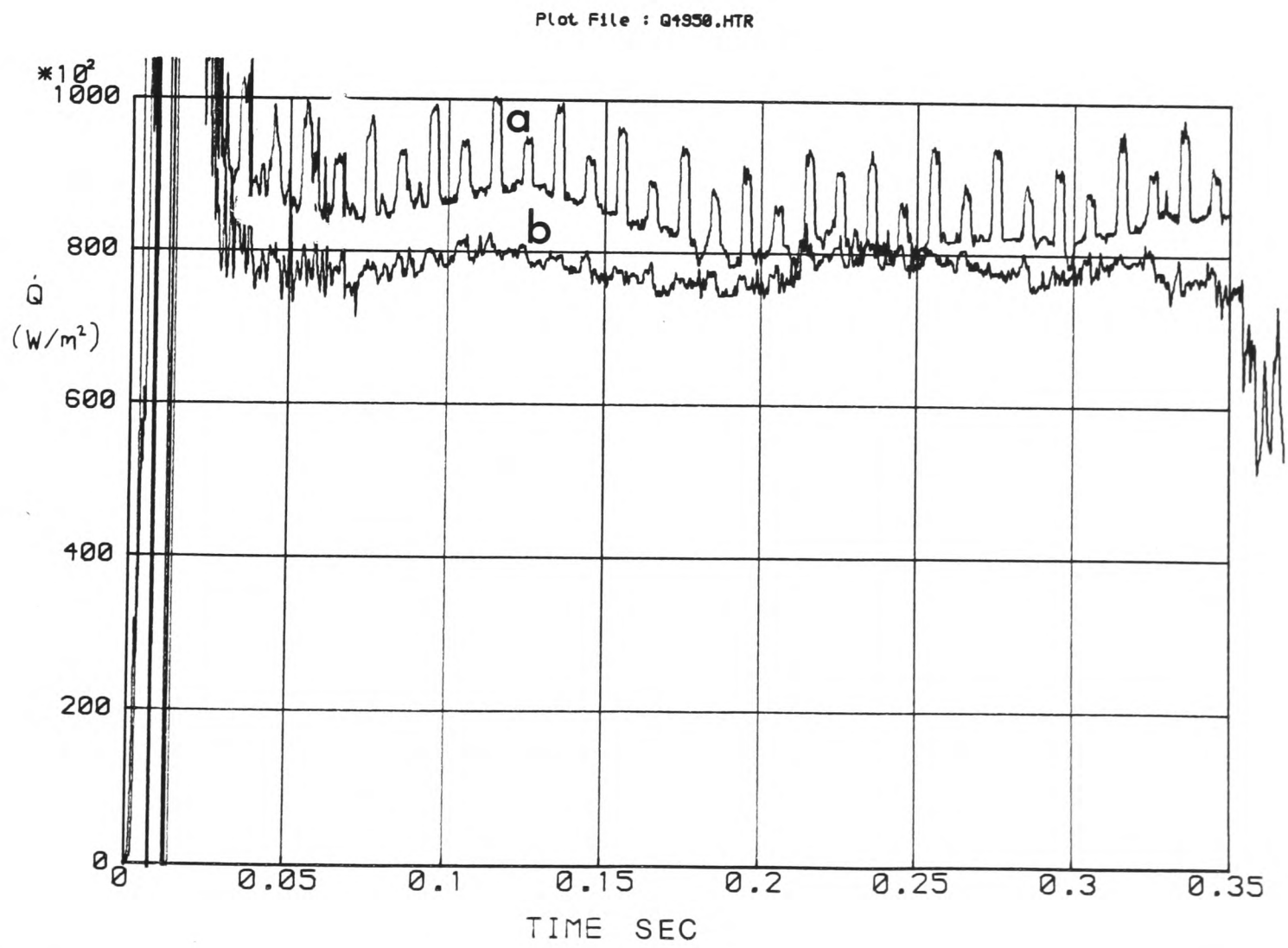

FIG. 7.20 Superimposed heat transfer rate from runs 4949 and 4950.

FIG. 7.21 Effect of imposing a 20kW pulse for 20ms on two-layered model.

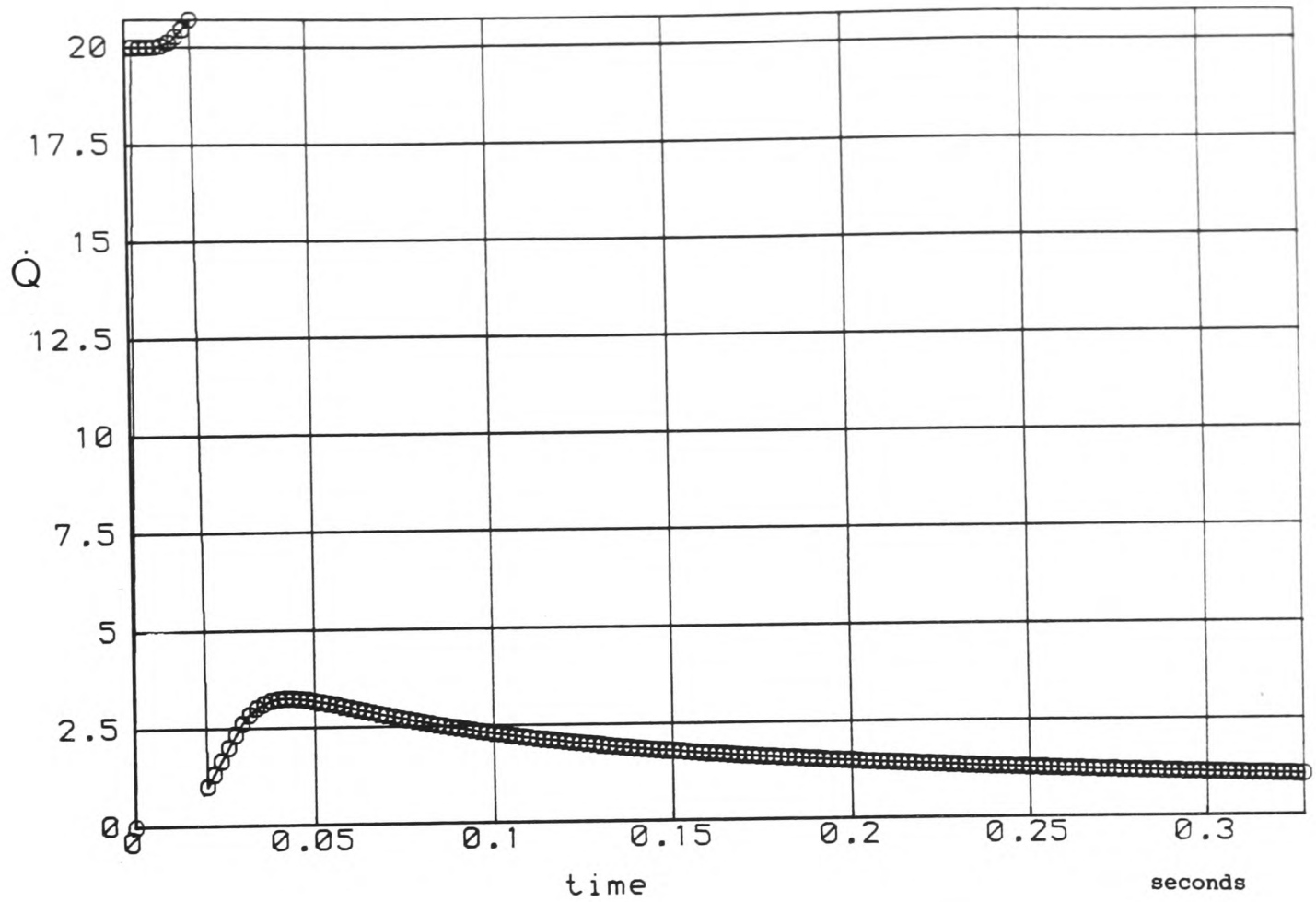

FIG. 7.22

Processed transient recorder sampled data

run 4956

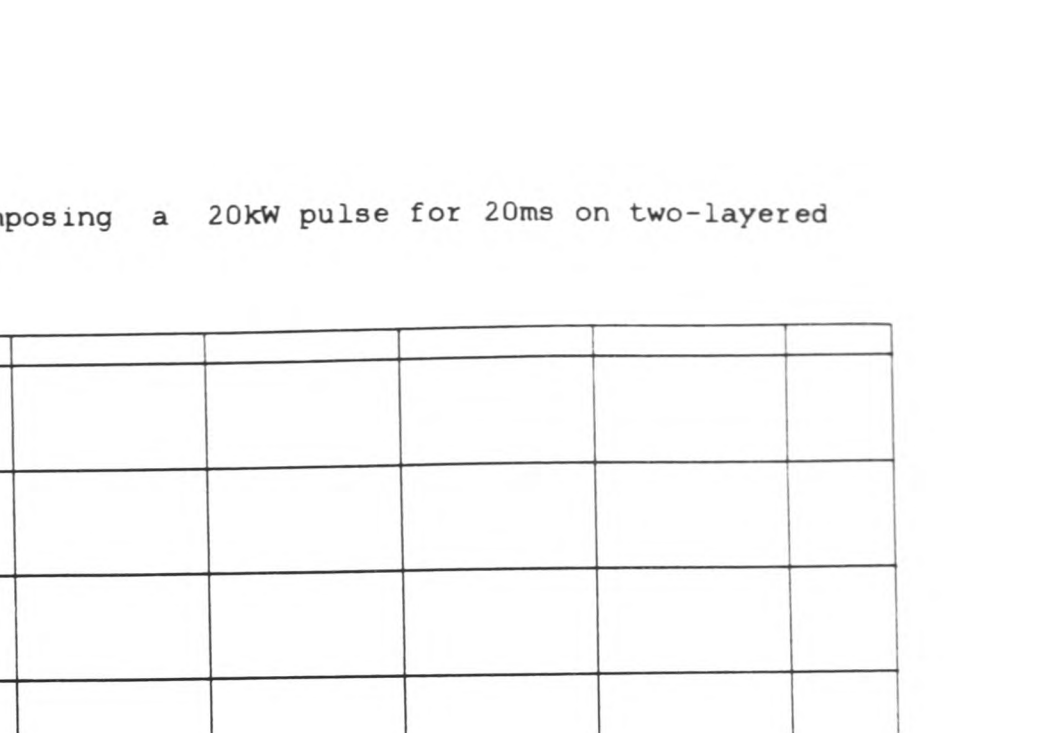

Processed computer sampled data

run 4956.